Faculteit Wetenschappen - Departement Fysica

Theory of quantum systems and complex systems

Phase transitions in driven-dissipative many-body quantum systems: Gutzwiller quantum trajectories and a study of mean-field validity

Proefschrift voorgelegd tot het behalen van de graad van doctor in de wetenschappen: fysica aan de Universiteit Antwerpen te verdedigen door

Dolf Huybrechts

Promotor
Prof. dr. Michiel Wouters

Antwerpen, 2021

Members of the jury

Prof. dr. Milorad Milošević (chair) - *University of Antwerp*
Prof. dr. Nick Van Remortel - *University of Antwerp*
Prof. dr. Michiel Wouters (supervisor) - *University of Antwerp*
Prof. dr. Davide Rossini - *University of Pisa*
Prof. dr. Vincenzo Savona - *École polytechnique fédérale de Lausanne*

List of publications

- D. Huybrechts and M. Wouters, "Cluster methods for the description of a driven-dissipative spin model", Phys. Rev. A **99**, 043841 (2019).
- D. Huybrechts, F. Minganti, F. Nori, M. Wouters, and N. Shammah, "Validity of mean-field theory in a dissipative critical system: Liouvillian gap, $\mathbb{PT}$-symmetric antigap, and permutational symmetry in the XYZ model", Phys. Rev. B **101**, 214302 (2020).
- D. Huybrechts and M. Wouters, "Dynamical hysteresis properties of the driven-dissipative Bose-Hubbard model with a Gutzwiller Monte Carlo approach", Phys. Rev. A **102**, 053706 (2020).

These publications are cited in the main text as [1–3].

Acknowledgements

"Writing a book is a horrible, exhausting struggle,
like a long bout with some painful illness.
One would never undertake such a thing if one were not driven on
by some demon whom one can neither resist nor understand."
- George Orwell

With this thesis I conclude the four years of working on my PhD. It contains a majority, but certainly not all, of my work on my adventures in quantum physics. And contrary to what one may think after reading the above quote, it was an absolute joyful and enriching experience that I would repeat in a heart beat. Naturally, I have to thank many people for their help, guidance, and support throughout these years. First and foremost I wish to express my utmost thanks to my supervisor prof. dr. Michiel Wouters for giving me the opportunity of pursuing a PhD under his excellent supervision. His ability to patiently explain complicated subjects in an easily understandable and rigorous way as well as his availability whenever such question arose (and believe me, they arise a lot), made that I have spent these years in an extremely suitable research environment. Combined with the freedom and independence he gives his PhD students, one could not ask for anything more in a supervisor. I also need to thank prof. dr. Jacques Tempere, my master thesis supervisor and head of our group, for bringing me into contact with prof. Wouters and this thesis subject four years ago. Without doubt his guidance, teaching and help have led me to where I am today.

And this brings me to the group of people with whom I had the privilege to share these doctoral studies, my peers and co-workers in the TQC group. They are also a big part of the reason why this research environment was so enjoyable over the last years. Whenever someone needed something, another would gladly offer help and assistance. I will remember the absolute ludicrous discussions that were held during our lunch breaks, which were welcome distractions throughout a day of hard work. They also made me realise where the movie clichés of super villian physicists come from... Thank you for all the fun Nick, Wouter (x2), Wout,

Mathias, Senne, Dietrich, Timour, Matthew and Lennart. I wish to express my explicit thanks to my direct co-workers dr. Mathias Van Regemortel and dr. Wouter Verstraelen for numerous useful discussions, and I sincerely hope we have the opportunity to continue collaborating in the future. I also want to thank Senne Van Putte for the discussions we had on the thesis subject.

During my PhD I had the privilege to come into contact with many interesting and knowledgeable people. I am to be called lucky to have met and have been able to collaborate with prof. dr. Franco Nori, dr. Nathan Shammah, and dr. Fabrizio Minganti. As far as collaborators go I am sure they are among the best out there. They have immersed me in an extremely pleasant and interesting research cooperation, taking me under their wing and guiding me throughout this journey. I am happy to have gotten to know you. I want to express my utmost thanks and gratitude to dr. Fabrizio Minganti, especially for all his help during the writing of this manuscript and during the preparation of the defence. His availability any time I asked, his suggestions, remarks, and effort were indispensable and are highly appreciated. My thanks also goes to Michele Pugno for his assistance with computational problems.

Of course these years also contained moments of hardship as well as quite a few curses (as you could imagine after reading the quote). I wish to thank my family, and especially my parents for creating the opportunities to arrive where I am now. Their unyielding support and encouragement is all I could ask for. I also thank my girlfriend's family for their interest and support as well as creating a warm envirionment ideal for concentrating on my research. A very special thanks goes to my girlfriend as she is without doubt the one who experienced and helped me get through the rough parts. If there was any doubt already, it is a certainty now that I can be quite the workaholic. Thank you for your understanding and patience with me. Your support and love has helped me to get through this, you are my rock.

I also thank the members of the jury for their thorough reading of the thesis, suggestions, and remarks. Their interesting questions and our discussions have broadened my view and allowed me to improve the manuscript.

Dolf Huybrechts

Samenvatting

Faseovergangen in gedreven-dissipatieve veeldeeltjes kwantumsystemen: Gutzwiller-kwantumtrajecten en een studie van de geldigheid van de gemiddeld veld benadering

Het is ongeveer honderd jaar geleden dat de grote denkers van het begin van de twintigste eeuw een theorie hebben geïntroduceerd die de wetten van de fysica op de kleinste schaal behandelt. De nood aan de ontwikkeling van deze theorie vond zijn oorsprong in het falen van de klassieke fysica om fenomenen als het spectrum van een zwarte straler en het foto-elektrisch effect te beschrijven. Een cruciale observatie was dat licht kan worden gediscretiseerd in kleine pakketjes energie, energiekwanta, die we nu fotonen noemen. Dit is ook waar de baanbrekende theorie de oorsprong van zijn naam vindt: kwantumfysica. Ze is gebaseerd op de verbijsterende notie dat een foton zich als een golf en als deeltje kan gedragen. Uit het dubbele spleet experiment is overigens gebleken dat elk object dat klein genoeg is, zoals een elektron, ook zulk gedrag vertoont. Bovendien hangt het gedrag in hoge mate af van het feit of het wordt geobserveerd of niet, evenals van de manier waarop het wordt geobserveerd. Maar dat is niet alles: volgens de regels van de kwantumfysica kan een object zich in meerdere toestanden tegelijk bevinden. Denk bijvoorbeeld aan het beroemde gedachte-experiment van "Schrödingers kat", maar dan met een heel kleine kat. Deze kwantumtheorie, die ons voorziet van wetten voor materie op de kleinste schaal, heeft geleid tot een revolutie in de fysica. Ze opent een enorm perspectief aan mogelijkheden voor theoretisch en experimenteel onderzoek en technologische vooruitgang. Ze vormt de basis van geavanceerde technologieën, bijvoorbeeld vanwege het vermogen om de werking van halfgeleiders te beschrijven.

In de afgelopen decennia hebben experimentele vooruitgang en technologische verbeteringen toegang gegeven tot een hele reeks kwantumsystemen die zeer nauwkeurig kunnen worden gecontroleerd. Naast het gebruik van kwantumfysica om fysische verschijnselen te verklaren en te beschrijven, zijn onderzoekers in staat

een hele reeks interessante kwantumsystemen te ontwikkelen en hun eigenschappen te benutten om allerlei toepassingen te bedenken. Dit heeft geleid tot de verkenning van nieuwe kwantumtechnologieën zoals kwantumcomputing en kwantumsimulatie. Hiernaar wordt vaak gerefereerd als een nieuwe revolutie in de wereld van de kwantumfysica, namelijk de tweede kwantumrevolutie.

Een veelheid aan systemen die van belang zijn voor kwantumsimulatie en kwantumtechnologieën bevinden zich in het gebied van kwantumoptica. Dit is de theorie die beschrijft hoe licht op kwantumniveau interageert met materie. Een eigenschap van kwantumoptische systemen is dat licht de neiging heeft om gemakkelijk naar een omgeving te worden gedissipeerd. Anders gezegd, fotonen kunnen vrij gemakkelijk uit het systeem van interesse ontsnappen. Energieverliezen zijn hierbij onvermijdelijk. Een dergelijk systeem wordt een open kwantumsysteem genoemd en vereist een beschrijving die fundamenteel verschilt van gesloten kwantumsystemen waar dergelijke verliezen niet aanwezig zijn.

De vooruitgang in de beschikbare experimentele platformen en het vermogen om uitgebreide systemen experimenteel te bestuderen, hebben ook geleid tot een verhoogde interesse in de theoretische beschrijving van deze veeldeeltjes open kwantumsystemen. Een moeilijkheid in de theoretische studie is de schaarste aan exacte analytische oplossingen. Dit hangt samen met het ontbreken van het concept van vrije energie in deze open systemen. Daarom is men meestal gedwongen om de dynamica van deze systemen numeriek te simuleren. Echter, net als bij gesloten kwantumsystemen, loopt men al snel tegen de beperkingen aan van een zeer snel groeiende Hilbertruimte waarmee rekening moet worden gehouden als het systeem wordt vergroot. Neem bijvoorbeeld een veeldeeltjessysteem dat bestaat uit een aantal twee-niveausystemen: al voor een klein aantal wordt dit snel onhandelbaar op hedendaagse computers. Exacte (numerieke) oplossingen zijn daardoor meestal beperkt tot systemen van ongeveer twintig twee-niveausystemen. Voor systemen met meer dan twee niveaus zijn exacte oplossingen al snel volledig onhaalbaar. Bovendien, als men de dichtheidsmatrix rechtstreeks wil oplossen of als men in het Liouvillian-superoperatorformalisme wil werken, wordt de beperking zelfs nog strenger. Omdat men gewoonlijk geïnteresseerd is in de thermodynamische limiet, b.v. voor de studie van faseovergangen, is dit uiteraard een grote beperking.

Over het algemeen moet men dus zijn toevlucht nemen tot benaderingsmethoden om de fysica van deze systemen te beschrijven. De geldigheid van deze benaderingen is natuurlijk modelafhankelijk, en wordt meestal ook sterk beïnvloed door de parameterregimes van het model. In het afgelopen decennium is er veel

theoretisch werk geleverd om methoden te ontwikkelen die de simulatie van deze veeldeeltjes open kwantumsystemen mogelijk maken. Deze inspanningen zijn nog steeds aan de gang. In deze thesis zullen we ons concentreren op twee paradigmatische systemen die in de literatuur veel interesse hebben opgewekt vanwege hun algemeenheid. Het eerste is een model waarmee we spinsystemen kunnen bestuderen: het XYZ anisotrope Heisenberg-model met dissipatie. Ten tweede bestuderen we een bosonisch systeem beschreven door het Bose Hubbard-model met dissipatie, d.w.z. een systeem waarbij fotonen op elke site met elkaar interageren en de mogelijkheid hebben om naar naburige sites te springen. Eerst zullen we de geldigheid van de aanname van het gemiddelde veld bestuderen in volledig geconnecteerde open kwantumsystemen. Hiertoe bekijken we een methode die de permutationele invariantie in deze systemen benut, waardoor een exacte kwantumbeschrijving mogelijk is tot ongeveer honderd spins. Deze methode wordt vervolgens toegepast op het dissipatieve volledig geconnecteerde XYZ Heisenberg-model, waarin we een dissipatieve faseovergang bestuderen die samenhangt met het breken van een $\mathbb{Z}_2$-symmetrie. Onze berekeningen laten zien dat de gemiddeld veld theorie in de thermodynamische limiet correct is in alle parameterregimes. Voor een intermediair aantal spins en voor grote anisotropie vinden we echter een significant verschil tussen de resultaten van de gemiddeld veld theorie en die van de volledige kwantumsimulatie. Onze resultaten laten zien dat de convergentie naar de gemiddeld veld resultaten onverwacht traag is. We hebben ook indicatoren van de faseovergang bestudeerd die kunnen worden gebruikt voor eindige-grootte studies, namelijk de bimodaliteitscoëfficiënt en de hoekgemiddelde-susceptibiliteit. In tegenstelling tot de bimodaliteitscoëfficiënt, slaagt de hoekgemiddelde-susceptibiliteit er niet in om de overgang vast te leggen. Dit is een opvallend verschil met betrekking tot lager-dimensionale studies. Vervolgens passen we dezelfde methode toe op het gedreven-dissipatieve volledig geconnecteerde Bose-Hubbard-model met sterke niet-lineariteit en getrunceerd tot p niveaus. We hebben geanalyseerd of een faseovergang, overeenkomend met een multistabiliteit in de gemiddeld veld resultaten, nog steeds aanwezig is in het volledig geconnecteerde model. Hiervoor hebben we een toolbox in Python ontwikkeld om de tijdsevolutie van volledig geconnecteerde p-niveau systemen te simuleren. Dit stelt ons in staat het volledig geconnecteerde model voor toenemende systeemgroottes exact te onderzoeken. We concentreren ons op een parameterregime waarbij de gemiddeld veld theorie tot vijf oplossingen voorspelt, wat resulteert in een rijk fasediagram. Een stabiliteitsanalyse heeft twee stabiele oplossingen aangetoond, alsook het ontstaan van tijdkristallijn

gedrag. Onze volledige kwantumstudie toont bewijs voor de aanwezigheid van een eerste-orde faseovergang, toegeschreven aan de multistabiliteit in de gemiddeld veld oplossingen, evenals een opkomende tristabiliteit die mogelijks gerelateerd is aan het bestaan van het tijdkristal dat in de gemiddeld veld oplossing aanwezig is. Een studie van het spectrum van de Liouvillian laat echter geen duidelijke tekenen zien van het ontstaan van imaginaire eigenwaarden waarvan het reële deel naar nul gaat naarmate de systeemgrootte toeneemt.

Na de geldigheid van het gemiddelde veld te hebben bestudeerd, voeren we een simulatiemethode in die het mogelijk maakt om verder te gaan dan de gemiddeld veld aanname. We introduceren de cluster-Gutzwiller Monte Carlo-methode, een kwantumtrajectbenadering waarmee zowel korte-afstandskwantumcorrelaties als klassieke lange-afstandscorrelaties kunnen worden opgenomen. Deze methode wordt toegepast op de studie van een dissipatieve faseovergang van een paramagnetische naar een ferromagnetische fase in een twee-dimensionaal kubisch rooster. De resultaten worden vergeleken met een geclusterde gemiddeld veld benadering. Rekening houdend met roosters van eindige grootte toonden we het ontstaan van een ferromagnetische fase, twee paramagnetische fasen en het mogelijke bestaan van een faseovergang die volledig kwantum van aard is aan. De inclusie van korte-afstandskwantumcorrelaties heeft een drastisch effect op het fasediagram, maar onze resultaten tonen aan dat het gebruik van lange-afstandskwantumcorrelaties essentieel is of dat het gebruik van meer geavanceerde methoden nodig is om de exacte resultaten kwantitatief te beschrijven. Een onderzoek naar de susceptibiliteitstensor toont aan dat de reciprociteit wordt gebroken, een eigenschap die niet wordt waargenomen in gesloten kwantumsystemen. Bovendien onderdrukt het vergroten van het magnetische veld de magnetisatie, wat ook in schril contrast staat met gesloten kwantumsystemen.

De cluster-Gutzwiller Monte Carlo methode wordt ook toegepast op het gedreven dissipatieve Bose Hubbard-model. Onder invloed van klassieke lange-afstandscorrelaties en korte-afstandskwantumcorrelaties worden de dynamische eigenschappen in een sterk interagerend regime bestudeerd. Door het dynamische hysteresis-oppervlak te bestuderen dat ontstaat door het sweepen door de coherente aandrijving, laten we zien dat het fasediagram voor dit systeem in kwalitatieve overeenstemming is met het Gutzwiller gemiddeld veld resultaat. Er zijn echter kwantitatieve verschillen en het opnemen van klassieke en kwantumcorrelaties veroorzaakt een significante verschuiving van de kritische parameters. Bovendien toonden we aan dat benaderingstechnieken die steunen op een unimodale verdeling,

zoals het gemiddelde veld en $1/z$ expansie, de fluctuaties in het aantal deeltjes drastisch onderschatten.

Ten slotte presenteren we een nieuwe methode om het laaggelegen spectrum van de Liouvillian efficiënt te bepalen. Ze biedt een uitstekende tool om de stationaire toestand van een dissipatief systeem nauwkeurig te berekenen, en om toegang te krijgen tot het deel van het spectrum dat het meest relevant is voor dynamica over langere tijden. Bovendien is het met deze methode, omdat ze gebaseerd is op tijdevolutie, mogelijk om het spectrum te berekenen voor systemen die anders onhandelbaar zouden zijn met een exacte methode. Onze resultaten kunnen worden uitgebreid tot generieke methoden voor tijdsevolutie, waardoor de langzaam vervallende processen al met een relatief korte tijdsevolutie kunnen worden beschreven.

Contents

CHAPTER 1

Overview

In this thesis the description of many-body open quantum systems governed by a Lindblad master equation will be studied. More specifically, questions such as the validity of the mean-field assumption in these open system will be adressed, as well as the influence of short-range quantum correlations and long-range classical correlations on the steady state and the dynamics of these systems. Furthermore, we introduce an efficient (numerical) method to calculate the low-lying spectrum of the Liouvillian superoperator.

In part I of this thesis we discuss the theory of open quantum systems. In chapter 2, we start by reviewing closed system time evolution and discuss how to treat a system that is coupled to an environment, more specifically a system which is weakly coupled to a Markovian environment. We first derive the Lindblad master equation through physical considerations and the application of several approximations. Thereafter, we give with an approach that is more closely connected to quantum information theory, an equivalent derivation. Through this approach we also introduce the quantum trajectory method. A discussion on the Liouvillian superoperator follows, and finally we discuss dissipative phase transitions. In chapter 3 we consider two paradigmatic models in the study of many-body quantum physics with light and matter. We discuss the dissipative XYZ Heisenberg model, as well as the driven-dissipative Bose Hubbard model. Mean-field results are examined and several methods to go beyond the mean-field are discussed.

In part II we will study the validity of the mean-field assumption in all-to-all connected open quantum systems. To this end, we review a method to exploit the permutational invariance present in these systems, allowing for an exact quantum description, in chapter 4. In chapter 5, this is applied to the dissipative all-to-all connected XYZ Heisenberg model where we study a dissipative phase transition

associated with the breaking of a $\mathbb{Z}_2$ symmetry. In chapter 6 we examine the driven-dissipative all-to-all connected Bose-Hubbard model with strong nonlinearity. We analyze whether or not a phase transition, corresponding to a multistability in the mean-field results, is still present in the all-to-all connected model. Furthermore, we explore the predictiveness of the mean-field results for the dynamics of the system in addition to its correspondence in the steady state.

After having studied the mean-field validity we introduce a simulation method that allows to go beyond mean-field in part III. In chapter 7 we present the cluster-Gutzwiller Monte Carlo method, a quantum trajectory approach that allows for the inclusion of short-range quantum correlations as well as long-range classical correlations. This method is applied to the study of a dissipative phase transition from a paramagnetic to a ferromagnetic phase, predicted by the mean-field approach, in a two-dimensional cubic lattice. Its results are compared with a cluster mean-field approach. Several peculiarities with respect to closed quantum systems are discussed. In chapter 8 the cluster-Gutzwiller Monte Carlo is applied to the driven-dissipative Bose Hubbard model. The dynamical properties in a strongly interacting regime are studied under the influence of short-range quantum correlations and long-range classical correlations.

In part IV we introduce a numerical method to efficiently and exactly determine the low-lying spectrum of the Liouvillian superoperator. In chapter 9 we discuss the Arnoldi method and generalize its utilization to the problem of open quantum systems described by a Lindblad master equation. The method is applied to several systems as a proof of concept.

Finally, in part V in chapter 10 we discuss the general conclusions and outlook of this thesis.

PART

I

OPEN QUANTUM SYSTEMS

CHAPTER 2

Theory of open quantum systems

It has been roughly a hundred years since the great minds of the early twentieth century have introduced a theory dealing with the laws of physics at the smallest scales. The need for the development of this theory found its origin in the failure of classical physics to describe phenomena like black body radiation and the photoelectric effect. One crucial observation was that light can be discretized in small packets of energy, quanta of energy, which is what we now call photons. This is also where the groundbreaking theory finds the origin of its name: quantum physics. It constitutes the mind-boggling notions that a photon can behave like either a wave or a particle, and any object that is small enough for that matter, e.g. an electron, as shown by the double slit experiment. Furthermore, its behavior highly depends on whether it is being observed or not, as well as the way it is observed. But that is not all, according to the rules of quantum physics, an object can be in several states at the same time, think for example of the famous thought experiment of "Schrödinger's cat", but with a very small cat.

This quantum theory which provides us with laws for matter at the smallest scales has led to a revolution in physics, opening a huge field of theoretical and experimental research and technological advances. It lies at the core of advanced technologies, for example because of its ability to describe the workings of semiconductors.

In the last few decades experimental progress and technological improvements have allowed access to a whole range of quantum systems that can be highly controlled. Besides the usage of quantum physics to explain and describe physical phenomena, researchers are able to engineer a whole range of interesting quantum systems and exploit their properties to devise useful systems. This has granted access to the exploration of new quantum technologies such as quantum computing and quantum simulation. This is often referred to as a new revolution in the world

of quantum physics, the *second quantum revolution*.

Many of the systems of interest for quantum simulation and quantum technologies are situated in the field of quantum optics. This is the theory that describes how light interacts with matter on a quantum level. A property of quantum optical systems is that light tends to be easily dissipated to an environment. Differently said, photons can escape quite easily from your system of interest and energy losses are unavoidable. Such a system is called an *open quantum system*, and requires a description that is fundamentally different from *closed quantum systems* where such losses are not present. In this chapter we will give a short summary of the time evolution in closed quantum systems and subsequently move on to discuss the theory of open quantum systems in more detail.

2.1 Closed system time evolution

The theory of closed quantum systems is part of the curriculum of any aspiring physicist. In this chapter we will give a very short overview of the basics of this theory [4, 5]. The postulates of quantum mechanics dictate that the time evolution of a state $|\psi(t)\rangle$ of a quantum system governed by a Hamiltonian $\hat{H}_S(t)$ is given by the Schrödinger equation

$$\frac{d}{dt}|\psi(t)\rangle = -i\hat{H}_S(t)|\psi(t)\rangle, \tag{2.1}$$

where we have set $\hbar$ equal to 1, as will be the convention in this thesis. This time evolution can also be expressed in terms of a unitary operator since the Hamiltonian $\hat{H}_S(t)$ is Hermitian. The solution to the Schrödinger equation then reads

$$|\psi(t)\rangle = \hat{U}(t, t_0)|\psi(t_0)\rangle, \tag{2.2}$$

where the unitary operator is given by

$$\hat{U}(t, t_0) = T_{\leftarrow} e^{-i\int_{t_0}^{t} \hat{H}_S(s)ds}, \tag{2.3}$$

with $T_{\leftarrow}$ the time ordering operator, ensuring that in a product of operators, they are ordered from right to left with increasing time arguments. When the Hamiltonian is time independent this operator reduces to

$$\hat{U}(t, t_0) = e^{-i\hat{H}_S(t-t_0)}. \tag{2.4}$$

Another way to describe the state of the system is through the density matrix. It allows one to describe the quantum state of systems of which the state is not entirely known. In other words, when the system resides in a state $|\psi_r(t)\rangle$ with a certain probability p_r for a collection of pure states $\{|\psi_r(t)\rangle\}$. Such a system is said to be in a mixed state. The density matrix can then be written as

$$\hat{\rho}(t) = \sum_r p_r |\psi_r(t)\rangle\langle\psi_r(t)|, \tag{2.5}$$

for which the probabilities p_r to be in a state $|\psi_r(t)\rangle$ have to sum to one. This is equivalent to ensuring that the density matrix represents a physical state. Formally, a general density matrix $\hat{\rho}$ has to satisfy several conditions to ensure its physicality:

- have trace equal to one: $\mathrm{Tr}\,[\hat{\rho}] = 1$,
- be Hermitian: $\hat{\rho} = \hat{\rho}^\dagger$,
- have nonnegative eigenvalues.

Note that the last two properties coincide with the density matrix being a positive semidefinite matrix.

The time evolution of such a density matrix can be obtained from the Schrödinger equation through the product rule

$$\frac{d}{dt}\hat{\rho}(t) = -i\left[\hat{H}_S, \hat{\rho}(t)\right]. \tag{2.6}$$

This then results in what is called the Liouville-von Neumann equation. It is this equation, or equivalently the Schrödinger equation, that allows one to calculate the time dynamics of a closed quantum system.

2.2 Open system time evolution

In the previous section we discussed the time evolution of a system under Hamiltonian dynamics, i.e. a closed quantum system. The system was described using only its own degrees of freedom, or in other words, the system was completely decoupled from any environment. In reality, however, this is a rather idealistic representation as the systems of our interest are usually part of a bigger system. A classical analog is for example the need to take into account a friction force when calculating the equations of motion for a falling object in our atmosphere.

Such a friction force finds its origin in the interaction of the falling object with its environment. In a quantum description the system can also be in contact with an environment, and exchange e.g. energy, particles, ... In what follows, when we talk about an environment we mean an environment that has relevant interactions with your system of interest. Differently said, it is an environment that is of importance for the description of the dynamics of the system of interest. There exist a whole range of possible environments, e.g. a heat bath, the electromagnetic vacuum, ... The coupling between this environment and the system can of course be very weak, but even then the influence of the environment cannot be trivially neglected. It is thus of great interest to create a theoretical framework dedicated to the description of these so-called open quantum systems. The theory is well established and a number of great textbooks exist, going into deep detail in the derivations of equations governing open system time evolution [5–8]. Generally, one assumes that the combination of the system of interest and its environment can be treated as a closed system in itself. Naively, one could expect that the framework for closed quantum systems is thus applicable. Unfortunately, the environments tend to be very complicated and they contain an immense amount of degrees of freedom. This makes it intractable to solve the combined dynamics. Depending on the type of environment, and its interaction with the system one usually can simplify this description through the application of several approximations. In what follows we will derive a master equation for the description of a certain class of open systems.

First, let us denote the Hamiltonian of the system of interest as $\hat{H}_S$. This is the system of which one wants to calculate observables and physical properties. The Hamiltonian of the environment will be denoted as $\hat{H}_E$, and the interaction between both the system and the environment as $\hat{H}_I(t)$. The Hamiltonian of the combined system can then be written as

$$\hat{H}_{S+E} = \hat{H}_S \otimes \mathbb{1}_E + \mathbb{1}_S \otimes \hat{H}_E + \hat{H}_I(t). \tag{2.7}$$

We have chosen to include time-dependent interactions, naturally one can also include time-dependent terms in the Hamiltonian describing the system, as well as the Hamiltonian describing the environment. Equation (2.7) immediately shows where one runs into difficulties when describing this combined system when the environment has a large number of degrees of freedom. Indeed, the combined Hilbert space can be written as the Kronecker product of the individual Hilbert

spaces of the system S and environment E

$$\hat{\mathcal{H}}_{S+E} = \hat{\mathcal{H}}_S \otimes \hat{\mathcal{H}}_E, \tag{2.8}$$

quickly making the description of the combined system intractable due to an enormous Hilbert space size. However, nothing is withholding us from writing down the equation governing the time evolution. Since we assumed that the combined system can be treated as a closed quantum system, this is governed by a Liouville-von Neumann equation

$$\partial_t \hat{\rho}_{S+E}(t) = -i \left[\hat{H}_{S+E}, \hat{\rho}_{S+E}(t)\right], \tag{2.9}$$

with $\hat{\rho}_{S+E}$ the density matrix of the combined system, and is thus unitary. Since we are interested only in the dynamics of S, one can remove the degrees of freedom of the environment E by tracing them away. This yields the reduced density matrix of the system $\hat{\rho}_S$

$$\hat{\rho}_S(t) = \mathrm{Tr}_E \left[\hat{\rho}_{S+E}(t)\right], \tag{2.10}$$

which we will call the system density matrix from now on. Note that due to the interaction with the environment the time evolution of this system density matrix generally can no longer be described through a unitary time evolution. In the next section we will derive a quantum master equation valid under certain assumptions that takes into account the influence of the environment and describes this non-unitary time evolution.

2.3 The Lindblad master equation

In the following we will present a derivation scheme for the evolution of an open quantum system which is *weakly coupled* to its *Markovian* environment. That is, an environment that has no memory of earlier interactions with the system. This is usually true for a very large environment, with respect to a small system. Indeed, an environment with an enormous amount of degrees of freedom will only be negligibly influenced by its weak interaction with a small system. Moreover, if the time at which correlations in the environment decay is small with respect to the time at which our system changes the assumption of a Markovian environment is well justified. Starting from the Liouville-von Neumann equation of the combined system in the interaction picture we will go through the steps where approximations,

endorsed by the above properties of the environment, lead to a simplified and elegant master equation [5, 6, 9].

First, let us make some assumptions regarding the properties of the system-environment coupling. Assume that at $t = 0$ their exist no no correlations between the system and the environment, i.e. $\hat{\rho}_{S+E}(0) = \hat{\rho}_S(0) \otimes \hat{\rho}_E(0)$. Moreover, since we assume a weakly-coupled environment, this will allow us to decouple the combined density matrix at *any* time $t \geq 0$ as

$$\hat{\rho}_{S+E}(t) = \hat{\rho}_S(t) \otimes \hat{\rho}_E, \tag{2.11}$$

since the build-up of correlations in the immense environment due to the small system will be negligibly small. This is also known as the *Born approximation*. The influence of the large environment on the small system, however, will not be negligible. Let us begin with the derivation, if we write down the Liouville-von Neumann equation in the interaction picture

$$\partial_t \hat{\rho}_{S+E}(t) = -i \left[\hat{H}_I(t), \hat{\rho}_{S+E}(t)\right], \tag{2.12}$$

it can be formally solved as

$$\hat{\rho}_{S+E}(t) = \hat{\rho}_{S+E}(0) - i \int_0^t dt' \left[\hat{H}_I(t'), \hat{\rho}_{S+E}(t')\right]. \tag{2.13}$$

By substituting this equation into (2.12) and tracing out the environment we gain an equation for the time evolution of the system density matrix up to second order in the system-environment coupling

$$\partial_t \hat{\rho}_S(t) = -\int_0^t dt' \mathrm{Tr}_E\Big[\left[\hat{H}_I(t), \left[\hat{H}_I(t'), \hat{\rho}_S(t') \otimes \hat{\rho}_E\right]\right]\Big]. \tag{2.14}$$

Where the *Born approximation* was applied and we have substituted the expression $\mathrm{Tr}_E\left[\hat{H}_I(t), \hat{\rho}_{S+E}(0)\right] = 0$, which can be done without loss of generality [10]. One should note that this equation still depends on the whole history of the system $\hat{\rho}_{S+E}(t') = \hat{\rho}_S(t') \otimes \hat{\rho}_E$. This is not desirable and is where the assumption of the Markovian nature will come into play. Indeed, this so-called *Markov approximation* allows us the neglect any memory of previous state configurations of the system and re-write the dynamics in what is known as the Redfield equation [11] or the

master equation in the Born-Markov form

$$\partial_t \hat{\rho}_S(t) = -\int_0^t dt' \mathrm{Tr}_E\Big[\big[\hat{H}_I(t), \big[\hat{H}_I(t'), \hat{\rho}_S(t)\otimes\hat{\rho}_E\big]\big]\Big], \tag{2.15}$$

that is, an equation where the future state of $\hat{\rho}_S$ only depends on its present state. The above equation however does not describe a dynamical semigroup. This means that it need not describe a physical time evolution for any initial condition, i.e. it need not be trace preserving and completely positive. To cure this we need to apply a final approximation, known as the *rotating wave approximation*.

Let us consider a quite general interaction Hamiltonian, which can be written as

$$\hat{H}_I = \sum_i \left(\hat{L}_i \otimes \hat{E}_i^\dagger + \hat{L}_i^\dagger \otimes \hat{E}_i\right), \tag{2.16}$$

where $\hat{L}_i$ are eigenoperators of the system Hamiltonian $\hat{H}_S$ and $\hat{E}_i$ act on the environment. Since $\hat{L}_i$ are eigenoperators of $\hat{H}_S$ they obey the commutation relations

$$\big[\hat{H}_S, \hat{L}_i\big] = -\omega_i \hat{L}_i \quad \text{and} \quad \Big[\hat{H}_S, \hat{L}_i^\dagger\Big] = \omega_i \hat{L}_i^\dagger. \tag{2.17}$$

Going to the interaction picture, these commutation relations allow us to write

$$\hat{L}_i(t) = e^{i\hat{H}_S t}\hat{L}_i e^{-i\hat{H}_S t} = e^{-i\omega_i t}\hat{L}_i, \tag{2.18}$$

and analogously for the hermitian conjugate. Substituting this expression for $\hat{H}_I(t)$ into (2.15) results in

$$\begin{aligned}\partial_t \hat{\rho}_S(t) = -\sum_i \sum_j \int_0^t dt' \mathrm{Tr}_E\Big[\big[&\hat{L}_i(t)\otimes\hat{E}_i^\dagger(t) + \hat{L}_i^\dagger(t)\otimes\hat{E}_i(t),\\ &\big[\hat{L}_j(t')\otimes\hat{E}_j^\dagger(t') + \hat{L}_j^\dagger(t')\otimes\hat{E}_j(t'), \hat{\rho}_S(t)\otimes\hat{\rho}_E\big]\big]\Big].\end{aligned} \tag{2.19}$$

One can now explicitly calculate the commutators of the above equation. Subsequently, the degrees of freedom of the environment can be removed from the equation by applying the trace over the environment. This yields terms containing expectation values of the form $\mathrm{Tr}_E\left[\hat{E}_i(t)\hat{E}_j^\dagger(t')\hat{\rho}_E\right] = \langle \hat{E}_i(t)\hat{E}_j^\dagger(t')\rangle_E$. These correlation functions are the correlation functions of the bath. By using the cyclic properties of the trace, that is, $\mathrm{Tr}\,[ABC] = \mathrm{Tr}\,[CAB] = \mathrm{Tr}\,[BCA]$, one can rewrite all terms containing environment operators as correlation functions of the environment. Note that since we assumed the density matrix of the bath $\hat{\rho}_E$ to be

time-independent, i.e. a stationary bath, these correlation functions depend only on the time difference. Under the assumption of quickly decaying correlation functions in the bath with respect to the timescale on which our system changes this thus allows us to make the substitution $t' \to t - s$, as well as increase the limit t of the integral to infinity since the integrand dissapears for t sufficiently large. This is exactly what is assumed for the validity of the *Markov approximation*. If one now substitutes (2.18) one can rewrite the equation, of which we will only show one term for the sake of clarity, as follows

$$\partial_t \hat{\rho}_S(t) = -\sum_{i,j} \left(\int_0^\infty ds e^{i(\omega_i - \omega_j)t} \hat{L}_i^\dagger \hat{L}_j \hat{\rho}_S(t) e^{i\omega_j s} \langle \hat{E}_i(t) \hat{E}_j^\dagger(t-s) \rangle_E + \dots \right). \tag{2.20}$$

It should be clear that the factor $e^{i(\omega_i - \omega_j)t}$ causes the term to quickly oscillate when $\omega_i \neq \omega_j$, resulting in it to average out to zero over the time scales at which $\hat{\rho}_S$ changes significantly. We can thus discard all terms where $i \neq j$, which is called the *rotating wave approximation*. This allows us the rewrite the equation as follows

$$\partial_t \hat{\rho}_S(t) = -\sum_j \left[\left(\frac{\gamma_j}{2} + i\delta_j \right) \hat{L}_j^\dagger \hat{L}_j \hat{\rho}_S(t) + \dots \right], \tag{2.21}$$

where we defined the integral over the correlation function of the environment as

$$\int_0^\infty ds e^{i\omega_j s} \langle \hat{E}_j(t) \hat{E}_j^\dagger(t-s) \rangle \equiv \frac{\gamma_j}{2} + i\delta_j. \tag{2.22}$$

The terms proportional with δ_j will cause a so-called Lamb shift of the energy levels in the Hamiltonian, these terms are usually neglected and we will no longer explicitely write them down in what follows. The coefficients γ_j represent the dissipation rate, i.e. the rate at which your system interacts with its environment. Assuming that the environment is initially in a vacuum state, i.e. $T = 0$, calculation of all remaining terms and after a transformation back to the Schrödinger picture, one finally arives at the following equation, which is known as the Gorini–Kossakowski–Sudarshan–Lindblad equation, or in short, the Lindblad master equation [12, 13]

$$\begin{aligned} \partial_t \hat{\rho}_S(t) &= -i \left[\hat{H}_S, \hat{\rho}_S(t) \right] + \sum_j \frac{\gamma_j}{2} \left(2\hat{L}_j \hat{\rho}_S(t) \hat{L}_j^\dagger - \left\{ \hat{L}_j^\dagger \hat{L}_j, \hat{\rho}_S(t) \right\} \right) \\ &= -i \left[\hat{H}_S, \hat{\rho}_S(t) \right] + \sum_j \gamma_j \mathcal{D} \left[\hat{L}_j \right] \hat{\rho}_S(t), \end{aligned} \tag{2.23}$$

where $\mathcal{D}[\hat{A}]$ represents a Lindblad dissipator of the form

$$\mathcal{D}[\hat{A}]\hat{\rho}_S(t) = \hat{A}\hat{\rho}_S(t)\hat{A}^\dagger - \frac{1}{2}\left(\hat{A}^\dagger\hat{A}\hat{\rho}_S(t) + \hat{\rho}_S(t)\,\hat{A}^\dagger\hat{A}\right). \tag{2.24}$$

For ease of notation we will from now on write the system density matrix $\hat{\rho}_S(t)$ as $\hat{\rho}(t)$. This concludes the derivation, from a physical point of view, of the master equation that governs the time evolution of a Markovian open quantum system. A quick inspection of the master equation shows us that if one were to "turn off" the coupling with the environment, the closed system dynamics governed by the Liouville-von Neumann equation are regained.

2.4 A quantum optical example: radiative damping in an optical cavity

Let us now apply what we have derived in the previous sections to a physical system. A typical example is the radiative damping in an optical cavity. That is, the dissipation of photons confined between two high quality mirrors where the cavity frequency is given by ω_c. As long as this cavity frequency is large with respect to the environment outside of the cavity, one can model the open system through a coupling between the field inside the cavity and the electromagnetic vacuum [14]. Moreover, interactions with the electromagnetic field are generally of Markovian nature, which is why the dynamics of such systems can be described by the Lindblad master equation. The reason for this is that the magnitude of the lifetimes of correlations in the environment are of the order of the inverse of the optical frequency, which is generally around the THz range [5, 7]. The timescale at which the system changes is of the order of the life times of optical excitations, which tend to be of the magnitude of the inverse of the MHz range [5, 7]. Now that we know that the conditions for our approximations are well satisfied we can derive the Lindblad master equation for such a system. We have

$$\hat{H}_S = \omega_c\hat{a}^\dagger\hat{a}, \tag{2.25}$$

for the free energy of the cavity mode. The free energy of the environment is given by

$$\hat{H}_E = \int d\omega\,\omega\hat{b}^\dagger(\omega)\hat{b}(\omega), \tag{2.26}$$

where ω denotes the various modes of the environment, of which we assumed there to be a continuum, hence the integral. And finally, a Hamiltonian describing the interaction between the cavity field and the electromagnetic field of the environment, which can be written as

$$\hat{H}_I = \int d\omega r(\omega) \left(\hat{a}^\dagger + \hat{a}\right) \left(\hat{b}^\dagger(\omega) + \hat{b}(\omega)\right), \tag{2.27}$$

with $r(\omega)$ the coupling strength. A transformation to the interaction picture allows us to write, using the commutation relations (2.17) , the following expression

$$\hat{H}_I(t) = \int d\omega r(\omega) \left(\hat{a}^\dagger \hat{b}(\omega) e^{i(\omega_c - \omega)t} + \hat{a}\hat{b}^\dagger(\omega)) e^{-i(\omega_c - \omega)t}\right), \tag{2.28}$$

where we have neglected the highly oscillating terms, i.e. terms with $\omega_c + \omega$, through the rotating wave approximation. The next step is substituting this into equation (2.20) and noting that we now have $\hat{L}_i(t) = \hat{L}_i e^{-i\omega_i t} = \hat{a}e^{-i\omega_c t}$ and $\hat{E}_i(t) \to \hat{b}(\omega)e^{-i\omega t}$, in the latter we used an arrow to indicate that we are now working in the continuum limit. Once again, only terms where $\omega = \omega'$ (with in the continuum limit, $i \to \omega$ and $j \to \omega'$) will survive due to the rotating wave approximation. Substitution of the interaction Hamiltonian then yields terms of the form of equation (2.22)

$$\frac{\gamma}{2} + i\delta_L \equiv \int_0^\infty ds e^{i\omega_c s} \langle \hat{E}_i(t) \hat{E}_j^\dagger(t-s) \rangle_E \to \int_0^\infty ds \int_0^\infty d\omega r(\omega) e^{i(\omega_c - \omega)s} \langle \hat{b}(\omega)\hat{b}^\dagger(\omega) \rangle_E, \tag{2.29}$$

where the trace over the environment of the environment operators becomes equal to one, $\langle \hat{b}(\omega)\hat{b}^\dagger(\omega)\rangle_E = 1$, due to the bosonic commutation relations. Note that we discarded the terms $\langle \hat{b}(\omega)\hat{b}(\omega)\rangle$ and $\langle \hat{b}^\dagger(\omega)\hat{b}(\omega)\rangle$ since we assumed the environment to be in the vacuum state. Additionally, the term $\langle \hat{b}^\dagger(\omega)\hat{b}^\dagger(\omega)\rangle$ could be neglected due to the rotating wave approximation. For simplicity, let us now also neglect the term δ_L corresponding to the Lamb shift, which would cause a shift in $\omega_c \to \omega_c'$, i.e. $\delta_L \to 0$. If we calculate all non-zero terms and also transform back to the Schrödinger picture, this yields

$$\partial_t \hat{\rho} = -i \left[\hat{H}_S, \hat{\rho}\right] + \frac{\gamma}{2} \left(2\hat{a}\hat{\rho}\hat{a}^\dagger - \left\{\hat{a}^\dagger \hat{a}, \hat{\rho}\right\}\right), \tag{2.30}$$

i.e. the master equation governing the radiative damping in an optical cavity.

In Fig. 2.1 we show the time evolution of this system where the initial state of the system is given by the pure state $|5\rangle$ in the Fock state representation, i.e. an

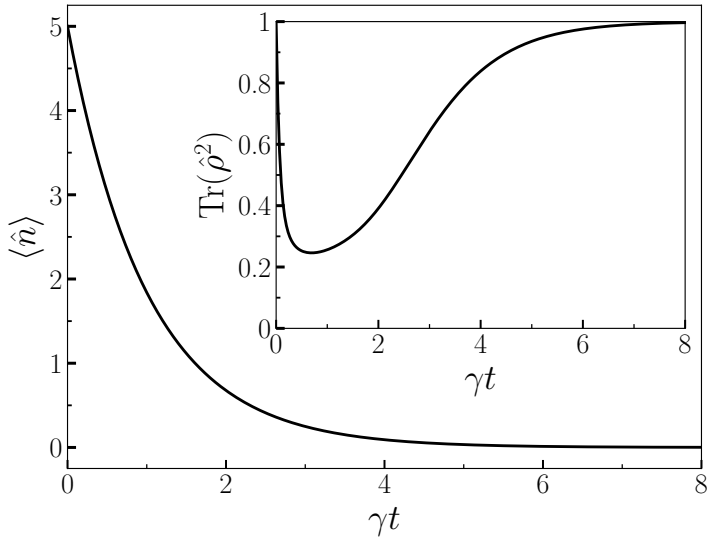

Figure 2.1: *Solution of the expectation value of the particle number* $\langle \hat{a}^\dagger \hat{a} \rangle$ *for an optical cavity where we have chosen* $\omega_c = \gamma = 1$. *The initial state of the system is given by the Fock state* $|5\rangle$. *Inset: the purity of the system's density matrix* $\hat{\rho}(t)$.

occupation of the cavity by five photons. Dissipation to the environment causes the system's state to relax to the pure state $|0\rangle$, i.e. no photons. However, as can be seen from a calculation of the purity of the system's state, shown in the inset of Fig. 2.1, the system's state first passes through a regime where the state becomes mixed. This mixing is due to the interaction of the system with its environment. Since no drive is present, the system evolves back to the pure Fock state $|0\rangle$ due to continuous loss of photons. It should be noted that in systems where a drive is present the system need not evolve to such a pure state, and the state at $t \to \infty$ is generally mixed.

2.5 From a measurement point of view

Previously we have introduced and derived the Lindblad master equation through physical considerations and applying approximations considering the nature of the coupling between the system and the environment. Instead of starting the derivation from the dynamics of the combined system, as we did in the previous section, we can make use of an approach that is more closely connected to quantum information theory. The approach is based on a process called quantum mapping,

that is the mapping of a density matrix into another one [4, 7, 8, 15]. It holds close connection to measurements and it will prove to be useful for the remainder of this chapter, more specifically for the derivation of the quantum trajectory approach in Section 2.6. Nonetheless, we will also use it to once again derive the Lindblad master equation and show its generality as a quantum Markov master equation.

2.5.1 Quantum maps and measurements

First, let us introduce the concept of a *quantum map*, that is a process $\mathcal{S}$ which transforms a density matrix into another one

$$\mathcal{S} : \hat{\rho}(t) \rightarrow \hat{\rho}(t') \Rightarrow \hat{\rho}(t') = \mathcal{S}\hat{\rho}(t), \tag{2.31}$$

where the process $\mathcal{S}$ is often called a super-operator, since it transforms an operator into an operator. Naturally, restrictions exist on the properties of $\mathcal{S}$ for the quantum map to transform a physical state into another physical state. The conditions are the following [7, 8]:
$\mathcal{S}$ is

1. trace preserving;
2. Hermiticity preserving;
3. a convex linear map;
4. is completely positive.

Such a quantum map will ensure that the conditions on the density matrix, introduced in section 2.1, are satisfied at all times. Now that we have introduced the framework needed for the time evolution of a physical state we can switch our attention to the influence of measurements on the system. We shall denote the action of a measurement through the formulation of a set of measurement operators $\hat{M}_r$ acting on the system. Each of these operators corresponds to a possible result r, or read-out, of the measurement experiment. The result of such a measurement will cause the system to be projected on a certain state. Assume a measurement is performed during a time δt, then the read-out result can be written down as

$$\hat{\rho}_r(t + \delta t) = \frac{\hat{M}_r|\psi(t)\rangle\langle\psi(t)|\hat{M}_r^\dagger}{\langle\psi(t)|\hat{M}_r^\dagger\hat{M}_r(t)|\psi(t)\rangle}, \tag{2.32}$$

this follows directly from the fact that the state of the system after the measurement and the read-out of the result can be written as

$$|\psi_r(t+\delta t)\rangle = \frac{\hat{M}_r|\psi(t)\rangle}{\sqrt{\langle\psi(t)|\hat{M}_r^\dagger\hat{M}_r|\psi(t)\rangle}}. \tag{2.33}$$

For ease of notation we define the probability p_r that such a measurement result takes place as

$$p_r = \langle\psi(t)|\hat{M}_r^\dagger\hat{M}_r|\psi(t)\rangle = \mathrm{Tr}\left[\hat{\rho}(t)\hat{M}_r^\dagger\hat{M}_r\right]. \tag{2.34}$$

Naturally, the sum over all possible measurement results should equal one: $\sum_r p_r = 1$, that is, a measurement of your system should always have a certain result r. As such one arrives at the following completeness relation for the set of operators $\hat{M}_r^\dagger\hat{M}_r$ since it has to be valid for any density matrix $\hat{\rho}$

$$\sum_r \hat{M}_r^\dagger\hat{M}_r = \hat{\mathbb{1}}. \tag{2.35}$$

This set of operators $\hat{M}_r^\dagger\hat{M}_r$ is often called a positive operator valued measure (POVM). It consists of all operators associated with possible measurement results. It also allows us to write the action of a measurement operator $\hat{M}_r$ on the density matrix in terms of a quantum map and thus a corresponding super-operator, indeed,

$$\hat{\rho}_r(t+\delta t) = \mathcal{S}_r\hat{\rho}(t) = \frac{\mathcal{M}_r\hat{\rho}(t)}{p_r} = \frac{\hat{M}_r\hat{\rho}(t)\hat{M}_r^\dagger}{p_r}. \tag{2.36}$$

Now assume that measurements are performed on the system, but they are *not* read out, then the state of the system after a time δt consists of the statistical mixture of the different conditional results. One can write

$$\hat{\rho}(t+\delta t) = \mathcal{M}\hat{\rho}(t) = \sum_r p_r\hat{\rho}_r(t+\delta t) = \sum_r \mathcal{M}_r\hat{\rho}(t) = \sum_r \hat{M}_r\hat{\rho}(t)\hat{M}_r^\dagger. \tag{2.37}$$

The last term of this equation is also known as the Kraus representation of the super-operator $\mathcal{M}$. The number of Kraus operators, or thus measurement operators, $\hat{M}_r$ is upper bounded by N^2 [8], with N the Hilbert space dimension of the system described by $\hat{\rho}(t)$. And more interestingly, in general, it can be shown through this Kraus sum formalism that any physical quantum map can be written in terms of at most N^2 Kraus operators [8]. The implications of this are quite noteworthy. As we are ultimately interested in the time evolution of the density matrix $\hat{\rho}(t)$

under influence of an environment, this implies that independently of the nature of this environment, this time evolution can be written down in terms of a set of operators bound by the square of the Hilbert space size of the system under consideration.

We have thus shown that the time evolution of a system's density matrix subject to measurements can be written in terms of a Kraus sum constituted by a set of measurement operators. This will prove quite useful for the derivation of the Lindblad master equation. The reason for this lies in the close connection of a measurement and its relation to an environment: for the performance of a measurement on the system the measurement apparatus can by all means be seen as an environment itself, and vice versa. Without an observer present to read-out the results the time evolution of such a system can thus be written as (2.37). It is this correspondence between measurements and the environment that can be exploited, and can also be used for a better understanding of the generality of the Lindblad master equation.

2.5.2 The master equation

We will now use the framework introduced in the previous subsection to make a derivation of the Lindblad equation (2.23). Let us write down the time evolution of a density matrix $\hat{\rho}(t)$ of the system. Up to first order and with δt small we can write the density matrix after an infinitesimal time step as

$$\hat{\rho}(t+\delta t) = \hat{\rho}(t) + \mathcal{O}(\delta t), \tag{2.38}$$

i.e. the initial density matrix $\hat{\rho}(t)$ and an infinitesimal change of order δt. As we have seen in the previous subsection one can also write this time evolution through its Kraus sum,

$$\hat{\rho}(t+\delta t) = \sum_r \hat{M}_r \hat{\rho}(t) \hat{M}_r^\dagger. \tag{2.39}$$

We can now make a proposal with regard to what we will denote as the operator $\hat{M}_0$, by remarking that it should be of order of unity, since $\hat{\rho}(t)$ can only infinitesimally change with δt. The other operators $\hat{M}_r$ ($r \neq 0$) should then be of order $\sqrt{\delta t}$. We can thus write

$$\hat{M}_0 = \hat{\mathbb{1}} - i\hat{K}\delta t, \quad \text{and} \quad \hat{M}_r = \sqrt{\gamma_r}\hat{L}_r\sqrt{\delta t}. \tag{2.40}$$

Where we have without loss of generality included a factor $\sqrt{\gamma_r}$ into the expression for the operators $\hat{M}_r$, for $r \neq 0$. One can write the operator $\hat{K}$ in terms of a

Hermitian part $\hat{H}$ and anti-Hermitian part $\hat{J}$, which allows us to write $\hat{K} = \hat{H} - i\hat{J}$. Now, we can rewrite (2.39) as

$$\hat{\rho}(t+\delta t) = \hat{\rho}(t) - i\delta t\left[\hat{H}, \hat{\rho}(t)\right] - \delta t\left(\hat{J}\hat{\rho}(t) + \hat{\rho}(t)\hat{J}\right) + \sum_{r\neq 0} \hat{M}_r \hat{\rho}(t)\hat{M}_r^\dagger, \tag{2.41}$$

where we can now use the completeness relation associated with the Kraus sum, which allows us to write

$$\sum_{r\neq 0} \gamma_r \hat{L}_r^\dagger \hat{L}_r = 2\hat{J}, \tag{2.42}$$

Substitution of this term into the expression of $\hat{\rho}(t+\delta t)$, as well as substituting the expressions for $\hat{M}_r$, and finally collecting the terms then yields

$$\dot{\hat{\rho}} = -i\left[\hat{H}, \hat{\rho}(t)\right] + \sum_r \frac{\gamma_r}{2}\left(2\hat{L}_r\hat{\rho}(t)\hat{L}_r^\dagger - \hat{L}_r^\dagger\hat{L}_r\hat{\rho}(t) - \hat{\rho}(t)\hat{L}_r^\dagger\hat{L}_r\right), \tag{2.43}$$

which is, as promised, of the Lindblad form we derived in Section 2.3. Note that following this derivation, no assumptions were made on the properties of $\hat{H}$, γ_r and $\hat{L}_r$. We know from our previous derivation that they respectively correspond to the system Hamiltonian, the dissipation rate and the coupling of the system with the environment. Moreover, the derivation here also shows that one can interpret the time evolution of the master equation as the influence of continuous un-read measurements on your system. It will be quite interesting to see what happens if we actually do read out the measurements, as we will closer inspect in section 2.6.

A final note should be made about the physical relevance of the above derivation [8] as we never explicitly made use of the *Born approximation* and *Markov approximation*. They are however of paramount importance. Firstly, for the above derivation to be valid one inherently needs the system and environment to be initially decoupled and in a product state. If this were not the case, the initial entanglement between system and environment could often have a non-neglible influence on the time evolution of the system, and thus $\hat{\rho}(t)$. Furthermore, for the same reason it is also important that the correlations in the environment caused by the interaction with the system decay rapidly with respect to the timescale at which the system changes. For this reason we emphasize that we never explicitely took the limit of $\delta t \to 0$, as is customary in a mathematical formulation. From a physicists perspective δt should be sufficiently large with respect to timescale at which the correlation functions of the environment decay, but also small enough with respect to the timescale at which the system changes for our time evolution

to describe a continuous change of the system. For an appropriate choice of δt this thus reconciles the above derivation with the *Born-Markov approximation*. It shows the generality of the Lindblad master equation for systems that are weakly coupled with a Markovian environment. Indeed, apart from the Markovianity of the environment, no assumptions were made with regard to its nature.

2.6 Quantum trajectories

Let us now move to the situation where we do read out the measurements performed on the system. This means that we will get a conditioned time evolution of the system, depending on the read-outs of the measurements. Let us assume that the state is initially prepared in a pure state $|\psi(0)\rangle$ then the time evolution of the state under continuous monitoring is given by (2.33)

$$|\psi(t+\delta t)\rangle \to \frac{\hat{M}_r|\psi(t)\rangle}{\sqrt{\langle\psi(t)|\hat{M}_r^\dagger \hat{M}_r|\psi(t)\rangle}}, \tag{2.44}$$

with r indicating the specific read-out of the measurement, δt small and the probability $p_r = \langle\psi(t)|\hat{M}_r^\dagger \hat{M}_r|\psi(t)\rangle$ that this type of read-out occurs. Such a conditional time evolution is called a quantum trajectory and can be written down in terms of a stochastic Schrödinger equation, which we will derive in this section. It should be clear that the quantum trajectory formalism grants information about the system in a way very similar to that of an actual experiment. Indeed, each measurement and its read-out changes the state of your system and the continuous monitoring causes the system to constantly be in a pure state. To gain knowledge about the density matrix of the system of interest one would have to repeat the experiment multiple times to be able to sample the density matrix, or any other observable of interest. Nevertheless, a single trajectory can give useful insights into the physical processes present in the system in a way the Lindblad master equation cannot. Examples of such physical processes are bistability and spontaneous symmetry breaking. The trajectory approach is more physical than the solution of the master equation since it can capture the (slow) switching between the bistable states or the spontaneously broken states.

For the sake of simplicity in the derivation, we assume that there are two types of measurements that can be performed on the system: $\hat{M}_0$ and $\hat{M}_1$. From (2.40)

we know that they can be written as

$$\hat{M}_0 = \hat{\mathbb{1}} - i\left(\hat{H} - i\frac{\gamma}{2}\hat{L}^\dagger\hat{L}\right)\delta t \quad \text{and} \quad \hat{M}_1 = \sqrt{\gamma\delta t}\hat{L}, \tag{2.45}$$

where we dropped the unnecessary subscript of $\hat{L}$. Since δt is small this allows us to interpret $\hat{M}_0$ as a *non-measurement* or the *zero read-out*. $\hat{M}_0$ will only marginally change the state of the system since it is of order unity, and one can say that "nothing" happens other than the smooth evolution of your system during the infinitesimal step with an effective, non-Hermitian, Hamiltonian

$$\hat{H}_{eff} = \hat{H} - i\frac{\gamma}{2}\hat{L}^\dagger\hat{L}. \tag{2.46}$$

Similarly, we know that p_0 will be close to one and this will also be the most likely result of the measurement. $\hat{M}_1$ however will occur with a much smaller probability, but will change the state of the system more abruptly. For this reason the operator $\hat{L}$ is often called the *jump operator*. In a quantum optical setting one could interpret this occurrence as e.g. the emission of a photon to the environment. The interpretation however is closely related to the nature of the measurement operators.

Let us denote the result for a measurement result "0" and a measurement result "1", corresponding to respectively the operators $\hat{M}_0$ and $\hat{M}_1$, during a time δt as $dN(t)$. That is, $dN(t)$ will be either equal to 0 or 1. Consequently, this allows us to note that the square of $dN(t)$ is again equal to $dN(t)$, and the probability of observing a measurement result "1" will be equal to p_1. This thus allows us to write

$$dN(t)^2 = dN(t) \quad \text{and} \quad \mathbb{E}\left[dN(t)\right] = p_1 = \gamma\langle\psi(t)|\hat{L}^\dagger\hat{L}|\psi(t)\rangle\delta t, \tag{2.47}$$

with $\mathbb{E}[\cdot]$ denoting a classical expectation value over different (independent) realizations. These properties allow us to write down the following time evolution of the wave function based on the conditional results of the measurement

$$|\psi(t+\delta t)\rangle = (1 - dN(t))\frac{\hat{M}_0|\psi(t)\rangle}{\sqrt{\langle\psi(t)|\hat{M}_0^\dagger\hat{M}_0|\psi(t)\rangle}} + dN(t)\frac{\hat{M}_1|\psi(t)\rangle}{\sqrt{\langle\psi(t)|\hat{M}_1^\dagger\hat{M}_1|\psi(t)\rangle}}. \tag{2.48}$$

We can then substitute the expressions for the measurement operators (2.45). By making an expansion of the denominator of the term corresponding to the $\hat{M}_0$

measurement up to order δt this will allow us to write

$$|\psi(t+\delta t)\rangle = (1-dN(t))\left[\hat{\mathbb{1}} + \frac{\gamma}{2}\delta t\langle\hat{L}^\dagger\hat{L}\rangle(t) - \frac{\gamma}{2}\delta t\hat{L}^\dagger\hat{L} - i\hat{H}\delta t\right]|\psi(t)\rangle + dN(t)\frac{\hat{L}|\psi(t)\rangle}{\sqrt{\langle\hat{L}^\dagger\hat{L}\rangle(t)}}, \tag{2.49}$$

where we introduced the notation $\langle\psi(t)|\hat{O}|\psi(t)\rangle = \langle\hat{O}\rangle(t)$, for ease of use. If we now subtract a term $|\psi(t)\rangle$ on both sides of the equation, as well as note that the term with $dN(t)\delta t$ is of higher order than δt due to (2.47) and can be discarded, we arrive at

$$d|\psi(t)\rangle = \left[\left(\frac{\gamma}{2}\langle\hat{L}^\dagger\hat{L}\rangle(t) - \frac{\gamma}{2}\hat{L}^\dagger\hat{L} - i\hat{H}\right)dt + \left(\frac{\hat{L}}{\sqrt{\langle\hat{L}^\dagger\hat{L}\rangle(t)}} - \hat{\mathbb{1}}\right)dN(t)\right]|\psi(t)\rangle, \tag{2.50}$$

by collecting both terms in $dN(t)$ and dt (where the notational transformation $\delta t \to dt$ was made). Clearly, the time evolution described by (2.50) is different from the time evolution described by the Lindblad master equation (2.23). The question thus remains, are both approaches equivalent or not? The answer is yes. As mentioned earlier the quantum trajectory approach is reminiscent of performing measurements in an experiment. To gain knowledge on an observable or the state of the system one needs to collect enough statistics through repeated experiments, or thus multiple quantum trajectories. By averaging over these trajectories one regains the Lindblad master equation. To prove this one can start by writing

$$d\left(|\psi(t)\rangle\langle\psi(t)|\right) = \left(d|\psi(t)\rangle\right)\langle\psi(t)| + |\psi(t)\rangle\left(d\langle\psi(t)|\right) + \left(d|\psi(t)\rangle\right)\left(d\langle\psi(t)|\right). \tag{2.51}$$

We can now take the expectation value $\mathbb{E}[\cdot]$ over different realizations on both sides of the above equation. Using that $\hat{\rho}(t) = \mathbb{E}[|\psi(t)\rangle\langle\psi(t)|]$ and (2.47) one straight-forwardly arrives at

$$d\hat{\rho}(t) = -idt\left[\hat{H},\hat{\rho}(t)\right] + dt\frac{\gamma}{2}\left(2\hat{L}\hat{\rho}(t)\hat{L}^\dagger - \hat{L}^\dagger\hat{L}\hat{\rho}(t) - \hat{\rho}(t)\hat{L}^\dagger\hat{L}\right), \tag{2.52}$$

which is indeed equivalent to the Lindblad master equation. In theory, one needs an infinite number of trajectories for $\mathbb{E}[|\psi(t)\rangle\langle\psi(t)|] = \hat{\rho}(t)$ to be valid. In practice however, a moderate number of trajectories allow you to get a very good estimate.

Note that a generalization to a higher number of measurement operators is easily made. We can introduce an arbitrary set of $dN_j(t)$ which are equal to 1 when a measurement of type j is observed, and equal to zero when it isn't. One then

arrives at the stochastic Schrödinger equation for a general set of measurement operators

$$d|\psi(t)\rangle = \sum_j \left[\left(\frac{\gamma_j}{2} \langle \hat{L}_j^\dagger \hat{L}_j \rangle(t) - \frac{\gamma_j}{2} \hat{L}_j^\dagger \hat{L}_j - i\hat{H} \right) dt + \left(\frac{\hat{L}_j}{\sqrt{\langle \hat{L}_j^\dagger \hat{L}_j \rangle(t)}} - \hat{\mathbb{1}} \right) dN_j(t) \right] |\psi(t)\rangle. \tag{2.53}$$

It should be clear that it is computationally less demanding to simulate a single trajectory than it is to simulate the density matrix with the master equation. In the latter one needs to simulate time evolution of an object of which the size is the square of the Hilbert space dimension $\mathcal{H}$. For the trajectory approach one needs only simulate the wave function, i.e. an object with the size of the Hilbert space $\mathcal{H}$. Of course, one needs to simulate multiple trajectories to collect enough statistics and retrieve the density matrix with a certain accuracy. However, the number of needed trajectories is usually a lot smaller than the Hilbert space dimension, resulting in a computationally more economic approach.

Importantly, one should note that the Lindblad master equation is invariant under the type of measurement operators used. We saw that the measurement operators need only satisfy the completeness relation and be positive. This means one can transform the measurement operators with a unitary operation $\hat{U}$, i.e. $\hat{M}_j \to \sum_j U_{kj} \hat{M}_j$, and still obtain the same time evolution (with U_{kj} the elements of $\hat{U}$). Substitution into the Lindblad master equation (2.23) indeed leaves the equation unchanged. This however, is no longer true in the quantum trajectory formalism. After averaging over a sufficient number of realizations one recovers the dynamics predicted by the Lindblad master equation. However, for a single trajectory the type of measurement has a drastic impact on its time evolution. Indeed, substitution of the unitary transformation into the stochastic Schrödinger equation (2.53) no longer leaves the equation unchanged. There are thus many ways to simulate the time evolution with quantum trajectories, depending on the type of measurements used. This is often referred to as the type of unravelling of the Lindblad master equation. In this thesis we will focus on one measurement scheme in particular: photon counting.

2.6.1 Photon counting

This unravelling scheme is based on continuous photon detection. A detector will give a click only when a photon is emitted to the environment. Not detecting a

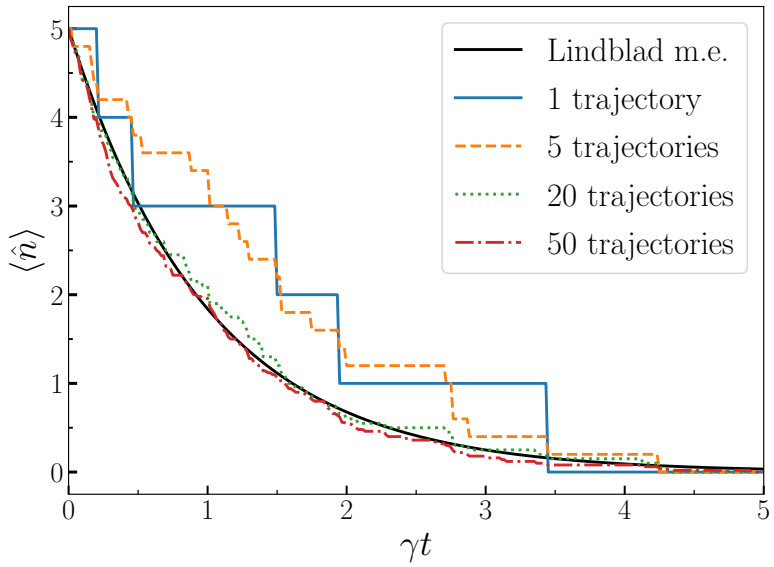

Figure 2.2: *Solution Lindblad master equation (m.e.) and trajectories for the optical cavity from section 2.4. We have chosen* $\gamma = \omega_c = 1$ *and* $|\psi(0)\rangle = |5\rangle$*. We show the results for an increasing number of trajectories (from 1 to 50).*

photon also gives us information on the state of the system. Such a scheme allows for some very straight forward measurement operators. In the quantum optical setting we can substitute $\hat{L}_j \to \hat{a}_j$ in (2.40) resulting in a time evolution governed by

$$d|\psi(t)\rangle = \sum_j \left[\left(\frac{\gamma}{2} \langle \hat{a}_j^\dagger \hat{a}_j \rangle(t) - \frac{\gamma_j}{2} \hat{a}_j^\dagger \hat{a}_j - i\hat{H} \right) dt + \left(\frac{\hat{a}_j}{\sqrt{\langle \hat{a}_j^\dagger \hat{a}_j \rangle(t)}} - \hat{\mathbb{1}} \right) dN_j(t) \right] |\psi(t)\rangle. \tag{2.54}$$

The term $\sum_j \frac{\gamma_j}{2} \langle \hat{a}_j^\dagger \hat{a}_j \rangle(t)$ ensures that the norm of $|\psi(t)\rangle$ remains equal to one since the term $\sum_j \frac{\gamma_j}{2} \hat{a}_j^\dagger \hat{a}_j$ in the effective non-Hermitian Hamiltonian (2.46) has a decrease of the norm as a result in its time evolution. Let us now apply this measurement scheme to the example of radiative damping in an optical cavity, introduced in section 2.4. Given that the system is initially in a Fock state the time evolution of the trajectory can be straight-forwardly predicted. The system stays in its initial state $|n\rangle$ under the Hamiltonian evolution, due to it being an eigenstate of $\hat{H}$. Only when the detector detects a photon, the system will jump to the state $|n-1\rangle$. Hence the name *jump operator*. The same process is then repeated until the system is in the state $|0\rangle$, where it will stay due to the absence of a driving term. This time evolution is depicted in Fig. 2.2 for the example of the optical cavity from section 2.4. Evidently, the results for different trajectories differ. If we average over an increasing number of trajectories we observe a convergence to the result predicted by the master equation, as expected.

Numerically this is implemented through a Monte Carlo scheme. At each time step one can check if the condition for a jump, $p_1 < \epsilon$, is satisfied, with ϵ a repeatedly sampled random number. If this condition is satisfied the jump operator is applied to the state, which at the same time is normalized. In the case of no jump, i.e. $p_1 \geq \epsilon$, the state evolves with the effective non-Hermiation Hamiltonian $\hat{H}_{eff}$ from (2.46). This scheme is repeated until the desired simulation time is reached. This can be straight forwardly generalized to systems with multiple jump operators. The general scheme can be found in appendix A.1.

2.7 The Liouvillian superoperator

The Lindblad master equation (2.23) contains the coherent dynamics of the closed system dynamics in the form of the commutator of the Hamiltonian with the system's density matrix, as well as the incoherent dynamics that finds its origin in

its coupling with an environment. This translates to the action of the Lindblad operators on the density matrix. One can thus re-write the master equation as the evolution of the density matrix through some specific action $L[\cdot]$

$$\partial_t \hat{\rho} = -i\left[\hat{H}, \hat{\rho}\right] + \sum_i \frac{\gamma_i}{2}\left(\hat{L}_i \hat{\rho} \hat{L}_i^\dagger - \left\{\hat{L}_i^\dagger \hat{L}_i, \hat{\rho}\right\}\right) \quad \Rightarrow \quad \partial_t \hat{\rho} = L[\hat{\rho}]\,. \tag{2.55}$$

This action that contains the systems dynamics can be translated to a super-operator formalism. Remember, in the language of *quantum maps* we could have written

$$\hat{\rho}(t+\delta t) = \hat{\rho}(t) + \mathcal{L}\delta t \hat{\rho}(t) = (1 + \mathcal{L}\delta t)\,\hat{\rho}(t) = e^{\mathcal{L}\delta t}\hat{\rho}(t). \tag{2.56}$$

since δt is small and note that $L[\cdot] \leftrightarrow \mathcal{L}$. In (2.56) both $(1 + \mathcal{L}\delta t) = e^{\mathcal{L}\delta t}$ as well as $\mathcal{L}$ are superoperators transforming an operator into another one. We will call the former the evolution operator $\mathcal{E} = e^{\mathcal{L}\delta t}$ and we will exploit its properties in chapter 9. For now we focus on the superoperator $\mathcal{L}$, from now on called the *Liouvillian superoperator* or *Liouvillian* in short.

Given an initial state $\hat{\rho}(0)$ one could write the density matrix at a time $t = n\delta t$ as

$$\hat{\rho}(t) = e^{\mathcal{L}t}\hat{\rho}(0), \tag{2.57}$$

for this reason the superoperator $\mathcal{L}$ is also called the generator of the time evolution and it contains all the information on the dynamics of the system. To be able to extract this information we will move to a new way of representing superoperators, that is, we will rewrite them as matrices. We are allowed to do this since the Liouvillian is a linear superoperator, i.e. $\mathcal{L}(a\hat{\rho}_a + b\hat{\rho}_b) = a\mathcal{L}\hat{\rho}_a + b\mathcal{L}\hat{\rho}_b$. In this formalism the density matrix is rewritten as a one dimensional vector, and the action on the density matrix can thus be rewritten as a matrix. Formally, this relies on the Choi-Jamiolkowski isomorphism, i.e. $|i\rangle\langle j| \rightarrow |i\rangle \otimes |j\rangle$, which allows you to transform your density matrix into a vector. To emphasize that a superoperator is written in matrix from, we will add a hat to the superoperators, as well as add bracket notation for the density matrix in its vector form: $\mathcal{L} \rightarrow \hat{\mathcal{L}}$ and $\hat{\rho}(t) \rightarrow |\hat{\rho}(t)\rangle$. This then allows one to write

$$\partial_t \hat{\rho} = \mathcal{L}\hat{\rho} \quad \Rightarrow \quad \partial_t |\hat{\rho}\rangle = \hat{\mathcal{L}}|\hat{\rho}\rangle. \tag{2.58}$$

The size of this superoperator is the square of the density matrix dimension. We will refer to this as the Liouvillian space dimension, or the dimension of the

Liouvillian.

One can once again solve this differential equation and this results in

$$|\hat{\rho}(t)\rangle = e^{\hat{\mathcal{L}}t}|\hat{\rho}(0)\rangle. \tag{2.59}$$

The dynamics of the system is now captured by the matrix $\hat{\mathcal{L}}$, for which we can use an eigendecomposition to extract all information on the time evolution. Note again that a simple transformation can transform the vectorized density matrix back into the standard two-dimensional representation. The key to the dynamics and the properties of the system under consideration can thus be captured through the properties of this Liouvillian superoperator. This not only allows you to time evolve your system but as explained in the next section it also gives access to properties regarding dissipative phase transitions. However, due to the quadratic increase in the dimension of this matrix with respect to the matrices needed to describe the Lindblad master equation, this approach is usually unfeasible for the description of the time evolution of the system when treating it in the full, unreduced, Hilbert space. As we will see in chapter 4, once one can reduce the dimension of the Liouvillian, due to e.g. the presence of symmetries in the system. In such a situation this approach will prove to be very useful.

2.7.1 Liouvillian spectrum

Much like how an eigendecomposition of the Hamiltonian in closed systems grants you all the information on the system you need, this role is taken by an eigendecomposition of the Liouvillian in open quantum systems obeying the Lindblad master equation. One should however note that the spectrum of the Liouvillian is entirely different from the Hamiltonian spectrum. The latter grants you the eigenstates of the system and their corresponding energies, which are real due to the Hamiltonian being Hermitian. If we assume a superoperator corresponding to the action of the right-hand side of the Liouville Von-Neumann equation in a closed system (2.6), the eigenvalues of this superoperator will be purely imaginary. In the case of the Liouvillian superoperator this is no longer true. This comes from the fact that the Liouvillian $\hat{\mathcal{L}}$ is non-Hermitian and the eigenvalues need not be real. Moreover, the left and right eigenvectors will in general be different. We can write

$$\hat{\mathcal{L}}|\hat{\rho}_i\rangle = \lambda_i|\hat{\rho}_i\rangle = \left(\lambda_i^{\mathrm{Re}} + i\lambda_i^{\mathrm{Im}}\right)|\hat{\rho}_i\rangle, \tag{2.60}$$

$$\langle\hat{\sigma}_i|\hat{\mathcal{L}} = \langle\hat{\sigma}_i|\lambda_i = \langle\hat{\sigma}_i|\left(\lambda_i^{\mathrm{Re}} + i\lambda_i^{\mathrm{Im}}\right), \tag{2.61}$$

where λ_i, $|\hat{\rho}_i\rangle$ and $\langle\hat{\sigma}_i|$ respectively denote the eigenvalues and the right and left eigenvectors of the Liouvillian $\hat{\mathcal{L}}$. The upperscripts Re and Im denote the real and imaginary parts of λ_i. Let us also introduce the Hilbert-Schmidt inner product, defined as

$$\left(\hat{A}, \hat{B}\right) := \mathrm{Tr}\left[\hat{A}^\dagger \hat{B}\right]. \tag{2.62}$$

This inner product becomes particularly useful in our vectorized notation since

$$\mathrm{Tr}\left[\hat{A}^\dagger \hat{B}\right] = \sum_{r,s} A_{rs}^* B_{rs} = \langle\hat{A}|\hat{B}\rangle. \tag{2.63}$$

From the condition of trace preservation one can prove the existence of a left eigenvector $\langle\hat{\sigma}_0| = \langle\mathbb{1}|$ with an eigenvalue $\lambda_0 = 0$. One can write

$$\mathrm{Tr}\left[\hat{\rho}\right] = 1 \Leftrightarrow \mathrm{Tr}\left[\frac{d\hat{\rho}}{dt}\right] = 0 \Leftrightarrow \mathrm{Tr}\left[\mathbb{1}\mathcal{L}\hat{\rho}\right] = 0 \Leftrightarrow \langle\mathbb{1}|\hat{\mathcal{L}}|\hat{\rho}\rangle = 0 \Leftrightarrow \langle\mathbb{1}|\hat{\mathcal{L}} = 0. \tag{2.64}$$

One obtains the last result since this equality in the fourth term should hold for all density matrices $\hat{\rho}$. This also implies the existence of a right eigenvector $|\hat{\rho}_0\rangle$ with zero eigenvalue. The physical meaning of this will become clear when we rewrite the time evolution (2.59) in its spectral decomposition. Indeed, in general one can write

$$|\hat{\rho}(t)\rangle = \sum_j c_j e^{\lambda_j t}|\hat{\rho}_j\rangle, \tag{2.65}$$

where the coefficients c_j are time-independent and are determined by the initial state of the time evolution. Since our state needs to remain physical at all times this implies that the real part of all λ_i are non-positive [16]. If this were not the case the exponentials in (2.65) would go to infinity at long times, resulting in unphysical states. This allows us to call $|\hat{\rho}_0\rangle$ the *steady state*, since for long times $t \to \infty$ the system will converge to this specific state. The other eigenstates $|\hat{\rho}_i\rangle$ for which $\mathrm{Re}\left[\lambda_i\right] < 0$ can thus be interpreted as decaying processes as time evolves, i.e. they are responsible for the system's dynamics. The trace of these eigenstates should be zero. This is due to the Liouvillian evolution being a trace preserving quantum map. Since for $t \to \infty$ we have that $e^{\mathcal{L}t} = e^{\lambda_i t} \to 0$ for $\lambda_i \neq 0$, the trace of $\hat{\rho}_i$ should be zero. Note that the condition on the preservation of the trace implies the existence of at least one eigenvalue that is equal to zero. There is however no straight forward condition to determine whether there are multiple steady states

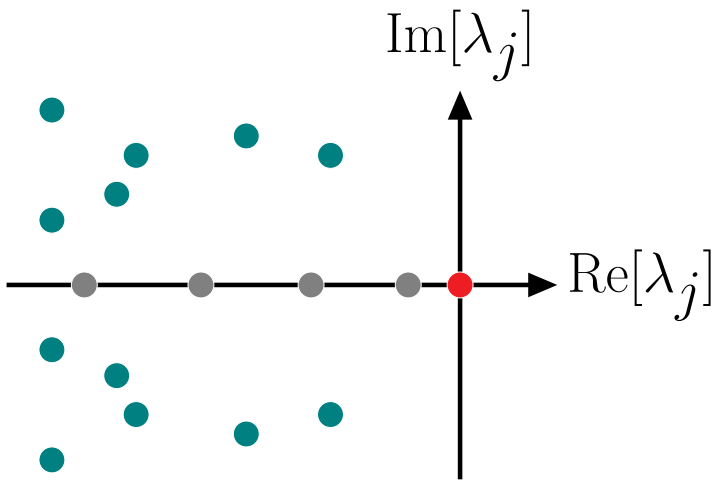

Figure 2.3: *Example of a Liouvillian spectrum. The red dot indicates the steady state, the gray dots indicate real (negative) eigenvalues, and the green dots indicate imaginary eigenvalues. The Liouvillian gap is given by the absolute value of the first grey dot from the right.*

or not, this highly depends on the specific model one is studying.

In what follows we will index the spectrum λ_i from 0 to M, with M the dimension of the Liouvillian. Additionally, we chose the indexing in such a way that $|\mathrm{Re}\,[\lambda_0]\,| \leq |\mathrm{Re}\,[\lambda_1]\,| \leq \cdots \leq |\mathrm{Re}\,[\lambda_M]\,|$. A typical Liouvillian spectrum is shown in Fig. 2.3. Note the reflection symmetry of the eigenvalues with respect to the real axis. This is due to the Hermiticity preservation of the Lindblad master equation, and thus the Liouvillian superoperator, i.e.

$$\mathcal{L}\hat{\rho}^\dagger = (\mathcal{L}\hat{\rho})^\dagger\,, \tag{2.66}$$

which can easily be checked by substituting this into the master equation for any matrix $\hat{\rho}$. This implies that for each eigenvalue $\lambda_i = \lambda_i^{\mathrm{Re}} + i\lambda_i^{\mathrm{Im}}$ with non-zero imaginary part ($\lambda_i^{\mathrm{Im}} \neq 0$) there also exists an eigenvalue $\lambda_i^* = \lambda_i^{\mathrm{Re}} - i\lambda_i^{\mathrm{Im}}$

Apart from the steady state $|\hat{\rho}_0\rangle$ another eigenstate and its eigenvalue are of paricular interest, namely $|\hat{\rho}_1\rangle$ and λ_1. This is the slowest (time dependent) process present in the dynamics of the system. The timescale of this process is thus determined by the real part of λ_1, which is what we call the *Liouvillian gap*. This Liouvillian gap will play an important role in the study of dissipative phase transitions. $|\hat{\rho}_1\rangle$ being the slowest process immediately shows one of the problems one can run into when simulating the dynamics of an open system,

Method	Advantage	Disadvantage
Liouvillian Diagonalization	Determines $\hat{\rho}_{\text{ss}}$ and any the dynamics of any $\hat{\rho}(t)$ via eigendecomposition.	Fast-exponential size of the Liouvillian, computationally costly diagonalization.
Time evolution of $\hat{\rho}(t)$	Numerically exact dynamics with no noise, less costly than Liouvillian diagonalization	In the presence of slow processes, long simulations. Still computationally costly for large systems.
Quantum Trajectories	Evolution of wave function can be done more efficiently than the evolution of $\hat{\rho}(t)$, *also for larger systems.*	The results are noisy and need to be integrated over many quantum trajectories. Same problem as the evolution of $\hat{\rho}(t)$ in the presence of slow processes.

Table 2.1: *Advantages and disadvantages of the standard methods to study the steady state and dynamics of an open quantum system.*

and in particular if one wishes to study the steady state. Indeed, if λ_1 is small or approximately zero one has to time evolve for a very long time if one wishes to obtain the steady state. This problem persists in both the master equation formalism as well as the quantum trajectory approach. It is thus of interest to be able to directly calculate the steady state through an eigendecomposition. We will discuss this in more detail in chapter 9.

If one is able to not only calculate the Liouvillian but also its spectrum one thus has access to all dynamics of the system. Calculating the eigendecomposition of a large matrix however is computationally very demanding. Due to the exponential growth that the Hilbert space of a many-body quantum system exhibits, and the quadratic dimension of the Liouvillian with respect to the Hilbert space dimension, one naturally quickly runs into the limits of this approach.
A treatment of the dynamics on the level of the master equation, quantum trajectories or the Liouvillian has its own advantages and disadvantages, which are listed in table 2.1. To push beyond the limits of the exponentially large Hilbert spaces, one is left with making an appropriate choice for the system under study and one has to apply approximate methods to overcome these limitations. In chapter 3 we give an overview of state-of-the-art methods applied to paradigmatic models that will be the topic of this thesis: the dissipative XYZ Heisenberg model and the driven-dissipative Bose-Hubbard model.

2.8 Dissipative phase transitions

The study of phase transitions take a central role in physics. In this thesis we will be studying so-called dissipative phase transitions. That is, phase transitions that find their origin in a competition between the Hamiltonian dynamics of the system under consideration and the dynamics due to its coupling with an environment. In particular, the competition between interaction, driving and dissipation processes can lead to exotic physics, such as a transition from a photonic Mott insulator to a superfluid phase [17–21], similar to that observed with ultracold atoms confined in optical lattices [22, 23]. Moreover, in the limit of a very strong nonlinearity one enters the regime of photon-blockade [24–27], where the presence of two photons inside the cavity becomes practically impossible. This effect has been observed experimentally both in a single atom in a cavity [28] and in a single superconducting circuit [29]. Before we further clarify this type of phase transitions, let us first revisit thermal and quantum phase transitions. Generally, phase transitions occur as a result of competing processes in a physical system. When a certain control parameter, that is linked to the dominance of one of the two competing processes, passes a certain critical value, a phase transition takes place. For thermal phase transitions this is closely linked to the Helmholtz free energy $F = U - TS$, where the system's internal energy competes with the entropy [30]. The internal energy is trying to reach a minimum, whereas the entropy strives to reach a maximum. When the temperature is small, the contribution of the entropy is small and the free energy is dominated by the internal energy. This results in an ordered state. As temperature increases one comes to a point where the entropy starts to dominate and as a result a phase transition to an unordered, entropic state occurs. Another class of phase transitions is given by quantum phase transitions [31]. Assume a quantum system governed by a Hamiltonian $\hat{H}(g)$, where g indicates a system parameter, e.g.

$$\hat{H}(g) = \hat{H}_a + g\hat{H}_b. \tag{2.67}$$

For such a system it is possible for the energy gap $\Delta = E_1 - E_0$ between the ground state $|\psi_0\rangle$ and the first excited state $|\psi_1\rangle$ to vanish in the thermodynamic limit at a certain critical value $g = g_c$, i.e. $\lim_{g\to g_c} E_1(g) - E_0(g) \to 0$. The vanishing of the energy gap is typically accompanied by a non-analicity in the energy of the system, leading to an abrupt change in the ground state of the system. This usually coincides with a change in the nature of the correlations in the ground state and thus a quantum phase transition. If $\hat{H}_a$ and $\hat{H}_b$ are non-commuting

terms, i.e. $\left[\hat{H}_a, \hat{H}_b\right] \neq 0$, such a vanishing energy gap can lead to second order phase transitions associated with a spontaneously broken symmetry.

Both thermal phase transitions and quantum phase transitions have in common that they can be determined through a (free-)energy analysis [30, 31]. This is no longer true for out-of-equilibrium dissipative systems [32–37]. By properly designing the coupling with the environment and the driving mechanisms, it is possible to stabilize phases without an equilibrium counterpart [38–44]. Nonetheless, one can draw a similarity with quantum phase transitions: where the ground state and the first excited state are of main interest in the study of quantum phase transitions this place is taken by the steady-state and the slowest decaying process in the treatment of dissipative systems. Both the ground state and the steady state can be found as the eigenvector of the zero eigenvalue of respectively the Hamiltonian and the Liouvillian superoperator. The same goes for the first excited state and the slowest decaying process. In dissipative systems we will thus be interested in the behavior of the Liouvillian gap to signal the onset of a dissipative phase transition. For a first order phase transition this means the Liouvillian gap is closed at the critical point, signaling a bimodal stationary state. Note that the imaginary part of λ_1 is also required to go to zero [35]. Furthermore, it can be shown that for second-order phase transitions which are associated with a symmetry breaking that the Liouvillian gap closes throughout the region of this broken symmetry [35]. The closure of the Liouvillian gap is accompanied by a slowing down of the dynamics of the system. Indeed, for a time t sufficiently large the system's state can be written as

$$\hat{\rho}(t) = \hat{\rho}_{ss} + c_1 e^{\lambda_1 t} \hat{\rho}_1. \tag{2.68}$$

This is also referred to as the critical slowing down of the dynamics near criticality. It is here that a trajectory approach can provide one with additional information with respect to a density matrix approach. The reason for this is that even though the density matrix does not change anymore at $t \to \infty$, the wave function $|\psi\rangle$ in the trajectory approach does. In fact, $|\psi\rangle$ will explore all states $|\tilde{\psi}_j\rangle$ that build up the steady state density matrix $\hat{\rho}_{ss} = \sum_j p_j |\tilde{\psi}_j\rangle\langle\tilde{\psi}_j|$. In finite-size systems, where the Liouvillian gap λ_1 is finite, this allows for the observation of for example the various symmetry broken phases along the evolution of the trajectory for a system close to, or in, a symmetry broken phase due to the structure imposed on $\hat{\rho}_1$ and $\hat{\rho}_{ss}$ by this symmetry [35, 45], given a suitable choice of unravelling.

2.8.1 Dissipative time crystals

An interesting phase that can arise in out-of-equilibrium systems is a dissipative time crystal, also referred to as a boundary time crystal (BTC). The concept and possible existence of time crystals was first mentioned in a work by Wilczek [46] in closed quantum systems. He introduced the concept of a system where time translational invariance was spontaneously broken, much like how the continuous spatial translation symmetry is broken in crystal lattices. Hence the name "time crystal". This work sparked a lot of discussion on the existence of such a phase [47–50]. Subsequently, a no-go theorem was derived ruling out the existence of these time crystals in the ground state as well as at thermal equilibrium [51]. Recently however, in a work by Khemani et al. it was claimed that the proof contained an error rendering it invalid for $T \neq 0$ [52]. Going beyond the equilibrium systems that were ruled out by the no-go theorem, the existence of a time crystal was proposed in Floquet systems with periodic driving. Such a system breaks the discrete time translational invariance since observables can oscillate at multiple times the driving frequency [53–55]. These systems are also referred as discrete time crystals or Floquet time crystals and have been experimentally observed [56, 57]. In this thesis, we will focus on those time crystals occurring in dissipative, non-unitary, systems [58–66]. Hence the name dissipative time crystal, or BTC. The term "boundary" comes from the interpretation of the system of interest $\hat{H}_S$ being on the boundary of a bulk system $\hat{H}_E$, i.e. the boundary of a larger system [58]. As we have seen in section 2.2, this is exactly the type of system we are studying. When our system of interest resides in a BTC phase, it exhibits periodical behavior in the long time limit, i.e. $t \to \infty$, in the expectation value of a system operator $\hat{O}$. Such a phase thus breaks the time translational invariance that is an underlying symmetry of the Liouvillian. Moreover, in contrast with the Floquet time crystal, the system can break continuous time translational symmetry. That is, the frequency of the oscillation does not depend on the driving frequency but rather the various parameters in the system and the strength of the coupling with the environment. The emergence of such a BTC can once again be extracted from the properties of the Liouvillian spectrum. It is signaled by the disappearance of the real part of an eigenvalue λ as the system approaches the thermodynamic limit, while its imaginary part converges to a nonzero value [67–69]. The same is true for an eigenvalue λ^* due to (2.66). In the thermodynamic limit these eigenvalues become purely imaginary and thus cause oscillating behavior

to occur in the expectation value of an operator $\hat{O}$ that has an overlap with the corresponding eigenstates.

CHAPTER 3

Many-body open quantum systems: paradigmatic models and theoretical techniques

Many-body quantum physics with light and matter is at the center of intense research, being at the crossroad of condensed matter, statistical mechanics, quantum optics, and quantum information. In these open quantum systems, excitations, energy, and coherence are continuously exchanged with the environment, and they can be driven via pumping mechanisms [5, 8, 10]. Experimentally, light-matter interactions can be studied using Rydberg atoms confined between high-quality mirrors [8], superconducting circuits [70, 71], semiconductor cavities [72–74], and optomechanical systems [75]. In many of these setups, a key role is played by the "photons", that is, electromagnetic field excitations dressed by the matter degrees of freedom, thus permitting a finite effective photon-photon interaction (e.g., the polariton [14, 76, 77]). The experimental advances of the last decade provided the opportunity to realize extended lattices of resonators, allowing to explore criticality in this out-of-equilibrium context. While quantum or thermal phase transitions can be determined by (free-)energy analysis [30, 31], their dissipative counterparts need not obey the same paradigm [32–44]. There exists a plethora of theoretical examples discussing the emergence of such dissipative phase transitions for photonic systems [78–94], lossy polariton condensates [95–97], and spin models [32, 42, 44, 98–108]. Moreover, some key experiments proved the validity of the theoretical predictions in single superconducting cavities [109] and lattices of superconducting resonators [110, 111], Rydberg atoms in optical lattices [112, 113], optomechanical systems [75, 114], exciton-polariton condensates [14, 115], and

semiconductor micropillars [116, 117].
The advancements in the available experimental platforms, and their ability to experimentally study extended systems, have also led to an increased interest in the theoretical description of these many-body open quantum systems. One difficulty in the theoretical study is the scarcity of exact analytical solutions. This is linked to the absence of a free energy concept in these open systems. Hence, one is usually forced to numerically simulate the dynamics of these systems. However, just as is the case for closed quantum systems, one quickly runs into the restrictions of a very quickly growing Hilbert space that needs to be taken into account as the system is enlarged. Indeed, assume a many-body system consisting of a number N p-level systems. The Hilbert space dimension D of the wave function of such a system will grow exponentially as

$$D = p^N = e^{\log(p)N}. \tag{3.1}$$

Even for a two-level system this quickly becomes intractable on present-day computers. For example, for two-level systems exact (numerical) solutions are usually limited to a system consisting of about 16 two-level systems. As p becomes larger exact solutions are completely infeasible. Furthermore, if one wishes to directly solve for the density matrix or work in the Liouvillian superoperator formalism the restriction becomes even more severe. As one is usually interested in the thermodynamic limit, e.g. for the study of phase transitions, this is obviously a big limitation.

Generally, one thus has to resort to approximative methods to describe the physics of these systems. The validity of these approximations is of course model dependent, and usually also heavily influenced by the parameter regimes of said model. In the last decade a lot of theoretical work has been invested to develop methods that allow for the simulation of these many-body open quantum systems and efforts are still ongoing. As we have seen in the previous chapter there exist various equivalent ways to study the dynamics of an open quantum system described by a Lindblad master equation. Depending on the model at hand as well as the properties that are of interest one either chooses for a quantum trajectory description, a Lindblad master equation description, or a description on the level of the Liouvillian superoperator. The various approximation schemes that have been derived and studied in the literature all start from one of these approaches. It goes without saying that each of them will also have their own strengths and

disadvantages, usually largely determined by the system under consideration.

In this thesis we will focus on two paradigmatic systems that have gained interest in the literature due to their generality. The first one is a model that allows us to study spin systems, the XYZ anisotropic Heisenberg model with dissipation. Secondly, we study a bosonic system described by the Bose Hubbard model with dissipation, i.e. a system where photons interact with each other on each site and have the possibility to jump to neighboring ones. In the following sections we will give an overview of these models as well as several methods that have been applied to study them, starting with mean-field solutions and subsequently more complicated simulation schemes.

3.1 The dissipative XYZ Heisenberg model

In the limit of a very strong on-site photon-photon interaction, also referred to as the nonlinearity, one enters the regime of *photon-blockade* [24–27], where the presence of two photons inside the cavity becomes practically impossible. This effect has been observed experimentally both in a single atom in a cavity [28] and in a single superconducting circuit [29]. Interestingly, a system of coupled superconducting resonators [19, 110, 118–120] or Rydberg atoms [100, 121–125] can be mapped onto an effective spin model. Indeed, if the photon blockade occurs at each site in the system they are all reduced to two-level systems, i.e. systems with a ground state $|g\rangle$ (no photon) and an excited state $|e\rangle$ (one photon). One can then easily map $|g\rangle \rightarrow |\downarrow\rangle$ and $|e\rangle \rightarrow |\uparrow\rangle$. In this regard, the XYZ Heisenberg model describes, with a high degree of generality, these systems and other spin models. In the XYZ model, each spin interacts with its nearest neighbors via an anisotropic Heisenberg Hamiltonian

$$\hat{H}_{XYZ} = \frac{1}{Z} \sum_{\langle i,j \rangle} \left(J_x \hat{\sigma}_i^x \hat{\sigma}_j^x + J_y \hat{\sigma}_i^y \hat{\sigma}_j^y + J_z \hat{\sigma}_i^z \hat{\sigma}_j^z \right), \tag{3.2}$$

where Z indicates the coordination number, $\langle i, j \rangle$ indicates the sum over nearest-neighbor links, J_α ($\alpha = x, y, z$) represent the coupling strengths of spin-spin interactions, $\hat{\sigma}_i^\alpha$ are the Pauli matrices of the i-th spin. Since we consider $J_x \neq J_y \neq J_z$, we will refer to this anisotropic Heisenberg model as an XYZ model. If such a system weakly interacts with a Markovian environment, its dynamics is captured via a Lindblad master equation [5, 8] (see chapter 2). In the simplest model, the environment induces the system to relax in a preferential direction, e.g, aligning

the spins along the z-direction which coincides with a relaxation of the excited state $|e\rangle$ ($|\uparrow\rangle$) to the ground state $|g\rangle$ ($|\downarrow\rangle$). This can occur with a mechanism that flips a single spin towards the negative direction of the z-axis, with γ quantifying the rate of spin-flip processes. Note that we have chosen the dissipation rate γ to be identical on each site, as will be the convention throughout this thesis. The state of the system is thus captured by a density matrix $\hat{\rho}(t)$ evolving via

$$\frac{\partial\hat{\rho}(t)}{\partial t} = \mathcal{L}\hat{\rho}(t) = -i\left[\hat{H}_{XYZ}, \hat{\rho}(t)\right] + \gamma\sum_{j=1}^{N}\mathcal{D}[\hat{\sigma}_j^-]\hat{\rho}(t), \tag{3.3}$$

where N is the number of two-level systems, $\hat{\sigma}_j^{\pm} = (\hat{\sigma}_j^x \pm i\hat{\sigma}_j^y)/2$ are the raising and lowering operators for the j-th spin, and $\mathcal{L}$ is the Liouvillian superoperator. Throughout most of this thesis we will mainly limit ourselves to local dissipation with a rate γ, unless specifically mentioned otherwise. Due to its relative generality and simplicity, this model has been taken both as an example of a system exhibiting dissipative phase transitions, as well as a benchmark to test numerical methods. A single-site Gutzwiller mean-field (MF) theory can already retrieve a rich phase diagram for this model [42]. Numerical studies, some capable of including long-range correlations, have confirmed a critical behavior in two-dimensional lattices and the absence of criticality in 1D [1, 44, 104, 107, 126–128], as we will see in closer detail in the next subsections. We emphasize that the rich XYZ model phase diagram in different regimes is a cornerstone of the study of many-body spin quantum systems, magnetism, spin dynamics and quantum phase transitions [125]. Indeed, it is the most general case of the Ising model and of the XXZ model, of the Lipkin-Meshkov-Glick model and other spin-squeezing Hamiltonians, to which it can fall onto, for the appropriate choice of parameters [101].

3.1.1 Mean-field analysis

The first step in studying a quantum many-body system is usually a mean-field approach. Interestingly, a Gutzwiller mean-field study of this model has already shown a very rich phase diagram containing a paramagnetic phase, a ferromagnetic phase, an antiferromagnetic phase, spin density waves and a staggered XY phase [42]. In this study one assumes the system to be described by a factorized density matrix

$$\hat{\rho}_S = \bigotimes_{j=1}^{N}\hat{\rho}_j, \tag{3.4}$$

which allows one to derive expressions from the Lindblad master equation. It is worth noting that on the level of the mean field it is possible to derive analytical equations for the first magnetic moments in the steady state,

$$M_\alpha^{\mathrm{SS}} = \frac{1}{N}\sum_j \left\langle \hat{\sigma}_j^\alpha \right\rangle, \tag{3.5}$$

that is by solving the equation

$$\frac{\partial}{\partial t}\mathrm{Tr}\left[\hat{\rho}\left(\frac{1}{N}\sum_j \hat{\sigma}_j^\alpha\right)\right] = 0. \tag{3.6}$$

This then results in

$$M_x^{\mathrm{SS}} = \pm\sqrt{2M_z^{\mathrm{SS}}\left(M_z^{\mathrm{SS}}+1\right)\frac{J_y - J_z}{J_x - J_y}}, \tag{3.7a}$$

$$M_y^{\mathrm{SS}} = \mp\sqrt{2M_z^{\mathrm{SS}}\left(M_z^{\mathrm{SS}}+1\right)\frac{J_z - J_x}{J_x - J_y}}, \tag{3.7b}$$

$$M_z^{\mathrm{SS}} = -\frac{\gamma}{4}\frac{1}{\sqrt{\left(J_y - J_z\right)\left(J_z - J_x\right)}}. \tag{3.7c}$$

This allows one to calculate a range of interesting observables of the system. Indeed, the local density matrices of this system can be written in terms of their Bloch sphere representation

$$\hat{\rho}_j = \frac{1}{2}\left(\mathbb{1} + \vec{\epsilon}\cdot\vec{\hat{\sigma}}\right), \tag{3.8}$$

With $\vec{\epsilon}$ the Bloch vector, which contains the magnetization in the x, y and z-direction, and $\hat{\sigma}$ the Pauli matrices. Which gives access to e.g. the Von Neumann entropy. It should be noted that this mean-field approach immediately grants access to the thermodynamic limit. Furthermore, by employing a stability analysis it is possible to come to a condition that allows to check for the presence of the various earlier mentioned states. This results in the rich phase diagram depicted in Fig. 3.1. For a more elaborate discussion of such a stability analysis we refer to either Ref. [42] or chapter 5 were we will perform a similar stability analysis.

3.1.2 Beyond Mean-field: results and methods

The research in the literature has predominantly focussed on the parameter regime where the mean-field solutions predict a transition from the paramagnetic phase

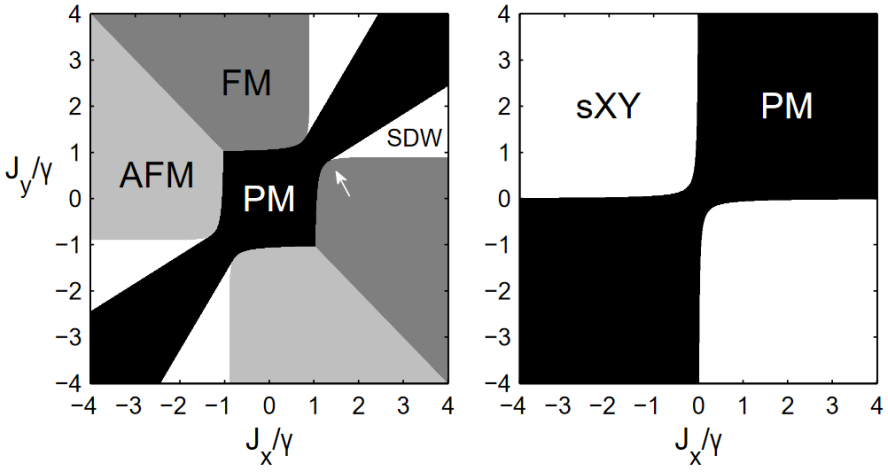

Figure 3.1: *Gutzwiller mean-field solution of the* XYZ *Heisenberg model with local dissipation. [Left panel] For* $J_z/\gamma = 1$ *one finds a paramagnetic phase (PM), a ferromagnetic phase (FM), an antiferromagnetic phase (AFM) and a spin-density wave phase (SDW). The white arrow points to a Lifshitz point, i.e. a point where the PM, FM and SDW phase coexist. [Right panel] For* $J_z = 0$ *one finds a paramagnetic phase and a staggered XY phase (sXY). These figures originate from Ref. [42].*

to the ferromagnetic phase as J_y/γ is increased. More precisely for the parameters $J_x/\gamma = 0.9$, $J_z/\gamma = 1$ and $J_y/\gamma > 0$. Furthermore, the studies are typically limited to two-dimensional square lattices. If we discuss the transition from the paramagnetic to the ferromagnetic phase in what follows we also refer to this parameter regime. Let us now discuss several methods that go beyond the previous mean-field approach.

As a first extension to the Gutzwiller mean-field approach at the level of the master equation, one can consider an ansatz for the density matrix that includes close-range quantum correlations. This can again be done by assuming a product density matrix, but instead of taking the product of the individual site density matrices one beholds a cluster of neighboring sites and takes the product of the density matrices of this cluster [44, 129–131]

$$\hat{\rho} = \bigotimes_C \hat{\rho}_C. \tag{3.9}$$

The various clusters in the system are often also called the plaquettes. It should be clear that the numerical complexity of this method scales exponentially with

the number of sites in the respective clusters. Hence, this method is unable to capture any long-range correlations but allows for the study of the influence of short-range quantum correlation in the thermodynamic limit. Note that clusters of size one correspond to the Gutzwiller mean-field approach in (3.4). Another extension of the Gutzwiller mean-field approach of the previous subsection can also be made in a quite similar fashion through a trajectory approach. Instead of factorizing the density matrix one factorizes the wave function [128]

$$|\psi\rangle = \bigotimes_{j=1}^{N} |\psi_j\rangle. \tag{3.10}$$

The advantage of such an approach is that due to the stochastic nature of the quantum trajectories this approach includes long-range classical correlations, which were not included in the density matrix Gutzwiller mean-field approach. However, exactly due to these classical correlations the trajectory does not immediately grant access to the thermodynamic limit as one needs to keep track of these correlations spreading throughout the system. The inclusion of classical correlations thus comes at the cost of having to perform a finite-size scaling to gain access to the thermodynamic limit. Both of the above methods predict a re-entrance of the paramagnetic phase for large values of J_y/γ, where the mean-field predicts the ferromagnetic phase to persist until infinity, in a study of two-dimensional cubic lattices. Furthermore, a wider study of the phase diagram shows that the inclusion of close-range quantum correlations has a dramatic influence on the phase diagram. The phase diagram, shown in Fig. 3.2, predicted by the cluster mean-field approach (3.9) in a two-dimensional lattice shows that the ferromagnetic region shrinks and becomes finite. This phase diagram will be discussed in more detail in chapter 7.

As both these methods give promising and interesting results, a natural extension is of course a cluster-Gutzwiller approach on the level of the wave function [1], which we will discuss in detail in chapter 7 and 8. Another extension based on clusters comprises of a linked-cluster expansion [127].

Where the previous methods based on a factorization are approximative in their "guess" for the proper wave function or density matrix, there also exists a method that aims to reduce the Hilbert space of the problem by only taking the relevant states for the dynamics of the system into account. This method is called the corner space renormalization method [104, 132], and finds the origin of its name in the act of only resorting to a "corner" of the Hilbert space to describe the system.

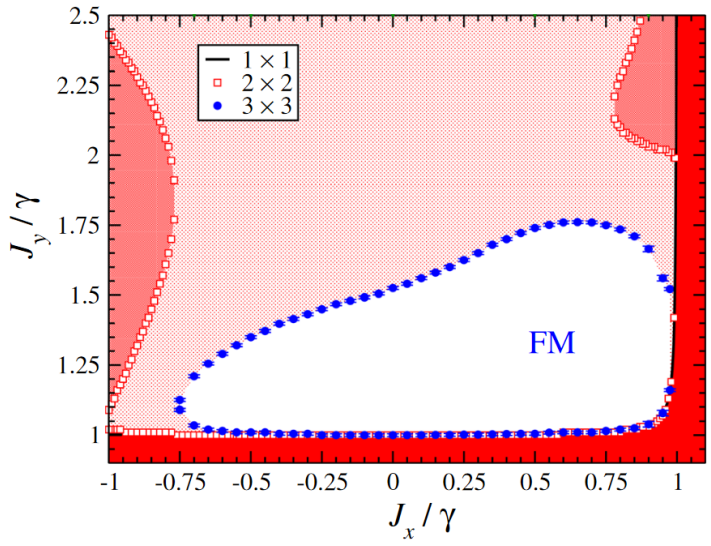

Figure 3.2: *Cluster mean-field phase diagram for the* XYZ *Heisenberg model with local dissipation and* $J_z/\gamma = 1$. *The single-site mean field (black full line) predicts a ferromagnetic phase until infinity as* J_y/γ *is increased. Inclusion of short-range quantum correlations through clusters of size* 2×2 *(red squares) and* 3×3 *(blue circles) show the shrinking of the ferromagnetic region and a re-entrance of the paramagnetic phase (red regions, the darkest color indicates a paramagnetic region in all simulations) along the* J_y/γ *axis. These figures originate from Ref. [44].*

In this method one starts by simulating the exact solution of a small system (where small means that one can still solve it numerically). An eigendecomposition of the steady state density matrix then allows for the determination of the most relevant states. One can then construct a "new" Hilbert space of a system that is quadratic the size of the small system by taking the tensor product of the original (reduced) Hilbert space with itself. One can then once again perform an eigendecomposition of the bigger system and repeat the process to gain access to bigger systems. The specific number of relevant states that needs to be taken into account is highly depending on the convergence of the method, which is usually greatly influenced by the specific parameter regime. If convergence is reached however, one can say that the obtained result is numerically exact. Such a method grants access to a finite-size scaling of the systems properties as well as the entanglement properties [104]. One has to note that in a regime where the system is described by a highly mixed state, this method can experience issues with convergence. This is due to the increased number of states that need to be taken into account to accurately describe the systems entropic state, which can quickly go beyond what is feasible in numerical calculations.

Another related class of approximative methods is given by the tensor network approaches. On the level of the wave function one can resort to a matrix product state ansatz (MPS) in one dimension or a matrix product operator approach (MPO) on the level of the density matrix. Both these approaches perform very well in for a one dimensional system [133, 134]. They were also used to show that in one dimension ferromagnetic order is not present in the steady state [44]. With an infinite matrix product operator approach (iMPO) the study in one dimension was extended to the dynamics of the system where it was shown that no critical dynamics occur (it however does in two dimensions) [107].

In two dimensions the tensor network method can be extended with so-called projected entangled pair states (PEPS). To gain access to the thermodynamic limit methods based on infinite projected entangled pair states are also being investigated and show promise in regions where they converge [135, 136]. Recently, numerical approaches based on neural network ansatzes [137–142] have also been applied, also showing promise for the description of larger lattices. An extension of the previously mentioned cluster methods in combination with methods such as the corner approach or neural network approaches, allowing bigger cluster sizes, comprise an interesting and active pursuit of research.

For a more elaborate discussion of the different simulation methods we refer to

their respective papers, the interested reader can also find an overview in a review paper by Weimer et al. [143].

A special case where one can exactly study up to the order of a hundred spins is the all-to-all coupled Hamiltonian. By exploiting the permutational symmetry present in the system one can drastically reduce the size of the Liouvillian. This method has allowed to study the validity of the mean-field approximation in the all-to-all connected version of this system [2] and will be discussed in detail in chapter 4 and 5.

3.2 The driven-dissipative Bose-Hubbard model

In the case of a weak(er) nonlinearity, i.e. a weak(er) on-site photon-photon interaction than in the previous section, the optical cavity will no longer describe a two-level system. Rather, it will be a bosonic system that can be described as a p-level system, or in principle, a system with an unbound set of number states ($p \to \infty$). Let us consider a nonlinearity of the Kerr type, of which the strength of the photon-photon interaction in a cavity is given by U and in which photons can "hop" between nearest-neighboring cavities with an amplitude J due to quantum tunneling. If we drive our system with a coherent laser drive with laser frequency ω_L and strength F which has a detuning of $\Delta = \omega_L - \omega_C$ with respect to the cavity frequency ω_c then the Hamiltonian of this system is given by the so-called Bose Hubbard Hamiltonian. In the frame rotating with the drive frequency one has

$$\begin{aligned}\hat{H}_{BH} = &\sum_i \left(-\Delta \hat{a}_i^\dagger \hat{a}_i + \frac{U}{2}\hat{a}_i^\dagger \hat{a}_i^\dagger \hat{a}_i \hat{a}_i + F\left(\hat{a}_i + \hat{a}_i^\dagger\right)\right) \\ &- \frac{J}{z}\sum_{\langle i,j\rangle}\left(\hat{a}_i^\dagger \hat{a}_j + \hat{a}_j^\dagger \hat{a}_i\right),\end{aligned} \tag{3.11}$$

with z the number of nearest neighbors and $\sum_{\langle i,j\rangle}$ a sum over all these nearest-neighbor pairs. The dynamics of the driven-dissipative Bose Hubbard model are then governed by a Lindblad master equation describing the time evolution of the density matrix

$$\frac{d\hat{\rho}}{dt} = -i\left[\hat{H}_{BH}, \hat{\rho}\right] + \frac{\gamma}{2}\sum_i \left(2\hat{a}_i \hat{\rho} \hat{a}_i^\dagger - \hat{\rho}\hat{a}_i^\dagger \hat{a}_i - \hat{a}_i^\dagger \hat{a}_i \hat{\rho}\right), \tag{3.12}$$

with γ the dissipation rate and the annihilation operator $\hat{a}_i$ being the jump (Lindblad) operator, i.e. the loss of a photon. A schematic description of this

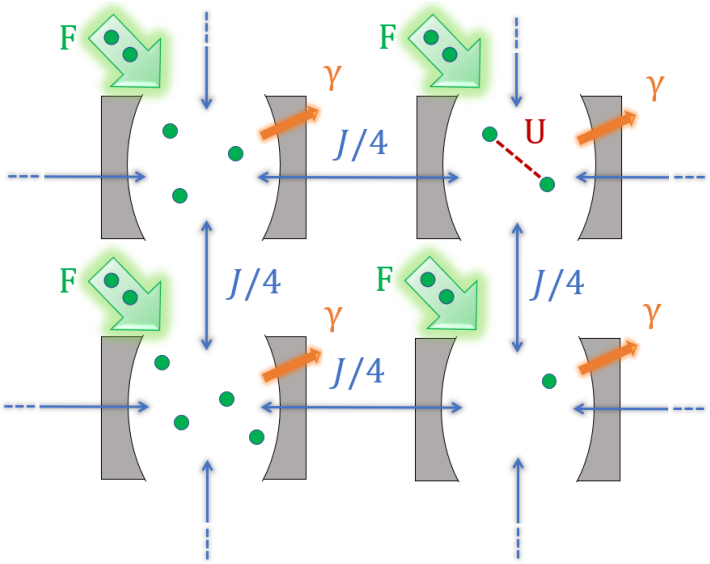

Figure 3.3: *Graphical depiction of a square lattice of optical cavities with cavity frequency ω_C, where photons are represented as green circles. A coherent laser with frequency ω_L is present as a drive with pump strength F. Photon-photon interactions are present under the form of a Kerr non-linearity U. Photons dissipate from the individual cavities with a dissipation rate γ. Hopping of the photons is possible between neighbouring cavities due to tunneling, with a hopping amplitude $J/4$.*

system is shown in Fig. 3.3.

The driven-dissipative Bose-Hubbard model has been extensively studied [3, 85–87, 91, 132, 144–148]. It combines physics of optical bistability [149], well known from nonlinear optics, with the phenomenon of the Mott insulator [22], familiar from condensed matter physics. However, since exactly solving a system of multiple two-level systems is already a burdensome task, it should be clear that solving the equation (3.12) exactly is numerically infeasible already for a small number of cavities due to the larger local Hilbert spaces. Hence, even numerical exact solutions are infeasible for very small systems and one needs to resort to approximate methods. Furthermore, the large number of tunable parameters causes this system to be notoriously difficult to study. As a result, the literature has predominantly focussed on studying a small number of cavities of which the cutoff in local Hilbert space, i.e. $n_{\max}$ of the Fock state $|n_{\max}\rangle$, can reach fairly high values, depending on the method used to study the system. In this thesis however, as well as the next subsections, the focus will lie on describing extended lattices, with the thermodynamic limit as the ultimate goal.

3.2.1 Mean-field analysis

Similarly to the previous section, one can perform a mean-field analysis by assuming that the density matrix of the collective system of cavities can be written in terms of a product density matrix, i.e. a Gutzwiller mean-field approach. This coincides with decreasing the complexity of the model to that of a single site. Furthermore, it once again allows us to derive an analytical solution. The mean-field decoupling allows one to write $\hat{a}_i^\dagger \hat{a}_j = \langle \hat{a}_i^\dagger \rangle \hat{a}_j + \hat{a}_i^\dagger \langle \hat{a}_j \rangle - \langle \hat{a}_i^\dagger \rangle \langle \hat{a}_j \rangle$ and subsequently derive a self-consistent equation for $\langle \hat{a}_j \rangle = \langle \hat{a} \rangle$ [87, 150, 151],

$$\langle \hat{a} \rangle = -\frac{2\phi_J}{\delta} \frac{{}_0F_2(;1+\delta,\delta^*;8|\phi_J|^2)}{{}_0F_2(:\delta,\delta^*;8|\phi_J|^2)}. \tag{3.13}$$

with $\phi_J = (F - J\langle \hat{a} \rangle)/U$ the renormalized drive, $\delta = -(2\Delta + i\gamma)/U$ the dimensionless detuning and ${}_0F_2(;a,b;z)$ the hypergeometric function. The solution for $\langle \hat{a} \rangle$ grants direct access to higher order correlators [151], e.g. the particle number expectation value $\langle \hat{n} \rangle = \langle \hat{a}^\dagger \hat{a} \rangle$ [150]. It allows one to construct a phase diagram for this system, shown in Fig. 3.4 , taken from Ref. [87]. The figure shows the photon number at the 4-photon resonance, i.e. $1 + 2\Delta/U = 4$ and for small dissipation $\gamma = U/20$ with respect to the nonlinearity U. As one can see from the modest particle number

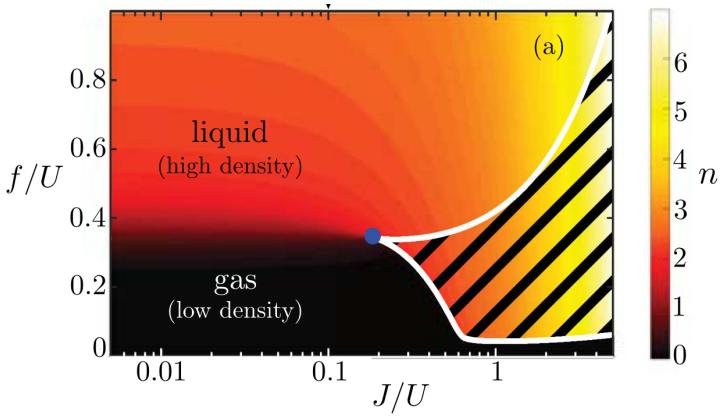

Figure 3.4: *Gutzwiller mean-field solution of the Bose Hubbard model with local dissipation and coherent drive. The system is chosen at the 4-photon resonance* $1 + 2\Delta/U = 4$ *and a small dissipation* $\gamma = U/20$ *with respect to the nonlinearity* U *is applied. The phase diagram consists of a low-density phase (gas), a high-density phase (liquid) which has a steep crossover for small* J/U*. For higher values of* J/U *this transforms into a first-order transition and a regime of coexistence emerges. The bistable region is bounded by the white lines. This figure originates from Ref. [87, 146].*

expectation value in the phase diagram, the results obtained for this parameter lean towards a stronger nonlinearity. In Ref. [87] the authors formulate a gas-liquid phenomenology, where they associate the low-density phase with a gas and the high-density phase with a liquid. They report a region with a steep crossover from the low density phase to the high density phase as the pumping strength F/U is increased, for small values of J/U. However, as the hopping amplitude J/U is increased this steep crossover transforms into a transition of first-order indicating a bistable regime.

Additionally, another often used approach is the Gross-Pitaevskii mean-field approach. It consists of assuming that the state of each cavity j can be described by a coherent state $|\alpha_j\rangle$. That is, a state that obeys the relation $\hat{a}_j|\alpha_j\rangle = \alpha_j|\alpha_j\rangle$. In other words, the density matrix of each site j can be written as $\hat{\rho}_j = |\alpha_j\rangle\langle\alpha_j|$. It turns out that such an assumption is quite good in the semi-classical regimes where the photon number is on the larger side. However, in the strong coupling regime with small occupation number it is usually not adequate. For such an ansatz one can rewrite the time evolution according to the Lindblad master equation of the system (3.12) in terms of time evolution of the fields α_j, which can be written in a

Gross-Pitaevskii like equation

$$\frac{\partial \alpha_j}{\partial t} = \left[-i\left(\Delta - U\left(|\alpha_j|^2 - 1\right) - \gamma/2\right)\right]\alpha_j - i\frac{J}{z}\sum_{j'}\alpha_{j'} + iF. \tag{3.14}$$

In the steady state, i.e. when the time derivative is zero, one can then rewrite this equation as

$$F^2 = |\alpha|^2\left[\left(\Delta + J - U|\alpha|^2\right)^2 + \gamma^2/4\right], \tag{3.15}$$

where we assumed the system to be homogeneous, i.e. $\alpha_j = \alpha$. Such an approach is usually thought of being classical since no entanglement between multiple cavities is possible and the on-site density matrix represents a pure state at all times. The method thus fails to describe a mixed state.

In this thesis we will mainly focus on regions with strong photon-photon interaction, which leads to a lower occupation number. More specifically, one of the parameter regimes of interest is the bistable region in Fig. 3.4. In this region the condition of a coherent state is not always satisfied. Hence, when mentioning mean-field results with regards to the Bose-Hubbard model we will be referring to those obtained via the Gutzwiller mean-field approach, unless specified otherwise. In the next subsection we will review several (numerical) approaches that have been used to study the driven-dissipative Bose-Hubbard model (in extended lattices) and which go beyond the previous mean-field methods.

3.2.2 Beyond Mean-field: results and methods

As was the case for lattices of two-level systems, the corner space renormalization method can also be applied to the Bose Hubbard model [88, 132]. Of course, in the limit of weak photon-photon interactions one is restricted to a small collection of interacting cavities. If the local Hilbert space however is small, e.g. in the limit of a stronger nonlinearity it is still possible to use the method to obtain results for larger lattices [132]. It was shown that mean-field predictions can be rather accurate in regions where the on-site interaction U does not compete with the hopping amplitude J, i.e. if J is sufficiently small with respect to U. In regions where they do compete, significant deviations can be present between the "exact" solution and the mean-field predictions.

Building onto the Gutzwiller mean-field approach, a self-consistent expansion in the inverse coordination number $1/z$ of the lattice was applied [152]. They showed large density fluctuations in the gas-liquid transition of Fig. 3.4. Unfortunately,

this method could not be used to study the hysteretic regime, as it does not always converge in this regime.

If one is interested in the parameter region where U is small, one can resort to the so-called Truncated Wigner approach [14, 153, 154]. This approach solves the problem of the coherent ansatz not being able to describe a mixed state. It does so by sampling various initial conditions and simulating stochastic trajectories to build up the density matrix. It stems from being able to write the master equation as a third-order differential equation for the quasi-probability Wigner function. This is nothing more than an alternative way to represent the density matrix. In the limit of small U however, one can reduce this equation to one of second order since the third order terms are proportional to U. The remaining problem can then be rewritten in terms of a Langevin equation for the complex fields $\alpha_j(t)$

$$\frac{\partial \alpha_j}{\partial t} = \left[-i\left(\Delta - U\left(|\alpha_j|^2 - 1\right) - \gamma/2\right)\right]\alpha_j - i\frac{J}{z}\sum_{j'}\alpha_{j'} + iF + \sqrt{\gamma/2}\chi(t), \tag{3.16}$$

with $\chi(t)$ normalized random complex Gaussian noise obeying the relations $\langle\chi(t)\chi(t')\rangle = 0$ and $\langle\chi(t)\chi^*(t')\rangle = \delta(t-t')$. Note that this is exactly the same as equation (3.14) with added complex Wiener noise. The truncated Wigner approach was applied to extended lattices of the Bose-Hubbard model and has shown remarkable results when compared to the corner method [91]. It was applied to study first-order phase transitions, showing that they do not occur in one dimension, indicating a lower-critical dimension of $d < 2$. In a continuing study the role of disorder was studied on the criticality of the first-order transition [147]. An efficient sampling method to compute configuration averages in disordered systems, of which the dynamics are described by a stochastic evolution, was introduced. They showed that criticality was suppressed in 2 dimensions, as was indicated by an exponential decrease in space of the correlation functions. Related to this truncated Wigner approach is the functional integral approach applied in Ref. [86].

The truncated Wigner approach however not always obtains good results, even in the limit of small U, as was shown in a study of spontaneous Beliaev-Landau scattering out of equilibrium through the use of a hierarchy of correlation functions [155]. On the quantum trajectory level one can opt for a Gaussian description. That is, one assumes the state of the system can be described with the knowledge of its first and second moments. This approach is known as the Gaussian quantum trajectory approach and has been applied to extended lattices of the quadratically

driven Bose-Hubbard model [92–94]. This quadratically driven model was also studied in Ref. [89] with a mean-field density matrix decoupling, where the phase transition associated with a $\mathbb{Z}_2$ symmetry was investigated. Furthermore, a study of the model with single photon drive as well as a quadratic drive has been performed in Ref. [156], a Gutzwiller trajectory approach based on a diffusive unravelling, also known as homodyne measurements, was used as well as an MPS approach. Studies that employ tensor network approaches have mostly been limited to one dimensional Bose Hubbard chains [88, 157–159].

PART

II

MEAN-FIELD VALIDITY IN OPEN ALL-TO-ALL CONNECTED QUANTUM SYSTEMS

CHAPTER 4

Permutational invariance in open quantum systems

In this chapter we will introduce a framework that will allow us to exploit permutational symmetry in open all-to-all connected quantum systems to drastically reduce the number of states one needs to keep track of. It will allow us to decrease the exponential scaling of the dimension of the Liouvillian space to a polynomial one. This grants access to the exact numerical simulation of many-body open quantum systems to an extent that would be infeasible in the full space. The contents of this chapter are based on a work by Gegg et al. [160] and hold close relation to works by Shammah et al. [161]. These frameworks will be used in chapter 5 and 6, we then apply this to study the dissipative XYZ Heisenberg model and the driven-dissipative Bose Hubbard model.

4.1 Two-level systems

To illustrate how one can exploit permutational symmetry to reduce the size of the Liouvillian, we will first resort to the simplest example where we have a collection of interacting two-level systems. Let us first look at the individual two-level system and how the states of this system can be represented. We will denote the states of the two-level system as $|0\rangle$ and $|1\rangle$. This allows us to write a general density matrix of a two-level system as

$$\hat{\rho} = \begin{pmatrix} c_{00} & c_{01} \\ c_{10} & c_{11} \end{pmatrix} = c_{00}|0\rangle\langle 0| + c_{01}|0\rangle\langle 1| + c_{10}|1\rangle\langle 0| + c_{11}|1\rangle\langle 1|. \tag{4.1}$$

The explicit notation in its ket and bra form will prove to be rather useful in the framework we will be presenting. To clarify this we extend the size of our system by adding a second two-level system. The density matrix will now be a 4×4 matrix that can be represented as

$$\hat{\rho} = \sum_{i,j,k,l} c_{ik}^{jl} \left(|i\rangle\langle j| \otimes |k\rangle\langle l| \right) = \sum_{i,j,k,l} c_{ik}^{jl} |ik\rangle\langle jl|. \tag{4.2}$$

It should be clear that this is straight forwardly extended for larger systems with size N, and results in 4^N terms, i.e. the square of the Hilbert space size of the wave function which is equal to 2^N. We will now introduce a new representation for an element $|k_1 k_2 ... k_N\rangle\langle k_1' k_2' ... k_N'|$ that will keep track of how many sites are in a respective local state $|i\rangle\langle j|$. Assume the state has n_{00} sites in $|0\rangle\langle 0|$, n_{01} sites in $|0\rangle\langle 1|$, n_{10} sites in $|1\rangle\langle 0|$, and n_{11} sites in $|1\rangle\langle 1|$, then we will write for the operator

$$|k_1 k_2 ... k_N\rangle\langle k_1' k_2' ... k_N'| = \hat{O}\left[n_{00}, \mathbf{v}_{00}, n_{01}, \mathbf{v}_{01}, n_{10}, \mathbf{v}_{10}, n_{11}, \mathbf{v}_{11} \right]. \tag{4.3}$$

In this new notation we have introduced the sets $\mathbf{v}_{ij} = \{ s : |i\rangle_s\langle j|_s \}$ that keep track of which sites are in the respective local states $|i\rangle_s\langle j|_s$, where s denotes the specific site. Note that the order in which we place the n_{ij} and v_{ij} in the righthandside of (4.3) is arbitrarily chosen, and could have been placed in any order while still representing the same state. Nonetheless, we shall work with the order introduced above.

Up till now we have only written down a new way of representing the basis of the density matrix, we still need to keep track of as many states as are present in the full space. The advantage of this notation however becomes particularly clear when we assume the system's state to be permutationally invariant. This permutational invariance implies that any and all permutations on the sites of the system leaves the state of the system unchanged. Let us illustrate this with an example of three two-level systems. Observe the state $|100\rangle\langle 100|$, which can be written as

$$\begin{aligned} |100\rangle\langle 100| &= |1\rangle_1\langle 1|_1 \otimes |0\rangle_2\langle 0|_2 \otimes |0\rangle_3\langle 0|_3 \\ &= \hat{O}\left[2, \{2,3\}, 0, \emptyset, 0, \emptyset, 1, \{1\} \right], \end{aligned} \tag{4.4}$$

which immediatly tells us that there are $n_{00} = 2$ sites in state $|0\rangle\langle 0|$, $n_{01} = 0$ sites in state $|0\rangle\langle 1|$, $n_{10} = 0$ sites in state $|1\rangle\langle 0|$ and $n_{11} = 1$ site in state $|1\rangle\langle 1|$. Note that the subscripts on the kets and bras in (4.4) indicate the specific site and we use $\emptyset$

to indicate an empty set. The non-empty sets of sites corresponding to this state are thus $\mathbf{v}_{00} = \{2, 3\}$ and $\mathbf{v}_{11} = \{1\}$. It should be clear that the n_{ij} stay unchanged under a permutation of the sites, whereas the sets $\mathbf{v}_{ij}$ do change. Indeed, on the above state we can perform permutations that will yield two non-trivial results, namely the states

$$|010\rangle\langle 010| = |0\rangle_1\langle 0|_1 \otimes |1\rangle_2\langle 1|_2 \otimes |0\rangle_3\langle 0|_3, \quad \text{with} \quad \mathbf{v}_{00} = \{1, 3\}, \mathbf{v}_{11} = \{2\}, \tag{4.5}$$

$$|001\rangle\langle 001| = |0\rangle_1\langle 0|_1 \otimes |0\rangle_2\langle 0|_2 \otimes |1\rangle_3\langle 1|_3, \quad \text{with} \quad \mathbf{v}_{00} = \{1, 2\}, \mathbf{v}_{11} = \{3\}. \tag{4.6}$$

The coefficients corresponding to the above states can in general however be different from each other, depending on the initial conditions of the system. It is in the special case where one cannot distinguish between the various sites, and when the coefficients of the states that transform into each other under a permutation are equal to each other, that a drastic decrease in the number of states one needs to take into account will occur. Indeed, in such a situation the system is permutationally invariant and one can discard the information from the sets $\mathbf{v}_{ij}$ and resort to a much simpler notation

$$\hat{O}[n_{00}, \mathbf{v}_{00}, n_{01}, \mathbf{v}_{01}, n_{10}, \mathbf{v}_{10}, n_{11}, \mathbf{v}_{11}] \rightarrow \hat{O}[n_{00}, n_{01}, n_{10}, n_{11}]. \tag{4.7}$$

This means that the number of states one needs to keep track of becomes much smaller since the number of states will decrease to the number of permutational invariant subspaces in the full Hilbert space. That is, the number of states that cannot be transformed into each other under a permutation. Another permutational invariant subspace could for example be generated from the state $|110\rangle\langle 110|$ by applying all possible permutations. From our earlier example we can already see that the three respective states form a permutational invariant subspace and can now be represented by a single state. Evidently, a permutational invariant description of a system imposes restrictions on the system itself, which should satisfy the condition of indistinguishability. In the next section we will go in further detail on the conditions of the system for the permutational invariant approach to be applicable. The remainder of this section will discuss the decrease in complexity as a result of the permutational invariance. The number of permutational states

in a permutational invariant subspace of a certain set $\{n_{ij}\}$ can be calculated as

$$R\left(\{n_{ij}\}\right) = R\left(n_{00}, n_{01}, n_{10}, n_{11}\right) = \binom{N}{n_{00}, n_{01}, n_{10}, n_{11}} = \frac{N!}{n_{00}!n_{01}!n_{10}!n_{11}!}. \tag{4.8}$$

Which is nothing more than the multinomial coefficient, that is the number of ways to order N interchangeable objects into the boxes with index ij equal to 00, 01, 10 and 11 such that each box contains n_{ij} elements. In equation (4.8) we introduced a more compact notation to indicate the set of n_{ij}, i.e. n_{00}, n_{01}, n_{10} and n_{11}, as $\{n_{ij}\}$. Also note that $n_{00}+n_{01}+n_{10}+n_{11} = N$, i.e. each site is in one of the possible ketbra states. The reduction in the number of coefficients one needs to keep track of for a collection of N two-level systems can then be straightforwardly calculated by determining the number of sets $\{n_{00}, n_{01}, n_{10}, n_{11}\}$ that satisfy the condition

$$\sum_{i,j=0,1} n_{ij} = n_{00} + n_{01} + n_{10} + n_{11} = N. \tag{4.9}$$

Each set $\{n_{ij} : \forall i, j \in \{0,1\}\}$ characterizes a subspace of permutational invariant states and by calculating their number we will have determined the number of states we need to keep track of. It can be calculated by solving the following sum, for which we refer to appendix B.1 for the derivation, which results in

$$D\left(N\right) = \sum_{n_{00}+n_{01}+n_{10}+n_{11}=N} 1 = \binom{N+3}{N} = \frac{1}{6}\left(N+3\right)\left(N+2\right)\left(N+1\right). \tag{4.10}$$

Which is a drastic reduction with respect to the number of elements in the density matrix represented in the full space of the density matrix. Indeed, the number of coefficients is exponential in size, more specifically 4^N, whereas the permutational invariant basis shows a polynomial scaling with the system size N of order three. Finally, one can use the multinomial theorem [162] to prove that the sum over the coefficients of each permutational invariant subspace recovers the total number of coefficients in the exact treatment

$$D_{\text{Exact}}\left(N\right) = \sum_{n_{00}+n_{01}+n_{10}+n_{11}=N} R\left(n_{00}, n_{01}, n_{10}, n_{11}\right) = 4^N. \tag{4.11}$$

A useful expression in this new representation will be the completeness relation, which can now be written as

$$\begin{aligned} &\sum_{k_1,k_2,\ldots,k_N=0,1} |k_1 k_2 \ldots k_N\rangle\langle k_1 k_2 \ldots k_N| = \mathbb{1}, \\ \Leftrightarrow\ &\sum_{n_{00}=0}^{N} \sum_{\text{sets}} \hat{O}[n_{00}, \mathbf{v}_{00}, 0, \emptyset, 0, \emptyset, N - n_{00}, \mathbf{v}_{11}] = \mathbb{1}, \\ \Leftrightarrow\ &\sum_{n_{00}=0}^{N} \binom{N}{n_{00}} \hat{O}[n_{00}, 0, 0, N - n_{00}] = \mathbb{1}, \end{aligned} \tag{4.12}$$

where $\sum_{\text{sets}}$ runs over all possible unique sets $\mathbf{v}_{ij}$ and we also wish to note that $\mathbf{v}_{00} \cup \mathbf{v}_{11} = \{1, 2, \ldots, N\}$, i.e. the set of all sites in the system. In the last equation we used (4.7) and (4.8), where the multinomial coefficient could be written as a binomial coefficient due to both n_{01} and n_{10} being equal to zero.

4.2 Conditions for a permutational invariant time evolution

The conditions to describe the system in its permutational invariant basis can be summarized under the *indistinguishability* of the sites in the system. If all sites are indistinguishable from each other, a permutation will evidently leave the system unchanged. We are of course interested in being able to calculate the time evolution of such a system in the permutational invariant framework. Let us go into deeper detail what this means for the system's state, as well as the Hamiltonian and dissipation governing the time evolution of the system. As a first condition, already mentioned in the previous section, we can impose that all coefficients of states inside a certain permutational invariant subspace should be equal to each other. If this were not the case one still needs the full Hilbert space of coefficients to describe the system. This condition alone is of course not enough to obtain indistinguishability in the system itself. Indeed, the Hamiltonian will impose a certain structure on our collection of sites, e.g. a 1D chain of sites, a 2D lattice of sites, ... Even if we observe a permutational invariance in the notation of the states, it need not be present if we were observing the physical sites of the system. This can be easily illustrated with an example of four connected two-level systems on a chain as illustrated in 4.1, where the on-site interactions are identical for

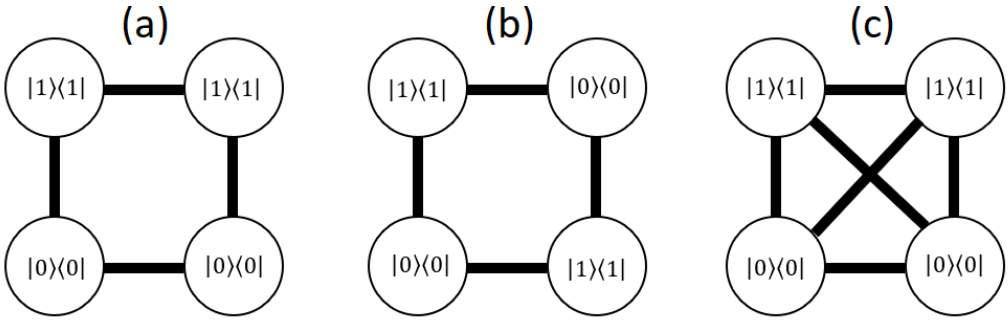

Figure 4.1: *Schematical illustration of a chain of four two-level system in the states* ***(a)*** $|1100\rangle\langle 1100|$ *and* ***(b)*** $|1010\rangle\langle 1010|$. ***(c)*** *Schematical description of four all-to-all connected two-level systems in a state with* $n_{00} = n_{11} = 2$. *Any permutation performed on this all-to-all connected system leaves the system invariant.*

each two-level system as well as the nearest-neighbor interaction strength between each two-level system. Let us look at the specific state $|1100\rangle\langle 1100|$ depicted in panel (a) of Fig. 4.1, which through a permutation could be transformed into $|1010\rangle\langle 1010|$, depicted in panel (b) of Fig. 4.1. For this specific case one could distinguish between both states. Indeed, for the first state each site has one neighbor in a local state $|0\rangle\langle 0|$ and the other neighbor in the local state $|1\rangle\langle 1|$. For the second state, after the permutation, each site has two neighbors in the same local state, different from the state of the site itself. It should be clear that under the same interaction between the neighboring sites the result would be different for the above states. To reconcile with the indistinguishability condition all sites present in the system should be connected to each other as depicted on panel (c) of Fig. 4.1. In other words, the framework from section 4.1 requires an all-to-all connected Hamiltonian. Furthermore, all links inside the system should have the same interaction strength and the on-site interactions should also be identical at each site. More practically, this means that the systems Hamiltonian must be able to be written in terms of collective operators. That is in terms of, for a general local operator $\hat{x}_j$, operators of the form

$$\hat{X} = \sum_{j}^{N} \hat{x}_j, \tag{4.13}$$

which are also referred to as collective processes. This finally brings us to the conditions on the dissipation. There are two possible dissipation schemes that are of interest to us in this thesis and that fulfill the condition of indistinguishability. The first one is (identical) local dissipation at each site, i.e. the local Lindblad operator at each site j is identical. The other is collective dissipation of all sites at the same time and with the same lindbad operator, that is

$$\hat{L} = \sum_j \hat{L}_j, \tag{4.14}$$

where once again for all j we have that the local Lindblad operators are identical. It is also allowed to have a combination of both local dissipation and collective dissipation, both obeying the above requirements.

With this we can summarize the conditions to obtain a system where the sites are indistinguishable from each other and we can thus utilize the framework that exploits the permutational invariance in the system to drastically reduce the complexity for its time evolution. The system should

- be all-to-all coupled, with identical local Hamiltonians for each site;
- have identical local dissipation or collective dissipation, or a combination thereof;
- start in an initial state that is permutational invariant.

For such a system the sites in the system are *indistinguishable* from each other, and will be so at all times.

4.3 Time evolution

We now have all components needed to calculate the time evolution of an open quantum system governed by the Lindblad master equation (2.23) in a reduced space. One way to achieve this is to note that the time evolution of the expectation value of an operator $\hat{X}$ can be written as

$$\begin{aligned} \partial_t \langle \hat{X} \rangle &= \partial_t \mathrm{Tr}\left[\hat{X}\hat{\rho}\right] = \mathrm{Tr}\left[\hat{X}\partial_t\hat{\rho}\right] \\ &= -i\mathrm{Tr}\left[\hat{X}\left[\hat{H},\hat{\rho}\right]\right] + \frac{\gamma}{2}\sum_j \left(2\mathrm{Tr}\left[\hat{X}\hat{L}_j\hat{\rho}\hat{L}_j^\dagger\right] - \mathrm{Tr}\left[\hat{X}\left\{\hat{L}_j^\dagger\hat{L}_j,\hat{\rho}\right\}\right]\right), \end{aligned} \tag{4.15}$$

where we substituted (2.23). Let us now observe the operator $\hat{X}$ as one of the elements of the operator basis in the permutational reduced Liouvillian space

$$\hat{X} = \hat{O}[n_{00}, n_{01}, n_{10}, n_{11}], \tag{4.16}$$

where we define the expectation value of this operator as

$$\begin{aligned} \rho[n_{00}, n_{01}, n_{10}, n_{11}] &= \mathrm{Tr}\left[\hat{O}[n_{00}, n_{01}, n_{10}, n_{11}]\,\hat{\rho}\right] \\ &= \left\langle \hat{O}[n_{00}, n_{01}, n_{10}, n_{11}] \right\rangle. \end{aligned} \tag{4.17}$$

When one calculates the expectation value of all the $\hat{O}[n_{00}, n_{01}, n_{10}, n_{11}]$ in the permutational reduced basis we gain access to all coefficients of the density matrix. Indeed, the above expectation values are equal to the expansion of the density matrix into the new basis, i.e. a projection, and thus yield the coefficients of $\hat{\rho}$. This allows us to construct a system of equations of motion of all $\rho[n_{00}, n_{01}, n_{10}, n_{11}]$ governed by (4.15). Let us first introduce a new notation where we take into account the number of states in a permutational invariant subspace by multiplying $\rho[n_{00}, n_{01}, n_{10}, n_{11}]$ with $R(n_{00}, n_{01}, n_{10}, n_{11})$

$$\xi[n_{00}, n_{01}, n_{10}, n_{11}] = \frac{N!}{n_{00}!n_{01}!n_{10}!n_{11}!}\rho[n_{00}, n_{01}, n_{10}, n_{11}]. \tag{4.18}$$

This will come in quite handy when calculating expectation values of general operators since it directly takes into account the number of identical coefficients in $\hat{\rho}$. Furthermore, it also allows to prevent numerical errors. Let us give the example of the calculation of the trace, by using the completeness relation of (4.12), one finds

$$\begin{aligned} \mathrm{Tr}[\hat{\rho}] &= \sum_{n_{00}=0}^{N} \binom{N}{n_{00}} \mathrm{Tr}\left[\hat{O}[n_{00}, 0, 0, N - n_{00}]\,\hat{\rho}\right] \\ &= \sum_{n_{00}=0}^{N} \binom{N}{n_{00}} \rho[n_{00}, 0, 0, N - n_{00}] \\ &= \sum_{n_{00}=0}^{N} \xi[n_{00}, 0, 0, N - n_{00}] = 1. \end{aligned} \tag{4.19}$$

It should be clear that the binomial coefficients can become very big, while the expectation values of the operators $\rho[...]$ will become very small, as system size increases. Their product would lead to very big numerical errors, showing the practical convenience of working with ξ rather than ρ. What is left now is to

determine the effect of the operators inside the Lindblad master equation onto the operators $\hat{O}[n_{00}, n_{01}, n_{10}, n_{11}]$ and write the equations in terms of their expectation values, i.e. $\xi[n_{00}, n_{01}, n_{10}, n_{11}]$.

4.3.1 The effect of operators

The calculation of the equation of motion governing the time evolution of (4.15) is very straight forward due to the conditions on the system's Hamiltonian and the dissipation as discussed in section 4.2. Let us first focus on local operators, that is operators acting on a single site s, and more specifically the Hamiltonian contributions. The restraints allow one to rewrite the part of the Hamiltonian acting on the individual sites, i.e. the local Hamiltonian $\hat{H}_{local}$, in terms of collective operators, that is a sum over the operators acting on the individual sites

$$\hat{H}_{local} = \sum_s \hat{H}_s = \sum_{k,l=0,1} h_{kl} \sum_s |k\rangle_s\langle l|_s. \tag{4.20}$$

Determining the action of the local Hamiltonian thus depends on the action of general operator $|k\rangle_s\langle l|_s$ on an operator $\hat{O}[n_{00}, n_{01}, n_{10}, n_{11}]$, and then calculating the expectation value as discussed in the previous section. The action of $|k\rangle_s\langle l|_s$ is easily calculated, given that the site s is in a state $|l\rangle_s\langle j|_s$ it will lower the number n_{lj} by one, and increase the number n_{kj} by one: $|k\rangle_s\langle l|_s l\rangle_s\langle j|_s = |k\rangle_s\langle j|_s$. Naturally, we no longer know in which state the site s is, but this gives no problem whatsoever due to the formulation in terms of the collective operators. We know that there are n_{l0} sites in a local state $|l\rangle\langle 0|$ and n_{l1} sites in a local state $|l\rangle\langle 1|$, we will thus have $n_{l0} + n_{l1}$ non-zero contributions under the action of $\sum_s |k\rangle_s\langle l|_s$. Let us write down an example for $h_{01}\sum_s |0\rangle_s\langle 1|_s$. Explicitly one can write

$$\begin{aligned}
&\langle h_{01} \sum_s |0\rangle_s\langle 1|_s \hat{O}[n_{00}, n_{01}, n_{10}, n_{11}]\rangle \\
&= h_{01}\left(n_{10}\left\langle \hat{O}[n_{00}+1, n_{01}, n_{10}-1, n_{11}]\right\rangle + n_{11}\left\langle \hat{O}[n_{00}, n_{01}+1, n_{10}, n_{11}-1]\right\rangle\right) \\
&= h_{01}\left(n_{10}\rho\left[n_{00}+1, n_{01}, n_{10}-1, n_{11}\right] + n_{11}\rho\left[n_{00}, n_{01}+1, n_{10}, n_{11}-1\right]\right).
\end{aligned} \tag{4.21}$$

This is trivially extended to the other values of k and l. An inspection of the Lindblad master equations learns us that one also needs to calculate terms where these operators act from the right, rather than the left. The calculations are analogous to the one above, with the difference that now other n_{ij} will decrease

and increase, for our example in (4.21) one finds

$$\begin{aligned}&\langle h_{01}\hat{O}[n_{00},n_{01},n_{10},n_{11}]\sum_s |0\rangle_s\langle 1|_s\rangle \\ &= h_{01}\left(n_{10}\rho\left[n_{00}+1,n_{01},n_{10}-1,n_{11}\right]+n_{10}\rho\left[n_{00},n_{01},n_{10}-1,n_{11}+1\right]\right).\end{aligned} \tag{4.22}$$

Similarly, one can use the same straight forward calculations to determine the result of an operator acting on both sides of $\hat{O}[n_{00},n_{01},n_{10},n_{11}]$. This allows one to calculate the local contributions from the terms with the Hamiltonian commutator as well as the dissipative part of equation (4.15) for local dissipation. To obtain the equations in terms of $\xi[\dots]$ rather than $\rho[\dots]$ we can multiply both sides of (4.15) with the multinomial factor of $\hat{O}[n_{00},n_{01},n_{10},n_{11}]$ and note that one can easily rewrite the multinomial factor on the right-hand side to correspond to the new states, for example for the first term of (4.22) we have after multiplication with (4.8)

$$\begin{aligned}h_{01}n_{10}\frac{N}{n_{00}!n_{01}!n_{10}!n_{11}!}&\rho\left[n_{00}+1,n_{01},n_{10}-1,n_{11}\right] \\ &= h_{01}(n_{00}+1)\xi\left[n_{00}+1,n_{01},n_{10}-1,n_{11}\right],\end{aligned} \tag{4.23}$$

which thus results in an equation for the time evolution containing $\xi[\dots]$ rather than $\rho[\dots]$, as desired. The non-local contributions, e.g. the two-site interaction terms in the Hamiltonian, can be calculated in a very similar way. One can rewrite the non-local Hamiltonian as

$$\hat{H}_{nonlocal} = \sum_{i,j,k,l}\left[\sum_{s,r\neq s}\left(a_{ij}|i\rangle_s\langle j|_s\right)\otimes\left(b_{kl}|k\rangle_r\langle l|_r\right)\right], \tag{4.24}$$

and note that this once again consists of the local operators $|i\rangle_s\langle j|_s$ and $|k\rangle_r\langle l|_r$. The only difference is them being applied subsequently. It is not too hard to see that the result of such operators will make the individual numbers n_{ij} change by an increment equal to either zero, one or two. Indeed, a first local operator will act on the initial state, transforming it into a new one as we have seen before. The second local operator will then act on the new state, again transforming it into yet a new one. The only thing one needs to keep in mind that is different from letting two local collective operators act on a state is that the sum is now given by $\sum_{s,r\neq s}$ and not $\sum_s\sum_r$. This means one should keep track of where the first local operator "sends" the specific site. One could keep track of this through the sets $\mathbf{v}_{ij}$, but

their information is still redundant. It is enough to know that the set of the n_{ij} that is decreased no longer contains site s since it is now in the set of the $n_{i'j'}$ that is increased. Let us write this down for the example $a_{01}b_{01}|0\rangle_s\langle 1|_s \otimes |0\rangle_r\langle 1|_r$ multiplying a general state $|n_{00}, n_{01}\rangle\langle n_{10}, n_{11}|$ from the left

$$\begin{aligned} a_{01}b_{01}\sum_{s,r\neq s}\langle|0\rangle_s\langle 1|_s \otimes |0\rangle_r\langle 1|_r\hat{O}[n_{00}, n_{01}, n_{10}, n_{11}]\rangle \\ =a_{01}b_{01}n_{10}(n_{10}-1)\rho\left[n_{00}+2, n_{01}, n_{10}-2, n_{11}\right] \\ + a_{01}b_{01}n_{11}(n_{11}-1)\rho\left[n_{00}, n_{01}+2, n_{10}, n_{11}-2\right] \\ + 2a_{01}b_{01}n_{10}n_{11}\rho\left[n_{00}+1, n_{01}+1, n_{10}-1, n_{11}-1\right] \end{aligned} \tag{4.25}$$

This equation can also be written in terms of $\xi[\dots]$ rather than $\rho[\dots]$ similarly to (4.23). The procedure for the result of an operator acting on the right side of the operator $\hat{O}[n_{00}, n_{01}, n_{10}, n_{11}]$ is equivalent to the above. With the procedures laid out in the subsection one is thus able to construct the equation of motion for each $\xi[n_{00}, n_{01}, n_{10}, n_{11}]$ in our reduced basis. The knowledge of their value at each moment in time provides us with all the information one needs, as well as the possibility to calculate all possible expectation values of operators since the expectation value of an operator $\hat{A}$ can be written as we did for the trace in (4.19). That is, by using the completeness relation (4.12) which allows us to write

$$\langle\hat{A}\rangle = \sum_{n_{00}=0}^{N}\binom{N}{n_{00}}\mathrm{Tr}\left[\hat{\rho}\hat{A}\hat{O}[n_{00}, 0, 0, N-n_{00}]\right], \tag{4.26}$$

which can in turn be rewritten in terms of $\xi[\dots]$ when calculating the action of $\hat{A}$ on $\hat{O}[n_{00}, 0, 0, N-n_{00}]$ in a similar fashion as we have done before. Evidently, the operator $\hat{A}$ should be similar to e.g. (4.20) and (4.24), in the sense that it should not discriminate between different sites in the system.

4.4 The Liouvillian superoperator

With the information from the previous section one is able to construct the equations of motion for each $\xi[n_{00}, n_{01}, n_{10}, n_{11}]$ by substituting the operator $\hat{O}[n_{00}, n_{01}, n_{10}, n_{11}]$ into (4.15) and multiplying both sides with the corresponding multinomial coefficient. Some re-ordening of the coefficients then allows one to

write

$$\partial_t \xi\left[n_{00}, n_{01}, n_{10}, n_{11}\right] = \sum_{\mathbf{n}} c_{\mathbf{n}} \xi\left[\mathbf{n}\right]. \tag{4.27}$$

Where the sum over $\mathbf{n}$ indicates the sum over all sets $\left\{n'_{00}, n'_{01}, n'_{10}, n'_{11}\right\}$ with a non-zero contribution, i.e. a non-zero coefficient. From the previous section we already know that for a Hamiltonian with at most two-point interactions a certain state can only couple to those states with a maximum difference of two for at most one n_{ij}. This means that the number of non-zero contributions in (4.27) is a lot smaller than the total number of permutational invariant subspaces, see (4.10), that we will denote as D for the sake of simplicity. Let us assign a label from 1 to D to each possible $\xi\left[n_{00}, n_{01}, n_{10}, n_{11}\right]$ in our basis

$$\xi\left[n_{00}, n_{01}, n_{10}, n_{11}\right] \rightarrow \xi_i. \tag{4.28}$$

It is then straight forward to see that the system of equations that obey (4.27) can be rewritten in a linearised system of the form

$$\partial_t \begin{pmatrix} \xi_1 \\ \dots \\ \xi_{\mathcal{D}} \end{pmatrix} = \begin{pmatrix} l_{11} & \dots & l_{1\mathcal{D}} \\ \vdots & \ddots & \vdots \\ l_{\mathcal{D}1} & \dots & l_{\mathcal{D}\mathcal{D}} \end{pmatrix} \begin{pmatrix} \xi_1 \\ \dots \\ \xi_{\mathcal{D}} \end{pmatrix}. \tag{4.29}$$

Since the collection of all ξ_i, that is $\{\xi_i : \forall i \in [1, D]\}$ contains all coefficients of the density matrix, up to a multinomial factor, this is once again equivalent to a superoperator description of the Lindblad master equation. Indeed, the Liouvillian superoperator in the permutationally reduced basis is given by

$$\hat{\mathcal{L}}_{perm} = \begin{pmatrix} l_{11} & \dots & l_{1\mathcal{D}} \\ \vdots & \ddots & \vdots \\ l_{\mathcal{D}1} & \dots & l_{\mathcal{D}\mathcal{D}} \end{pmatrix} \tag{4.30}$$

of which the dimension scales with the third order of the number sites N in the system. Moreover, as noted before, most of the coefficients l_{ij} are equal to zero. This results in a Liouvillian superoperator which not only has modest dimensions but is also sparse. It goes without saying that this allows one to study systems, using an exact numerical approach, with a number of sites that is a lot bigger than one could usually reach due to the exponential scaling with system size.

4.5 Connection with Dicke states

Another way to obtain the reduction in Liouvillian space size through use of the permutational symmetry in the system is by using a representation with Dicke states [160, 161]. It is a different basis representation that leads to the same conclusions as the ones derived in the previous chapter, but for two-level systems only. It is at the basis of the numerical toolbox that we will use in chapter 5. Let us first clarify what a Dicke state is and subsequently show its relation with the previous representation. The Dicke states form a usefull basis when describing the so-called Dicke model [163]. It describes the collective interaction of a single bosonic mode with a set of N two-level systems. Its Hamiltonian is given by

$$\hat{H}_{\text{Dicke}} = \omega_c \hat{a}^{+}\hat{a} + \frac{\omega_z}{2}\sum_{j=1}^{N}\hat{\sigma}_j^z + \frac{\gamma}{\sqrt{2}}\left(\hat{a}+\hat{a}^{\dagger}\right)\sum_{j=1}^{N}\hat{\sigma}_j^x, \tag{4.31}$$

which, as can directly be observed from the Hamiltonian, can be formulated in terms of collective operators, i.e. $\hat{J}^z = \frac{1}{2}\sum_{j=1}^{N}\hat{\sigma}_j^z$ and $\hat{J}^x = \frac{1}{2}\sum_{j=1}^{N}\hat{\sigma}_j^x$. It is customary to write the Dicke Hamiltonian in terms of spin-(1/2) operators which is why we added the factor $\frac{1}{2}$ in the definition of these collective operators. The Dicke states are then the eigenvectors of the collective (pseudo)-spin operators $\hat{\mathbf{J}}^2 = \left(\hat{J}^x\right)^2 + \left(\hat{J}^y\right)^2 + \left(\hat{J}^z\right)^2$ and $\hat{J}_z$ [160, 161, 164]

$$\hat{\mathbf{J}}^2|j,m\rangle = j(j+1)|j,m\rangle, \tag{4.32}$$

$$\hat{J}_z|j,m\rangle = m|j,m\rangle, \tag{4.33}$$

with $j \leq \frac{N}{2}$ and $|m| \leq j$, j and m can be either integers or half integers and the minimum value of j is given by 0 or 1/2 for N respectively even and odd. This immediatly sheds light on why these Dicke states form an interesting basis to study this model. Indeed, they allow for a reduction in the Hilbert space dimension of 2^N to a space that scales polynomially with order two for the desription of collective processes, a feat that finds its origin in the permutational symmetry of the collective operators. The advantage of using this basis is of course not limited to the Dicke model. Any system of which the time evolution can be written in terms of collective operators will be able to exploit the Dicke basis and acquire a drastic reduction in complexity, given that they also describe collective processes

(cfr. 4.2). Each Dicke state $|j,m\rangle$ has a degeneracy [161, 163] of

$$d_N^j = (2j+1)\,\frac{N!}{\left(\frac{N}{2}+j+1\right)!\left(\frac{N}{2}-j\right)!}, \tag{4.34}$$

which stands central in its ability to reduce the number of states needed to describe the systems time evolution. Similarly to the previous sections one can then move to describing the density matrix in terms of the outerproducts of this new basis and gain a desription that is equivalent. The most straight-forward way to show a direct link with the previous formalism is through the symmetric Dicke states. These Dicke states are defined as $j = N/2$ and can be written as a symmetric superposition of the uncoupled local states $|0\rangle$ and $|1\rangle$, that is

$$\left|\frac{N}{2}, k-\frac{N}{2}\right\rangle = \frac{1}{\sqrt{\binom{N}{k}}}\mathcal{S}\left[|0\rangle^{\otimes N-k}|1\rangle^{\otimes k}\right], \tag{4.35}$$

with $\mathcal{S}$ the symmetrisation operator that will take the sum over all possible products of $N-k$ sites in a state $|0\rangle$ and k sites in a state $|1\rangle$. As an example we will show the relation of an outer product of (4.35) with our previous formalism. This yields

$$\left|\frac{N}{2}, k-\frac{N}{2}\right\rangle\left\langle\frac{N}{2}, k-\frac{N}{2}\right| = \frac{N!(N-k)!}{k!}\sum_{r=0}^{M}\sum_{\text{sets}}\hat{O}[N-k-r, r, r, k-r], \tag{4.36}$$

with $M = \min(k, N-k)$ since $\max(n_{00}) = N-k$ and $\max(n_{11}) = k$ and they cannot become negative. We also used the fact that

$$n_{00}+n_{01} = N-k = n_{00}+n_{10} \quad \text{and} \quad n_{10}+n_{11} = k = n_{01}+n_{11}. \tag{4.37}$$

Furthermore, the sum over all sets $\{n_{00}, n_{01}, n_{10}, n_{11}\}$ with these respective values is once again given by a multinomial coefficient and find its origin in the product of the sum over all possible products of the states $|0\rangle$ and $|1\rangle$ (and their conjugate) from the symmetrisation operator $\mathcal{S}$. If we then calculate the expectation value of the outer product of (4.35) one finds a relation between both approaches, that is

$$\left\langle\left|\frac{N}{2}, k-\frac{N}{2}\right\rangle\left\langle\frac{N}{2}, k-\frac{N}{2}\right|\right\rangle = \frac{N!(N-k)!}{k!}\sum_{r=0}^{M}\xi\left[N-k-r, r, r, k-r\right]. \tag{4.38}$$

The representations of Dicke states other than the symmetric ones of (4.35) can be obtained by a standard approach equivalent to the one for the construction of Clebsch-Gordan coefficients [165], i.e. by iteratively applying the collective raising and lowering operators $\hat{J}^+$ and $\hat{J}^-$, given by $\hat{J}^\pm = \frac{1}{2}\sum_j \hat{\sigma}_j^\pm$. For these cases other than the symmetric Dicke state it can however be quite bothersome to derive a relation with the previous formalism like (4.38). From the example however, it is clear that there exists an equivalence between both approaches, both leading to a reduction of Liouvillian space that scales polynomially with order three [160, 161]. For two-level systems the choice of the approach one uses thus remains free, and will most likely be influenced by ones preference. The extension to n-level many body systems is more evident from the approach introduced in the previous sections. Furthermore, open source numerical packages exist that implement both approaches [161, 166–168]. In this thesis we will use the PIQS module implemented in QUTIP (Python) [167, 168] which is based on the Dicke basis formalism for our study of two-level systems detailed in chapter 5. An implementation of the work by Gegg et al. also exists in C/C++ and is called PSIQUASP [166]. For our study of the p-level systems we have however implemented this formalism into a Python module, on which the details can be found in appendix B.2, which will be used for the results in chapter 6.

4.6 p-level systems

The formalism from the previous sections can be straight-forwardly extended to p-level systems. Instead of only four numbers n_{ij} there will now be p^2 numbers n_{ij}. This means that in general we will have

$$\xi\left[\{n_{ij}\}\right] = \xi\left[n_{00}, n_{0p-1}, \ldots, n_{p-10}, \ldots, n_{p-1p-1}\right]. \tag{4.39}$$

This also means that the number of states inside a permutational invariant subspace for a certain set of $\{n_{ij}\}$ will now be given by the multinomial coefficient

$$R\left(\{n_{ij}\}\right) = \frac{N!}{n_{00}!\ldots n_{0p-1}!\ldots n_{p-10}!\ldots n_{p-1p-1}!}, \tag{4.40}$$

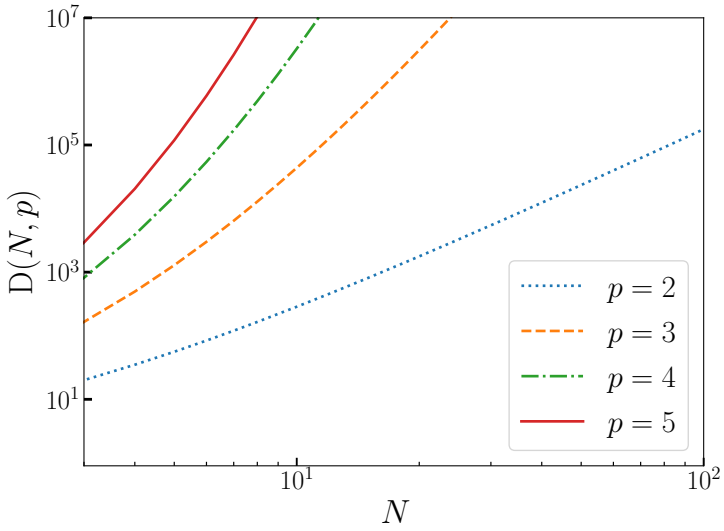

Figure 4.2: *Dimension of the Liouvillian in the permutational invariant basis as a function of N all-to-all connected p-level systems, for $p = 2$ (blue dotted line), $p = 3$ (orange dashed line), $p = 4$ (green dash-dotted line), and $p = 5$ (red full line).*

and the number of permutational invariant subspaces, i.e. the number of unique sets $\{n_{ij} : \forall i, j \in \{0, 1, \ldots, p-1\}\}$, now reads

$$D(N, p) = \sum_{n_{00}+\cdots+n_{p-1p-1}=N} 1 = \binom{N + p^2 - 1}{N}, \tag{4.41}$$

of which the derivation is presented in appendix B.1. In Fig. 4.2 we show the dimension of the Liouvillian for various p-level systems as a function of the number of all-to-all connected sites. From (4.41) follows that the dimension of the reduced Liouvillian space of an p-level system will scale polynomially with a power of $p^2 - 1$. It should be clear that the action of the operators is also straigt-forwardly generalized. Indeed, the number of possible $|k\rangle_s\langle l|_s$ that can act on a single site increase, as well as the number of different n_{ij}. They will however still only increase and decrease their specific $n_{k\cdot}$ values they can act upon, just as was the case for the two-level system. Nothing fundamental thus changes with regard to the earlier derived results. The only difference is there being more terms present in the equations of motion due to the increase in states. The Liouvillian superoperator stays sparse nonetheless.

CHAPTER 5

Mean-field validity in the XYZ Heisenberg model

In this chapter, we investigate the properties of an all-to-all (or fully) connected dissipative XYZ Heisenberg model. The permutational method which we use here is exact (that is, no approximation on the model has been done). Exact computations on open-spin systems have been carried out for systems up to 16 spins [107]. This work pushes this boundary far beyond this limit.

In the general study of a quantum system, one can think of the all-to-all connected model with uniform coupling as one in which the dimension increases as the number of neighbours is increased. In this regard, it is "common wisdom" that in a high-dimensional model $d \gg 1$, in the thermodynamic limit fluctuations are suppressed and the correct result should be captured by a mean-field decoupling procedure [98, 99]. The resulting steady-state density matrix is then a tensor product of identical local density matrices. Even if this can be argued for thermodynamic systems (where Landau-Ginzburg theory can be applied to determine phase transitions [169]), the lack of free energy analysis does not allow such an easy argument in open quantum systems. We will consider the simplest type of non-thermal bath to try to address this question. Even if the mean field were to work, what is not clear is how the system behavior scales up to the infinite spin number. The high degree of symmetry of the all-to-all connected system allows for a dramatic reduction of the computational cost of the numerical calculations [161]. Moreover, many atoms-in-cavity experiments can be recast as all-to-all connected models by the mediation of the electromagnetic field, which collectively interacts with the atoms [170]. However, since in these systems there is a limited number of particles, identifying the correct observables to characterize the emergence of the phase transition is of paramount importance. In this chapter, we will investigate

the phase transition from a paramagnetic phase with no magnetization in the xy-plane ($\langle\hat{\sigma}^x\rangle = \mathrm{Tr}\left\{\hat{\rho}_{\mathrm{ss}}\hat{\sigma}_j^x\right\} = 0$, $\langle\hat{\sigma}^y\rangle = \mathrm{Tr}\left\{\hat{\rho}_{\mathrm{ss}}\hat{\sigma}_j^y\right\} = 0$) to a ferromagnetic phase with finite magnetization in the xy-plane ($\langle\hat{\sigma}^x\rangle \neq 0$, $\langle\hat{\sigma}^y\rangle \neq 0$) which is expected to happen in the thermodynamic limit of the XYZ model for anisotropic coupling $J_x \neq J_y$ [1, 42, 44, 88, 104, 126, 128]. Note that at $T = 0$ and in the absence of dissipation no quantum phase transition of this kind exists in this system. We provide a thorough study of the spin structure factor, the collective magnetization, the bimodality coefficient and the angular averaged susceptibility. We also characterize less experimentally accesible quantities signaling the phase transition, as the Von Neumann entropy of the steady state and the Liouvillian spectrum and its gap. We test which one fares better in this intermediate regime to capture the onset of criticality.

5.1 The model

If we consider an all-to-all connected model with uniform couplings, i.e., all the spins interact with each other with the same strength, the Hamiltonian in Eq. (3.2) can be recast as

$$\hat{H} = \frac{1}{2\,(N-1)}\left[J_x\left(\hat{S}^x\right)^2 + J_y\left(\hat{S}^y\right)^2 + J_z\left(\hat{S}^z\right)^2\right], \tag{5.1}$$

where we have introduced the collective operators $\hat{S^\alpha} = \sum_{i=1}^{N}\hat{\sigma}_i^\alpha$ for $\alpha = x, y, z$. Notice the factor 2 is due to the fact that in Eq. (3.2) the sum is over the links while to obtain Eq. (5.1) we have to sum over the sites. Moreover, in the all-to-all connected model, the coordination number $Z = N - 1$. Moreover, note that in our lattice the ratio between the number of sites and the dimension of the lattice N/d is thus of order one for large lattices, while in the usually defined thermodynamic limit, the number of sites diverges with respect to the dimension.

For our study we will include local dissipation as well as collective dissipation. The collective dissipation becomes $\mathcal{D}[\sum_j \hat{\sigma}_j^-] = \mathcal{D}[\hat{S}^-]$. In this regard, in the all-to-all connected model, the Hamiltonian and collective dissipation processes will tend to create entangled states, while local dissipation will disentangle them.

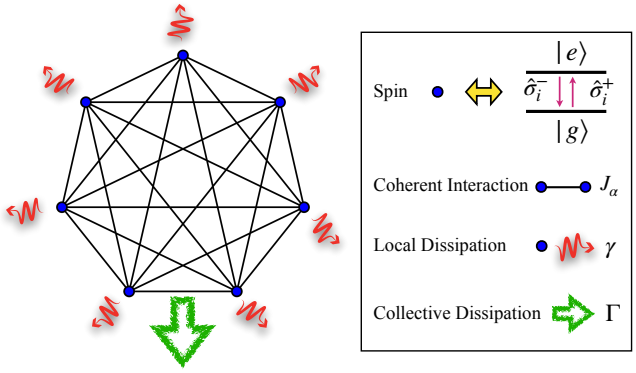

Figure 5.1: *Sketch of the dissipative* XYZ *model, with local and collective dissipation. In the legend we illustrate the possibility of implementing the spin model on an ensemble of two-level systems, or (artificial) atoms, interacting with an electromagnetic field. Each two-level system can switch between a ground state, $|g\rangle$, and excited state, $|e\rangle$. While the spin-spin interactions, $\propto J_\alpha$, of the all-to-all connected lattice, can be mediated by the coherent interaction with the photonic field, its collective mode dissipates, at a rate $\propto \Gamma$, and all other spin-flip mechanisms contribute to local dissipation, $\propto \gamma$.*

The Lindblad master equation of this system is given by

$$\begin{aligned}\frac{\partial\hat{\rho}(t)}{\partial t} = \mathcal{L}\hat{\rho}(t) = -i\left[\hat{H},\hat{\rho}(t)\right] + \gamma\sum_{j=1}^{N}\mathcal{D}[\hat{\sigma}_j^-]\hat{\rho}(t) \\ + \frac{\Gamma}{N-1}\mathcal{D}[\sum_{j=1}^{N}\hat{\sigma}_j^-]\hat{\rho}(t),\end{aligned} \tag{5.2}$$

where Γ represents the dissipation rate characterizing the collective spin-flip process.

5.1.1 Experimental implementations of an all-to-all connected model

We envision that the predictions that will be detailed in this chapter can be observed in experiments with noisy quantum simulators [171] and long-range interaction, based on a broad variety of platforms: atomic clouds [122], Rydberg atoms [100, 102, 121, 123, 125], trapped ions [172–175], as well as in solid state [58, 176], e.g., in superconducting circuits [40, 71, 110, 177–179] and especially in hybrid superconducting systems [180], where a bosonic field mediates the effective spin-

spin interactions. Indeed, Ref. [125] shows the feasibility of investigating exactly the all-to-all connected XYZ model in Rydberg atoms. Probing the dissipative regime studied here only requires the implementation of a weak coupling to an additional cavity mode allowing for dispersive measurement of the radiated field. Trapped ions provide another platform on which to engineer long-range spin interactions [173–175] and already allow one to investigate dissipative phase transitions with tens of two-level systems, which can also be locally manipulated [181].

Superconducting circuit elements and condensed matter magnetic degrees of freedom can be combined to implement hybrid quantum systems. One such example is provided by a collection of nitrogen vacancies (NV) or color centers in diamond interacting with the magnetic field controlled by a superconducting resonator. This platform offers the advantage of large N spins, actually implementing a good approximation of the thermodynamic limit since $N \approx 10^{12}$–10^{16} there, and physical conditions that allow to explore various regimes of both collective and local dissipation. The former is determined by the superconducting resonator quality factor, the latter by the intrinsic impurities of the condensed matter system and couplings to the crystal lattice. In these systems, superradiant light emission has been recently observed [180, 182], as well as steady-state bistability and critical slowing down [183]. In the bad-cavity regime, the cavity mode decay allows an adiabatic elimination of the bosonic degree of freedom, allowing the implementation of effective spin Hamiltonians, while tuning spin sub-ensembles in and out of resonance allows to vary N and thus study system-size scaling [180].

5.2 Liouvillian spectrum and phase transition

We begin our analysis by studying the spectral properties of the Liouvillian, which can signal the emergence of phase transitions [35]. As noted in section 2.8, a fundamental role in the system dynamics is played by $\hat{\rho}_1$, that is the eigenmatrix associated to the smallest eigenvalue λ_1 bigger than zero, which describes the slowest relaxation scale towards the steady state. A phase transition takes place in the thermodynamic limit when λ_1 becomes exactly zero, both in its real and imaginary parts. For any finite size of the system under consideration, however, $\lambda_1 \neq 0$. Nevertheless, the study of λ_1 and $\hat{\rho}_1$ provides much useful information about the scaling and nature of the transition [91].

Furthermore, as we will see in subsection 5.2.2, the all-to-all connected XYZ model exhibits a symmetry in its Liouvillian spectrum that will allow a numerically

more efficient calculation of this Liouvillian gap.

5.2.1 Symmetry breaking and phase transition

The Lindblad master equation (3.3) is invariant under a π-rotation of all the spins around the z-axis ($\hat{\sigma}_i^x \to -\hat{\sigma}_i^x$, $\hat{\sigma}_i^y \to -\hat{\sigma}_i^y$ $\forall i$). Thus, the system admits a $\mathbb{Z}_2$ symmetry, that is, there is a superoperator $\mathcal{Z}_2$ such that

$$\mathcal{Z}_2\hat{\rho}(t) = \prod_{j=1}^{N} \exp\left\{\left(-i\pi\hat{\sigma}_j^z\right)\right\}\hat{\rho}(t)\prod_{j'=1}^{N} \exp\left\{\left(+i\pi\hat{\sigma}_{j'}^z\right)\right\}, \tag{5.3}$$

and one can verify that $[\mathcal{L}, \mathcal{Z}_2] = 0$. While in a Hamiltonian system the presence of a symmetry implies a conserved quantity, this is not always the case for Liouvillian symmetries [67, 69, 184]. A symmetry of an out-of-equilibrium system, however, implies that the steady-state cannot have an arbitrary structure. In our case, $\hat{\rho}_{\text{ss}}$ must be an eigenmatrix of $\mathcal{Z}_2$, such that $\mathcal{Z}_2\hat{\rho}_{\text{ss}} \propto \hat{\rho}_{\text{ss}}$. In turn, this means that, for any finite size system $\langle\hat{\sigma}_i^x\rangle = \langle\hat{\sigma}_i^y\rangle = 0$ for all sites i.

The symmetry breaking takes place when, in the thermodynamic limit, $\lambda_1 = 0$ allows to have two steady states with nonzero and opposite magnetization. We thus expect to observe a second-order phase transition associated to this symmetry breaking of $\mathbb{Z}_2$ [35]. For a finite-size system, $\lambda_1 \neq 0$, such symmetry breaking cannot be directly witnessed. However, the precursors of the phase transition can be inferred both via spectral analysis and via an extensive study of the scaling of observables.

5.2.2 $\mathbb{PT}$-symmetry and Liouvillian antigap

There exists a class of non-Hermitian Hamiltonian systems which are invariant under the composition of unitary (parity $\mathcal{P}$) and anti-unitary (time-reversal $\mathcal{T}$) transformations: the $\mathcal{PT}$-symmetry [185–187]. This $\mathcal{PT}$-symmetry cannot be directly extended to the Liouvillian case, due to the dissipative nature of the contractive dynamics [188]. However, certain systems admit a $\mathcal{PT}$-symmetric transformation once a shift parallel to an average damping rate is added to $\mathcal{L}$ [189]. Therefore, the $\mathbb{PT}$-symmetry of $\mathcal{L}$ is not a superoperator symmetry (that is, it does not describe a property of the steady state). Instead, it is a spectral property related to the emergence of a reflection symmetry of the eigenvalues in the complex plane, i.e., introducing a dihedral (D_2) symmetry. Indeed, there exist a real number $\eta > 0$ such that, for all the eigenvalues λ_i, there exist a $\lambda_j = -2\eta + \lambda_i$.

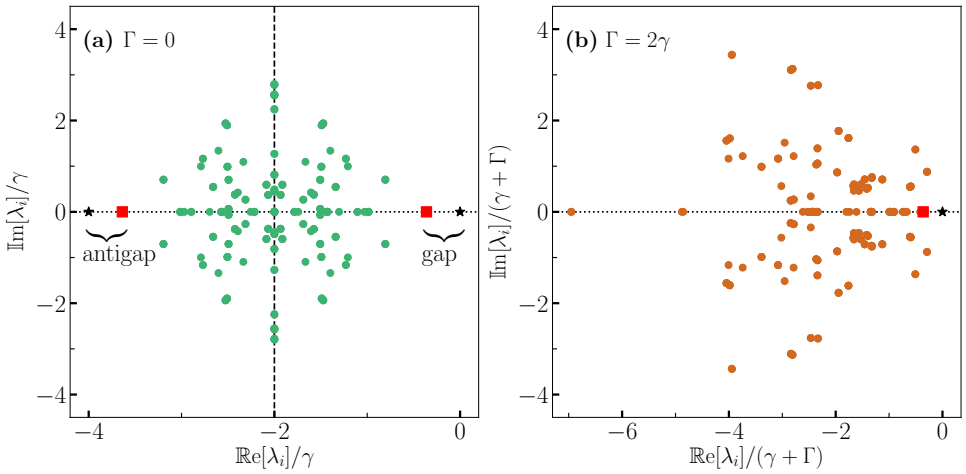

Figure 5.2: *Liouvillian spectrum for the dissipative* XYZ *model with local dissipation only,* $\Gamma = 0$ *[panel (a)], and both local and collective dissipation,* $\Gamma = 2\gamma$ *[panel (b)]. Here* $N = 4$ *and we choose* $J_x/(\gamma + \Gamma) = 0.6$, $J_y/(\gamma + \Gamma) = J_z/(\gamma + \Gamma) = 1$. *We mark* λ_0 *and* λ_1 *with a black star and a red square, respectively. All other eigenvalues* λ_i *are marked by circles. (a) The* $\mathbb{PT}$*-symmetry of the Liouvillian with only local dissipation is visible by the additional plane symmetry (vertical dashed line) of the eigenvalues (green circles). The Liouvillian gap and the Liouvillian* antigap *of the* $\mathbb{PT}$*-symmetric model are highlighted, showing the correspondence of* λ_0 *with* λ_M *(black star), and* λ_1 *with* λ_{M-1} *(red square). (b) The Liouvillian spectrum with local and collective dissipation, showing no* $\mathbb{PT}$*-symmtery.*

This can be easily visualized by plotting the eigenvalues of the Liouvillian in the complex plane $\lambda_j = x_j + i\, y_j$.

The $\mathbb{PT}$-symmetry results in a reflection symmetry of the eigenvalues with respect to a line $x = -\eta$ parallel to the imaginary axis [189–191]. The spectrum of the dissipative all-to-all connected XYZ spin model is shown in Fig. 5.2, setting $N = 4$, $J_x = 0.6 J_z$ and $J_y = J_z$. In Fig. 5.2 (a) we consider the case of homogeneous local dissipation, $\Gamma = 0$ in Eq. (3.3), and for comparison, the case of collective and local dissipation is shown in Fig. 5.2 (b), $\Gamma = 2\gamma$ in Eq. (3.3), showing instead no additional symmetry in the spectrum. We have verified that the absence of $\mathbb{PT}$-symmetry occurs also in the case of collective dissipation only, $\gamma = 0$, $\Gamma \neq 0$. Similarly, also in the case of local dephasing and local pumping, the Liouvillian spectrum of the model displays the additional dihedral symmetry typical of $\mathbb{PT}$-symmetry.

To clarify the discussion, let us consider a $\mathbb{PT}$-symmetric Liouvillian with $(M+1)$ eigenvalues. Therefore, there exists an eigenmatrix $\hat{\rho}_M$ whose eigenvalue is λ_M, which is the symmetric counterpart of $\hat{\rho}_{\rm ss}$. Since $\lambda_0 = 0$ and $\lambda_M = -2\eta$, we can directly access the value of η. Similarly, we can define the eigenmatrix $\hat{\rho}_{M-1}$ which mirrors $\hat{\rho}_1$, and an "antigap" λ_{M-1}, such that $\lambda_{M-1} - \lambda_M = \lambda_1$. This property allows for an easier numerical computation of the gap and associated $\hat{\rho}_1$. Indeed, if one is interested in computing only a few eigenvalues of the Liouvillian, one could resort to an iterative diagonalization method, based on Krylov subspaces. This method works extremely well for large-magnitude eigenvalues. However, if one is interested in computation of small eigenvalues, this method performs worse since one has to invert the matrix $\mathcal{L}$, so that the eigenvalues of smallest magnitude become the most relevant ones. Moreover, for non-Hermitian matrices, this method is known to be unstable [192]. Knowing that the Liouvillian is $\mathbb{PT}$-symmetric (and knowing η) can mitigate these numerical problems: by considering the shifted Liouvillian $\mathcal{L}' = \mathcal{L} + 2\eta\, \mathbb{1}$, the steady state is characterized by $\lambda'_0 = 2\eta$ and $\lambda'_1 = 2\eta - \lambda_1$, where $\mathbb{1}$ is the identity matrix. Since $\lambda'_1 = -\lambda_{M-1}$, we will call the eigenmatrix obtained like that the $\mathbb{PT}$-symmetric antigap.

In a XYZ spin system, a sufficient condition to have this $\mathbb{PT}$-symmetric behavior is to have dissipation only on the border of the chain [190]. This condition is trivially satisfied for the all-to-all connected XYZ spin model with local dissipation, since all spins are at the border of the system.

5.2.3 Closing of the Liouvillian gap: critical slowing down

As detailed in Sec. 5.2.1, the occurrence of a second-order phase transition in the *XYZ* model is marked by the closing of the Liouvillian gap in a whole region. In Fig. 5.3 we compute the Liouvillian gap exploiting the $\mathbb{PT}$-symmetric *antigap* method introduced in Sec. 5.2.2.

In Fig. 5.3 (a), the real part of the Liouvillian gap, $\lambda = |\mathrm{Re}[\lambda_1]|$, is calculated as a function of J_y (normalizing both quantities by a fixed value of γ), for various system sizes, N, also setting $J_z = \gamma$, $J_x = 0.6\gamma$. In panel (a), no critical behavior is observed for small or negative values of J_y/γ, hinting at the absence of an antiferromagnetic phase.

For positive J_y, the gap tends to close abruptly after $J_y/\gamma \simeq 1$. The minimum is for $J_y/\gamma \simeq 3$ for $N = 10$, and for larger values of J_y/γ we see that the Liouvillian gap again increases. However, by comparing $\lambda(N)$ for different system sizes, we see that for $J_y > \gamma$, $\lambda(N) > \lambda(N+1)$. This aspect corroborates the idea that a second-order dissipative phase transition is occurring, as these are characterized by a closing of the gap over an extended region of the control parameter [35].

The presence of a critical slowing down (i.e., of a diverging timescale) can be argued from Fig. 5.3 (b). The minimum of the Liouvillian gap for each curve of panel (a) is plotted against the system size N in a log-log plot, showing an excellent fit by a power law $\min(\lambda/\gamma) = \beta N^{\alpha}$ with exponent $\alpha = -0.3$. We conclude that for $N \to \infty$ there is a diverging timescale associated to $1/\lambda$, resulting in the presence of multiple steady states.

Our results are thus in agreement with the MF predictions, indicating a ferromagnetic (FM) to paramagnetic (PM) phase transition. Having demonstrated via spectral analysis the presence of the paramagnetic-to-ferromagnetic phase transition and the absence of an antiferromagnetic regime, we focus now the properties of the steady-state density matrix, obtained both via Gutzwiller MF analysis and via exact numerical calculation.

5.3 Mean field phase diagram

The Gutzwiller ansatz for the system density matrix amounts to assuming that $\hat{\rho}(t)$ is the tensor product of identical density matrices, each one representing the state of the j-th spin, $j = 1, \ldots, N$. Under this hypothesis, the Lindblad master

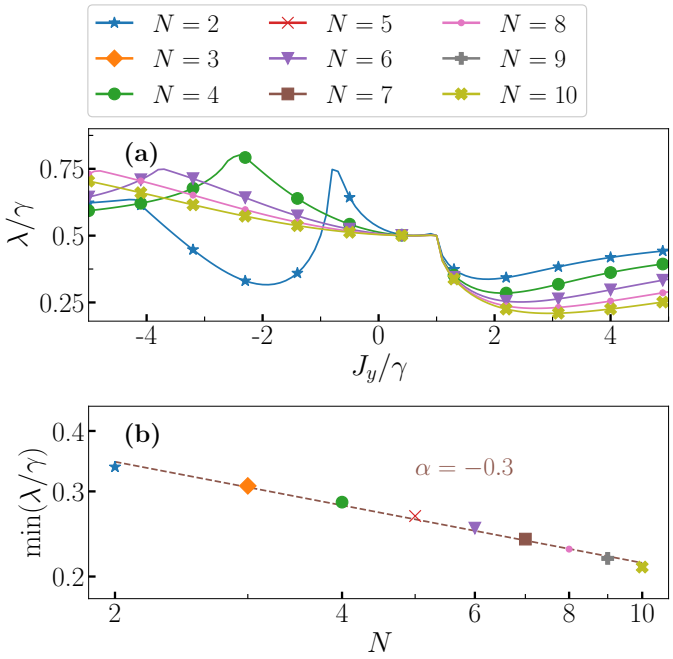

Figure 5.3: *Study of the Liouvillian gap, in units of the local dissipation rate, γ, and its critical slowing down for the dissipative* XYZ *model with local dissipation only. The system parameters are chosen as specified in Fig. 5.4 panel (b). (a) The Liouvillian gap, λ, is plotted as a function of J_y/γ for various system sizes, $N = 2, \ldots, 10$. The markers are only a guide for the eye (101 points have been calculated for each value of N). (b) The minimum of the Liouvillian gap, normalized by γ, for each of the curves in the top panel is plotted as a function of the system size N in a log-log plot, showing a linear scaling of the Liouvillian gap typical of phase transition [$\min(\lambda) \propto N^{\alpha}$, with exponent $\alpha = -0.3$] leading to a critical slowing down in the thermodynamic limit.*

equation (5.2) can be recast as:

$$\partial_t \langle \hat{\sigma}^x \rangle = 2\left(J_y - J_z\right) \langle \hat{\sigma}^y \rangle \langle \hat{\sigma}^z \rangle - \frac{\tilde{\gamma}}{2} \langle \hat{\sigma}^x \rangle + \frac{\Gamma}{2} \langle \hat{\sigma}^x \rangle \langle \hat{\sigma}^z \rangle , \tag{5.4a}$$

$$\partial_t \langle \hat{\sigma}^y \rangle = 2\left(J_z - J_x\right) \langle \hat{\sigma}^x \rangle \langle \hat{\sigma}^z \rangle - \frac{\tilde{\gamma}}{2} \langle \hat{\sigma}^y \rangle + \frac{\Gamma}{2} \langle \hat{\sigma}^y \rangle \langle \hat{\sigma}^z \rangle , \tag{5.4b}$$

$$\partial_t \langle \hat{\sigma}^z \rangle = 2\left(J_x - J_y\right) \langle \hat{\sigma}^x \rangle \langle \hat{\sigma}^y \rangle - \tilde{\gamma}(\langle \hat{\sigma}^z \rangle + 1) - \frac{\Gamma}{2}\left(\langle \hat{\sigma}^x \rangle^2 + \langle \hat{\sigma}^y \rangle^2\right), \tag{5.4c}$$

having defined $\tilde{\gamma} = \gamma + \Gamma/(N-1)$ and $\langle \hat{\sigma}^\alpha \rangle$ the single-site approximation of the Pauli matrix expectation values, with $\alpha = x,\ y,\ z$.

Equation (5.4) cannot be analytically solved, even in the steady state ($\partial_t \langle \hat{\sigma}^\alpha \rangle = 0$). Indeed, the inclusion of collective emission introduces nonlinear terms that, for Eq. (5.4a) and Eq. (5.4b) are similar to the Hamiltonian ones, hinting at the fact that they contribute to entanglement generation in the dynamics. Similarly, the presence of local dissipation prevents the equation of motion from being simplified, since the spin length, Eq. (C.10), is not preserved. Both the local and collective dissipation, however, act as an effective transverse magnetic field in the z direction.

We plot the MF solution to Eq. (5.4) in Fig. 5.4 in the case $\Gamma = 2\gamma$ [panel (a)] and in the case $\Gamma = 0$ [panel (b)]. The total dissipation ($\gamma + \Gamma$) is kept fixed. We notice that both MF solutions predict a second-order phase transition and that the value of J_y triggering the phase transition is the same in both cases. However, the two plots exhibit a different dependence of the mean values $\langle \hat{\sigma}^\alpha \rangle$ on J_y, with $\alpha = x,\ y,\ z$. In the presence of local and collective dissipation [panel (a)], the transition appears to be sharper than in the presence of local dissipation only [panel (b)].

5.3.1 Local dissipation only

Here, we briefly analyze the case $\Gamma = 0$ in Eq. (5.4), which was extensively investigated in Refs. [1, 42, 44, 88, 104, 107, 126, 128, 193] in lower dimensions and in Ref. [101] in infinite dimension. We notice that, in this case, Eqs. (5.4) only contain nonlinear *homogeneous* terms, and one can thus obtain $\langle \hat{\sigma}^\alpha \rangle_{\rm ss}$ exactly. A discussion of the properties of this model in presence of only collective dissipation can be found in App. C.2.

We study the mean-field phase diagram through an instability analysis analogous to the one performed for the nearest-neighbor XYZ Hamiltonian [42]. We determine the instability of the paramagnetic phase in the xy-plane to a d-dimensional perturbation with wave vector $\vec{k}$. Due to the all-to-all connected

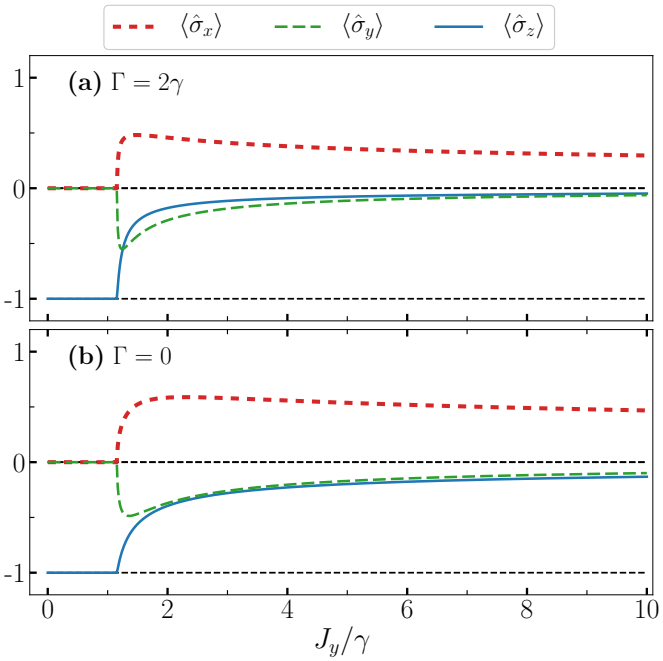

Figure 5.4: *Steady-state solution of the mean-field equations* (5.4) *in the case* $\Gamma = 2\gamma$ *[panel (a)] and in the case* $\Gamma = 0$ *[panel (b)], having fixed the value* $(\gamma + \Gamma) = 1$. *The parameters used here are* $J_x/(\gamma+\Gamma) = 0.6$, $J_z/(\gamma+\Gamma) = 1$ *and* $N \to \infty$. *The horizontal black dashed lines correspond to* $\langle\hat{\sigma}_\alpha\rangle = 0, -1$.

structure, the perturbations with wave vector $\vec{k} = (k_1, k_2, ..., k_d)$ are restricted by k_l only being able to attain the values 0 and π. For such analysis the presence of an antiferromagnetic phase is nonphysical for any value of the coupling parameters. Hence, the mean-field phase diagram consists only of a paramagnetic phase and a ferromagnetic one. The latter is present when the condition

$$-\frac{\gamma^2}{16} > (J_x - J_z)\left(J_y - J_z\right), \tag{5.5}$$

is fulfilled. We refer to appendix C.1 for the complete derivation. In the following, we will choose $J_x/\gamma = 0.6$ and $J_z/\gamma = 1$. Consequently, we can define the critical y-coupling J_y^c as the minimal J_y satisying Eq. (5.5), i.e.,

$$\frac{J_y^c}{\gamma} = \frac{J_z}{\gamma} + \frac{\gamma}{16\,(J_z - J_x)} = 1.15625. \tag{5.6}$$

The absence of an antiferromagnetic phase in this all-to-all connected model can be expected. Each spin is connected to every other spin in the system, and no unique spatial structure is present for this type of interaction. It is impossible for the spins to take alternating directions with respect to their neighbors. The results of this instability analysis lead to the phase diagram shown in Fig. 5.5, where the black dash-dotted curves show the transition boundary between both phases according to the mean-field approximation.

Having derived the MF solutions and the phase diagram, we will now proceed to study the dynamics in the full quantum formalism, beyond results found for dissipative spin-boson models [37, 194]. Since we show that, at the MF level, the model with local and collective dissipation displays a second-order phase transition similar to the local dissipation only case, we will at first focus on the latter case.

5.4 Calculation of physical quantities

In this section we introduce the general definitions of the spin-structure factor, z-magnetization, and Von Neumann entropy, also providing their mean-field expressions. We will utilize these physical quantities in the next section to study the validity of the mean field across the phase diagram. We also introduce the bimodality coefficient and the angular averaged susceptibility, which will be used to identify the critical point of the transition from the paramagnetic phase to the ferromagnetic phase.

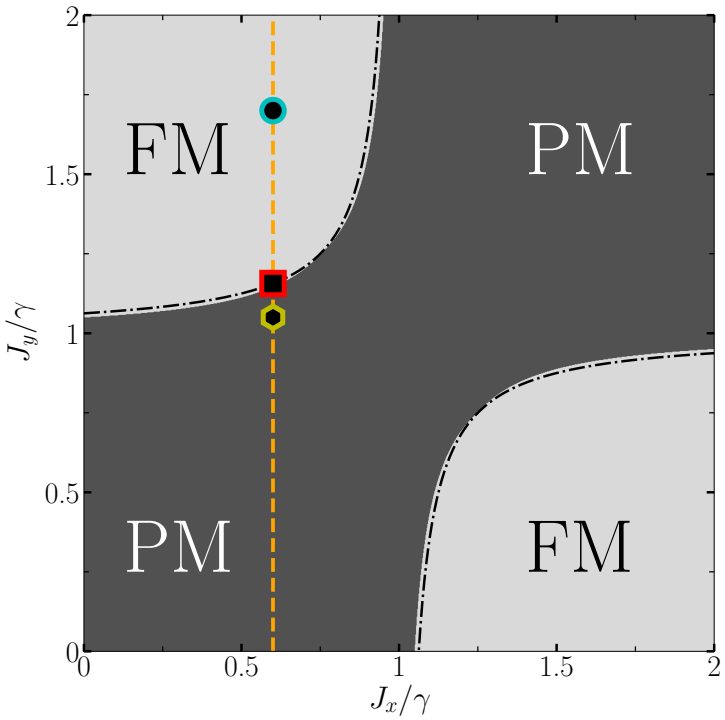

Figure 5.5: *Phase diagram for local dissipation only, where* $\Gamma = 0$ *and* $J_z/\gamma = 1$. *The phases are determined from the intersection in the bimodality coefficient curves for in the* x *and* y *direction for* $N = 50$ *and* $N = 60$, *i.e. the transition from a paramagnetic phase (PM) to a ferromagnetic phase (FM) in the* xy*-plane. The black dash-dotted curves show where the transition takes place in the mean-field approximation, while the background color defines the PM (dark grey) and FM (light grey) regions from calculations using the bimodality coefficient in the full quantum model (discussed in Sec. 5.5.2). The orange vertical dashed line is located at* $J_x = 0.6\gamma$ *and shows the cut that will be used in the next figures to characterize the phase transition. The three points on the cut* $J_x/\gamma = 0.6$ *indicate the values of* J_y/γ *which will be used for bench-marking the MF with the full quantum solutions:* $J_y/\gamma = 1.1$, *in the PM phase (hexagon with yellow contour), at criticality,* $J_y/\gamma = 1.15625$ *(square with red contour), and at* $J_y/\gamma = 1.7$ *in the moderately anisotropic FM region (circle with a cyan contour).*

5.4.1 Spin structure factor and z-magnetization

To identify the possible agreement of the mean-field theory with the exact numerical solutions we study the order parameter of the system. Due to the $\mathbb{Z}_2$-symmetry present in the system we cannot rely on the magnetization in the x- and y-direction.

As a result we study the steady-state spin structure factor, which is calculated as follows

$$S^{\alpha\beta}(\mathbf{k}) = \frac{1}{N(N-1)} \sum_{j,l\neq j} e^{i\mathbf{k}\cdot(\mathbf{j}-\mathbf{l})} \langle \hat{\sigma}_j^\alpha \hat{\sigma}_l^\beta \rangle, \tag{5.7}$$

where α, $\beta = x$ or y and where $\langle \hat{\sigma}_j^\alpha \hat{\sigma}_l^\beta \rangle = \mathrm{Tr}[\hat{\sigma}_j^\alpha \hat{\sigma}_l^\beta \hat{\rho}_{\mathrm{ss}}]$. It contains information on the orientation of the spins with respect to each other. Ferromagnetic order is present in the xy-plane if the steady-state spin structure factor in the x-direction or (and) the y-direction is different from zero. We note that in Eq. (5.7) the spin structure factor is defined without the contribution of the self-energies, i.e. the sum over the sites considers only different spins. We can thus calculate these quantities even for permutational-symmetric systems, subtracting the single-site contributions to the total second moments. If we consider $S^{xx}(\mathbf{k}=0)$ or $S^{yy}(\mathbf{k}=0)$ (from here on out we drop the $\mathbf{k}=0$), they predict a ferromagnetic phase when they are nonzero and a paramagnetic phase when they are both equal to zero. Besides being able to identify the phase we are also interested in the quantitative agreement of the mean-field theory with the exact solutions. To this end, we also study the z-magnetization in the steady state, $M_z = \mathrm{Tr}[\hat{\rho}_{\mathrm{ss}}\hat{S}^z]/N$, which can be readily calculated without the limitations of the $\mathbb{Z}_2$-symmetry.

The mean-field spin structure factor and z-magnetization

The system of mean-field equations in Eq. (5.4) is analytically solvable for the steady state for local dissipation only. By equating the time derivative equal to zero we find the following solutions for the magnetization in each direction

$$M_{x\,\mathrm{MF}} = \pm\sqrt{2M_{z\,\mathrm{MF}}\,(M_{z\,\mathrm{MF}}+1)\,\frac{J_y - J_z}{J_x - J_y}}, \tag{5.8a}$$

$$M_{y\,\mathrm{MF}} = \mp\sqrt{2M_{z\,\mathrm{MF}}\,(M_{z\,\mathrm{MF}}+1)\,\frac{J_z - J_x}{J_x - J_y}}, \tag{5.8b}$$

$$M_{z\,\mathrm{MF}} = -\frac{\gamma}{4}\frac{1}{\sqrt{(J_y - J_z)\,(J_z - J_x)}}. \tag{5.8c}$$

One can also easily prove that the steady-state spin structure factor in the x-direction can be written as

$$S^{xx}_{\mathrm{MF}} = (M_{x\,\mathrm{MF}})^2 = 2M_{z\,\mathrm{MF}}\,(M_{z\,\mathrm{MF}}+1)\,\frac{J_y - J_z}{J_x - J_y}, \tag{5.9}$$

by using the Gutzwiller mean field properties. The calculation in the y-direction is analogue.

5.4.2 Von Neumann entropy

The study of the Von Neumann entropy of the steady state allows for an interesting extension of our analysis of the system, since in standard thermodynamics a second-order phase transition is associated to a change in the entropy of the system. The Von Neumann entropy reads

$$S = -\sum_i p_i \log(p_i), \tag{5.10}$$

with p_i the eigenvalues of the density matrix. It can thus provide information on the mixed nature of the steady-state density matrix, $\hat{\rho}_{\mathrm{ss}}$. Usually in many-body studies one is able to calculate this observable only for small systems. However, similarly to the other variables in this work, we are able to calculate it up to the order of $N = 95$ spins. The Von Neumann entropy is an extensive quantity and in the main text we study the Von Neumann entropy per spin: $S(N)/N$.

The mean-field Von Neumann entropy

The mean-field entropy can be calculated by noting that the density matrix can be written in its Bloch sphere representation $\hat{\rho} = \frac{1}{2}\left(\mathbb{1} + \vec{\epsilon}\cdot\vec{\hat{\sigma}}\right)$. With $\vec{\epsilon}$ the Bloch vector, which contains the magnetization in the x, y and z-direction, and $\hat{\sigma}$ the Pauli matrices. The eigenvalues are given by $p = (1 \pm |\vec{\epsilon}|)/2$. These eigenvalues can be readily calculated from the steady-state mean-field equations (5.8) and give access to the MF approximation of the Von Neumann entropy through (5.10),

$$\frac{S_{\mathrm{MF}}}{N} = -\frac{(1+J)}{2}\ln\left(\frac{(1+J)}{2}\right) - \frac{(1-J)}{2}\ln\left(\frac{(1-J)}{2}\right), \tag{5.11}$$

where $J^2 = \langle \hat{S}^2 \rangle = \mathrm{Tr}[\hat{S}^2\hat{\rho}(t)]$ is the expectation value of the total spin length [c.f Eq. (C.10)] in the mean-field approximation.

The Von Neumann entropy solely depends on J in Eq. (5.11), illustrating the fact that states with maximum spin length, lying on the surface of the Bloch sphere, have minimum entropy. Instead, the entropy increases with decreasing spin length until the value $S_{\mathrm{MF}}/N = \ln(2)$, which is indeed the maximum entropy of a qubit.

In particular, we can express Eq. (5.11) explicitly in terms of the steady-state values $\langle\hat{\sigma}^x\rangle_{\text{ss}}$, $\langle\hat{\sigma}^y\rangle_{\text{ss}}$ and $\langle\hat{\sigma}^z\rangle_{\text{ss}}$. These results would be true independently of the model under consideration and even for the system dynamics, given the nature of the Gutzwiller-mean-field ansatz, for two-level systems, $\langle\hat{\sigma}_i^z\hat{\sigma}_j^z\rangle_{\text{ss}} \approx \langle\hat{\sigma}^z\rangle_{\text{ss}}^2$.

5.4.3 Bimodality coefficient

Using the permutational invariance present in this system, one is able to calculate results for a higher number of spins than usually feasible with other techniques. However, finite-size effects are still present, hampering our ability to make a good estimate of the point of transition from the paramagnetic to the ferromagnetic phase using the order parameter. An indicator which is extremely suited for making a good estimate of this transition point is the bimodality coefficient, defined as

$$B_c = \frac{m_2^2}{m_4}, \tag{5.12}$$

with m_n being the n-th moment of an observable. The bimodality coefficient gives information on the bimodal nature of the operator used to calculate the moments. This bimodal nature indicates the presence of a ferromagnetic phase or a paramagnetic phase. A bimodal distribution for $\sum_i \sigma_i^x$, being the magnetization in the x-direction, indicates a ferromagnetic phase and typically has values close to $B_c = 1$. A paramagnetic phase, i.e. a unimodal distribution, is indicated by smaller values for B_c. A Gaussian distribution with zero mean has a value $B_c = 1/3$ [107, 195]. Note that the bimodality coefficient is closely related to the Binder cumulant [196, 197].

Besides information on the nature of the phases at a specific parameter, the bimodality coefficient can also be used to indicate the transition point between the different phases. The curves for the bimodality coefficient for different system sizes intersect, providing an estimate of the critical point. In finite-size systems, these intersection points coincide due to power-law dependence of correlations on the system size around the critical point. In our case, since different number of spins correspond to different dimensions, this intersection point changes. However, for sufficiently large systems this transition point should converge, indicating the phase transition.

We are interested in the presence of a ferromagnetic or paramagnetic phase in the xy-plane, and as such we study the emergence of ferromagnetic order in either the x or y direction. The second and fourth moments of $\hat{\sigma}_i^x$ and $\hat{\sigma}_i^y$ are readily

calculated in the permutational invariant basis, as they are expectation values of global operators.

5.4.4 Angular averaged susceptibility

A divergence in the susceptibility indicates the existence of a second order phase transition. To calculate the susceptibility we use the scheme presented in Ref. [104]. If a small magnetic field of intensity h is applied in the xy-plane as a probe,

$$\hat{H}_B(h,\theta) = h\sum_i \left(\cos(\theta)\hat{\sigma}_i^x + \sin(\theta)\hat{\sigma}_i^y\right), \tag{5.13}$$

it explicitly breaks the $\mathbb{Z}_2$-symmetry of the system. By obtaining the perturbed steady state $\hat{\rho}(h,\theta)$ for $\hat{H}_{\text{ext}}(h,\theta) = \hat{H} + \hat{H}_B(h,\theta)$, the resulting magnetization reads

$$M_\alpha = \frac{1}{N}\sum_{j=1}^{N} \text{Tr}\left[\hat{\rho}(h,\theta)\hat{\sigma}_j^\alpha\right], \qquad \alpha = x,\ y. \tag{5.14}$$

Calling $h_x = h\cos(\theta)$ and $h_y = h\sin(\theta)$, the magnetic response in the linear regime is

$$\vec{M}(h,\theta) = \begin{pmatrix} \chi_{xx} & \chi_{xy} \\ \chi_{yx} & \chi_{yy} \end{pmatrix} \begin{pmatrix} h\cos(\theta) \\ h\sin(\theta) \end{pmatrix}, \tag{5.15}$$

where the susceptibility tensor is defined as

$$\chi_{\alpha\beta} = \left.\frac{\partial M_\alpha}{\partial h_\beta}\right|_{h\to 0}. \tag{5.16}$$

A scalar value can be obtained from this susceptibility tensor through angular averaging of the determinant, i.e.,

$$\chi_{\text{av}} = \frac{1}{2\pi}\int_0^{2\pi} \left.\frac{\partial|\vec{M}(h,\theta)|}{\partial h}\right|_{h\to 0} d\theta. \tag{5.17}$$

The mean-field angular averaged susceptibility can be calculated through numerically solving the mean-field equations with an applied field as stipulated above and also applying Eq. (5.17).

5.5 Mean-field validity across the phase diagram

To compare the mean-field analysis to the full quantum solution, we interpret the all-to-all coupled spin system as a d-dimensional system. Every time we add a spin the dimension of the system is also increased by one. This implies that a d-dimensional system consists of d spins and that infinite dimensions are reached when the system has an infinite amount of spins. Hence, we test if mean-field theory becomes exact in infinite dimensions, i.e., for an infinite number of spins.

In the following, we use the permutational invariant quantum solver (PIQS) [161], a module of QuTiP, the Quantum Toolbox in Python [167, 168], developed to efficiently solve problems with permutational invariance. This is an open-source computational library that leverages the flexibility of numerical and scientific Python libraries (NumPy and SciPy) and implements efficient numerical techniques by interfacing with the Intel Math Kernel Library (MKL). Performance is enhanced by using compiled scripts in Cython and by natively supporting cross-platform parallelization on clusters, with open multi-processing (Open MP) [167, 168]. To obtain the steady-state density matrix, we will use the `direct` method of the `qutip.steadystate` solver, which is based on the lower-upper (LU) decomposition of the Liouvillian matrix to solve the equation $\mathcal{L}\hat{\rho}_{\rm ss} = 0$. The results are exact up to numerical tolerance (having set the absolute tolerance to 10^{-12}) [1]. We will characterize criticality by calculating the expectation values of operators on the steady-state density matrix of the system, i.e., $\langle \hat{A} \rangle_{\rm ss} = \mathrm{Tr}[\hat{A}\hat{\rho}_{\rm ss}]$, and by investigating the properties of $\hat{\rho}_{\rm ss}$.

Based on the preliminary study of the MF solution and of the Liouvillian gap, see Figs. 5.3 and 5.5, and Secs. 5.2.3 and 5.3, we can identify three main regions in the phase diagram of the XYZ model: (i) Paramagnetic far from criticality ($J_y \leq J_x$); (ii) Critical ($J_x < J_y \leq J_y^{\rm h}$); (iii) Highly anisotropical ($J_y > 2.3\gamma = J_y^{\rm h}$), see discussion in Sec. 5.5.3. The paramagnetic one (i) seems to present a saturation of the Liouvillian gap and no antiferromagnetic phase for $J_y \leq 0$. We may argue that this region can be safely approximated by a MF solution. We numerically tested this hypothesis, and found it to be correct (not shown).

In the critical region (ii), a fundamental question is the determination of both the existence and the position of the critical point. Regardless of our ability to

[1] The interested reader can find a series of notebooks dealing with similar systems in the section "Permutational invariant Lindblad dynamics" of the QuTiP project tutorials http://qutip.org/tutorials.

determine the transition point, we are able to access the validity of the mean-field solutions through a finite size scaling. For almost-critical anisotropy, we will consider three domains: (1) The paramagnetic region before the transition $J_x < J_y < J_y^c$; (2) The critical point according to MF prediction $J_y = J_y^c$; (3) The ferromagnetic region $J_y^c < J_y < J_y^h$. These are respectively represented as the yellow hexagon, the red square and the blue circle in the phase diagram of Fig. 5.5.

Finally, we are interested in the properties of the high-anisotropy phase (iii). The MF does not predict a second phase transition to a paramagnetic phase. Nevertheless, several different methods [42, 44] have pointed out that this regime of parameters leads to a completely different behavior with respect to the standard ferromagnetic phase.

Note that in all the curves in this section, which show the behavior of the system as a function of J_y/γ, the markers on the curves are a guide for the eye, and each curve is obtained from a simulation of a 100 points. We also computed more values of the system size N than those shown in those figures.

In the following we choose, unless specified otherwise, $J_z = \gamma$, $J_x = 0.6\gamma$ and we vary J_y.

5.5.1 Critical region

To characterize the properties of the steady state, we consider the spin-structure factor in the x-direction,

$$S^{xx}(N) = \frac{1}{N(N-1)} \sum_{j \neq l} \langle \hat{\sigma}_j^x \hat{\sigma}_l^x \rangle_{\mathrm{ss}}, \tag{5.18}$$

the z-magnetization,

$$M_z = \langle \hat{S}^z \rangle_{\mathrm{ss}}/N = \mathrm{Tr}[\hat{S}^z \hat{\rho}_{\mathrm{ss}}]/N, \tag{5.19}$$

and the Von Neumann entropy,

$$S = S[\hat{\rho}_{\mathrm{ss}}] = -\sum_i p_i \log(p_i), \tag{5.20}$$

where p_i are the eigenvalues of the density matrix $\hat{\rho}_{\mathrm{ss}}$. While at MF level it is possible to have $\langle \hat{\sigma}^x \rangle \neq 0$, for any finite-size system the $\mathbb{Z}_2$ symmetry imposes $\langle \hat{\sigma}^x \rangle = 0$ (see the discussion in section 5.2.1). Ferromagnetic order is present in the xy-plane if the steady-state spin structure factor in the x-direction or (and) the y-direction is different from zero. The magnetization M_z, instead, is expected

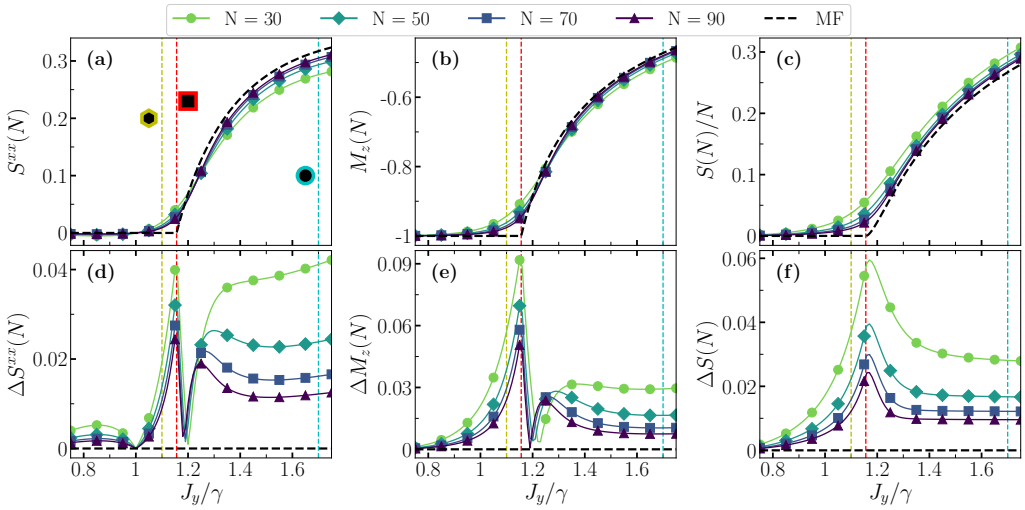

Figure 5.6: *Study of the paramagnetic to ferromagnetic dissipative phase transition in the presence of only local dissipation for the system parameters specified in Fig. 5.4 panel (b). The first row shows the steady-state spin structure factor in the x-direction [panel (a)], the z-magnetization [panel (b)], and the Von Neumann entropy per spin [panel (c)] as a function of J_y for different system sizes (N increases for darker curves). The markers are a guide for the eye, 100 points are calculated for each curve. The second row shows the absolute value of the difference between the variables in the corresponding upper panel and the mean-field value for $N \to \infty$. (d) $\Delta S^{xx}(N) = \left(S^{xx}(N) - S^{xx}_{MF}(N)\right)/N$. (e) $\Delta M_z(N) = \left(M_z(N) - M_{z\,MF}(N)\right)/N$. (f) $\Delta S(N) = \left(S(N) - S_{MF}(N)\right)/N$. See Eq. (5.21) for details. In all panels, the black dashed curve represents the MF value. The dashed vertical lines refer to the points chosen in Fig. 5.5 and also studied for the system-size scaling in Fig. 5.7: the PM phase (yellow line, hexagon marker); the critical point (red line, square marker); the FM phase (cyan line, circle marker).*

to show a first order discontinuity, according to the mean-field prediction. Finally, we will use the Von Neumann entropy per spin $S(N)/N$, it is an indicator of the degree of mixedness of the steady state.

In Fig. 5.6 we plot the spin structure factor [panel (a)], the z-magnetization [panel (b)], and the Von Neumann entropy [panel (c)] in the region $0.75 < J_y/\gamma < 1.75$ for different values of N, and we compare them to the results obtained via MF analysis (black dashed curve). Note that we define the point where the mean field predicts a change between the PM and FM phases as the critical point. All the three top panels of Fig. 5.6 show that the results of the full quantum simulations

become closer to the MF prediction by increasing the number of sites. Nevertheless, we notice that the results at the critical point are still in visible disagreement with respect to those obtained via MF analysis.

We thus identify a paramagnetic and a ferromagnetic phase in qualitative agreement with the mean-field calculations. Note that, as a result of finite-size effects, the transition from the paramagnet to the ferromagnet is smoothed, making it difficult to pinpoint the exact location of the phase transition. Even more so as the region close to the transition is subject to sizeable fluctuations. We will return to the determination of the point of transition in subsection 5.5.2.

Normally, one expects the finite-size effects to disappear in the thermodynamic limit. To better quantify whether the exact quantum solutions retrieve the mean-field results for $N \to \infty$, we study the absolute difference between the full quantum solution and the MF prediction for corresponding N,

$$\Delta S^{xx}(N) = |S^{xx}(N) - S^{xx}_{\mathrm{MF}}(N)|, \tag{5.21a}$$

$$\Delta M_z(N) = |M_z(N) - M_{z\,\mathrm{MF}}(N)|, \tag{5.21b}$$

$$\Delta S(N) = |S(N) - S_{\mathrm{MF}}(N)|, \tag{5.21c}$$

for the steady-state spin structure factor, the z-magnetization, and the Von Neumann entropy, respectively. How these quantities fare as a function of J_y is shown in panels (d-f) of Fig. 5.6. The discrepancies are largest at the critical point (marked by a vertical red dashed line in each panel) and in general the MF tends to perform better in the anisotropic FM region, $J_y > J_z, J_x$ than in the PM region. We will investigate the highly anisotropic region in more detail in Sec. 5.5.3. As a general trend, we see that, as the system size is increased, the difference between the MF and the computed quantities from the quantum $\hat{\rho}_{\mathrm{ss}}$ becomes smaller. However, the three curves display different behaviors in their scaling properties.

In Fig. 5.7 we show the finite-size scaling of the solution towards the MF, for the quantities of Eq. (5.21), for the three regions: (i) Paramagnetic, $J_y/\gamma = 1.1$ [panel (a)]; (ii) Critical, $J_y/\gamma = J_{y,c}/\gamma$ [panel (b)]; (iii) Ferromagnetic, $J_y/\gamma = 1.7$ [panel (c)]. We notice that all the results display a power-law behavior up to good approximation. Thus, we perform a power-law fit of the form $y = \beta N^{\alpha_i}$ for unknowns coefficients β and α_i. Clearly, α_i are negative for each observable, i.e., the mean-field solutions are in fact exact in the thermodynamic limit. However, different quantities in different regimes present different behaviors. We notice that

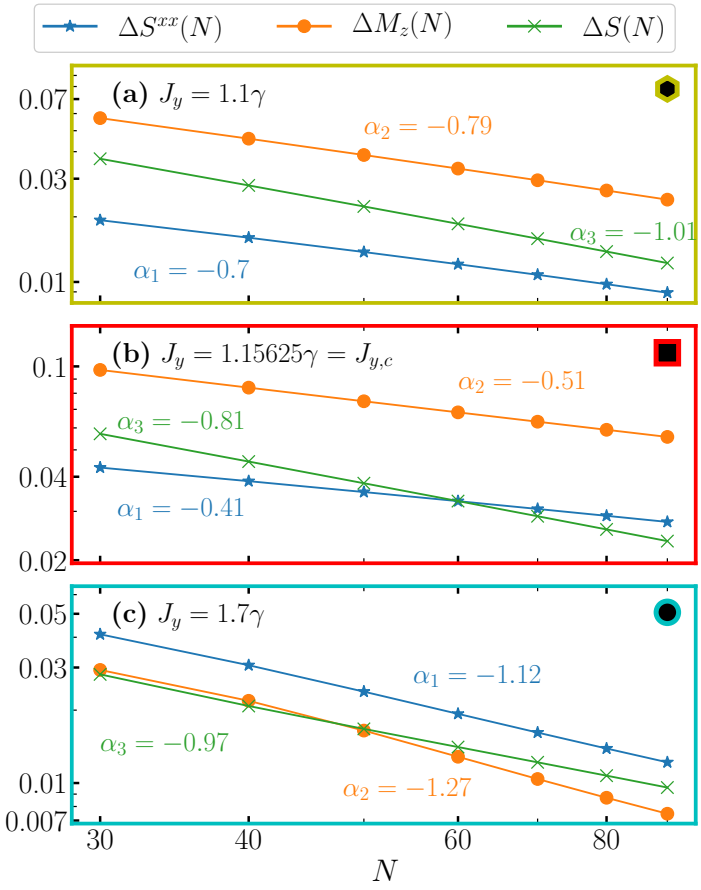

Figure 5.7: *The panels show the finite size scalings of the quantities plotted in Fig. 5.6 for $J_y/\gamma = 1.1$ [panel (a)], $J_y/\gamma = J_{y,c}/\gamma$ [panel (b)], and $J_y/\gamma = 1.7$ [panel (c)]. We show the exponents α of a power law fit of the form $y = \beta N^{\alpha_i}$ next to the curves, for unknown coefficients β and α_i. The absolute difference of the spin-structure factor with respect to the MF prediction, for corresponding value of N, is marked by a blue line with stars and fit by α_1. Similarly, in each panel the z-magnetization MF difference is marked by an orange line with circles and exponent α_2, while the Von Neumann entropy is marked by a green line with crosses, the exponent for the fit given α_3. The markers in the top-right corner of each panel refer to the points in the phase diagram of Fig. 5.5.*

the ferromagnetic phase presents the highest convergence rate, the critical region being the slowest-converging one. This is surprising, since even if the critical point is at lower entropy than the ferromagnetic region, the latter can be better captured by a Gutzwiller ansatz. Indeed, the ferromagnetic structure is not that of an ordered phase in which all the spin tends to be aligned, but every spin is, instead, in the same mixed state. Instead, at criticality, the system shows significant fluctuations around the MF results, which slows the convergence rate regardless of the less mixed nature of the system.

5.5.2 Pinpointing the phase transition: Success of the bimodality coefficient and failure of the averaged susceptibility

Having proved that the MF results recover the expected outcomes in the thermodynamic limit, we turn our attention now to the study of the critical point in finite size systems. Indeed, in any experiment, one cannot access an infinite number of spins, but instead one has to infer the presence of criticality via finite-size scaling. In this regard, we consider which quantity can better infer the existence of a phase transition in the thermodynamic limit.

In panel (a) of Fig. 5.8 we show results for $J_x = 0.6\gamma$. The vertical black dash-dotted line shows the mean-field prediction for the position of the phase transition, the vertical red dashed line shows the position as predicted by the point of intersection of the bimodality coefficient, $B_c = \langle(\hat{S}^x)^2\rangle_{\rm ss}^2/\langle(\hat{S}^x)^4\rangle_{\rm ss}$, between the curves $N = 50$ and $N = 60$. It is clear that finite-size effects impose a quantitative difference with the mean-field prediction for the location of the phase transition. Comparing the results for finite-size systems to those of the MF (Fig. 5.5), the qualitative behavior is, however, in good agreement. Moreover, the phases on either side of the transition coincide. On the left we see the values of the bimodality coefficient approaching 1/3, indicating a unimodal, i.e., paramagnetic, region. And, on the right side, they approach 1, indicating a bimodal region, i.e., a ferromagnetic one.

One can wonder if there actually is a quantitative agreement in the thermodynamic limit and if not, how large the quantitative deviation from the mean-field value is. To obtain a better idea of this we show the point of transition as predicted by the point of crossing of the bimodality coefficient curves for N and $(N+5)$ as a function of $1/N$ in panel (b) of Fig. 5.8. As the system size increases, the point of transition moves towards the mean-field critical point. Even though we can simulate systems with a number of spins of the order of a hundred, we are still

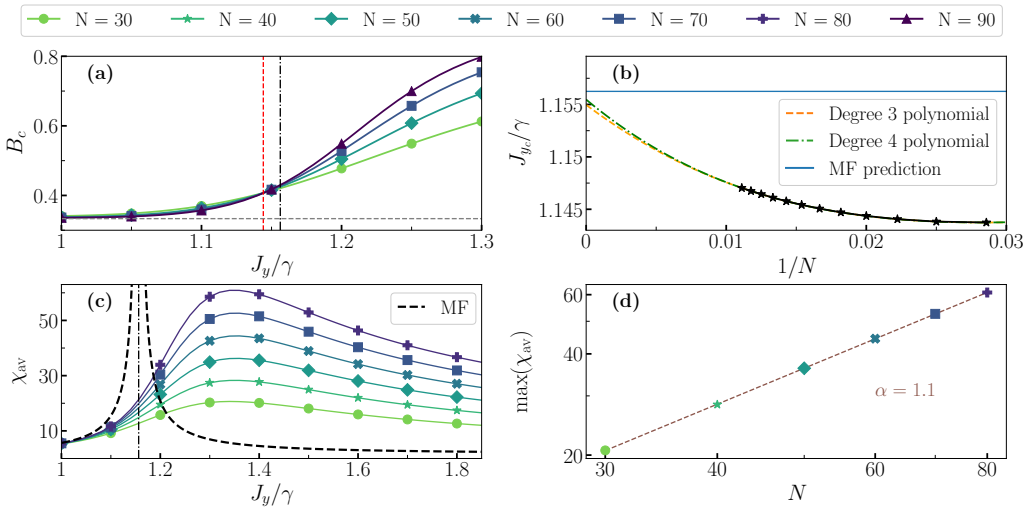

Figure 5.8: *Study of the location of the phase transition using bimodality coefficient (upper row) and the angular averaged susceptibility (lower row) for the system parameters specified in Fig. 5.4 panel (b). (a) Bimodality coefficient in the x-direction. Where the critical point in the mean-field (black dash-dotted line) is* $J_{y,mf} = 1.15625\gamma$ *and in the exact solution (red dashed line)* $J_{y,e} = 1.144\gamma$*, as determined by the intersection of the* $N = 50$ *and* $N = 60$ *curves. The (grey) horizontal dashed line indicates the value* 1/3*, expected for the PM phase. (b) Point of transition as predicted by the intersection of the bimodality coefficient for systems with* N *and* $(N + 5)$ *spins (black full line with stars). The (blue) horizontal line indicates the mean-field prediction and the (orange) dashed and (green) dash-dotted curves respectively show a polynomial fit of degree three and four. The lower panels show a study of the angular averaged susceptibility for increasing system size* N*. (c) The angular averaged susceptibility,* χ_{av}*, is studied as a function of* J_y*. The black dash-dotted line shows the mean-field critical point. (d) Scaling of the maximum of the angular averaged susceptibility as a function of the systems size* N*. The log-log fit extracts an exponent* $\alpha = 1.1$*.*

far away from the thermodynamic limit. To get an estimate of the convergence in the thermodynamic limit we make a polynomial fit of third (orange dashed line) and fourth degree (green dash-dotted line). These results show us that in the thermodynamic limit the critical point is recovered with a reasonable, although not excellent, accuracy.

In Fig. 5.8 (c) and (d) we report on a study of the angular averaged susceptibility χ_{av} (see Sec. 5.4.4 for a definition). We find that this quantity *is not a good predictor* of the position of the phase transition for finite number of spins N in the all-to-all connected XYZ spin model with local dissipation. Even if for small N values the maximum of the susceptibility keeps shifting toward bigger J_y/γ as N increases, for bigger N the peak is at a value $J_y \simeq 1.35\gamma$ [Fig. 5.8(c)]. This value is different from that of the transition point predicted by the MF. However, χ_{av} becomes divergent for $N \to \infty$, as shown in panel (d). A log-log fit of the maximum extracts an exponent $\alpha = 1.1$. We conclude that the angular averaged susceptibility, while signaling a divergence, is not associated to the one of the symmetry breaking. This is in stark contrast with lower dimensional cases [104].

5.5.3 Highly anisotropic regime: Highly-entropic ferromagnet

We now focus onto the study of the high-anisotropy regime. We define it as the region of J_y/γ where the phase is ferromagnetic but S^{xx} decreases. In our case, this corresponds to $J_y > 2.3\gamma$. We verified that this point coincides exactly to that where the bimodality coefficient obtained via the MF solution starts to decrease. In this regard, the high-anisotropy regime is the one where, by increasing J_y, the ferromagnetic peaks in the probability distribution of the magnetization become less distinguished.

As already stated, this regime is particularly interesting. Indeed, far from isotropy, the simultaneous creation of two spin excitations is energetically favorable. The Hamiltonian part tends to create correlations in the lattice while dissipation can act continuously to destroy them. The competition between the two actions creates very mixed and correlated states. Indeed, the state remains very entropic even in the limit in which the Hamiltonian should dominate the dynamics.

Figure 5.9 shows a detailed study of the steady-state spin structure factor in the x-direction. We recall that in Fig. 5.6 we found that, for low anisotropy (i.e. $|J_x - J_y|$ small), the exact results converged quite well to the mean-field calculations, for the steady state spin structure factor as well as for the other quantities. For large anisotropy, this appears no longer true, as illustrated by panel (a) up to

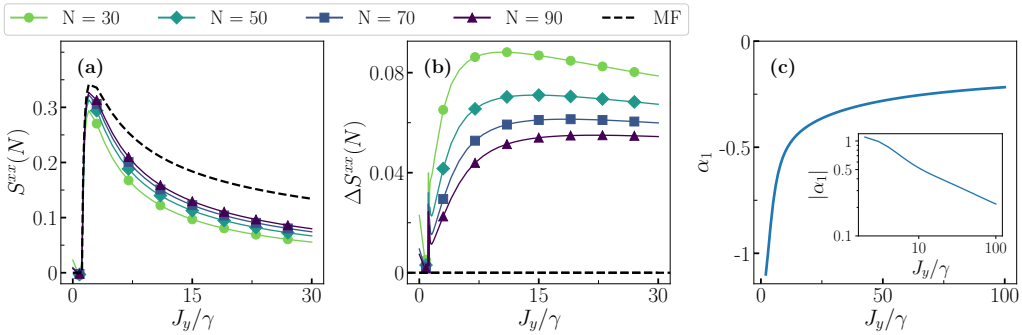

Figure 5.9: *Study of the highly anisotropic ferromagnet and of the mean-field approximation validity, for local dissipation only. We set the system parameters as specified in Fig. 5.4 panel (b) and study the spin structure factor as a function of J_y for different system sizes (lighter to darker curves as N increases). (a) Spin structure factor, $S^{xx}(N)$, calculated from the steady-state density matrix obtained from the Liouvillian in a fully-quantum picture. (b) Absolute difference between $S^{xx}(N)$ and the MF approximation for corresponding N. (c) A power-law fit of the form $y = \beta N^{\alpha_1}$ is performed for $S^{xx}(N)$ for various points of J_y, using all the curves for different N in panel (a), but up to the value $J_y/\gamma = 100$. The inset highlights the variations in scaling with a log-log plot of $|\alpha_1|$.*

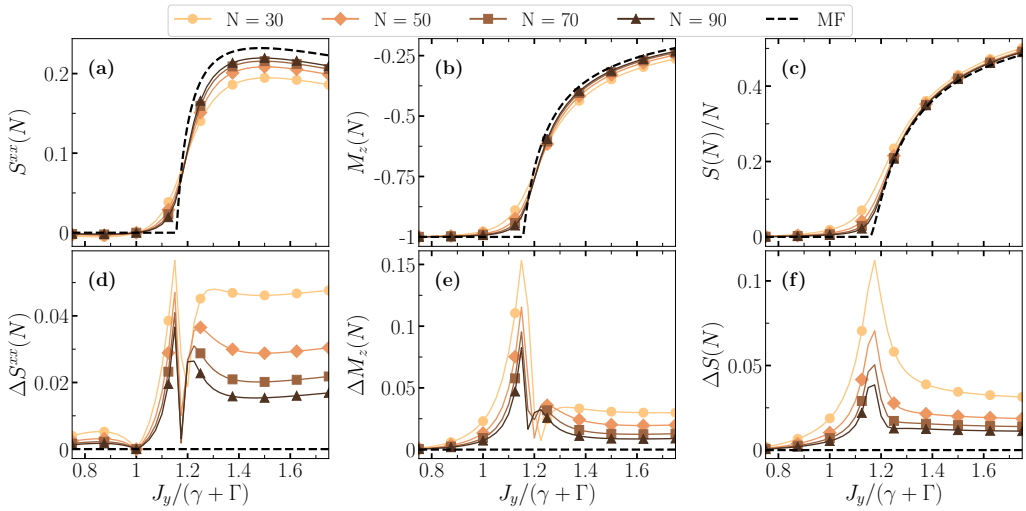

Figure 5.10: *Study of the system in the presence of both local and collective dissipation near the paramagnetic to ferromagnetic dissipative phase transition for the system parameters specified in Fig. 5.4 panel (a). The plots show the same quantities and parameter range for $J_y/(\gamma+\Gamma)$ as Fig. 5.6 (there $\Gamma = 0$). (a) Spin structure factor, $S^{xx}(N)$. (b) z-magnetization, $M_z(N)$. (c) Von Neumann entropy per spin, $S(N)/N$. In all upper panels, the black dashed curve represents the MF value for $N \to \infty$. The lower panels highlight the difference with respect to the corresponding mean-field quantities for the same value N. The lower panels highlight the difference with the mean field for fixed N, see Eq. (5.21). (d) $\Delta S^{xx}(N) = \left(S^{xx}(N) - S^{xx}_{MF}(N)\right)/N$. (e) $\Delta M_z(N) = \left(M_z(N) - M_{z\,MF}(N)\right)/N$. (f) $\Delta S(N) = \left(S(N) - S_{MF}(N)\right)/N$.*

$J_y/\gamma = 30$. In panel (b) we highlight the difference to the mean-field prediction, Eq. (5.21). A study on the scaling of the exponent,$S^{xx}(N) \propto N^{\alpha_1}$, is given in panel (c), for each point J_y/γ, up to $J_y/\gamma = 100$, extracting the exponent for different values of N. Even though the scaling predicts a very slow convergence to the mean-field (e.g. $N^{-0.22}$ for $J_y/\gamma > 60$) we derive a very different description of this regime. Since these exponents tend to zero for larger J_y, the MF prediction become less and less accurate the deeper we go in the anisotropic regime. The inset in 5.9(c) provides a log-log scale of $|\alpha_1|$ versus J_y/γ to even better illustrate the presence of different scaling regimes. The plots of Fig. 5.6 and Fig. 5.9 show that the correctness of the mean-field solutions depends on the parameter regime. More specifically: for low anisotropy it holds, and for larger anisotropy it does not.

We conclude that, even if there is not a second phase transition, in actual realization of the model the high-anisotropy regime can be seen as profoundly different from the low-anisotropy ferromagnet. Not only does the order parameter in the MF become smaller and smaller, but the convergence of the full quantum solution towards the MF also becomes slower and slower. In this regard, the thermodynamic limit in the high-anisotropy region of the phase diagram seems to be inaccessible for experimental studies.

5.5.4 Benchmark in the presence of local and collective dissipation

Finally, we consider the most general case in Eq. (5.2), for $\gamma \neq 0$ and also $\Gamma \neq 0$, i.e. we study the interplay of local and collective dissipation. The results of our numerical investigations are summarized in Fig. 5.10 and Fig. 5.11. The main observations are that the nature and position of the phase transition is not modified by the inclusion of collective dissipation, while some more refined qualitative features are affected, as also predicted by the MF solutions.

Notably, the phase transition seems to become sharper, as highlighted both by the magnetization and spin structure behavior as a function of J_y across the critical region, in panels (a) and (b) of Fig. 5.10. Similar features where observed when studying the Lipkin-Meshkov-Glick model with local and collective dissipation [101]. The Von Neumann entropy, shown in panel (c), displays an excellent agreement with the MF prediction as the system size increases. Note that, similarly to Fig. 5.6, the markers on the curves provide a guide for the eye, and 100 points are calculated for each curve as a function of J_y. In the lower row of Fig. 5.10, panels (d)-(f), we more precisely measure the difference from the MF result, showing that

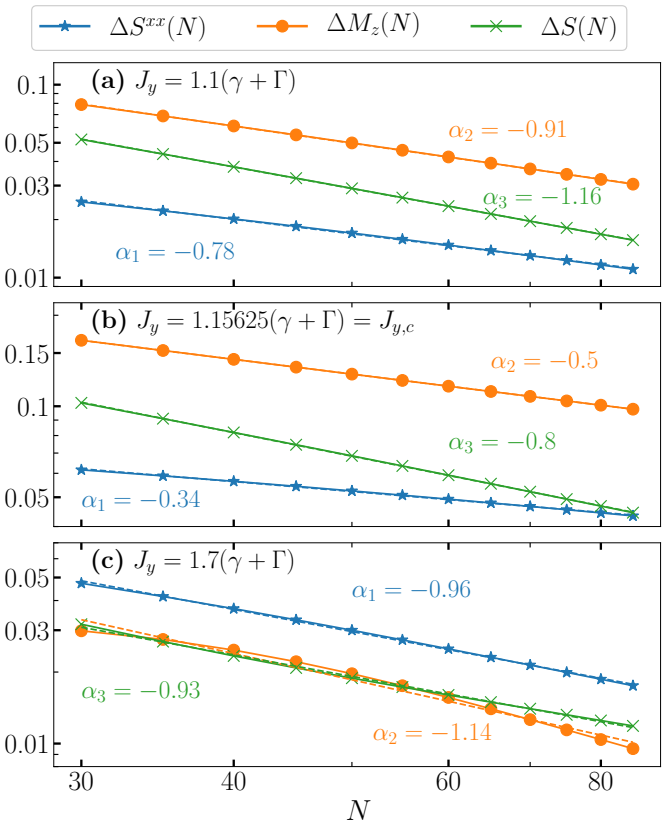

Figure 5.11: *Study of the system-size scaling, extracted from the quantities plotted in Fig. 5.10, in the presence of both local and collective dissipation across the paramagnetic to ferromagnetic dissipative phase transition. The same conventions as in Fig. 5.7 are used to refer to the difference between full-quantum simulation and MF prediction for the spin structure factor, the z-magnetization and the Von Neumann entropy. (a) We set* $J_y = 1.1\gamma$*, (b)* $J_y = J_{y,c}$ *and (c)* $J_y = 1.7\gamma$*.*

the highest discrepancies occur at the point of the phase transition and as the J_y/γ normalized anisotropic coupling is increased.

Moreover, in Fig. 5.11 we report the scaling of these quantities, as a function of N, in the PM region [panel (a)], at criticality [panel (b)], and in the FM region with moderate anisotropy with respect to the $|J_y - J_x|$ ratio [panel (c)]. Interestingly, panel (b) shows that at criticality, the same exponents as for the local dissipation case (see Fig. 5.7) for α_2 (z-magnetization) and α_3 (Von Neumann entropy per spin) are expected, with a slight discrepancy for α_1 (spin structure factor). Similarly to the local-dissipation-only dynamics, in the FM anisotropic region, shown in panel (c), the system is well described by the MF even for low number of spins, as highlighted by $\Delta M_z(N)$, which decreases faster than a power-law behavior. Indeed, the magnetization absolute difference with respect to the MF displays a remarkable non-linear trend, that does not seem well captured by a linear fit in a log-log plot (a fit would produce $\alpha_2 = -1.14$, shown as a dashed orange curve). This highlights the competition of processes governed by different scaling laws, hinting at the competition between local and collective dissipation even for remarkably large system sizes, $N \approx 100$.

5.6 Conclusions

The analysis performed in this chapter provides a benchmark for spin models on the correctness of mean-field theory in all-to-all connected dissipative systems. We studied the steady-state properties of an all-to-all connected dissipative spin model and tested the validity of the Gutzwiller mean-field approximation in capturing them.

Specifically, we considered the benchmark model of the XYZ anisotropic Heisenberg spin system, subject to both local and local-and-collective dissipation in the Lindblad form. This model is particularly interesting because it shows a second-order phase transition from a paramagnetic to a ferromagnetic phase. Moreover, for large anisotropy, this model presents a highly entropic regime which was debated to be a different phase according to cluster mean-field computations [44].

We simulated systems up to $N = 95$ spins exploiting the permutational symmetry of the model [161]. We demonstrate that, in both cases, the mean field correctly captures the physics in the thermodynamic limit. However, the scaling in the low-anisotropy regime strongly differs from that in the high-anisotropy one:

while in the former the agreement is also quantitative, in the latter the mean-field approximation fares worse. In this regard, we may advocate for the presence of strong correlations also in the all-to-all connected model. Even if we find no signs of a second phase transition, we may still argue that the high-anisotropy ferromagnetic regime is physically different from the lower-anisotropy ferromagnet. Recently, the validity of the mean-field assumption in this type of system has also been rigorously proven in Ref. [198].

Concerning more technical points, in absence of collective dissipation, we exploit the Liouvillian $\mathbb{PT}$-symmetry [189] to efficiently compute the spectral properties of the Liouvillian superoperator. In the presence of this weak symmetry the spectrum presents a second symmetry axis beyond the complex conjugation one. That, in turn, implies the existence of a state symmetric with respect to the steady state, and one associated to the first-excited eigenmatrix of the Liouvillian. The numerical computation of these two states is much easier than finding the real gap and steady state. We thus introduced the antigap of $\mathbb{PT}$-symmetric Liouvillian systems, which is equivalent to the true Liouvillian gap, and thus marks criticality in open quantum systems [32, 35].

The possibility to study a large range of spin system sizes allowed us to address the question of how to better characterize the emergence of criticality in finite-size systems. Our results indicate that the physics of systems out-of-equilibrium is more challenging to infer than one would naively expect, even in the best case scenario of all-to-all connected models, where dimensionality should induce a rapid decrease in correlations and fluctuations. Additionally, we have proven the resilience of the paramagnetic to ferromagnetic phase transition in the presence of both local and collective dissipation, finding that the presence of the two mechanisms does not change the nature of the phase transition. In both cases, one observes a second order phase transition, and the onset of criticality is for the same parameters. These indications are especially relevant to a broad variety of experimental platforms in which the dissipative phase transition can be studied, such as trapped ions, Rydberg atoms, superconducting circuits, and in solid state, especially with hybrid superconducting systems. More generally, these results provide a benchmark for the validity of mean-field approximations in understanding the experimental results obtained with noisy intermediate scale quantum simulators.

The all-to-all connected geometry under consideration constitutes also an ideal benchmark for linked-cluster expansion theories [199]. In the limit of weak spatial fluctuations, the effect of correlations is known to produce a correction scaling

as the inverse of the coordination number to the Gutzwiller mean-field limit, and therefore MF results are expected to be exact [146, 200]. As pointed out in Ref. [127], however, around second-order critical points correlations diverge, and higher-order correlation schemes should be taken into consideration to properly capture the behavior in the critical region. Finally, we also stress that linked-cluster expansions explicitly deal with an infinite lattice size, while our study is a finite-size one.

As a future outlook, we note that the interplay between local and collective dissipation beyond the all-to-all connected model demands further investigation with the adoption of both analytical and numerical approximate techniques. Furthermore, it will also be interesting to investigate the system's time evolution toward the steady state, as transient processes shall display even starker differences between mean-field or classical results and full quantum dynamics [101, 201–206]. Indeed, the present study focuses on the steady-state properties of the model, i.e., those which are permutationally invariant. Phenomena breaking this spatial symmetry, however, may arise in the dynamics towards the steady state.

The results of this chapter were published in Ref. [2].

CHAPTER 6

Dissipative phase transitions and boundary time crystals in all-to-all connected dissipative p-level systems

The physics of dissipative phase transitions has been associated with the emergence of several phenomena, such as lasing, [207–210], bistability and hysteresis [78, 79, 82, 83, 86, 87, 91, 151, 211, 212], and symmetry breaking [2, 42, 44, 81, 83, 88, 89, 104, 107, 213–216]. Similarly to dissipative phase transitions, boundary time crystals (BTCs) are critical phenomena, which are associated with the spontaneous emergence of nondecaying oscillations in open quantum systems. Here, we will consider BTCs (see section 2.8.1), i.e., those time crystals emerging despite the action of dissipation, where the long-time dynamics of the system, whose underlying dynamics is invariant under time translation, develops a periodicity [58–64, 66].

Many of the previously cited works, as well as those cited in chapter 3, deal with two very extreme cases. On the one hand, two-level systems can be thought of as bosonic resonators in the presence of a very strong interaction, where only two levels can be excited and the other transitions are so much detuned that they play no role in the dynamics. On the opposite side, when dealing with bosonic systems, one is considering the infinite number of excitations. Here, instead, we consider generalized p-level systems, where several interactions can compete in determining the physics of the system. In particular, we will consider the physics of the driven-dissipative p-level lattices in the presence of drive and (uniform) local dissipation. This system is known to display criticality both for $p = 2$ and for $p = \infty$. However, the role of the dimension is not clear in determining the transition point. Note that for $p = \infty$ the model system under consideration is the driven-dissipative

Bose Hubbard model introduced in chapter 3. Furthermore, a mean-field analysis shows the emergence of a BTC phase for this class of systems. Notably, we find that such a crystalline phase cannot be captured by a Gross-Pitaevskii equation (i.e., coherent state approximation (3.14)): a time crystalline phase emerges in the following analysis only when the mean-field equations display five solutions. The Gross-Pitaevskii equation, however, can at most display three solutions. As such, the emerging time crystal is in a quantum state and not a semiclassical state.

To confirm or disprove the results of the mean-field approach, similarly to chapter 5, we will once again exploit the permutational invariance that is present in an all-to-all connected p-level system. We have implemented a code in Python that allows us to construct a reduced Liouvillian for $p \geq 2$ (see appendix B.2 for a code example and chapter 4 for the theoretical framework). Furthermore, using a technique that we developed, and which is discussed in chapter 9, we manage to determine the low-lying part of the Liouvillian spectrum, and as such we can argue about the emergence of dissipative phase transitions and BTCs for the considered size of the system.

6.1 The system and its time evolution

We consider a Bose-Hubbard driven-dissipative lattice characterized by two types of interaction. It reads

$$\begin{aligned}
\hat{H} &= \sum_j \left(\hat{H}_j^{\text{Kerr}} + \hat{H}_j^p \right) + \hat{H}^{\text{Hop}}, \\
\hat{H}_j^{\text{Kerr}} &= -\Delta \hat{a}_j^\dagger \hat{a}_j + \frac{U}{2} \left(\hat{a}_j^\dagger \right)^2 \left(\hat{a}_j \right)^2 + F \left(\hat{a}_j^\dagger + \hat{a}_j \right), \\
\hat{H}_j^p &= \frac{W}{p!} \left(\hat{a}_j^\dagger \right)^p \left(\hat{a}_j \right)^p, \\
\hat{H}^{\text{Hop}} &= -\frac{J}{2^D} \sum_{\langle j,l \rangle} \left(\hat{a}_j^\dagger \hat{a}_l + \text{h.c.} \right),
\end{aligned} \tag{6.1}$$

where $\hat{H}^{\text{Kerr}}$ is the local Kerr-resonator Hamiltonian, $\hat{H}_j^p$ is a $p-$photon interaction, and $\hat{H}_{j,l}^{\text{Hop}}$ describes the hopping between sites j and l. The operators $\hat{a}_j^\dagger$ ($\hat{a}_j$) are the creation (annihilation) operators of the j-th site. The other parameters are: Δ the detuning, U the Kerr non-linearity, and F the pumping strength. The p-photon interaction strength is given by W. For consistency between lattices of different dimensions D, the hopping amplitude J is renormalized by the connectivity 2^D.

The dissipation is uniform and constant, and the time evolution reads

$$\partial_t \hat{\rho} = \mathcal{L}\hat{\rho} = -i[\hat{H}, \hat{\rho}] + \gamma \sum_j \mathcal{D}[\hat{a}_j]\hat{\rho}, \tag{6.2}$$

where the dissipator $\mathcal{D}\left[\hat{a}_j\right]\hat{\rho}$ is given by

$$\mathcal{D}[\hat{a}_j]\hat{\rho} = \hat{a}_j\hat{\rho}\hat{a}_j^\dagger - \frac{1}{2}\left(\hat{a}_j^\dagger\hat{a}_j\hat{\rho} + \hat{\rho}\hat{a}_j^\dagger\hat{a}_j\right). \tag{6.3}$$

We will assume that W dominates the dynamics, so that we can introduce a cutoff in the Hilbert space at $p-1$ excitations. In case $p = 2$, the system is the standard driven XY model. For $p = 3$, we are considering qutrits instead of qubits, and so on. In the following, we will be mainly interested in the cases $p \geq 3$, representing a generalization of qubit dynamics. As such, we will indicate the Hamiltonian $\hat{H}$ of a p-level bosonic system with a subscript ${}_{(p)}$, e.g. ${}_{(p)}\hat{H}$. Furthermore, we will adopt the shorthand notation that ${}_{(p)}\hat{a}$ is the truncated creation operator, e.g.,

$${}_{(3)}\hat{a} = \begin{pmatrix} 0 & 1 & 0 \\ 0 & 0 & \sqrt{2} \\ 0 & 0 & 0 \end{pmatrix}. \tag{6.4}$$

We will study an all-to-all connected geometry of the p-level lattice of resonators. In this all-to-all system, the hopping term reads:

$${}_{(p)}\hat{H}^{\mathrm{Hop}} = -\frac{J}{N-1}\sum_{j\neq l}\left({}_{(p)}\hat{a}_j^\dagger\,{}_{(p)}\hat{a}_l + \mathrm{h.c.}\right). \tag{6.5}$$

In this chapter we will consider the following parameter values with γ as the unit of energy, $U = 20\gamma$, $J = 1.5U$, $\Delta = \frac{1}{3}U$ and vary $F = \tilde{F}U$.

6.2 Mean-field equation of motion

We begin our discussion of this model by considering the Gutzwiller mean field. Within such an approximation, the state of the system is described as a tensor product, reading

$$\hat{\rho}(t) = \bigotimes_j \rho_j(t) \tag{6.6}$$

where ρ_j is the local density matrix of the j-th site. These approaches have been studied in the context of bistability and phase transitions, both in the bosonic

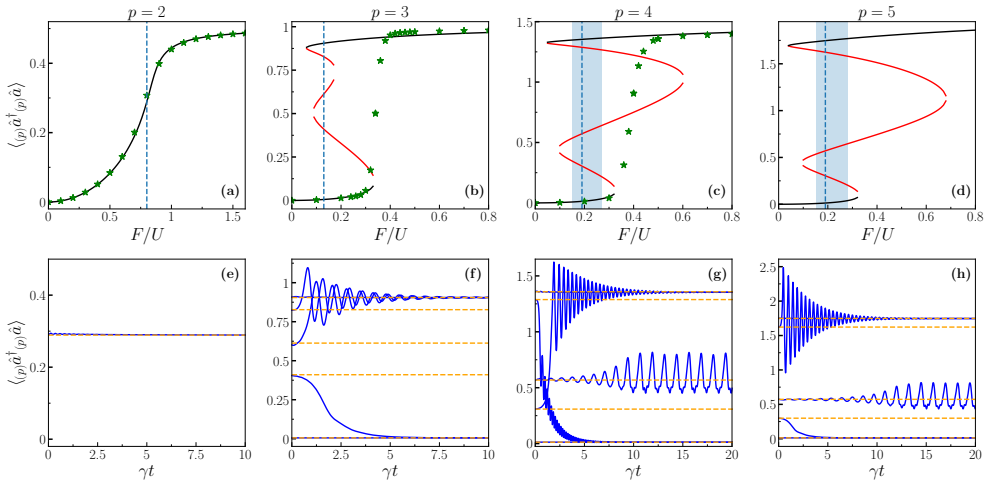

Figure 6.1: *Mean-field and exact steady-state solutions for the multistable mean-field region. Mean-field solutions are shown as stable solutions (black lines) and unstable solutions (red lines) and exact solutions for N all-to-all coupled sites are shown as green stars, for (a) $p = 2$ and $N = 35$, (b) $p = 3$ and $N = 17$, (c) $p = 4$ and $N = 9$, and (d) $p = 5$ (no exact solutions shown). A dynamical stability analysis of for a certain value of F/U for each of the p values is shown in (e) $F/U = 0.8$, (f) $F/U = 0.13$, (g) $F/U = 0.19$ and (h) $F/U = 0.19$. The mean-field steady state solutions are shown as orange dashed lines, the dynamical evolution from these initial states (with an added perturbation) is shown by blue lines for each of the initial steady states. For $p \geq 4$ and certain values of F/U periodical behaviour is observed as $t \to \infty$ for certain initial states. These regions are indicated by a light blue area in (c) and (d). Parameters used: $J/U = 1.5$, $\Delta = \frac{1}{3}U$, and $U = 20\gamma$.*

limit ($W = 0$) [79, 87, 145, 151] and in the hard-core limit ($W \to \infty$) and $p = 2$ [2, 59, 66, 198]. Interestingly, the intermediate regime where Kerr nonlinearity can play a role, but the full bosonic ladder cannot be fully explored has never been taken into consideration. Under such a truncation hypothesis, the Hamiltonian reads:

$$\begin{aligned} {}_{(p)}\hat{H}^{\mathrm{MF}} = &- \Delta_{(p)}\hat{a}^{\dagger}{}_{(p)}\hat{a} + \frac{U}{2}\left[{}_{(p)}\hat{a}^{\dagger}\right]^2\left[{}_{(p)}\hat{a}\right]^2 + \\ &\left[\left(F - J\left\langle {}_{(p)}\hat{a}^{\dagger}\right\rangle\right){}_{(p)}\hat{a} + \mathrm{h.c.}\right]. \end{aligned} \tag{6.7}$$

Consequently, we define the self-consistent Liouvillian as

$${}_{(p)}\mathcal{L}^{\mathrm{MF}} = -i[{}_{(p)}\hat{H}^{\mathrm{MF}}, \cdot] + \gamma\mathcal{D}[{}_{(p)}\hat{a}]\cdot, \tag{6.8}$$

where the dot $\cdot$ indicates where $\hat{\rho}$ can be substituted. At first, we are interested in finding the self-consistent steady states, such that

$${}_{(p)}\mathcal{L}^{\mathrm{MF}}\hat{\rho}_{\mathrm{ss}}^{\mathrm{MF}} = 0. \tag{6.9}$$

We plot the solution to the self-consistent equation in Fig. 6.1(a)-Fig. 6.1(d) for increasing values of the cutoff p. While for $p = 2$ we see just one solution, multiple solutions emerge for $p > 2$. As such, a few remarks are necessary. First, as discussed in, e.g., [35, 83, 85, 211], the presence of multiple steady states at the mean-field level is an indication of an emerging criticality. Therefore, we would expect that a system with $p = 3$ would already display a critical behaviour. In other words, for $p = 3$, there should be a nontrivial competition between the detuning and the interaction in determining the steady state of the system for this set of parameters.

Second, we notice that there are more than three solutions. This is a remarkable fact since the Gross-Pitaevskii equation (i.e., assuming $\hat{\rho}_j(t) = |\alpha(t)\rangle\langle\alpha(t)|$ where $|\alpha\rangle$ is a coherent state) yields *at most* three solutions. While in a standard GPE approach one usually finds two stable and one unstable solution, here it is unclear which solutions are stable and which are not. As such, in Fig. 6.1(e)-Fig. 6.1(h) we plot a numerical study of the stability of the solutions. That is, we numerically solve

$$\partial_t\hat{\rho}(t) = {}_{(p)}\mathcal{L}^{\mathrm{MF}}\hat{\rho}(t), \quad \hat{\rho}(0) = \hat{\rho}_{\mathrm{ss}}^{\mathrm{MF}} + \delta\hat{\rho}, \tag{6.10}$$

for each of the solution of $\hat{\rho}_{\mathrm{ss}}^{\mathrm{MF}}$ (also indicated as orange dashed lines), $\delta\hat{\rho}$ being

a small variation. In Fig. 6.1(a)-Fig. 6.1(d), stable solutions (black lines) will be characterized by a negative exponent (i.e., the system will rapidly converge to $\hat{\rho}_{\rm ss}^{\rm MF}$) while unstable ones (red lines) will be characterized by a positive exponent (the solution will diverge away from it). The value of F for which the solution is considered is marked as a dashed light-blue vertical line. For $p = 2$, where there is a unique solution, we observe that it is always stable. For $p \geq 3$, instead, we observe that there are two stable solutions and three unstable ones. Surprisingly, however, when we consider $p = 4$ or $p = 5$ we see that one of the unstable solutions develops a periodic behaviour, indicating the presence of a time crystal. We verified for several values of the pumping strength around the choice of F in the figures that time crystalline behaviour occurs. This region is marked by a light blue area in Fig. 6.1(c)-Fig. 6.1(d). We have verified that such behaviour of the mean-field solutions persist as p is increased, i.e. untill convergence is met.

The analysis of such a rich phase diagrams justifies the necessity to do full quantum simulations in order to better understand the characteristics of this system. In particular, two questions need to be answered:

1. Is there really a phase transition for $p \geq 3$ when we consider an all-to-all connected model?

2. Is the MF analysis predictive also of the dynamics of the system and not only of its steady state? As such, is there really an emergent time crystal also in the quantum limit?

6.3 Full quantum study I: dissipative phase transition

The reduction in complexity due to the exploitation of the permutational invariance in combination with the method from chapter 9 to calculate the low-lying spectrum, and thus the steady state, allows us to calculate exact full quantum solutions for the all-to-all connected system. In this study we will consider (i) $p = 3$ and up to $N = 17$ cavities; (ii) $p = 4$ and up to $N = 9$ cavities.

The multistability in the mean-field solution becomes a first-order phase transition for the full quantum model in the thermodynamic limit, and it should be witnessed by a sudden jump in the particle number. Since we consider finite systems, however, this discontinuity is somewhat smoothened. Nonetheless, it is a good indicator of emerging criticality. In Fig. 6.1 we show the particle number expectation value for: Fig. 6.1(a) $p = 2$ and $N = 35$; Fig. 6.1(b) $p = 3$ and $N = 17$;

Fig. 6.1(c) $p = 4$ and $N = 9$ as green stars. For the two-level system, we confirm that the mean-field solutions are quite predictive of the full quantum solution, even for a relatively small N [2, 198]. This correspondence is also present for the stable branches in $p = 3$ and $p = 4$, again for a quite small number of cavities. Furthermore, both for $p = 3$ and $p = 4$, the data confirm the expected emerging criticality, in the form of a steep transition from the low particle number branch to the high one, associated with the mean-field multistability. Since we will be interested also in the emergence of time crystals, below we will focus on the study of the $p = 4$ system, although similar results were found for $p = 3$ (not shown).

To further characterize the emerging criticality, we consider the low-lying Liouvillian spectrum in Fig. 6.2(a)-Fig. 6.2(c), where we show the 5 "slowest" eigenvalues of the Liouvillian for $p = 4$ for $N = 3, 7, 9$. We indicate purely real eigenvalues with black dots, whereas eigenvalues with non-zero imaginary part are red crosses. In the thermodynamic limit, the fact that λ_1 becomes zero in both real and imaginary part signals the first-order phase transition. As such, the Liouvillian gap, i.e. the real part of λ_1, describing the convergence rate towards the steady state, is an excellent indicator of criticality. As shown in Fig. 6.2(a)-Fig. 6.2(c) the minimum of the gap indeed closes as the system size increases. This is also shown in Fig. 6.2(d), where we plot the maximum of the timescale $\tau_1 = 1/\lambda_1$, showing a power-law trend as we increase the system size. Interestingly, one can find another emerging minimum in the low-lying Liouvillian spectrum, particularly visible in Fig. 6.2(c). A power law scaling of this minimum, in the form of the maximum of the timescale $\tau_4 = 1/\lambda_4$, is shown in Fig. 6.2(e), clearly indicating a diverging timescale, albeit with a much smaller exponent (≈ 0.10) than in the case for the first-order transition one (≈ 1.57). Nonetheless, this behaviour signals that in the thermodynamic limit, a *tristability may be present*.

Such a tristable behaviour could be associated with an emerging time crystal, since as it has been shown in [64, 217], the emergence of a time crystal can be associated with a point-wise closure of the Liouvillian gap (i.e., an emerging $U(1)$ symmetry of the system).

6.4 Full quantum study II: time crystal

Similarly to the first-order phase transition, an emerging time crystal is a critical phenomenon. In this case, some eigenvalues acquire zero real part but they retain a nonzero imaginary eigenvalue. From Fig. 6.2(a)-(c) however, we do not see the

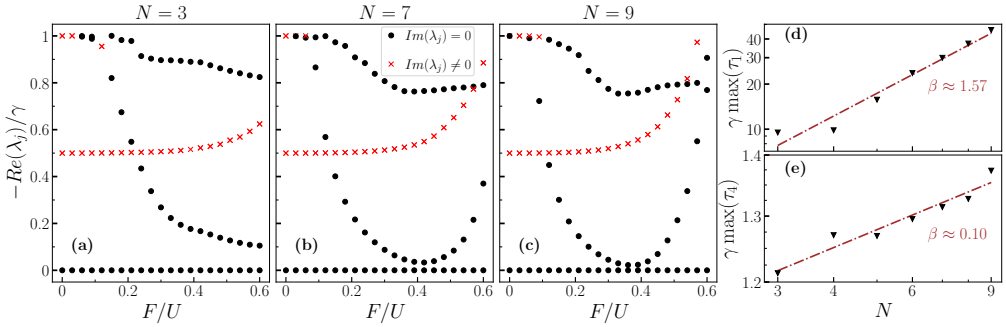

Figure 6.2: *The Liouvillian spectrum showing the 5 "slowest" eigenvalues for a system with $p = 4$ for severel system sizes: (a) $N = 3$, (b) $N = 7$ (c) $N = 9$. A power law fit $\propto \left(\tau_1^{\max}\right)^{\beta}$ (dark red dash-dottes line) scaling of the maximum of the timescale $\tau_1 = 1/(-Re\,(\lambda_1))$ (black triangles), i.e. minimum of the Liouvillian gap, is shown in (d). A power law exponent of $\beta \approx 1.57$ is found. A similar scaling is shown for $\tau_4 = 1/(-Re\,(\lambda_4))$ in (e) for the minimum that is emerging in $-Re\,(\lambda_4)$, where an exponent of ≈ 0.10 is found. Other parameters are as in Fig. 6.1.*

emergence of such an eigenvalue, if at all present. A possible reason may be that, for the observed system sizes, we are still far from criticality. Subsequently, it may be needed to go "deeper" into the Liouvillian spectrum.

In Fig. 6.3(a)-(c) we show these low-lying spectra of which the real part goes up to $\approx 1.5\gamma$ as a function of system size for values of F/U in the region where the mean-field predicts periodical behaviour. Whereas the presence of the first-order phase transition is again quickly observed, the presence of an imaginary eigenvalue of which the real part goes to zero as system size increases is not. Our analysis thus finds no signs of emerging time crystalline behaviour in the full-quantum treatment.

To verify whether a time crystal does (or does not) occur, we are currently following two directions: (i) extending our study of the low-lying spectrum for eigenvalues of which the absolute value of the real part goes beyond 1.5γ. (ii) considering a different set of parameters ($J/U = 5$) where also the system with $p = 3$ displays limit cycles at the mean-field level. As such, we hope to reach higher-dimensional systems, where we could capture signs of an emergent time-crystal structure.

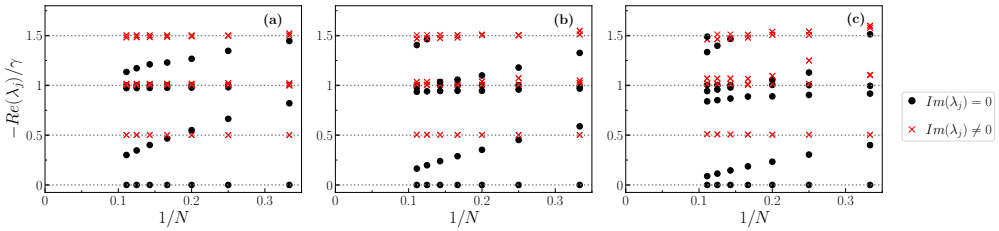

FIGURE 6.3: *The Liouvillian spectrum for eigenvalues of which the real part goes up to* $\approx 1.5\gamma$ *as a function of* $1/N$ *in the region where the mean-field predicts time crystalline behaviour for* $p = 4$ *and (a)* $F/U = 0.15$*, (b)* $F/U = 0.2$*, and* $F/U = 0.25$*. Eigenvalues with no imaginary part are marked with black dots, whereas those with non-zero imaginary part are marked as red crosses. Other parameters are as in Fig. 6.1.*

6.5 Conclusions

We have studied a model where the mean-field steady-state solutions predict a rich phase diagram, containing multistability for $p \geq 3$ and an observed time crystalline phase for $p \geq 4$. This time crystalline phase occurs in the region where the mean field predicts five steady-state solutions. Since such behaviour cannot be captured through a coherent state ansatz (i.e. GP equation) this phase is expected to come forth from the pure quantum properties of the system. In our full quantum analysis we find that criticality survives in these systems where the local Hilbert space cutoff is forcefully limited. Moreover, we have found clear evidence of a first-order phase transition as well as indications for the presence of a tristability. Furthermore, already for small N the mean-field predictions (away from criticality) hold close correspondence to the exact solutions. A study of the emergence of imaginary eigenvalues whose real part goes to zero as N is increased has given no clear sign of time crystalline behaviour. Further investigation is ongoing by doing a more in depth study of the Liouvillian spectrum as well as a study of different parameter regimes that allow for the study of systems with a higher number of sites.

PART

III

CLUSTER-GUTZWILLER METHODS FOR THE DESCRIPTION OF OPEN QUANTUM SYSTEMS

CHAPTER 7

Cluster methods for the description of the dissipative XYZ Heisenberg model

In the previous chapters we have focussed on the Gutzwiller mean-field approach and its validity in highly dimensional all-to-all connected open quantum systems. Now, we will shift our attention to lower dimensional open systems where the mean-field theory introduced in chapter 3 is expected to fall short of, at least, quantitavely describing the system in most regimes. More specifically, we will study two-dimensional cubic lattices with periodic boundary conditions and briefly discuss one dimensional chains. In this chapter an extension to the mean-field approach is introduced, namely the cluster-Gutzwiller quantum trajectory approach, and it will be applied to the dissipative XYZ Heisenberg model. We will also refer to this method as the cluster-Gutzwiller Monte Carlo approach (CGMC). Furthermore, its results will be compared with the cluster mean-field approach (see (3.9)), which is a master equation approach. We will also comment on several peculiarities of this open system that arise from mean-field theory with respect to closed quantum systems.

7.1 The model system

We again study the anisotropic XYZ Heisenberg Hamiltonian (3.2)

$$\hat{H} = \sum_{\langle i,j \rangle} \left(J_x \hat{\sigma}_i^{(x)} \hat{\sigma}_j^{(x)} + J_y \hat{\sigma}_i^{(y)} \hat{\sigma}_j^{(y)} + J_z \hat{\sigma}_i^{(z)} \hat{\sigma}_j^{(z)} \right), \tag{7.1}$$

this time on a cubic spin lattice. Note that in the above Hamiltonian we have discarded the coefficient with the coordination number $1/Z$ from (3.2). The reason for this stems from the literature, where predominantly this choice of convention is

used in works that focus on the beyond-mean field treatment of this model [1, 44, 104, 107, 126–128, 131]. This can be done without loss of generality, one however needs to pay attention that e.g. mean field equations in this chapter will slightly differ from those that have been derived in chapter 5. The above Hamiltonian governs the unitary part of the time evolution of the system. The total time evolution of the system is governed by a Lindblad Equation with dissipation along the z-axis

$$\partial_t \hat{\rho} = -i\left[\hat{H}, \hat{\rho}\right] + \frac{\gamma}{2}\sum_j \left(2\hat{\sigma}_j^{(-)}\hat{\rho}\hat{\sigma}_j^{(+)} - \left\{\hat{\sigma}_j^{(+)}\hat{\sigma}_j^{(-)}, \hat{\rho}\right\}\right). \tag{7.2}$$

With γ the decay rate of the spins and $\hat{\sigma}_i^+$ ($\hat{\sigma}_i^-$) the raising (lowering) operators along the z-axis. We thus study the case of local dissipation only.

From this moment on, we will consider the parameters $J_x = 0.9\gamma$ and $J_z = \gamma$, unless stated differently, and vary J_y.

7.2 Cluster methods

We will compare our results with the cluster mean-field method (CMF) [44]. The mean-field approach [42] predicts a transition from a paramagnetic phase to a ferromagnetic phase for this parameter set at $J_y \approx 1.04\gamma$. By including quantum correlations in the CMF [44] the existence of another transition from the ferromagnetic phase to the paramagnetic phase is observed. Such a behaviour is also observed when one includes classical spatial correlations by using the Gutzwiller Monte Carlo approach (GMC) [128]. A natural extension is then of course a cluster-Gutzwiller Monte Carlo approach, where the inclusion of short-range quantum correlations is combined with the inclusion of classical spatial correlations. It is worth noting that the nature of the steady state in the regime where the previous methods predict a re-entrance of the paramagnetic state is still largely under debate [107]. In this regime of large anisotropy the transition point from the ferromagnetic phase to a paramagnetic phase is largely dependent on the method used, as well as possible cluster sizes. Furtermore, several of the above methods that we discussed in chapter 3 do not reach convergence in this region.

In this section we will first give a more in depth introduction to the CMF approach and then move onto the introduction of the CGMC approach.

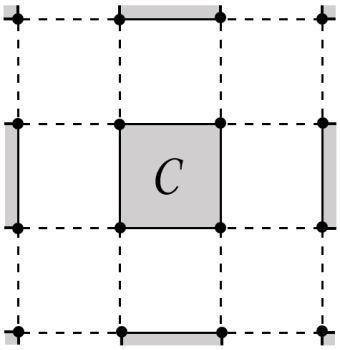

Figure 7.1: *This figure shows the lattice layout with 2×2 clusters on a two-dimensional lattice. Each cluster is shown as a grey area and contains a set of ('connected') lattice points. Inside these clusters quantum correlations between the different sites are included. Since numerical simulation can only be performed for small clusters we will refer to these quantum correlations as short-range quantum correlations.*

7.2.1 Cluster mean-field approach

As we have introduced in chapter 3, the cluster mean-field approach corresponds to the introduction of a factorized density matrix ansatz for the density matrix of the system of interest

$$\hat{\rho} = \bigotimes_C \hat{\rho}_C. \tag{7.3}$$

It consists of a division of the lattice into multiple (non-overlapping) clusters or plaquettes, as illustrated on Fig. 7.1. If one substitutes (7.3) into the lindblad master equation of the system one can straight forwardly derive an equation for the time evolution of the density matrix of a certain cluster C. If one assumes the clusters to be of identical size N_c, i.e. they all have the same dimensions $N_c \times N_c$ and thus consist of N_c^2 lattice sites, the translational invariance of the system can be exploited. It then suffices to derive the time evolution of only one cluster C, since the time evolution of the density matrices of all other clusters C' will be identical to it. After subsitution of (7.3) into the master equation (7.2) and taking the partial trace of all sites that are not in the set of sites inside the cluster C one then yields

$$\partial_t \hat{\rho}_C = -i \left[\hat{H}_{CMF}, \hat{\rho}_C\right] + \frac{\gamma}{2} \sum_{j \in C} \left(2\hat{\sigma}_j^{(-)} \hat{\rho} \hat{\sigma}_j^{(+)} - \left\{\hat{\sigma}_j^{(+)} \hat{\sigma}_j^{(-)}, \hat{\rho}\right\}\right). \tag{7.4}$$

Where the cluster mean-field Hamiltonian $\hat{H}_{CMF}$ can be written as

$$\hat{H}_{CMF} = \hat{H}_C + \hat{H}_{\mathcal{B}(C)}, \tag{7.5}$$

where $\hat{H}_C$ only contains interactions within the cluster C, given by

$$\hat{H}_C = \sum_{\alpha=x,y,z} \sum_{\langle i,j\rangle | i,j \in C} J_\alpha \hat{\sigma}_i^{(\alpha)} \hat{\sigma}_j^{(\alpha)}. \tag{7.6}$$

The term $\hat{H}_{\mathcal{B}(C)}$ describes the interactions along the boundary $\mathcal{B}$ of the cluster C, i.e.: the interactions between sites inside the cluster and their nearest neighbours outside this cluster, also called the mean-field interactions. This term is given by

$$\hat{H}_{\mathcal{B}(C)} = \sum_{\alpha=x,y,z} \sum_{\langle i,j\rangle | i \in C, j \notin C} J_\alpha \hat{\sigma}_i^{(\alpha)} \langle \hat{\sigma}_j^{(\alpha)} \rangle. \tag{7.7}$$

Rewriting $\hat{H}_{CMF}$ in terms of these two Hamiltonians allows one to quickly see that close-range quantum correlations are incorporated through the "exact" treatment of the sites inside C in (7.6). However, long-range quantum correlations are missing in this type of approximation due to the mean-field treatment on the boundaries of the cluster, i.e. $\hat{H}_{\mathcal{B}(C)}$ in (7.7). By including more lattice sites into the cluster one can increase the range of the quantum correlations. One will however quickly run into the problem of the exponentially growing Hilbert space of such a cluster. To keep the dimension of the Hilbert space limited only small clusters will be studied and the importance of short-range quantum correlations will be determined. Notably, due to the translational invariance and the mean-field treatment on the boundaries of the cluster, the results one obtains from such a treatment are valid for an infinitely sized lattice. Additionally, if one constrains the size of the cluster to only one lattice site, one regains the standard Gutzwiller mean-field approach.

Recently, some interesting proposals to combine existing methods with this cluster mean-field approach have come forth. For example, one could use the corner renormalization method to calculate results for larger cluster sizes that would be unreachable in a brute force matter. This would combine the strength of the corner method with the ability of the cluster mean-field approach to simulate infinite size lattice systems.

In Ref. [44] the CMF approach was applied to the dissipative XYZ Heisenberg model and they found that close-range quantum correlations have a dramatic impact on the mean-field phase diagram, as shown in Fig. 3.2. A re-entrance

of the paramagnetic phase was observed as J_y/γ was increased. Furthermore, it was argued that this re-entrant paramagnetic phase is different in nature from the paramagentic phase for small J_y/γ. A study of the purity has shown that the system's density matrix becomes fully mixed in the limit of high J_y/γ, while for low J_y/γ it has a purity close to one. Note that this is reminiscent of the entropic ferromagnet observed in the highly anistotropic regime in our study in chapter 5. Even though no re-entering paramagnetic phase was observed in this study, the nature of the ferromagnetic phase also shows different characteristics between the regimes of low and high J_y/γ.

Interestingly, the drastic change through the inclusion of close-range quantum correlations is unheard of in equilibrium systems. The difference occurs due to the ordered (ferromagnetic) steady state finding its origin in a dynamical evolution, whereas in closed systems in equilibrium the ordering emerges from the properties of the free energy. This once again emphasizes the intriguing differences between closed and open systems.

7.2.2 Cluster-Gutzwiller Monte Carlo approach

The (cluster-)Gutzwiller approach can also be applied in a quantum trajectory formalism. Instead of evolving a factorized density matrix one evolves a factorized wave function

$$|\psi\rangle = \bigotimes_C |\psi_C\rangle. \tag{7.8}$$

As we have seen in chapter 2, a continuous monitoring of the spin flips that occur in the system allows for a stochastic simulation of the dynamics of the system. In between the detection of these quantum jumps the wave function will evolve according to

$$|\psi(t)\rangle = \frac{\exp\left(-i\hat{H}_{\mathrm{CGMC}}t\right)|\tilde{\psi}\rangle}{||\exp\left(-i\hat{H}_{\mathrm{CGMC}}t\right)|\tilde{\psi}\rangle||}, \tag{7.9}$$

with $\tilde{\psi}$ an initial (normalized) wave function. Note that the time evolution generated by

$$\hat{H}_{CGMC} = \sum_C \left[\hat{H}_C + \hat{H}_{\mathcal{B}(C)} - i\frac{\gamma}{2}\sum_{i\in C}\hat{\sigma}_i^+\hat{\sigma}_i^-\right], \tag{7.10}$$

does not preserve the norm due to the non-Hermitian term that contains the dissipation rate γ. When a spin-flip is detected a quantum jump is made in the

evolution of the wave function

$$|\psi(t)\rangle \rightarrow \frac{\hat{\sigma}_i^-|\psi(t)\rangle}{||\hat{\sigma}_i^-|\psi(t)\rangle||}, \tag{7.11}$$

after which the wave function continues evolving according to (7.9). The cluster mean-field Hamiltonian (7.10) implements the deterministic time evolution in the manifold of cluster-Gutwiller states according to the time-dependent variational principle (see appendix D). Since the dissipation is given by a spin-flip on a certain site, the quantum jump does not cause the wave function to leave this variational manifold and Eq. (7.11) is readily applicable. Furthermore, due to the factorized nature of (7.8) one obtains a system of coupled equations for each individual $|\psi_C\rangle$ and consequently an expression that governs the time evolution (7.9) for each cluster, given by

$$\partial_t|\psi_C\rangle = -i\left[\hat{H}_C + \hat{H}_{\mathcal{B}(C)} - i\frac{\gamma}{2}\sum_{i\in C}\hat{\sigma}_i^+\hat{\sigma}_i^-\right]|\psi_C\rangle. \tag{7.12}$$

The time evolution can then be determined through a standard numerical differential equation solver. For the numerical implementation and the determination of the times at which the quantum jumps take place we refer to appendix A.1.

This approach allows for the inclusion of long-range classical correlations in the description of the system due to the stochastic nature of the quantum jumps in the evolution of a single trajectory. With long-range we refer to all correlations beyond the used cluster size. Due to the stochastic nature however, the system can no longer be regarded as translationally invariant. The approach thus no longer allows for results in infinite sized lattices, as was the case for the master equation treatment in (7.4). One is limited to simulating lattices of finite size. Consequently, the complexity of the approach scales as $N_C N_c^2$, where N_C the number of clusters. Nonetheless, information on the thermodynamic limit can be extracted through a finite-size scaling of the obtained results. The inclusion of classcial correlations has thus come at the cost of the infinite lattice description of the cluster mean-field.

The simplest case of (7.8) is the one with cluster size one, that is a standard Gutzwiller ansatz of the wave function, which has been studied in Ref. [128]. As an example to get familiar with this trajectory description we show a trajectory of

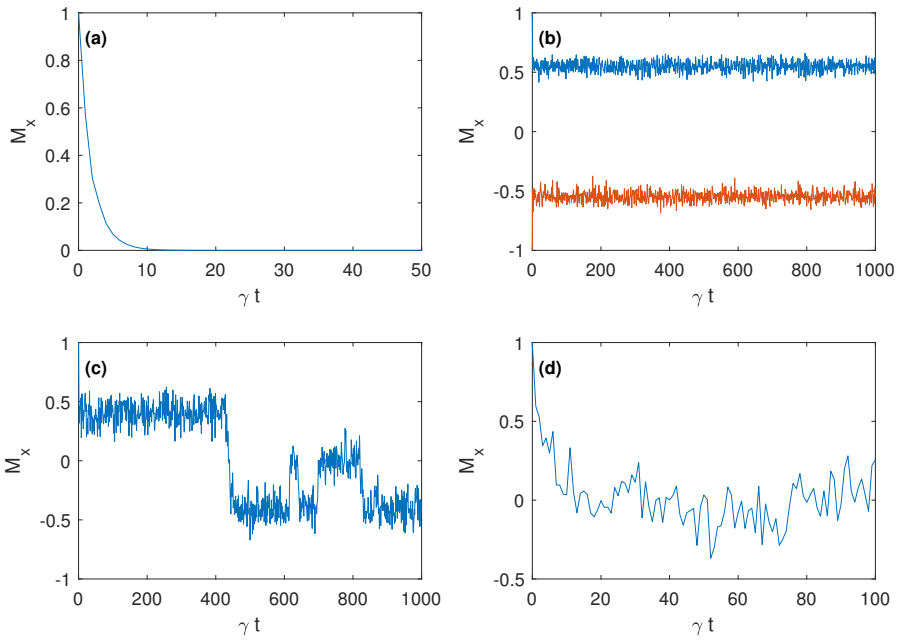

Figure 7.2: *The magnetization in the* x*-direction obtained through a Gutzwiller Monte Carlo approach for a* 6×6 *lattice with parameters* $J_x = 0.9\gamma$ *and* $J_z = \gamma$ *and various values for* J_y*:* ***(a)*** $J_y = \gamma$*,* ***(b)*** $J_y = 1.2\gamma$*,* ***(c)*** $J_y = 1.8\gamma$ *and* ***(d)*** $J_y = 2.5\gamma$*. Each trajectory was started in an initial state where all spins point in the positive* x*-direction, except for panel* ***(b)*** *where the red curve starts in an initial state in the negative* x*-direction.*

the $x-$magnetisation of a $N \times N$ lattice, that is

$$M_x = \frac{1}{N^2} \sum_j \langle \hat{\sigma}_j^x \rangle, \tag{7.13}$$

with $N = 6$ and for various parameter sets in Fig. 7.2. In Fig. 7.2 (a) one can see a quick relaxation to a paramagnetic phase as time evolves. Such a result is expected because of symmetry: due to $J_y = J_z$ the unitary dynamics governed by the Hamiltonian conserves the x-magnetisation. The continuously occuring spin flip processes in the negative z-direction will however cause the x-magnetisation to diminish until it is equal to zero. In Fig. 7.2 (b) one can clearly observe the ferromagnetic phase of which the direction of the spins is determined by their initial configuration. For this parameter choice, the coupling between the different spins is able to counteract the spin flips in the negative z-direction. Fig. 7.2 (c) shows an example of a transition region where the system jumps between the two ferromagnetic branches and a paramagnetic phase at relative long timescale. From this quantum trajectory one can expect a re-entrance of the paramagnetic state for increased values of J_y. This is exactly what is observed in Fig. 7.2 (d) where on average the magnetization will be zero.

7.3 Steady-state spin structure factor

In order to investigate the dissipative phase transition between a paramagnetic and ferromagnetic state, we will consider the steady-state spin structure factor $S^{xx}(\mathbf{k} = 0)$ as defined in (5.7). We use this correlation function rather than the spontaneous magnetization itself, because in a finite system, the $\mathbb{Z}_2$-symmetry does not spontaneously break and we wish to compare our results with exact solutions. Alternatively, a (small) magnetic field could be applied to break the symmetry, as will be discussed in section 7.4. A non-zero value of the steady-state spin structure factor indicates a region with ferromagnetic correlations. A zero value has a wider range of possibilities such as a paramagnetic region, an anti-ferromagnetic region and spin density waves. To distinguish between these regions different values of the wave vector $\mathbf{k}$ have to be studied. We have verified that the zero value coincides with a paramagnetic phase.

We simulate the dynamics of a trajectory over a minimum total time of $10.000/\gamma$ and obtain the steady-state solutions by time averaging over this single trajectory. Generally, the number of independent points in this time window is of the same

order as the length of the time window, i.e.: proportional to 10.000. However, at certain points in the phase diagram, for example near a transition between regions or at certain cluster sizes, the need to use larger time windows may arise. This is because the time for two points to become uncorrelated, and thus independent, may be larger in these cases and the time window thus contains less independent points. Increasing the time window with a factor 2 to 5 is usually sufficient to obtain a good accuracy. The results of our numerical simulations are shown in Fig. 7.3, where the spin structure factor was obtained for a 4×4 lattice with various cluster sizes. It is clear that increased incorporation of quantum correlations present for larger cluster sizes significantly affects the spin correlations.

Both the 1×2 and 2×2 clusters show the existence of the ferromagnetic region and show qualitatively the same behaviour as predicted by the CMF [44] and the GMC [128]. The clusters however, are able to find a non-zero value for $S^{xx}_{ss}(0)$ for values of $J_y < 0.9\gamma$. This behaviour is not captured by the single-site Gutzwiller ansatz [128] or the mean-field [42] and thus originates from quantum correlations. In the GMC [128] the ferromagnetic region becomes smaller with growing system size and the transition to the paramagnetic region becomes sharper. The inset of Fig. 7.3 shows that by including clusters of size 1×2 and 2×2 this behaviour is captured already for smaller lattice sizes. Increasing the cluster size makes the sharpening steeper and occur for smaller values of J_y. This shows the importance of quantum correlations in the simulation of an open quantum system. This sharpening is what is to be expected when the size of the lattice grows (i.e. when the thermodynamic limit is approached).

By comparing the results for different cluster sizes with the exact solution of this lattice we see that for increasing cluster sizes the exact solution is approached more closely, but differences persist. It has to be noted that short-range quantum correlations are not enough to accurately approximate the exact solution for the 4×4 system. It remains to be seen if this stays true for larger lattices and if longer-range quantum correlations have to be taken into account as well.

As mentioned earlier, for values of the parameter J_y smaller than 0.9γ we find an unexpected buildup of spin-spin correlations. Where the mean-field theory predicts an all-zero steady-state spin structure factor we find a non-zero value by including clusters. This non-zero value is most pronounced in the exact solution. This behaviour is completely neglected by the classical mean-field theory and thus entirely driven by quantum fluctuations. The question remains whether a phase transition is present or not. It is however clear that short-range quantum

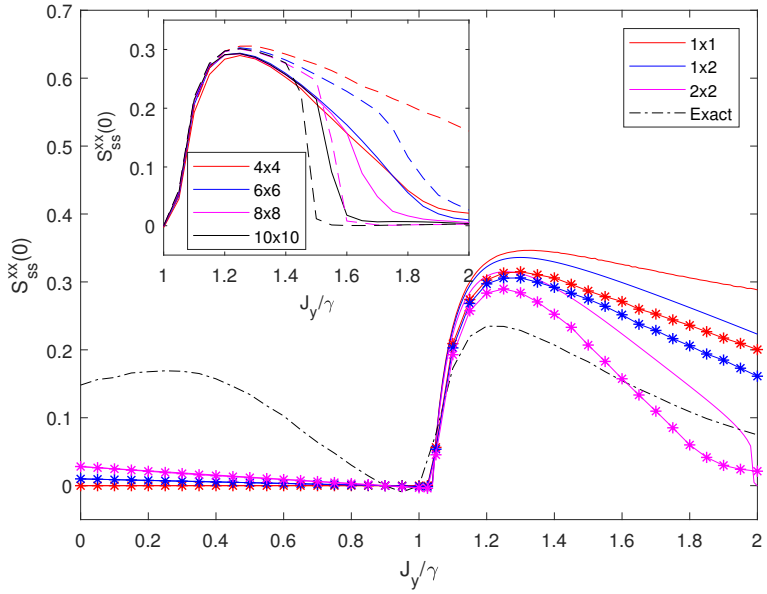

Figure 7.3: *(Color online) Steady-state spin structure factor of a* 4×4 *lattice with* 1×1 *clusters (first top right line),* 1×2 *clusters (second top right line) and* 2×2 *clusters (third top right line) for the CGMC (stars) and the CMF (full lines). The dash-dotted line is the exact solution of the* 4×4 *lattice obtained by using quantum trajectories for the time evolution of the full Hilbert space. Note that the* 1×1 *CMF is the usual mean-field result. The CGMC qualitatively predicts the same ferromagnetic and two paramagnetic regions as the CMF [44]. Additionally we observe the possible existence of a phase transition completely missed by mean-field theory for values of* $J_y < 0.9\gamma$.
Inset: steady-state spin structure factor of a 4×4 *(first top right line),* 6×6 *(second top right line),* 8×8 *(third top right line) and* 10×10 *(fourth top right line) lattice with clusters of size* 1×2 *(dashed lines) and* 2×2 *(full lines) for the CGMC. Increasing the lattice size shows a sharpening of the transition, also found with the GMC [128]. This sharpening is steeper when larger cluster sizes are included.*

correlations do not capture the exact behaviour for small lattices and long-range correlations have to be included for a more accurate description.

A comparison with the CMF used in Ref. [44] can show us the importance of spatial correlations between the clusters, as they are not captured by the CMF. Fig. 7.3 shows the steady-state spin structure factor for several cluster sizes on a 4×4 lattice. The exact solution is found using the quantum trajectory approach. We notice two distinct areas, again for $J_y < 0.9\gamma$ and $J_y > 0.9\gamma$ (we will resp. call them the *left*-hand and *right*-hand side). On the left-hand side both the CMF and the CGMC match closely, giving a strong indication that only quantum correlations are important in this regime. On the right-hand side of the figure however, the CMF and CGMC match only qualitatively, in this regime both quantum and classical spatial correlations contribute. This confirms the difference between the buildup of order on the left and right-hand sides respectively.

In one dimension (1D) we can take clusters with larger linear size. In the top panel of Fig. 7.4 we look at a 1×12 lattice for which we can go up to 1×6 clusters. As was the case for the two-dimensional lattice, the exact solution was obtained using the quantum trajectory approach. We find that the behaviour of the steady-state spin structure factor is qualitatively captured by the cluster approach both in the left and right region for 1×6 clusters. It has to be noted that the system has no phase transition in the thermodynamic limit in 1D, which has been shown by using a matrix product operator ansatz for the density matrix [44]. The behavior of the spin structure factor for finite size systems does however give insight in the importance of the longer-range quantum correlations to describe the exact dynamics of the open quantum system. As one can see in Fig. 7.4, decreasing the size of the clusters results in a steady-state spin structure factor that differs strongly from the exact value, even negative values are found for values of $J_y > \gamma$ where they should be positive. For values of $J_y < \gamma$ the influence of increasing the cluster size can be clearly observed. By including longer-range quantum correlations the exact behaviour is matched more closely. For 1×2 clusters we find the same linear behaviour for the steady-state spin structure factor as found in the two dimensional case. By increasing the cluster size we can see a clear convergence to the same behaviour as the exact solution. Short-range quantum correlations are as such not sufficient for the description of the system and longer-range quantum correlations play an important role.

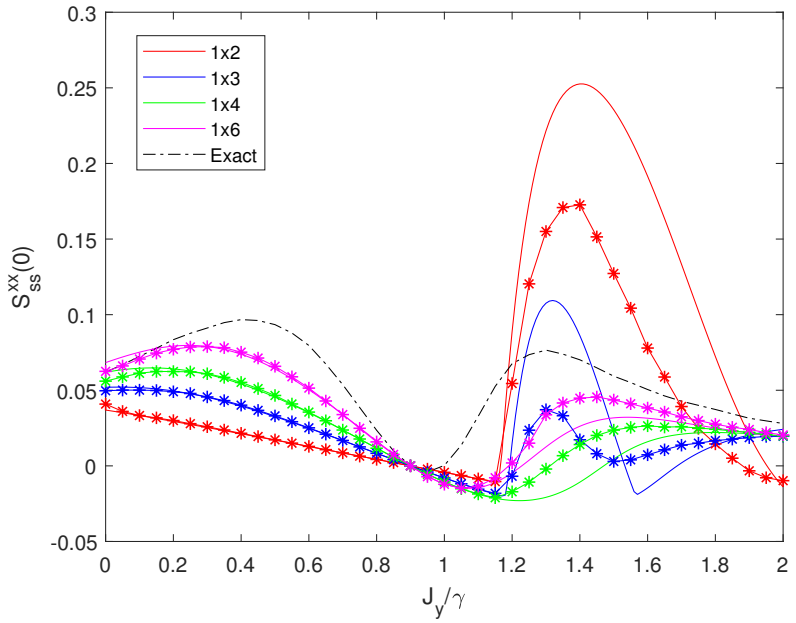

Figure 7.4: *(Color online) Steady-state spin structure factor of a* 1×12 *lattice with different cluster sizes using the CGMC (stars) and the CMF (full lines). The dash-dotted line is the exact solution of the* 1×12 *lattice obtained by using quantum trajectories for the time evolution of the full Hilbert space. The figure shows that through inclusion of longer-range quantum correlations, by increasing the cluster size, the exact behaviour is approached more closely for* $J_y < \gamma$*, we observe a convergence from the result with* 1×2 *clusters (bottom star line) up to the result with* 1×6 *clusters (top star line) to the exact result. Increasing the cluster size for values of* $J_y > \gamma$ *does not show a clear convergence pattern to the exact solution. The results for* 1×6 *clusters do however match the exact result most closely. These findings, both for* $J_y < \gamma$ *and* $J_y > \gamma$*, indicate short-range quantum correlations are not sufficient for the description of the system.*

To gain a better understanding of the ferromagnetic region missed by mean-field theory we show the steady-state spin structure factor for the exact solution of a 2×2, 3×3 and 4×4 lattice on the top panel of Fig. 7.5. The solution of the 2×2 and 3×3 was found by solving the master equation and the 4×4 solution was obtained with the trajectory approach. As can be seen from this figure, and as is expected for finite size systems, the region where the phase transition occurs is smoothed out and one could suspect that there is only a continuous change of the order parameter rather than an actual phase transition. In the parameter region $J_y/\gamma \in]0.9, 1[$ however the spin structure factor does decrease when the lattice size is increased (Note that the steady-state spin structure factor is always zero for the values $J_y = J_x$ and $J_y = J_z$ due to the unitary dynamics conserving respectively the magnetization in the z-direction and x-direction [44]). In order to check for the convergence as a function of increasing system size, we show in the bottom panel of Fig. 7.5 the behavior as a function of the system size, together with a fit to the power law dependence $S^{xx}_{ss}(0, L) = aL^b$, where L is the number of points along one dimension of the $L\times L$ lattice. In all cases, we find a negative exponent b, which is compatible with a vanishing of the spin structure factor in the thermodynamic limit. For $J_y = 0.95\gamma$ (in the middle of the interval), we find $b \approx -2.1$, close to the value $b = -2$, that is expected for a two-dimensional system with a finite correlation length.

7.4 An external magnetic field

The $\mathbb{Z}_2$-symmetry can be explicitly broken by applying a small magnetic field. In this section we will study the behaviour of the magnetization of the system as a function of the applied field in the x-direction and y-direction. An applied field $\vec{h} = h_x\vec{e}_x + h_y\vec{e}_y$ translates in adding a term $\hat{H}_B$ to the Hamiltonian $\hat{H}$ from (7.1)

$$\hat{H}_B = h\sum_i \left(\cos(\theta)\hat{\sigma}_i^{(x)} + \sin(\theta)\hat{\sigma}_i^{(y)}\right). \tag{7.14}$$

In Fig. 7.6 the magnetization in the y-direction is shown for a 4×4 lattice with 1×2 and 2×2 clusters as a function of h_y ($h_x = 0$) in the CMF. From the theory of closed quantum systems one would expect the magnetization to tend to ±1 for large h. This however is not the case as can be seen in the figure, both the x and y magnetization go to zero when the field is increased. To obtain a closer understanding of this behaviour we note that it is also present in the mean-field

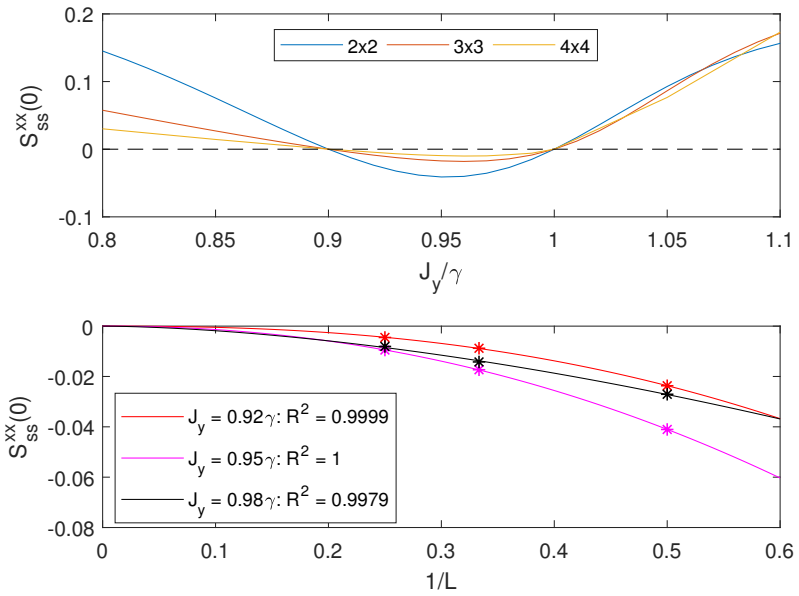

Figure 7.5: *(Color online) Top panel: the exact solution for the steady-state spin structure factor of a* 2×2*,* 3×3 *and* 4×4 *lattice. To exclude the possibility of the presence of a continuous variation of the order parameter rather than a phase transition driven by quantum correlations, we study if the steady-state spin structure factor in the region* $J_y \in]J_x, J_z[=]0.9\gamma, \gamma[$ *converges to zero in the thermodynamic limit. The solution of the* 2×2 *and* 3×3 *was found by solving the master equation and the* 4×4 *solution was obtained with the trajectory approach.*
Bottom panel: The behaviour of the steady-state spin structure factor through a fit as a function of lattice size from the known points of the 2×2*,* 3×3 *and* 4×4 *lattice for several values of* $J_y \in]J_x, J_z[$*:* $J_y = 0.92\gamma$ *(top line),* $J_y = 0.95\gamma$ *(bottom line) and* $J_y = 0.98\gamma$ *(middle line). The fit of a power law of the form* $S^{xx}_{ss}(0, L) = aL^b$ *for* $L\times L$ *lattices returns high* R^2*-values and converges to zero in the thermodynamic limit.*

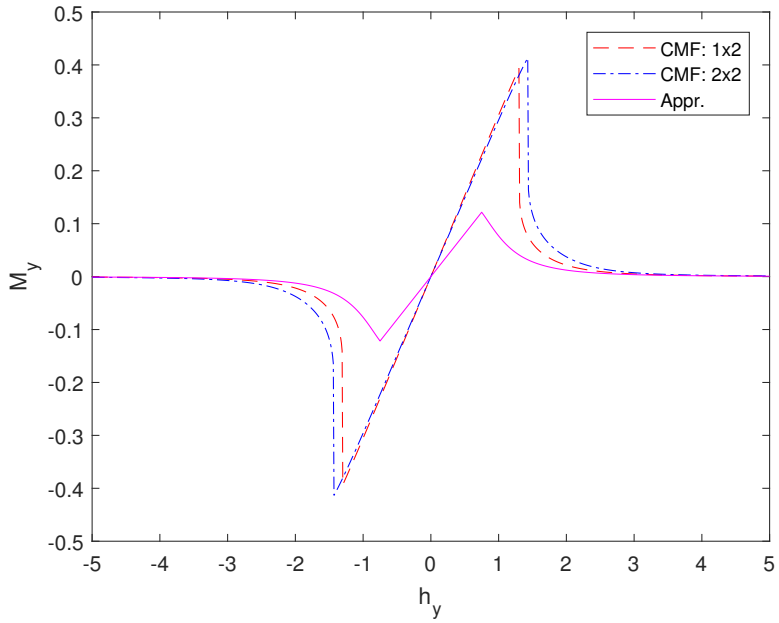

Figure 7.6: *(Color online) Magnetization in the y-direction as function of an applied magnetic field in the y-direction for* 1×2 *(dashed red line) and* 2×2 *(dash-dotted blue line) clusters in the CMF and the approximated mean-field solution (full purple line) which is valid in the limit of large* h_y *for* $J_y = 0.25\gamma$.

approximation, for which we can find analytic expressions. These expressions will enable us to shed light on this behaviour.
The system of mean-field equations in the steady-state can be written as

$$\begin{cases} -\frac{\gamma}{2}M_x + 2d(J_y - J_z)M_yM_z + 2h_yM_z = 0, \\ -\frac{\gamma}{2}M_y + 2d(J_z - J_x)M_xM_z - 2h_xM_z = 0, \\ -\gamma\,(M_z + 1) + 2d(J_x - J_y)M_xM_y \\ +\,2(h_xM_y - h_yM_x) = 0, \end{cases} \tag{7.15}$$

with d the dimensionality, γ the dissipation rate and M_x, M_y and M_z resp. the magnetization in the x, y and z direction. We look at the case where $h_y \neq 0$ and $h_x = 0$ (the reverse situation is analogue). With these parameters one can rewrite the system of equations as an expression for M_x and M_y in terms of M_z

$$M_x = \frac{1}{\gamma}\frac{4h_yM_z}{1 - \frac{16d^2}{\gamma^2}\left(J_y - J_z\right)\left(J_z - J_x\right)M_z^2}, \tag{7.16}$$

$$M_y = \frac{4d}{\gamma}(J_z - J_x)M_xM_z, \tag{7.17}$$

and an equation for M_z of which the solution remains to be found by substituting the above solutions for M_x and M_y into the last equation in (7.15). This equation has no analytic solution and has to be solved numerically. We can however use the knowledge that $M_z \to 0$ as $h_y \to \infty$. A more close study shows that for a growing field h_y, $h_yM_z \to 0$. With these conditions we can approximate the third equation of (7.15) to first order in M_z. We then find for large h_y

$$M_z = -\frac{1}{8}\frac{\gamma^2}{h_y^2}. \tag{7.18}$$

This relation shows that M_x and M_y go to zero for big applied fields, rather than ± 1. This is shown in Fig. 7.6 as the magenta line. Unlike in thermal equilibrium, the magnetization goes to zero for large magnetic field. The reason is that in the limit $|h_y| \to \infty$, the Zeeman term dominates the Hamiltonian, so that the eigenstates are simply the eigenstates of σ_y. The dissipation being in the orthogonal direction does not drive the system to the ground state, but rather destroys the coherence between the eigenstates. The resulting steady state is then the unit matrix, from which the zero magnetization follows.

For the special case of $J_x = J_y = J_z$ ($\gamma = 1$) the system of mean-field equations is analytically solvable without any approximations:

$$\begin{cases} M_x = -\dfrac{h_y}{\frac{1}{4} + 2\left(h_x^2 + h_y^2\right)}, \\ M_y = \dfrac{h_x}{\frac{1}{4} + 2\left(h_x^2 + h_y^2\right)}, \\ M_z = -\dfrac{1}{1 + 8\left(h_x^2 + h_y^2\right)}. \end{cases} \tag{7.19}$$

This is in agreement with the above result and is also true for small h_x and h_y. We can conclude that a large magnetic field will cause the system to have no magnetization at all.

Note the difference in sign between M_x and M_y in this special case. This sign difference implicates that we cannot interchange x and y without introducing a sign change. At first sight this might appear confusing because of the identical parameters $J_x = J_y = J_z$. Only the z-direction is fixed by the dissipation and so there appears to be no clear reason for a distinction between x and y. A closer look shows that one cannot interchange x and y because this changes the handedness of our coordinate system. This is reflected in the commutation relations of the Pauli matrices requiring that $\left[\hat{\sigma}^{(a)}, \hat{\sigma}^{(b)}\right] = 2i\epsilon_{abc}\hat{\sigma}^{(c)}$. To interchange $x \to y$ one could do $\hat{\sigma}^{(x)} \to \hat{\sigma}^{(x)}$ and $\hat{\sigma}^{(y)} \to -\hat{\sigma}^{(y)}$. This would however result in $\hat{\sigma}^{(z)} \to -\hat{\sigma}^{(z)}$ in order to satisfy the Pauli commutation relations. So x and y cannot be interchanged without changing the sign of z. This also results in the same coordinate system and thus no interchange was made in the end. As such there is no symmetry to transform x into y explaining why a sign difference can be present.

7.5 Angular averaged susceptibility

A divergence in the susceptibility indicates the existence of a phase transition. To calculate the susceptibility we use the scheme presented in [104] and as introduced in Sec. 5.4.4.

When we calculate the susceptibility tensor for different cluster and lattice sizes we find that $\chi_{xy} \neq \chi_{yx}$. This is strikingly different from the case of closed systems, where the susceptibility is found from the free energy F, $\chi_{xy} = \frac{\partial^2 F}{\partial h_x \partial h_y} = \frac{\partial^2 F}{\partial h_y \partial h_x} = \chi_{yx}$. We find this result even in the mean-field approximation. If we take the parameter values $J_x = J_y = J_z$ we find that $\chi_{xy} = -\chi_{yx}$ from (7.19). Numerical results show

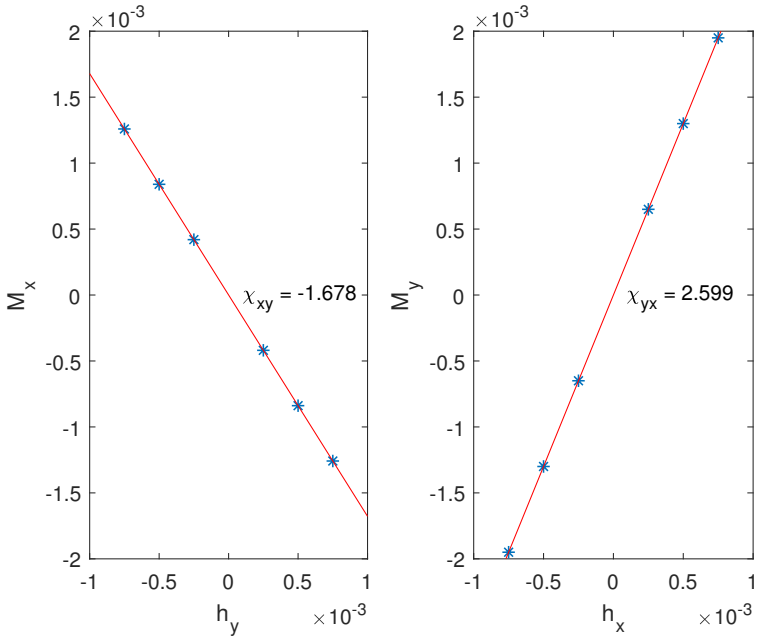

Figure 7.7: *(Color online) Exact solution of the magnetization (blue stars) of the system M_x in the x-direction (left panel) and M_y in the y-direction (right panel) under influence of a small magnetic field in respectively the y and x direction for a 3×3 lattice at coupling strength $J_y = 1.25\gamma$. This result is obtained through solving the master equation. The magnetization as function of the applied field is given by a linear function (red line), this means that $\chi_{\alpha\beta}$ is given by the slope of this linear function because of* (5.16)*. As is clear from both panels, χ_{xy} and χ_{yx} have different signs and furthermore we find that $|\chi_{xy}| \neq |\chi_{yx}|$.*

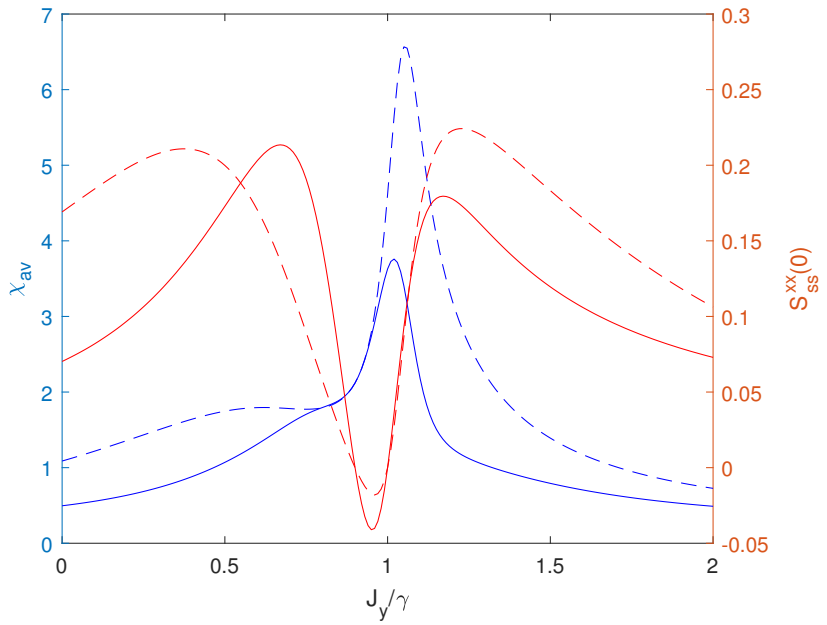

Figure 7.8: *(Color online) Exact solution of the average angular susceptibility (blue, two bottom lines) and steady-state spin structure factor (red, two top lines) of a 2x2 (full line) and 3x3 (dashed line) lattice as a function of J_y, obtained through solving the master equation. Both solutions show a 'shoulder' for $J_y < 0.9\gamma$. This shoulder could be a second peak in the susceptibility, masked by the higher peak on the right, suggesting a phase transition. The position of this peak corresponds to the non-zero region in the steady-state spin structure factor.*

that for general coupling parameters the magnitudes differ and in general we find $|\chi_{xy}| \neq |\chi_{yx}|$ and reciprocity is broken. This is shown in Fig. 7.7 by solving the master equation with an applied field for a 3×3 lattice at coupling strength $J_y = 1.25\gamma$. In closed quantum systems the existence of the free energy and the ability to interchange the partial derivatives imposes a symmetry on the system that need not be explicitly present in the system (e.g. a system where $J_x \neq J_y \neq J_z$). This result shows that the lack of a free energy in open quantum systems means no such symmetry is imposed.

Continuing our study of the phase diagram for the two-dimensional lattices we have two regions of interest. The earlier mentioned *right*-hand region, studied in [42, 44, 128], and secondly the *left*-hand region, discussed in section 7.3. In Fig. 7.8 the exact solution of the susceptibility for a 2×2 and 3×3 lattice is shown. They

were found by solving the master equation. Larger lattices are computationally not feasible and a more sophisticated method would have to be used, such as the Corner Space method [104], where the right-hand region of the susceptibility has been studied. The presence of a peak in the susceptibility could indicate a phase transition. Note the 'shoulder' which is present on the left side. This could indicate the presence of a second peak, partially masked by the higher peak on the right-hand side. These two peaks move away from each other when the lattice size is increased. The peak on the left however is not sharp and it remains to be seen whether it diverges for larger lattice sizes and whether a true phase transition is present. It should be noted that the positions of the shoulder do coincide with a sharp decrease of the steady-state spin structure factor. These findings show the possible presence of a phase transition which is completely missed when the quantum correlations are neglected. We also wish to remark that the study of the all-to-all connected model in chapter 5 does not show signs of such a transition. There, the ferromagnetic order (slowly) dissapears as the system size is increased, leading to a paramagnetic phase as predicted by mean-field theory. A study with bigger system sizes in two dimensions is thus needed to formulate a conclusive argument for its (non)existence.

7.6 Conclusions

We studied the dissipative XYZ Heisenberg model with the cluster-Gutzwiller Monte Carlo approach. This method allows for the inclusion of short-range quantum correlations as well as classical spatial correlations. Calculation of the steady-state spin structure factor shows the appearance of a ferromagnetic region and two paramagnetic regions also found in Ref. [44] and Ref. [128]. We show the possible existence of another ferromagnetic phase which is completely missed when quantum correlations are neglected. A calculation of the susceptibility tensor shows how reciprocity is broken, a feature not observed in closed quantum systems. Moreover, increasing the magnetic field suppresses the magnetization, this is also in contrast with closed quantum systems. We show that the inclusion of short-range quantum correlations causes the sharpening of the crossover between the ferromagnetic and paramagnetic region to occur for smaller lattice sizes. Even though short-range quantum correlations have a big impact on the phase diagram of the system it has to be noted that they only qualitatively match the exact results and long-range quantum correlations play an important role in the dynamics of

the system.

The results of this chapter were published in Ref. [1].

CHAPTER 8

Dynamical hysteresis properties of the driven-dissipative Bose-Hubbard model with a Gutzwiller Monte Carlo approach

In this chapter we will apply the (cluster-)Gutzwiller approach introduced in Sec. 7.2.2 to the driven-dissipative Bose-Hubbard model. We are specifically interested in the hystertic region predicted by a Gutzwiller mean-field treatment of the model [87] as can be seen in Fig. 3.4. The approach will allow us to go beyond the Gutzwiller approach for the density matrix, because the classical correlations in the system can be captured. It is intuitive that these classical correlations are important in the bistability region, because due to tunneling most of the time the cavities are all together in the low or the high particle number state. In finite systems, it is known that the bistability is destroyed by switching between the low and high photon number branches, which results in a smooth average photon number as function of pumping intensity. In the thermodynamic limit however, the switching time is expected to tend to infinity and true bistability to emerge. In order to access the steady-state predictions in the thermodynamic limit and for long times, we follow Ref. [82] and study the dynamical hysteresis and more specifically its scaling as a function of system size and sweeping velocity. We perform a study of the dynamical hysteresis, which includes its properties in the steady-state limit and a study of the compressibility and the correlation functions. Thereafter, we discuss the validity of a mapping of the driven-dissipative Bose Hubbard model onto a single cavity.

8.1 The Cluster-Gutzwiller Monte Carlo time evolution

The model Hamiltonian of the Bose-Hubbard model with nearest-neighbour hopping and a local Kerr non-linearity is given by (3.11). Dissipation is included through local (single) photon emissions, leading to a Lindblad master equation given by (3.12). The continuous measurement of these photon emissions once again allow us to treat the system with the (cluster)-Gutzwiller Monte Carlo approach. In between the detection of these quantum jumps the wave function will evolve according to

$$|\psi(t)\rangle = \frac{\exp\left(-i\hat{H}_{\mathrm{CGMC}}t\right)|\tilde{\psi}\rangle}{||\exp\left(-i\hat{H}_{\mathrm{CGMC}}t\right)|\tilde{\psi}\rangle||}, \tag{8.1}$$

with $\tilde{\psi}$ an initial (normalized) wave function. Note that the time evolution generated by

$$H_{\mathrm{CGMC}} = \sum_{C}\left[\hat{H}_C + \hat{H}_{\mathcal{B}(C)} - i\frac{\gamma}{2}\sum_{i\in C}\hat{a}_i^\dagger\hat{a}_i\right], \tag{8.2}$$

does not preserve the norm. In (8.2), $\hat{H}_C$ contains all local terms as well as the hopping terms with links inside the cluster C

$$\hat{H}_C = \sum_{i\in C}\left(-\Delta\hat{a}_i^\dagger\hat{a}_i + \frac{U}{2}\hat{a}_i^\dagger\hat{a}_i^\dagger\hat{a}_i\hat{a}_i + F\left(\hat{a}_i + \hat{a}_i^\dagger\right)\right) - \frac{J}{z}\sum_{\langle i,j\rangle|i,j\in C}\left(\hat{a}_i^\dagger\hat{a}_j + \hat{a}_j^\dagger\hat{a}_i\right), \tag{8.3}$$

and $\hat{H}_{\mathcal{B}(C)}$ contains the mean-field contributions of the nearest-neighbour links across the boundary $\mathcal{B}$ of the cluster C, that is

$$\hat{H}_{\mathcal{B}(C)} = -\frac{J}{z}\sum_{\langle i,j\rangle|i\in C, j\notin C}\left(\hat{a}_i^\dagger\langle\hat{a}_j\rangle + \hat{a}_i\langle\hat{a}_j^\dagger\rangle\right). \tag{8.4}$$

When an emitted photon is detected a quantum jump is made in the evolution of the wave function

$$|\psi(t)\rangle \to \frac{\hat{a}_i|\psi(t)\rangle}{||\hat{a}_i|\psi(t)\rangle||}, \tag{8.5}$$

after which the wave function continues evolving according to (8.1). This again corresponds to a system of coupled equations for the time evolution of each $|\psi_C\rangle$, similar to (7.12).

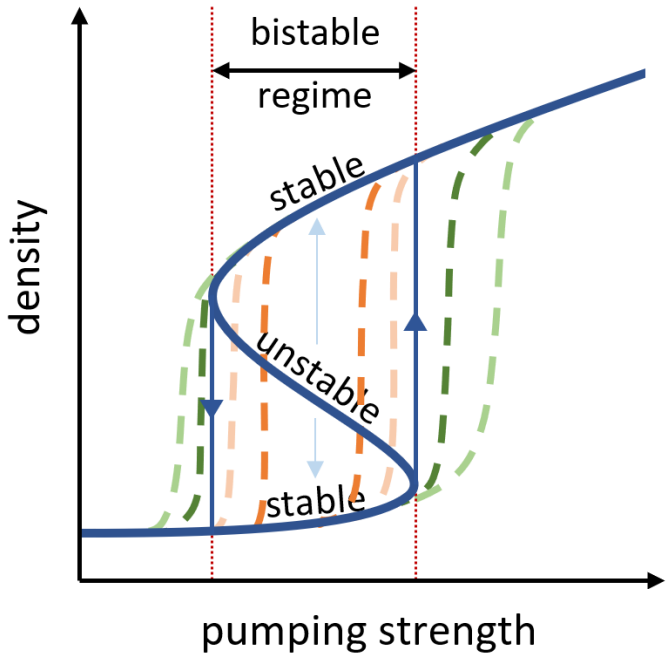

Figure 8.1: *(color online) Example of a bistable region in the driven-dissipative Bose-Hubbard model. There exist two stable branches and one unstable branch, which are the stable and unstable solutions of the mean-field approximation, shown as the blue line. The blue arrows indicates where the system undergoes a first-order phase transition in the steady-state limit, depending on which branch it was on. The two blue arrows mark the boundaries of the bistable regime. The light blue arrow indicates that deviations away from the stable solutions will quickly evolve back to these stable solutions. The dashed light green line shows the dynamical hysteresis curve for a finite sweeping velocity, the dashed dark green line shows the dynamical hysteresis curve for a sweeping velocity which was decreased with respect to the one of the light green dashed line. Similarly, the dashed orange lines show the dynamical hysteresis curves when fluctuations are taken into account, i.e. beyond mean-field, and switching between the branches is possible.*

8.1.1 Bistabile regime and its dynamical properties

The mean-field equation of the driven-dissipative Bose Hubbard model, consisting of using a Gutzwiller factorized ansatz for the density matrix to solve the master equation, predicts bistable behaviour for certain parameter regimes [87]. The bistable region is a region where the system has two stable states and one unstable state, as shown by the blue line on Fig. 8.1. Deviations from these stable states quickly cause the system to evolve back to one of these two stable solutions. As such, when the system resides on one of the two stable branches it also stays on this branch. Say the system resides on the bottom stable branch of Fig. 8.1 and the pumping strength is increased across the right boundary of the bistable regime, then the system only has one stable solution, being the top branch, instead of two. The system switches to this new state through a jump, marking a first-order phase transition. If one then decreases the pumping strength the system does not jump back to the lower branch but instead stays on the stable top branch. That is, until the pumping strength crosses the left boundary of the bistable regime and jumps back to the lower stable branch, again marking a first-order phase transition. This is called hysteresis and is characteristic for a first order phase transition.

The above is true for an infinitely slow sweep of the pumping strength, which gives information on the steady-state properties. However, instead of using an infinitely slow sweeping velocity to study the steady-state properties one can also study dynamical properties by resorting to a finite sweeping velocity. The faster one sweeps, the less time the system has to adapt to the new pumping strength. This allows the system to reside longer on its previously stable branch before it jumps to its new stable branch. This behaviour is shown on Fig. 8.1 where the dashed dark green line shows the behaviour for a finite sweeping velocity. The dashed light green line shows what is expected to happen when one increases the sweeping velocity with respect to the one of the dashed dark green line.

Another effect is observed when one allows fluctuations in the system. When these fluctuations are large enough it becomes possible for the system to jump to the other stable branch. As shown on Fig. 8.1 this happens most easily close to the boundaries of the hysteresis curve, since small fluctuations can already drive the system's state into a region where it quickly converges to the other stable state. This behavior is shown as the dashed dark and light orange lines, where the sweeping velocity is faster in the latter one. When the sweeping velocity decreases the system is able to jump to the top (bottom) branch for lower (larger)

values of the pumping strength since the system has a longer time to switch between the stable states. This naturally decreases the hysteretic region [82]. The influence of fluctuations then leads to the disappearance of the hysteretic region in the long-time limit in finite-size systems. Only in the thermodynamic limit it is possible for the hysteretic region to survive. This follows from the fact that as the system gets bigger, it becomes harder for fluctuations to make the entire system switch to the other branch.

Both the green and orange dashed lines show dynamical hysteresis curves. By studying them we gain information on the dynamical properties of the system. It is worth noting that it is hard to determine the dynamical hysteresis region, i.e. the pumping strength interval in which the system shows hysteretic behaviour. To avoid the usage of arbitrary definitions we study the hystertic surface defined as [82]

$$S_h = \int_{F_{start}}^{F_{end}} \left(n_\uparrow(F) - n_\downarrow(F)\right) dF, \tag{8.6}$$

which is the surface between the top ($n_\uparrow$) and bottom ($n_\downarrow$) branch of the hystertic curve of the single cavity particle number $\langle \hat{n} \rangle = \frac{1}{N} \langle \sum_i \hat{a}_i^\dagger \hat{a}_i \rangle$, with N the number of cavities in the lattice. F_{start} and F_{end} are chosen in such a way that the entire hystertic surface is enclosed.

The behaviour described above can also be found in the well studied and exactly solvable single cavity [149] in the thermodynamic limit where the photon number tends to infinity while the nonlinearity simultaneously tends to zero. The thermodynamic limit is important here, because otherwise quantum fluctuations cause switching between the two branches, washing out the hysteretic behavior. In the Gutzwiller mean-field solution of the Bose-Hubbard model, the thermodynamic limit is implicit because the equations of motion remain unaltered when the number of sites is increased, hence true bistable behavior is always present in this approximation. When classical and quantum fluctuations are included in the description of a finite-size driven-dissipative Bose-Hubbard model, this system can also switch between both branches. Incorporating them through the trajectory method and the cluster-Gutzwiller wave function ansatz is therefore expected to give drastic changes in the hysteretic surface, especially in the region where the transitions are expected to happen.

8.2 Dynamical hysteresis

In order to quantify the role of fluctuations in the driven-dissipative Bose-Hubbard model, we start by analyzing the dynamical hysteresis surface. If it tends to a zero value in the limit where the sweep time goes to infinity and in the thermodynamic limit of infinite system size, the system has no hysteretic phase transition. If on the other hand, the hysteretic surface tends to a nonzero value when sweeping slower and slower, even when the system size diverges, the system has a true hysteretic phase transition. In other words, in the thermodynamic limit and for the sweeping velocity tending to zero there are two possibilities: (i) the hysteresis surface disappears, resulting in a single curve which is the long-time limit average between both stable branches, i.e. there is one steady-state solution and (ii) the hysteresis surface converges to a finite value, meaning that when the system resides on one of both branches it will never jump to the other one, i.e. there exist two steady-state solutions.

In the following we perform a linear sweep in pumping strength, that is

$$\begin{aligned} F(t) = &\left(F_{start} + v_s t\right) \theta\left(t < \frac{t_s}{2}\right) \\ &+ \left(F_{end} - v_s\left(t - \frac{t_s}{2}\right)\right) \theta\left(t \geq \frac{t_s}{2}\right), \end{aligned} \tag{8.7}$$

with t_s the total sweep time and $v_s = \frac{2(F_{end} - F_{start})}{t_s}$ the sweep velocity. Throughout this chapter we work in the following parameter regime, unless specified otherwise: the relation between the Kerr non-linearity and dissipation rate is chosen as $\frac{U}{\gamma} = 20$ and the laser frequency is tuned to the 4-photon resonance $1 + \frac{2\Delta}{U} = 4$. The coupling parameter is $\frac{J}{U} = 0.5$. In each lattice we impose periodic boundary conditions. Note that in this parameter region a hysteretic region is predicted in the mean-field approximation [87]. The hysteresis surface will be calculated over F/U rather than F and the initial state of the system for each trajectory is given by a lattice of unoccupied cavities.

On Fig. 8.2 (a) we show hysteretic curves of the average single cavity particle number $\langle \hat{n} \rangle$ for various system sizes with an inverse sweeping velocity of $v_s^{-1}\gamma^2 = 25$. As the system size increases, so does the surface of the hysteresis curves. This coincides with the expectations from the previous section. Interestingly, it appears that the system does not converge to the mean-field hysteretic surface in the thermodynamic limit. This appears to be due to a large importance of fluctuations on the left side of the bistable region, where a big difference is present for the

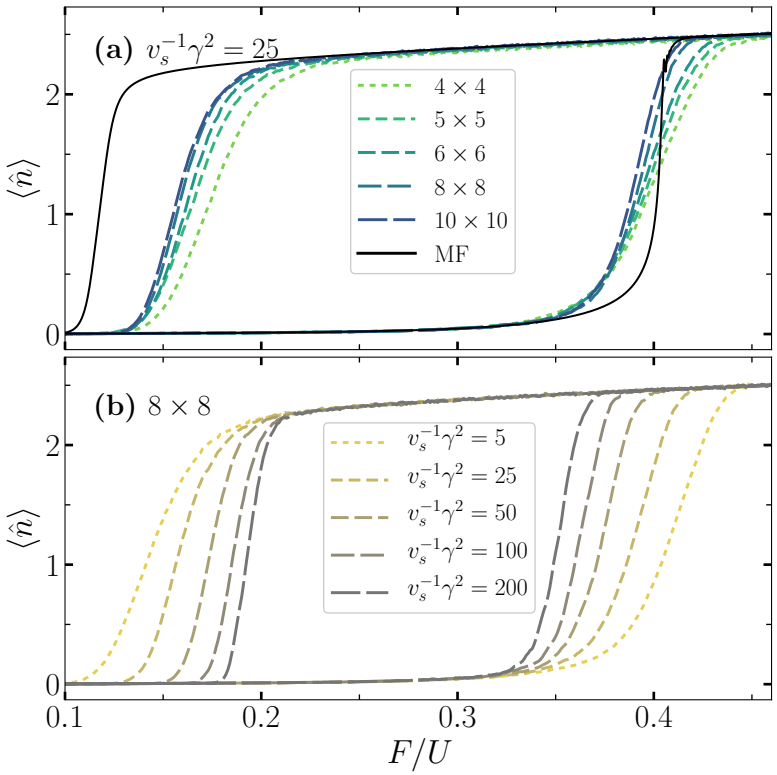

FIGURE 8.2: *(Color online)* ***(a)*** *Hysteresis curves of the single cavity particle number* $\langle \hat{n} \rangle$ *for various system sizes (dashed lines) at sweeping velocity* $v_s^{-1}\gamma^2 = 25$ *and the mean-field (MF) result (full black line) (and* $N_{tr}N \approx 10000$*, with* N_{tr} *the number of trajectories, and the cavity Hilbert size cutoff* $N_{Max} = 7$*).* ***(b)*** *Hysteresis curves of the single cavity particle number* $\langle \hat{n} \rangle$ *for various sweeping velocities for an* 8×8 *lattice of cavities (and* $N_{tr}N \approx 10000$*,* $N_{Max} = 7$*).*

transition from the top branch to the bottom branch with respect to the mean-field prediction. All values for the particle number, not including the ones near the transitions, are however in good agreement with the mean-field results.

On Fig. 8.2 (b) the hysteretic surface of a 8×8 lattice of cavities is shown for various sweeping velocities. As the sweeping velocities are decreased, i.e. the sweeping time is increased, the hysteretic surface decreases. This is according to the discussion in section 8.1.1.

For the example of the 8×8 lattice of cavities the hysteretic surface is still shrinking as the sweeping velocities are decreased. This continued decrease not only causes the system to move even further away from the mean-field hysteresis

surface but also questions whether it will converge to a finite value (ii) or not (i). We perform a more detailed study of the long-time limit in the following section in combination with a finite-size scaling in order to approach the thermodynamic limit. However, it has to be noted that the previous results give a first indication that through the inclusion of classical correlations the mean-field phase diagram will be qualitatively correct but quantitative differences are expected in the regions where these correlations and fluctuations become increasingly important, i.e. near the phase transition.

8.2.1 Steady-state and thermodynamic limit

Besides studying the long-time limit, i.e. the steady-state, we are also interested in the system's behaviour in the thermodynamic limit. Indeed, phase transitions are only well-defined in the thermodynamic limit and if we wish to compare our results to the steady-state mean-field phase diagram found in Ref. [87] we need to perform a finite-size scaling to gain access to this infinite-cavity limit. In Fig. 8.3 (a) we show the behaviour of the hysteretic surface of various 2D square lattices as a function of the sweeping velocities for a Gutzwiller ansatz of the wave function, i.e. cluster size one (full lines with circle markers), and a cluster wave function with clusters of size 1×2 (full lines with cross markers) with respect to the mean-field result (full black line), at $J/U = 0.5$. Note again that as the sweeping velocity is decreased the size of the hysteresis surface increasingly deviates from the mean-field result. Even as the thermodynamic limit is approached this is not expected to converge, since the results of the 6×6 and 8×8 lattices are already practically identical.

By performing a power law fit of the form $S_h = \beta(v_s^{-1})^{-\alpha}$, we can now determine the behaviour in the long-time limit and thus determine whether the hysteretic surface disappears due to the presence of classical (and quantum) fluctuations. For the observed parameter regime and finite system sizes the extrapolation of the hysteretic surface disappears in the limit of infinite sweeping time. However, it is worth noting that by increasing the system size the exponent of the power law decreases. The question then remains whether the exponent of this power law remains finite in the thermodynamic limit. If it were to become zero we can expect a finite hysteresis surface, i.e. there exists a parameter region where the system shows bistable behaviour in the long-time thermodynamic limit. The scaling of this exponent in the limit of infinite system size is shown as the dashed line with circle markers in Fig. 8.3 (c) . For the observed parameter regime we indeed see a

convergence to a non-zero exponent and thus marking the disappearance of the hysteretic region under the influence of classical fluctuations.

Furthermore, if we include short-range quantum correlations in the form of 1×2 clusters, on top of the classical correlations and on-site quantum correlations this behaviour becomes even more pronounced. This can easily be seen on Fig. 8.3 (a) where we show the hysteretic surface for 1×2 clusters on a 4×4 and 8×8 lattice (full lines with cross markers). The inclusion of these short-range quantum correlations causes a further decrease of the hysteresis surface. Moreover, as shown on Fig. 8.3 (c) there is also an increase in the magnitude of the exponent, signalling a faster convergence to a zero hysteretic surface in the thermodynamic limit. It is worth noting that the hysteresis surface exhibits a slow convergence to the power law in the long-time limit, i.e. one needs to simulate trajectories over a long time to obtain the asymptotic behavior. This could lead to (small) corrections on the power law exponents derived here. Additionally, we point out that the curves of the hysteresis surface display two power laws, the one studied in the long-time limit on Fig. 8.3 (c), but also the one in the short-time limit. The former is linked to the influence of fluctuations on the system, the latter is linked to the mean field response of the system to the changing pumping strength. Such double power law behavior is also found in experimental and theoretical studies of the single-cavity Bose Hubbard model [82, 116, 218].

Our results are in contrast with the mean-field phase diagram from Ref. [87] where a hysteretic region is predicted at $J/U = 0.5$. Fig. 8.3 indicates that the critical point in the hopping amplitude, where the system switches from a smooth crossover to a hysteretic crossover as the pumping strength is increased, shifts to higher values of J/U. This shift is expected to be larger as (longer-range) quantum correlations are included. To investigate more closely the (non)dissapearance of the hysteresis surface as a function of J/U we show Fig. 8.3 (b) where we calculated the hysteretic surface as a function of the sweeping velocity for various system sizes for $J/U = 2$, i.e. roughly an order of magnitude larger than the critical point in the mean-field study (where $J_c/U \approx 0,18$). We indeed see a decrease in steepness of the power law fits and the dashed line with triangle markers on Fig. 8.3 (c) show us that by increasing J/U the exponent has decreased and is approaching zero. From this result we argue that a new (and larger) critical point J_c/U exists where this exponent becomes equal to zero and thus predicts a hysteretic regime. However, a closer study of the region around J_c/U would be needed to pinpoint the exact location of the onset of the hysteretic regime and the nature of the critical

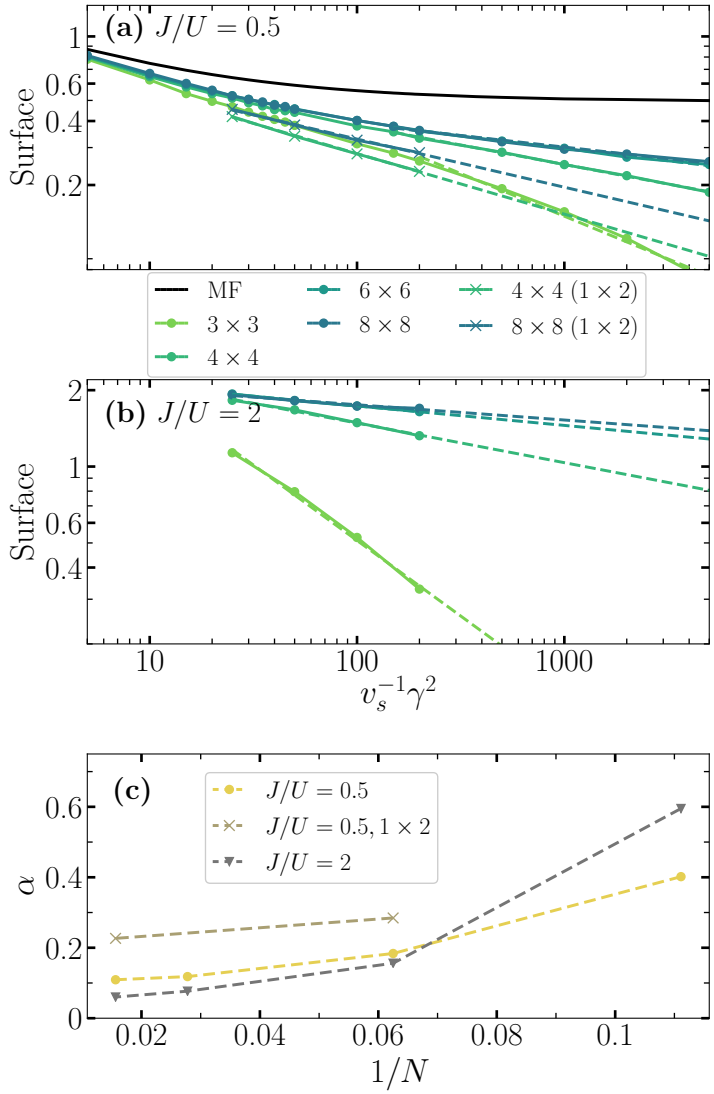

Figure 8.3: *(Color online)* **(a)** *[Top Panel] ($J/U = 0.5$) Hysteresis surface for various system sizes at different sweeping velocities for 1×1 ($N_{tr}N \approx 10000$, $N_{Max} = 7$ and $N_{tr} \approx 100 - 500$ when $v_s^{-1}\gamma^2 > 200$) and 1×2 clusters ($N_{tr}N \approx 5000$, $N_{Max} = 7$). The dashed lines are power law fits of the form $S_h = \beta(v_s^{-1}\gamma^2)^{-\alpha}$ in the long time limit.* **(b)** *[Middle Panel] ($J/U = 2$) Hysteresis surface for various system sizes at different sweeping velocities for 1×1 clusters ($min(N_{tr}N) \approx 5000$ and $max(N_{tr}N) \approx 20000$, $N_{Max} = 11$). The dashed lines are again power law fits in the long time limit.* **(c)** *[Bottom Panel] Exponent α of the power law fit $S_h = \beta(v_s^{-1}\gamma^2)^{-\alpha}$ for 1×1 clusters at $J/U = 0.5, 2$ and for 1×2 at $J/U = 0.5$.*

point.

We note that in order to obtain a nonzero hysteretic surface one first needs to take the thermodynamic limit before taking the long-time limit. We wish to point out that this observation is in agreement with a study performed in a, related, dissipative spin system in Ref. [108] where an MPO approach was used.

8.2.2 The compressibility

So far we have studied the surface of the hysteresis curve and indicated deviating behaviour with respect to the mean-field method as a result of incorporating fluctuations. We will now explicitly study these particle number fluctuations through the compressibility, that is defined as [87, 146]

$$\begin{aligned} K = \frac{\langle \hat{N}^2 \rangle - \langle \hat{N} \rangle^2}{\langle \hat{N} \rangle} &= 1 - \langle \hat{N} \rangle + \frac{1}{\langle \hat{N} \rangle} \langle \sum_{i,j} \hat{a}_i^\dagger \hat{a}_j^\dagger \hat{a}_i \hat{a}_j \rangle \\ &= 1 + \langle \hat{N} \rangle \Big[\sum_{i,j} g_{ij}^{(2)} - 1 \Big], \end{aligned} \tag{8.8}$$

with $\hat{N} = \sum_i \hat{a}_i^\dagger \hat{a}_i$ and $g_{ij}^{(2)} = \frac{\langle \hat{a}_i^\dagger \hat{a}_j^\dagger \hat{a}_i \hat{a}_j \rangle}{\langle \hat{N} \rangle^2}$. Note that for the Gutzwiller mean-field this reduces to $K = 1 + n \left(g_{ii}^{(2)} - 1 \right)$, with n the single site particle number.

On Fig. 8.4 (a) the particle number $\langle \hat{n} \rangle$ (full red line) and compressibility K (full brown line) of a 6×6 lattice are shown as well as the mean-field compressibility (full black line), both for a sweeping velocity of $v_s^{-1} \gamma^2 = 25$. We confirm that the transitions are accompanied by a presence of high fluctuations which peak at (or close to) the transition. Such a peak can also be observed from the mean-field result albeit with a strikingly lower amount of fluctuations. This discrepancy was expected as the trajectory method allows for jumps between the stable branches, a feature not included in the mean-field method. As our simulations show, this increase in compressibility can be of the order of a magnitude.

Similar to our observations in Fig. 8.2 (a), the positions of the maxima of the peaks are also shifted with respect to the mean-field results; at the transition from high to low particle number the mean-field maximum is also found for lower values of F/U. The position of the transition from low to high particle number is also similar for both methods. Away from the transition, the results for the compressibility coincide with the mean-field results and deviations only arise close to the transition. We have noted before that as the system size increases, it becomes harder for the entire system to switch to the other branch. As a result

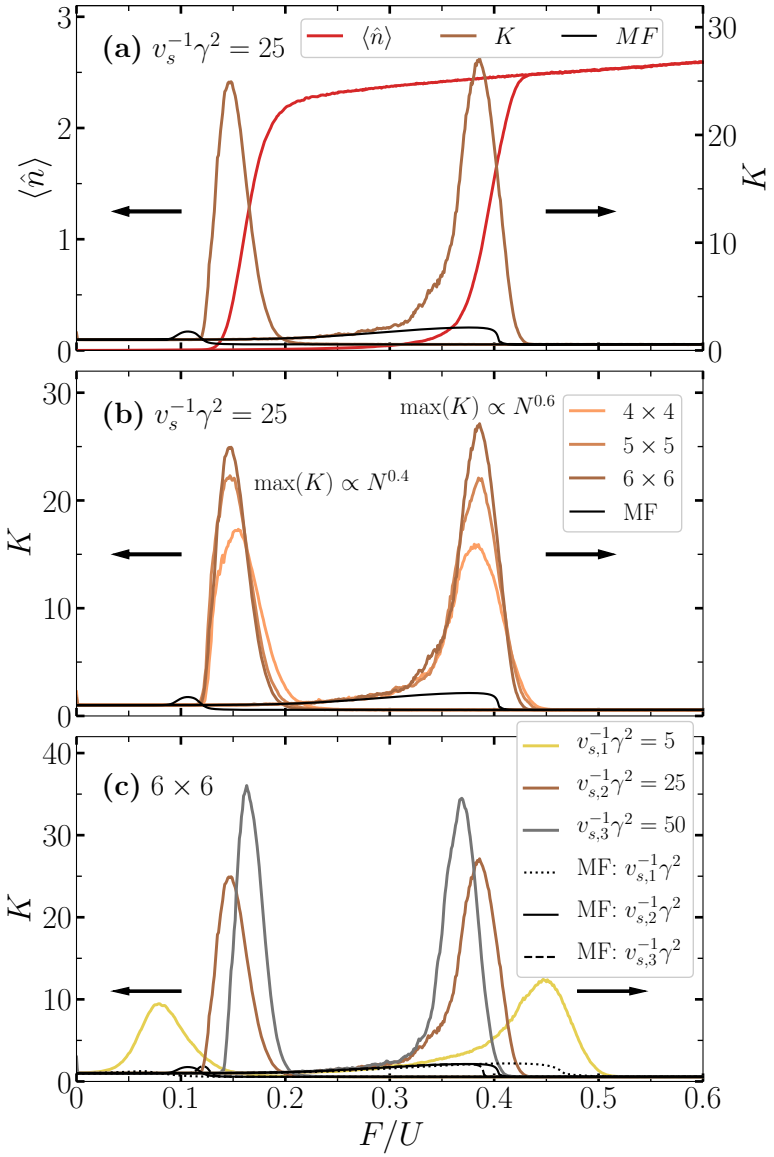

Figure 8.4: *(Color online)* ***(a)*** *Hystersis curve of the particle number per site and compressibility on a* 6×6 *lattice at sweeping velocity* $v_s^{-1}\gamma^2 = 25$ *(*$N_{tr}N \approx 25000$*,* $N_{Max} = 8$*). The mean-field (MF) compressibility is shown as a full black line.* ***(b)*** *Compressibility for various system sizes at a sweeping velocity of* $v_s^{-1}\gamma^2 = 25$ *(*$N_{tr}N \approx 25000$*,* $N_{Max} = 8$*). The mean-field (MF) compressibility is shown as a full black line. The power law fits are performed on the maxima of the compressibility of lattices of dimension* 5×5 *to* 8×8 *(not shown).* ***(c)*** *Compressibility of a* 6×6 *lattice for various for various sweeping velocities (*$N_{tr}N \approx 25000$ *and* $N_{tr}N \approx 40000$ *for* $v_s^{-1}\gamma^2 = 50$*,* $N_{Max} = 8$*). The mean-field (MF) compressibility for the various sweeping velocities are shown as black lines.*

overall higher fluctuations would be needed for a phase transition to occur in the system. This is indeed what we observe in Fig. 8.4 (b) where we show the compressibility for various system sizes at a sweeping velocity of $v_s^{-1}\gamma^2 = 25$. As the system size increases the fluctuations also increase. This is expected since the numerator of (8.8) is quadratic in $\hat{N}$ with respect to the denominator. Through a finite-size scaling we find a sub-extensive power-law scaling with system size of the maxima of both the left and right peaks, of which the exponents are respectively $0,4$ and $0,6$. This sub-extensive scaling is explained by the formation of domains when the system switches to another branch.

Additionally, we can study the behaviour of the compressibility for various sweeping velocities. We show the results of a 6×6 lattice on Fig. 8.4 (c). When a fast sweep (full yellow line) is performed, i.e. a high sweeping velocity, the system is driven through the hysteresis region at a very fast pace. The system thus does not have a lot of time to jump between the branches, but it does need to adapt its state very quickly to the new parameter values. This results in fluctuations which are smeared out, explaining the broader, but lower, peaks for high sweeping velocities. This effect decreases as the system gains more time to adapt to the sweeping parameter (full brown and gray line), resulting in narrower and taller peaks. The increased height of the peaks is due to the increased time the system has to jump between the branches, resulting in more fluctuations. This also means the system will be able to jump to the other branch at smaller (bigger) values for F/U when it is on the bottom (top) branch, which is why the peaks move towards each other as the sweeping velocity is decreased. This is in accordance with the shrinking hysteresis surface observed in the previous section.

The effect of including short-range quantum correlations is shown on Fig. 8.5 (a) for 1×2 and 1×3 clusters for a 6×6 lattice at sweeping velocity $v_s^{-1}\gamma^2 = 25$. There is no drastic change in the amount of fluctuations under the influence of the 1×2 clusters, however, they do cause a shift in the position of the transition. When we go one step further in the range of the quantum correlations, i.e. 1×3 clusters, no significant further shift is observed. This is an interesting result as it shows that already for small cluster sizes, the systems properties do not change significantly as longer-range quantum correlations are included, i.e. long-range quantum correlations are expected to be less important than in the case of the XYZ model in the previous chapter. In other words, by including only short-range quantum correlations, and thus modest computational resources, one can drastically increase the effectiveness of the Gutzwiller approximation.

8.2.3 The correlation function

The calculation of the compressibility required knowledge of the pair-correlation functions $g_{ij}^{(2)}$. We show the results for the correlation functions as a function of the distance $d = |\mathbf{i} - \mathbf{j}|$ for various parameters of F/U left, right and exactly on the maximum of the compressibility peak of the bottom and top branch on Fig. 8.5 (b) and Fig. 8.5 (c), respectively. For both branches we note that the system shows no off-site correlations in the regions left and right of the maximum in the compressibility. This explains the success of the mean-field approximation in this region. The on-site bunching in the low-particle number phase (F_l/U) and on the maximum is due to the 4-photon resonance. We also find slight on-site antibunching in the high-particle number phase. These results are in accordance with the mean-field theory and a self-consistent expansion in the inverse coordination number of the lattice [146]. We do find deviations for the off-site correlations at the peak of the compressibility, i.e. near the transition. Our method is able to capture the classical long-range correlations in the lattice, which are expected at the transition, and are missed by mean-field theory. It is due to these correlations that we see a big increase in the compressibility with respect to the mean-field theory.

As noted before, the influence of short-range quantum correlations is most pronounced at the transition from high particle number to low particle number, as can be seen on Fig. 8.5 (c) in the dashed lines with circle markers. We note a decrease in correlations with respect to the Gutzwiller wave function ansatz, but long-range correlations are still present. This decrease in correlations is responsible for the slightly lower maximum of the compressibility for the cluster simulations in Fig. 8.5 (a).

8.3 Mapping of the Bose-Hubbard model onto a single Kerr cavity

There exists a mapping of the Bose-Hubbard model with nearest-neighbour hopping (3.11) on the single Kerr cavity [85]. The mapping is realized by Fourier transforming the annihilation operator, that is

$$\hat{a}_i = \frac{1}{\sqrt{N}} \sum_k e^{ikx_i} \hat{a}_k, \tag{8.9}$$

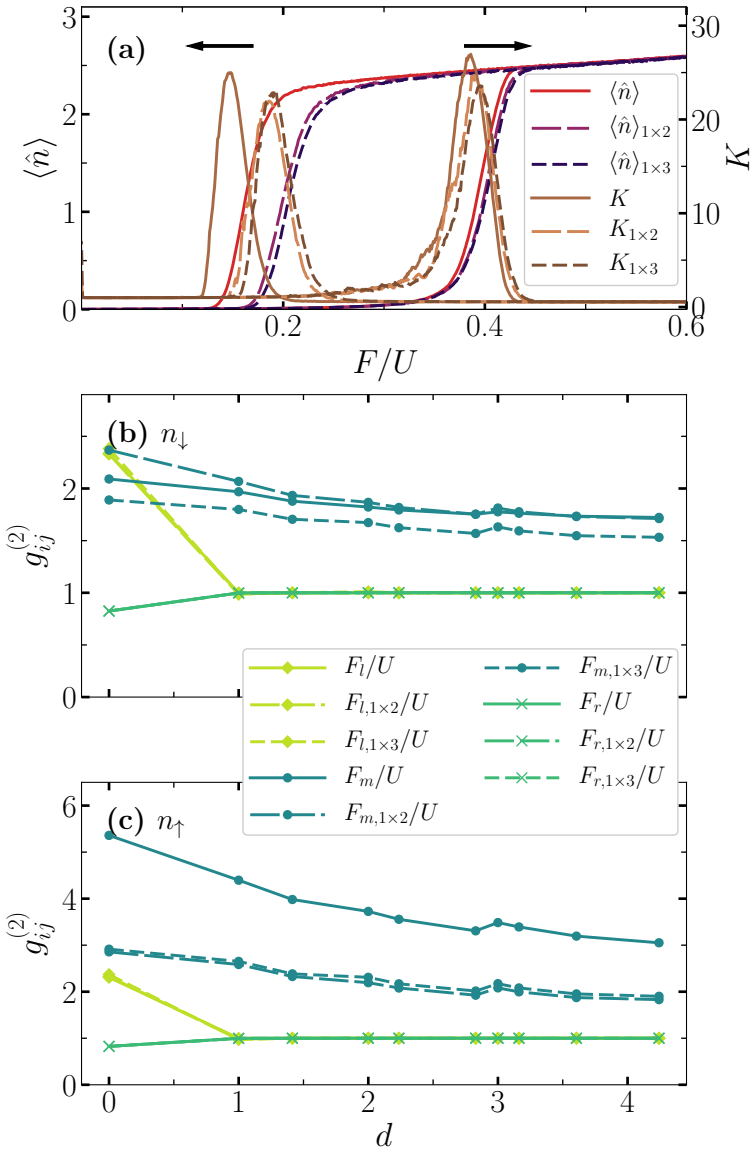

Figure 8.5: *(Color online)* ***(a)*** *Hystersis curve of the particle number per site and compressibility for various cluster sizes on a* 6×6 *lattice at sweeping velocity* $v_s^{-1}\gamma^2 = 25$ *(*$N_{tr}N \approx 25000$*,* $N_{Max} = 8$ *and* $N_{Max} = 9$ *for* 1×3 *clusters)).* ***(b)*** *Correlation function for various distances of the bottom branch for the* 6×6 *lattice of panel (a) with* $F_l/U = 0.05$*,* $F_r/U = 0.5$ *and* F_m/U *on the respective peaks of the compressibility in panel (a).* ***(c)*** *Correlation function for various distances of the bottom branch for the* 6×6 *lattice of panel (a).*

with x_i the spatial coordinates of cavity i. By substituting this in (3.11) one gets the equivalent Hamiltonian

$$\begin{aligned} H = &-\frac{J}{N}\sum_{\langle i,j\rangle}\sum_{k} 2\cos\left(kd_{ij}\right)\hat{a}_k^\dagger\hat{a}_k - \Delta\sum_k \hat{a}_k^\dagger\hat{a}_k \\ &+ \frac{F}{\sqrt{N}}\sum_i\sum_k\left(e^{-ikx_i}\hat{a}_k^\dagger + e^{ikx_i}\hat{a}_k\right) \\ &+ \frac{U}{2N}\sum_{k_1,k_2,k_3}\hat{a}_{k_1}^\dagger\hat{a}_{k_2}^\dagger\hat{a}_{k_3}\hat{a}_{k_1+k_2-k_3}, \end{aligned} \tag{8.10}$$

with $d_{ij} = |x_i - x_j|$. The main assumption that is made to map this onto a single Kerr cavity is the following. If one applies a homogeneous drive, only the $k = 0$ mode will be populated. The assumption is then that no nonlinear scatterings will be present and as a result none of the other modes will be populated. This allows all terms $k \neq 0$ in (8.10) to be neglected. This results in the following single Kerr cavity Hamiltonian

$$H = \omega_0\hat{a}_0^\dagger\hat{a}_0 + F_{eff}\left(\hat{a}_0^\dagger + \hat{a}_0\right) + \frac{U_{eff}}{2}\hat{a}_0^\dagger\hat{a}_0^\dagger\hat{a}_0\hat{a}_0, \tag{8.11}$$

where $\omega_0 = -\Delta - JZ$, $F_{eff} = F\sqrt{N}$ and $U_{eff} = \frac{U}{N}$. This is an interesting mapping because it can be used to study the thermodynamic limit of (3.11) by tuning $F_{eff} \to \infty$ and $U_{eff} \to 0$, keeping the product $U_{eff}F_{eff}^2$ constant. However, neglecting the nonlinear scatterings could make the above mapping invalid in certain parameter regimes. To study its validity we look again at the correlation function. In Fig. 8.6, we illustrate schematically the behavior of the correlation function in the $k = 0$ (red dashed line) and mean-field approximations (blue line). In the $k = 0$ approximation, all cavities are perfectly correlated, such that $g^{(2)}$ is flat. In the mean-field approximation on the other hand, correlations are entirely neglected, such that $g^{(2)} = 1$ for $d \neq 0$. For pump intensities far from the transition, Fig. 8.5 shows that the correlation function is close to one for $i \neq j$. This is consistent with the good agreement with the mean-field theory in this parameter regime. For the correlation function on the upper branch (F_r in Fig. 8.5 (c)), the correlation function is very flat, such that it is also compatible with the $k = 0$ model. This is however not the case in the low intensity (F_l) case. In the transition region, we have already seen that the mean-field approximation breaks down. Unfortunately, the correlation functions at F_m in Fig. 8.5 (b) are also not constant, such that neither the $k = 0$ is valid in the transition region. Physically, this is

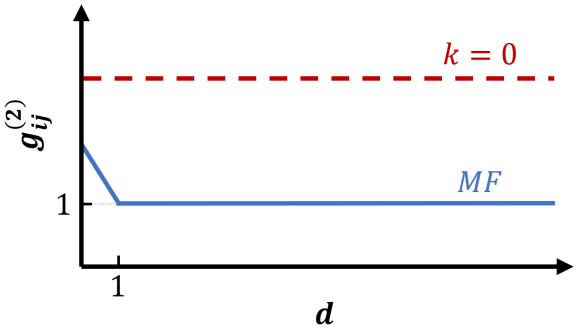

Figure 8.6: *(Color online) A qualitative visualisation of the correlation function for the mean-field method (blue line) and the mapping to the $k = 0$ mode (red dashed line).*

due to the formation of domains of high and low intensity in the switching region, which goes beyond the assumptions of the $k = 0$ model.

8.4 Conclusions

We have shown that by using the cluster-Gutzwiller Monte Carlo method, and thus the incorporation of classical correlations and short-range quantum correlations, the Gutzwiller mean-field phase diagram is qualitatively correct. The influence of the included fluctuations causes the critical hopping parameter J_c/U, indicating where the steep crossover of the system transforms into a first-order hysteretic phase transition, to shift to higher values. From the study of the particle number fluctuations we can conclude that away from the transition the results fall onto the mean-field results, also when close-range quantum correlations are included. This is confirmed by the absence of off-site correlations in these regimes, explaining the success of the mean-field method. At the transition we note a drastic increase in the particle number fluctuations, by an order of magnitude, with respect to the mean-field result. This increase finds it origin in the off-site correlations that are included through our method, and which are absent in mean-field theory. Additionally, a shift in the location of the transition from high to low particle number is also observed. This shift does not change significantly when more short-range quantum correlations are included, signalling that long-range quantum correlations are expected to be less important. We thus show that by a modest increase in computational resources the effectiveness of the approximation can be drastically improved. Finally, we show that care has to be taken when performing the mapping of an

extended Bose-Hubbard lattice onto a single Kerr cavity, especially in the proximity of a phase transition, i.e. regions where fluctuations and correlations are important.

The results of this chapter were published in Ref. [3].

PART

IV

LIOUVILLIAN DIAGONALIZATION

CHAPTER 9

Re-visiting Liouvillian diagonalization

The determination of the steady state and of the Liouvillian spectrum associated with a Lindblad master equation is a central and recurring problem in the study of open quantum systems. While the steady state describes the average physics of an open system once all the transient process have faded out, the spectrum gives access to the transient dynamics and to the states involved in it. The determination of the steady state often relies on the time evolution of a density matrix, while the spectral determination requires the diagonalization of the Liouvillian superoperator. Here, we propose a new method to efficiently obtain the Liouvillian spectrum and the steady state from short time evolution of a density matrix. The advantage of our method is twofold: (i) It provides an easy method that efficiently produces the steady state (shorter simulation time); (ii) It allows a complete understanding of the low-lying spectral properties of the Liouvillian without an additional computational cost. This method lends itself to the study of large systems, where the determination of the Liouvillian spectrum can be numerically demanding. Furthermore, it was applied in chapter 6 to calculate the low-lying spectrum of Liouvillians with dimensions up to the order of one million. Our results can be extended to generic time evolution methods, allowing to describe the long-lasting processes with a short dynamical evolution.

9.1 The reduced Liouvillian method and Krilov time evolution

As we discussed, knowing the Liouvillian eigenvalues and eigenmatrices allows a complete determination of the dynamics of an open quantum system. In many applications, however, one is not interested in characterizing all the possible processes which may take place in an open quantum system, but rather those

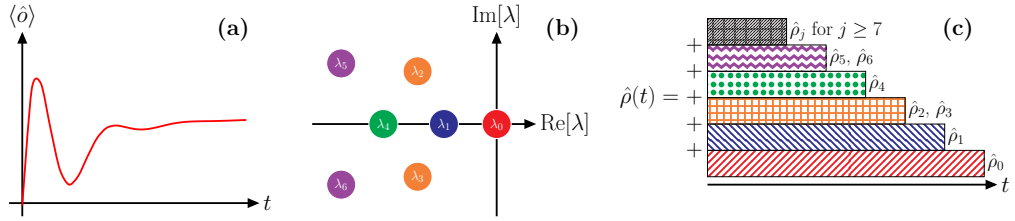

Figure 9.1: *Pictorial representation of the physical meaning of the time evolution of a density matrix from a spectral point of view. (a) The dynamics of a system governed by a Lindblad master equation has always some common characteristics. Indeed, after an initial transient dynamics, the system straightforwardly converges to its steady state. (b) These characteristics are clear from a Liouvillian spectrum point of view. Except from the steady state $\hat{\rho}_0$ characterized by $\lambda_0 = 0$, the eigenvalues characterizing the Liouvillian eigenmatrices have always negative real part (they describe decaying processes towards the steady-state) and they always appear as complex conjugate (they preserve the Hermiticity of a density matrix). (c) This translate in a specific form of the density matrix along its evolution. While at the beginning all the density matrices are relevant, as time passes the influence of the eigenmatrices $\hat{\rho}_j$ whose eigenvalues λ_j have large negative real part can be neglected from the dynamics. However, the slow-decaying eigenmatrices are always present in the dynamics.*

associated with the slow-decaying eigenstates of the Liouvillian superoperator.

In the following, we will introduce a new method capable of combining the exactness of the Liouvillian diagonalization, with the efficiency of time evolution of $\hat{\rho}(t)$. We will show that it is possible to construct a reduced Liouvillian allowing to obtain an extremely precise estimation of $\hat{\rho}_{\text{ss}}$ and $\hat{\rho}_i$ from short time evolutions of the density matrix. In other words, our method combines the advantages of both the time evolution methods and those of the Liouvillian diagonalization, being only partially affected by their disadvantages.

9.1.1 General idea behind the algorithm and its physical meaning

The main idea of the algorithm is to use the information encoded in the time evolution to efficiently reconstruct the spectrum of the Liouvillian. It is clear that, knowing the Liouvillian spectrum, it is possible to determine the time evolution of an open quantum system (Fig. 9.1). Using the spectrum of the Liouvillian we can

express the initial state as

$$\hat{\rho}(t=0) = \hat{\rho}_{\text{ss}} + \sum_{j\geq 1} c_j \hat{\rho}_j. \tag{9.1}$$

From this equation we get the time evolution as

$$\hat{\rho}(t) = \hat{\rho}_{\text{ss}} + \sum_{j\geq 1} c_j e^{\lambda_j t} \hat{\rho}_j. \tag{9.2}$$

In other words, it is trivial to see that, if we know $\hat{\rho}_j$ and λ_j, we can determine the time evolution of any density matrix by applying appropriate coefficients.

The other way around it is also possible. Since all the $\text{Re}\{\lambda_j\} \leq 0$, after a sufficient long time the system reaches its steady state and $\hat{\rho}(t) \simeq \hat{\rho}_{\text{ss}}$. Knowing $\hat{\rho}_0$ we can proceed backwards and determine all the other eigenmatrices, as depicted in Fig. 9.1 (c).

Obviously, this is a very inefficient method, which does not bring any numerical advantage to the determination of $\hat{\rho}_{\text{ss}}$, even if it allows to correctly determine the Liouvillian spectrum. Indeed, we are "throwing away" all the information about the Liouvillian spectrum accumulated along the dynamics [see Fig. 9.1 (c)]. After a short transient dynamics, the physics of the system is confined in the manifold spanned by the eigenmatrices of the Liouvillian with sufficiently small real part (in absolute value) of the eigenvalues, i.e., those states which are the slowest decaying. If $1/\Gamma$ is the typical decaying timescale of the system, the dynamics is described by those N eigenmatrices such that λ_j/Γ is sufficiently close to zero, i.e.,

$$\hat{\rho}(\Gamma t > 1) \simeq \hat{\rho}_{\text{ss}} + \sum_{1\leq j<N} c_j e^{\lambda_j t} \hat{\rho}_j. \tag{9.3}$$

Notice that we do not need to exactly know the eigenmatrices $\hat{\rho}_j$, but just their linear combination. In other words, if we are able to determine the span of the N relevant matrices, we can build up a basis for $\hat{\rho}(t > 1/\Gamma)$ and re-express the Liouvillian within this reduced basis. The newly obtained effective Liouvillian will be much smaller than the original one, reducing the computational cost of the diagonalization, but at the same time it would correctly determine the $\hat{\rho}_j$.

The advantages of this method are evident. Not only does it shorten the amount of time needed to obtain the steady state, but it also makes it possible to obtain an excellent estimation of the slow-decaying part of the Liouvillian $\hat{\rho}_j$.

Having clarified the physical idea behind the algorithm, the mathematical

formalization of this intuition can be provided in terms of Krilov subspaces, and the proposed algorithm will be a reinterpretation of the time evolution of an open quantum system in terms of Arnoldi iteration. We call such a procedure a *Krilov time evolution*.

9.1.2 Krilov subspaces, Arnoldi iteration, and evolution operator

Arnoldi iteration

Although a detailed description of Arnoldi iteration and Krilov subspaces goes beyond the purpose of this thesis, here we provide a brief description of the algorithm and of its main properties. We will use the previously-developed notation of operators and superoperators to highlight the context in which we will use it.

Suppose we want to determine part of the spectrum of a superoperator, say the Liouvillian $\mathcal{L}$. This task can be achieved via an iterative diagonalization known as Arnoldi iteration. The key idea behind this algorithm is that one can recursively apply n times the Liouvillian to a random matrix $\hat{\sigma}$ of norm one, producing the so-called Krilov matrix

$$K_n = \left\{\hat{\sigma}, \mathcal{L}\hat{\sigma}, \mathcal{L}^2\hat{\sigma} \ldots, \mathcal{L}^n\hat{\sigma}\right\}. \tag{9.4}$$

This method will highlight those eigenvalues of *largest* absolute value. Indeed, using the spectral decomposition of $\hat{\sigma}$ we have

$$\hat{\sigma} = \sum_i c_i\hat{\rho}_i \Rightarrow \mathcal{L}^n\hat{\sigma} = \sum_i c_i\lambda_i^n\hat{\rho}_i, \tag{9.5}$$

since, by definition, $\mathcal{L}\hat{\rho}_i = \lambda_i\hat{\rho}_i$.

The Arnoldi iteration builds up an orthonormal basis from the K_n via Grahm-Schmidt orthonormalization. If one calls $\hat{\sigma}_1 \ldots \hat{\sigma}_n$ the Arnoldi orthonormal basis obtained from K_n, and $\mathcal{S}_n$ the rectangular matrices whose columns are the n vectorialized Arnoldi operators, one can define an effective Liouvillian as

$$\mathcal{L}_n^{\text{eff}} = \mathcal{S}_n^\dagger\mathcal{L}\mathcal{S}_n. \tag{9.6}$$

In the limit in which $n \to N^2$, where N is the dimension of the Hilbert space, $\mathcal{L}^{\text{eff}}$ becomes the full Liouvillian $\mathcal{L}$, $\mathcal{S}$ being nothing but a change of basis.

The diagonalization of $\mathcal{L}^{\text{eff}}$ for $n \ll N^2$ is, in principle, efficient: $\mathcal{L}^{\text{eff}}$ is a relatively small and upper Hessenberg matrix (i.e. "almost" triangular):

$$\mathcal{L}_n^{\text{eff}} = \begin{bmatrix} l_{1,1} & l_{1,2} & l_{1,3} & \cdots & l_{1,n} \\ l_{2,1} & l_{2,2} & l_{2,3} & \cdots & l_{2,n} \\ 0 & l_{3,2} & l_{3,3} & \cdots & l_{3,n} \\ \vdots & \ddots & \ddots & \ddots & \vdots \\ 0 & \cdots & 0 & l_{n,n-1} & l_{n,n} \end{bmatrix}. \tag{9.7}$$

Importantly, one can diagonalize $\mathcal{L}_n^{\text{eff}}$ and obtain the (Ritz) eigenvalues $\lambda_{\text{j}}^{\text{eff}}(n)$ and eigenmatrices $\hat{\rho}_j^{\text{eff}}(n)$. In the limit in which the $\hat{\rho}_j^{\text{eff}}(n)$ approximates all the wanted $\hat{\rho}_j$, one can stop the iteration.

Notably, one never needs to compute explicitly the matrix elements $\mathcal{L}^{\text{eff}}$ via the similarity transformation in (9.6). The pseudocode for the Arnoldi iteration is provided in Algorithm 1 in appendix E.

The exponential map as an alternative operator

There are several reasons for which directly computing the Liouvillian spectrum via the Arnoldi method is impractical for large systems. First, the Liouvillian has a large exponential growth: for a Hilbert space of size N, the Liouvillian is a matrix of size N^2, making it impractical even to store its elements. Second, the Krilov subpaces tends to bring out the Liouvillian eigenvalues of large magnitude. This problem can be solved by using the inverse of $\mathcal{L}$. In this way, the most relevant vectors become those closest to zero. This, however, further increases the numerical cost of the diagonalization, and can lead to significant numerical errors due to numerical instabilities [219].

It is actually easier and numerically more efficient to resort to the time evolution of the system for large Hilbert spaces. Let us analyze more in detail the time evolution of an open system. Using the exponential Liouvillian map, see section 2.7, the evolution reads

$$\hat{\rho}(t) = \exp(\mathcal{L}t)\hat{\rho}(0). \tag{9.8}$$

Even if we never write the Liouvillian, or its exponential, we can formally introduce the evolution operator

$$\mathcal{E} = \exp(\mathcal{L}T), \tag{9.9}$$

where T is a time interval whose choice will be specified below. Consequently, we

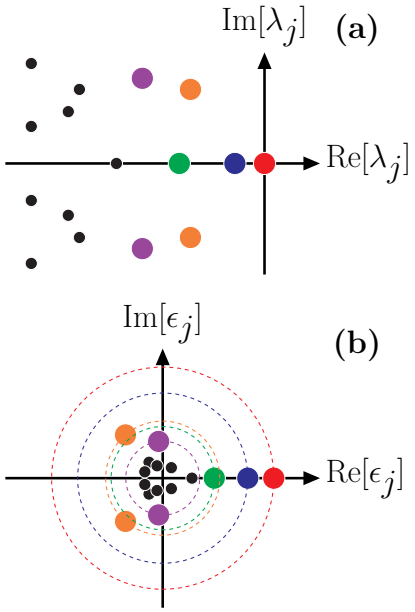

Figure 9.2: *Spectrum of the Liovillian [dots in (a)] vs spectrum of the corresponding evolution operator [dots in (b)]. While the steady state is the the zero of Liouvillian (red dot), ϵ_0 is the largest eigenvalue of $\mathcal{E}$, as it can be seen in (b) where the dashed lines represent the circles of radius* $\exp[\mathrm{Re}(\lambda_i)]$. *Thus, the Arnoldi iteration is well suited to obtain $\hat{\rho}_0$ from $\mathcal{E}$. Furthermore, the eigenvalues with the smallest real part acquire the larger magnitude [other colored dots in (a) and (b)], while the fast-decaying processes are condensed towards the zero.*

have

$$\hat{\rho}(T) = \mathcal{E}\hat{\rho}(0) = \exp(\mathcal{L}T)\hat{\rho}(0). \tag{9.10}$$

Within this representation, we can see the time dynamics up to a time nT as

$$\begin{aligned} K_n &= \{\hat{\rho}(0),\, \hat{\rho}(T),\, \hat{\rho}(2T),\, \ldots\, \hat{\rho}(nT)\} \\ &= \left\{\hat{\rho}(0),\, \mathcal{E}\hat{\rho}(0),\, \mathcal{E}^2\hat{\rho}(0)\, \ldots,\, \mathcal{E}^n\hat{\rho}(0)\right\}. \end{aligned} \tag{9.11}$$

Therefore, the time dynamics of $\hat{\rho}(t)$ is the Krilov subspace of $\mathcal{E}$. When computing the steady state from the time dynamics, one is only considering $\mathcal{E}^n\hat{\rho}(0)$ while discarding all the information stored in the construction of the Krilov subspace K_n. This is the mathematical formalization of the intuition depicted in Fig. 9.1(c).

Within this description, it is clear that we can apply the Arnoldi iteration to determine the spectrum of $\mathcal{E}$. Again, we stress that we never need explicitly to write $\mathcal{E}$ or $\mathcal{L}$, and each time step of this procedure has roughly the same numerical cost than a similar time evolution.

Why is it so much more advantageous to use $\mathcal{E}$ instead of $\mathcal{L}$? The first remark is that there is a direct correspondence between the eigenvalues of $\mathcal{E}$ and those of $\mathcal{L}$. Indeed, one has

$$\mathcal{E}\hat{\rho}_j = \epsilon_j\hat{\rho}_j = e^{\lambda_j T}\hat{\rho}_j \quad \Leftrightarrow \quad \mathcal{L}\hat{\rho}_j = \lambda_j\hat{\rho}_j. \tag{9.12}$$

The second fundamental remark is that, the Liouvillian spectrum, and thus that of $\mathcal{E}$, has some fundamental properties. In particular, the fact that all the λ_j are of negative real part means that $\hat{\rho}_0$ becomes the largest eigenvalue of $\mathcal{E}$, since $\epsilon_0 = e^{\lambda_0 T} = 1$. This can be easily seen in Fig. 9.2, where we show how the spectrum of $\mathcal{L}$ transforms into that of $\mathcal{E}$.

In other words, we can construct

$$\mathcal{E}_n^{\text{eff}} = \mathcal{S}_n^\dagger \mathcal{E} \mathcal{S}_n = \begin{bmatrix} e_{1,1} & e_{1,2} & e_{1,3} & \cdots & e_{1,n} \\ e_{2,1} & e_{2,2} & e_{2,3} & \cdots & e_{2,n} \\ 0 & e_{3,2} & e_{3,3} & \cdots & e_{3,n} \\ \vdots & \ddots & \ddots & \ddots & \vdots \\ 0 & \cdots & 0 & e_{n,n-1} & e_{n,n} \end{bmatrix}, \tag{9.13}$$

via application of the Arnoldi iteration without ever computing the Liouvillian or its exponential. Indeed, the algorithm is identical to the previously described having built the Krilov subspace via time evolution.

The pseudocode to realize the Krilov time evolution and determine the spectrum of the low-lying part of the Liouvillian is detailed in Algorithm 2 in appendix E.

The previously discussed algorithm, although perfectly working, may still present some difficulties for very large systems, since it may be necessary to store many density matrices before convergence is reached. This problem could be avoided by using an Implicitly Restarted Arnoldi Method (IRAM). Such an optimization goes beyond the purpose of this work and the development of an IRAM time evolution is one of the future perspectives.

9.2 Case study: the driven-dissipative Bose-Hubbard model

To prove the efficiency of our method, we consider the homogeneously driven-dissipative Bose-Hubbard model, introduced in chapter 3. It describes the physics of arrays of L resonators, where the photons in each site interact through a potential U, and they can hop between different sites with a strength J. The model is driven by a coherent pump of intensity F_j (j indicating the site), and the pump-to-cavity detuning is Δ. In the frame rotating at the pump frequency, its Hamiltonian is

$$\begin{aligned}\hat{H} = \sum_{j=1}^{L} \left[-\Delta \hat{a}_j^\dagger \hat{a}_j + \frac{U}{2} \left(\hat{a}_j^\dagger\right)^2 \left(\hat{a}_j\right)^2 + F_j \left(\hat{a}_j^\dagger + \hat{a}_j\right) \right] \\ - \frac{J}{z} \sum_{\langle j,l \rangle} \hat{a}_j^\dagger \hat{a}_l,\end{aligned} \tag{9.14}$$

where $\langle j, l \rangle$ indicates the sum on the nearest neighbours. The dissipation acts locally and uniformly in each site at a rate γ by ejecting single photons from each resonator. Thus, the Lindblad master equation and the associated Liouvillian reads

$$\partial_t \hat{\rho}(t) = \mathcal{L}\hat{\rho}(t) = -i \left[\hat{H}, \hat{\rho}(t)\right] + \gamma \sum_{j=1}^{L} \mathcal{D}[\hat{a}_j]\hat{\rho}(t). \tag{9.15}$$

The driven-dissipative Bose-Hubbard model is known to be characterized by a dissipative phase transition in the thermodynamic limit of infinite cavities. Furthermore, the emergence of time-crystal phases in asymmetrically driven cavities has been discussed in [63, 220]. As such, the finite-size driven-dissipative Bose-Hubbard model provides an ideal benchmark for our method, combining the difficulty of an emerging criticality with the large size of the Hilbert space of the

coupled resonators.

9.2.1 Uniform drive

In the following, we will consider the dimer and trimer cases (i.e., the number of sites L is either 2 or 3) We will start by considering two and three identical cavities, where the parameters will be fixed at $\Delta = 5\gamma$, $F_1 = F_2 = F = 4.5\gamma$, $U = 20\gamma$, and $J/z = 10\gamma$ (for consistency, the hopping term is renormalized by the connectivity z (the number of nearest neighbours).

The dimer

Here, we consider the case of two resonators, i.e., $L = 2$ in Eqs. (9.14) and (9.15). For this size of the system, and for the parameters considered, we find that the part of the spectrum shown below has reached convergence for a cutoff of $n_{max} = 7$, that is, we suppose that any element of a density matrix $\langle r|\hat{\rho}(t)|q\rangle$ is zero if $r > n_{max}$ or $q > n_{max}$, where $|r\rangle$ and $|q\rangle$ are Fock states. It follows that $\hat{H}$ is a 64×64 matrix, while the whole Liouvillian has size 4096×4096, a still diagonalizable object.

We will test our algorithm on two types of tasks: (i) Determine just the steady state [noted $\hat{\rho}_{\text{ss}}$]; (ii) Determine the m slowest eigenvalues and eigenmatrices [noted $\hat{\rho}_m$]. We check for the eigenvalues convergence every 10 timesteps. The condition of convergence we require is $\tau = \|\mathcal{E}\hat{\rho}_j - \epsilon_j^{\text{eff}}\hat{\rho}_j\| < 10^{-3}$. Note however that there exist multiple possible measures of convergence, e.g. $\left|\left\|\text{Tr}\left[(\hat{\rho}_j)^\dagger \mathcal{L}\hat{\rho}_j\right]\right\|^2 - \left\|\text{Tr}\left[(\hat{\rho}_j)^\dagger \mathcal{L}^2\hat{\rho}_j\right]\right\|\right| = \tau'$. First, let us give an overview of the computational effort required for each task on our local machine [Intel(R) Xeon(R) W-2135 CPU @ 3.70GHz (12 CPUs) and 128 Gb of RAM], i.e. exact diagonalization (ED) and our method, in the Table 9.1 below:

Table 9.1

	ED	$\hat{\rho}_{\text{ss}}$	$\hat{\rho}_5$	$\hat{\rho}_{10}$	$\hat{\rho}_{50}$
Computation time	43 s	8.5 s	11.75 s	15 s	42s
Final time		6 γ	8 γ	10 γ	42 γ
$\dim(\mathcal{L}^{\text{eff}})$	4096	120	160	200	280

Clearly, to obtain few values, for this limited system size, our method is much

faster than a Liouvillian ED. Nevertheless, if one is interested in getting many eigenvalues and eigenmatrices, our algorithms starts to be comparable with the Liouvillian ED (c.f. $\hat{\rho}_{50}$).

Besides the speed of the method, evidently one is also interested in the correctness of its predictions. In Fig. 9.3 we compare the results obtained for $\hat{\rho}_5$ and $\hat{\rho}_{10}$ through our method with the corresponding ones obtained via ED. In Figs. 9.3(a) and (b) we show the Liouvillian spectrum and the spectrum of the evolution operator, respectively. The red dots indicate the spectrum obtained through ED, while the blue vertical markers represent the results convergent up to $\hat{\rho}_5$, and the green vertical markers are the other five solutions up to $\hat{\rho}_{10}$. There is obviously an excellent agreement between our method and the exact results. Notably, even in the regions where the spectrum becomes "crowded", the obtained eigenvalues are indistinguishable from those resulting from ED. It should be noted that if one wishes to calculate more eigenvalues (c.f. $\hat{\rho}_{50}$ in Table 9.1), and especially if eigenvalues are not far apart, the method will require more time to be able to distinguish between them. In such cases a decrease of T can also allow for quicker convergence. In Fig. 9.3 (c) we see excellent correspondence of eigenvalues: our method determines the λ_j^{eff} almost up to the numerical precision of ED. This precision is not limited to the eigenvalues, as shown in Fig. 9.3 (d). Indeed, the overlap between the eigenmatrices obtained through ED ($\hat{\rho}_j$) and those obtained with method ($\hat{\rho}_j^{\text{eff}}$) shows a precision up to numerical error.

Summing up, for this simple model, we have thus demonstrated that our method is efficient and accurate for the spectrum of the Liouvillian superoperator.

Another important question is how the method presented here fares against other possible methods to extrapolate the steady state from a time evolution. Let us show here that our method is both faster and more precise. Consider, for example, $\langle \hat{n}_1 \rangle = \langle \hat{a}_1^\dagger \hat{a}_1 \rangle$, i.e., the expectation value of the particle number of the first cavity of the dimer. In panel (a) of Fig. 9.4 we show $\langle \hat{n}_1(t) \rangle$ for the same random initial state that we used for our algorithm. The vertical dotted lines indicate the final simulation times where our method reached convergence for the indicated number of eigenvalues and eigenmatrices ($\hat{\rho}_{\text{ss}}$, $\hat{\rho}_5$ and $\hat{\rho}_{10}$). This time is clearly much smaller than the one needed to reach the steady state through standard time evolution. Indeed, for $\gamma t = 15$, $\langle \hat{n}_1(t) \rangle$ significantly differs from the steady-state solution $\langle \hat{a}_1^\dagger \hat{a}_1 \rangle_{\text{ss}}$, marked with a horizontal orange dashed line.

Given the spectral structure in (9.2), one can extrapolate the steady state value from a long time dynamics. For example, once transient fast processes have

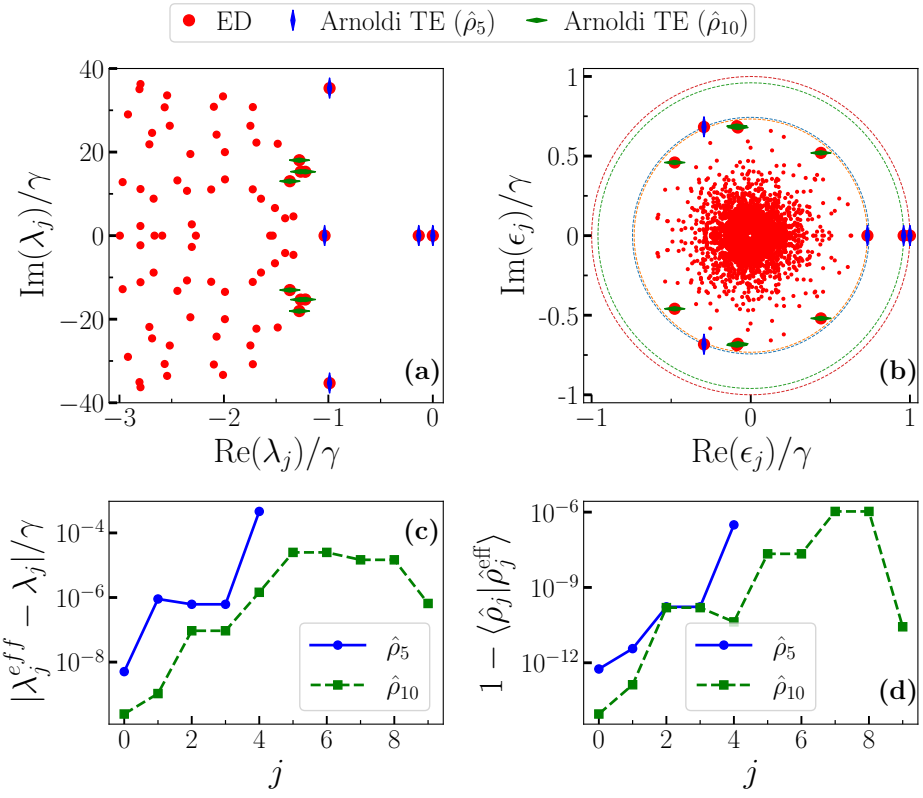

FIGURE 9.3: *Results for the Bose Hubbard dimer for the parameters* $\Delta = 5\gamma$, $F_1 = F_2 = 4.5\gamma$, $U = 20\gamma$, *and* $J = 10\gamma$ *and a cutoff* $n_{max} = 7$. ***(a)*** *Liouvillian spectrum obtained via the exact diagonalization (red dots) and our method for the 5 slowest states* $\hat{\rho}_5$ *(blue vertical markers) and the 10 slowest states* $\hat{\rho}_{10}$ *(green horizontal markers). Eigenvalues of which* $Re(\lambda_j)/\gamma < -3$ *have been discarded from the figure for clarity.* ***(b)*** *Spectrum of the evolution operator obtained via the exact diagonalization (red dots) and our method for* $\hat{\rho}_5$ *(blue vertical markers) and* $\hat{\rho}_{10}$ *(green horizontal markers).* ***(c)*** *Difference between the eigenvalues obtained with the ED* λ_j *and our method* λ_j^{eff} *for* $\hat{\rho}_5$ *(blue line with dots) and* $\hat{\rho}_{10}$ *(green dashed line with squares). The values have been re-scaled with a factor* $e^{0.3}$ *to clearly show their differences.* ***(d)*** *One minus the overlap between the eigenmatrices obtained via the ED and our method for* $\hat{\rho}_5$ *(blue line with dots) and* $\hat{\rho}_{10}$ *(green dashed line with squares).*

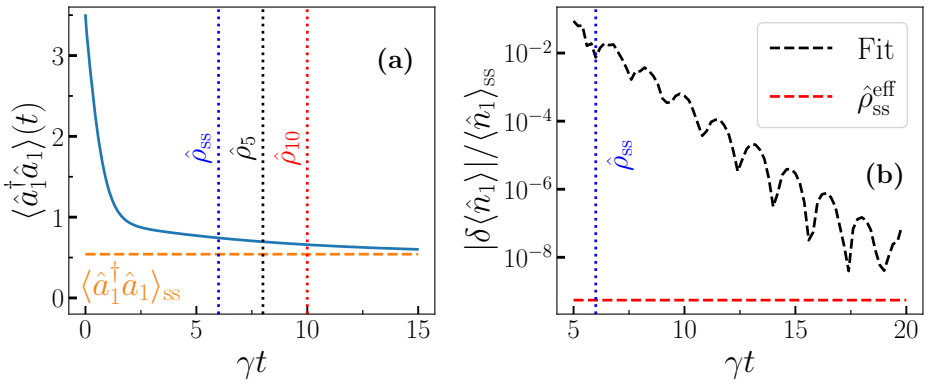

Figure 9.4: ***(a)*** *Time evolution of the expectation value of the particle number of the first cavity of the dimer* $\hat{n}_1 = \langle \hat{a}_1^\dagger \hat{a}_1 \rangle$ *(blue full line). The steady-state solution obtained via exact diagonalization, i.e.* $\langle \hat{a}_1^\dagger \hat{a}_1 \rangle_{\rm ss}$ *(orange dashed line). The final time where our method reached convergence is shown by vertical lines for* $\hat{\rho}_{\rm ss}$ *(blue dotted line),* $\hat{\rho}_5$ *(black dotted line) and* $\hat{\rho}_{10}$ *(red dotted line).* ***(b)*** *Relative difference between the expectation value of* $\hat{n}_1$ *obtained via ED and either our method (red dashed line) or a fit of the exponential decrease towards the steady state (black dashed line). The blue dotted indicates the time where our method reached convergence and obtained* $\hat{\rho}_{\rm ss}$*. Same parameters and initial state were used as in Fig. 9.3.*

washed out, one has:

$$\langle \hat{n}_1(t) \rangle = \langle \hat{n} \rangle_{\text{ss}} + \tilde{c}_1 e^{\lambda_1 t}, \tag{9.16}$$

where $\tilde{c}_1 = c_1 \langle \hat{a}_1^\dagger \hat{a}_1 \hat{\rho}_1 \rangle$. From this, one can extrapolate $\langle \hat{n} \rangle_{\text{ss}}$. In panel (b) of Fig. 9.4 we show as a function of time the relative error

$$\|\delta \langle \hat{n}_1 \rangle\| / \langle \hat{n}_1 \rangle_{\text{ss}} = \|\langle \hat{n}_1 \rangle_{\text{ss}}^{\text{eff}} - \langle \hat{n}_1 \rangle_{\text{ss}}\| / \langle \hat{n}_1 \rangle_{\text{ss}} \tag{9.17}$$

where $\langle \hat{n}_1 \rangle_{\text{ss}}^{\text{eff}}$ has been obtained either through this fitting method (black dashed line) or with our method for the case where convergency is reached for only the steady state $\hat{\rho}_{\text{ss}}$ (red horizontal dashed line). In other words, $\delta \langle \hat{n}_1 \rangle$ quantifies how accurate a prediction is at a time γt. It is clear that our method gives a result that is several orders of magnitudes more precise than the one obtained with the fitting method, even when we let the system evolve for times much longer than $\gamma t = 6$ required by our method (see Table 9.1).

The trimer

We will now consider the trimer, i.e. 3 connected cavities, for the same parameter regime. Convergence is also reached for a cutoff of $n_{\max} = 7$. By adding one cavity to the previous dimer, the Liouvillian of this system is no longer numerically exactly diagonalizable. Indeed, the Hilbert space now has a dimension of $8^3 = 512$ and the whole Liouvillian has size 262144×262144. The (low-lying) Liouvillian spectrum and the corresponding eigenmatrices are thus usually beyond what one can calculate. Using our method however, one is still able to efficiently obtain results. In Fig. 9.5 we show the 5 slowest processes in the Liouvillian spectrum of the trimer.

9.2.2 Asymmetric drive and time crystal in a dimer

As a final example, we turn our attention to an asymmetrically driven Bose Hubbard dimer. Recently, it was shown that for a certain choice of parameters a time crystalline phase emerges in the thermodynamic limit [63]. Its emergence is marked by the closure of the Liouvillian gap, i.e. the increase of the real part of largest non-zero eigenvalue as system size is increased, given that this eigenvalue also has non-zero imaginary part. Due to the reflection symmetry of the Liouvillian this thus coincides with two mirrored eigenvalues of which the real part approaches zero as system size is increased. We show the low-lying spectrum of such a model

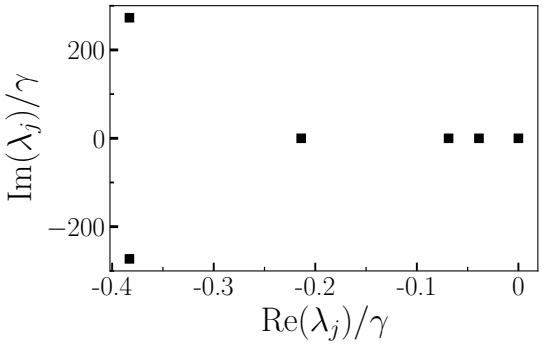

Figure 9.5: *Results for five slowest eigenvalues of the Bose Hubbard trimer for the parameters* $\Delta = 5\gamma$, $F_1 = F_2 = 4.5\gamma$, $U = 20\gamma$, *and* $J = 10\gamma$ *and a cutoff* $n_{\max} = 7$. *Note that due to the symmetry of the Liouvillian spectrum six eigenvalues are plotted.*

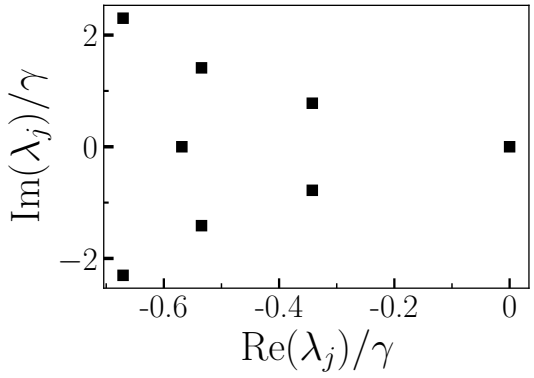

Figure 9.6: *Results of the low-lying Liouvillian spectrum for a Bose-Hubbard dimer with assymetrical drive for the parameters* $\tilde{F} = 1$ *where* $\tilde{F} = F\sqrt{U}/\gamma^{3/2}$, $U = 0.125\gamma$, $\Delta/\gamma = 2$, *and* $J/\gamma = 2$. *The local Hilbert space as a cutoff at* $N_{\max} = 28$.

in Fig. 9.6 for a parameter regime studied in Ref. [63].

9.3 Conclusions

We have presented a method to efficiently determine the steady state and the low-lying Liouvillian spectrum and eigenmatrices of an open quantum system governed by a Lindblad master equation. It only requires (short) time evolution of the open system and consequently allows the calculation of the low-lying Liouvillian spectrum for system sizes that would be inaccessible through exact diagonalization. Furthermore, for a sufficiently small number of eigenvalues the method is also more efficient than exact diagonalization. Preliminary testing has shown that the method can be generalized to the quantum trajectory formalism. This has exciting possibilities with respect to number of samples that would usually be needed when averaging over the trajectories. If one is able to construct a set of relevant states it would thus be possible to suppress the stochastic noise that is per construction present in the quantum trajectory formalism. As a future outlook we plan to further investigate this generalized application and formulate it in a rigorous mathematical framework.

PART

V

GENERAL CONCLUSIONS

CHAPTER 10

General conclusions and outlook

In part II we exploited the permutational invariance which is present in all-to-all connected models to test the validity of the Gutzwiller mean-field approximation. In particular, in chapter 5 we studied the all-to-all connected XYZ (anisotropic-Heisenberg) spin model with *local and collective* dissipation, comparing the results of mean-field (MF) theory with the solution of the Lindblad master equation. Exploiting the weak $\mathcal{PT}$-symmetry of the model (referred to as Liouvillian $\mathbb{PT}$-symmetry), we efficiently calculated the Liouvillian gap, introducing the idea of an *antigap*, and we demonstrated the presence of a paramagnetic-to-ferromagnetic phase transition. Leveraging the permutational symmetry of the model, we characterized criticality, finding exactly (up to numerical precision) the steady state for N up to $N = 95$ spins. We demonstrated that the MF theory correctly predicts the results in the thermodynamic limit in all regimes of parameters. However, for an intermediate number of spins and for large anisotropy, we find a significant difference between the results of the MF theory and those of the full quantum simulation. Our results show that the convergence to the mean-field results are unexpectedly slow. We also studied other witnesses of the transition, which can be used for finite-size studies, namely the bimodality coefficient and the angular averaged susceptibility. In contrast to the bimodality coefficient, the angular averaged susceptibility fails to capture the onset of the transition, in striking difference with respect to lower-dimensional studies. We also analyzed the competition between local dissipative processes (which disentangle the spin system) and collective dissipative ones (generating entanglement). The nature of the phase transition is almost unaffected by the nature of the dissipation.

Subsequently, in chapter 6 we developed a toolbox in Python to simulate the time evolution of all-to-all connected p-level systems. Similar to the previous study this has allowed us to study exactly the all-to-all connected model for increasing

system sizes. We have presented mean-field solutions in a parameter regime that shows a rich phase diagram, containing up to five solutions. A dynamical stability analysis has shown two stable solutions and also the emergence of time crystalline behaviour. Our full quantum study shows evidence for the presence of a first order phase transition, ascribed to the multistability in the mean-field solutions, as well as an emerging tristability that may be linked to the time crystal present in the mean-field solutions. A study of the Liouvillian spectrum however shows no clear signs of the emergence of imaginary eigenvalues of which the real part goes to zero as system size is increased. A reason for this may be that the simulated system sizes are too small to display the behavior from the thermodynamic limit. Further investigation is needed as it will answer the interesting question of whether the mean field is predictive also for the dynamics of the system.

In part III we introduced the cluster-Gutzwiller Monte Carlo method to study dissipative open quantum systems. In chapter 7, we used it to study the influence of short-range quantum correlations and classical spatial correlations on the phase diagram of the dissipative XYZ model with only nearest-neighbor interactions. Considering lattices of finite size we showed the emergence of a ferromagnetic phase, two paramagnetic phases and the possible existence of a phase transition which is entirely quantum in nature. The inclusion of short-range quantum correlations has a drastic effect on the phase diagram but our results show the inclusion of long-range quantum correlations or the use of more sophisticated methods are needed to quantitatively match the exact results. A study of the susceptibility tensor shows that reciprocity is broken, a feature not observed in closed quantum systems. In stark contrast with closed quantum systems, increasing the magnetic field suppresses the magnetization.

In chapter 8 we studied the dynamical properties of a driven-dissipative Bose-Hubbard model in the strongly interacting regime in chapter 8. By studying the dynamical hysteresis surface that arises by sweeping through the coherent driving strength we show that the phase diagram for this system is in qualitative correspondence with the Gutzwiller mean-field result. However, quantitative differences are present and the inclusion of classical and quantum correlations causes a significant shift of the critical parameters. Additionally, we showed that approximation techniques relying on a unimodal distribution such as the mean field and $1/z$ expansion drastically underestimate the particle number fluctuations. Finally, we have shown that a proposed mapping of the driven-dissipative many-body Bose-Hubbard model onto a single driven-dissipative Kerr model is not

accurate for parameters in the hysteresis regime.

Finally, in part IV we have presented a novel method to efficiently determine the low-lying spectrum of the Liouvillian. It provides a tool to accurately calculate the steady state of a dissipative system, as well as access the part of the spectrum most relevant to longer time dynamics. Furthermore, since it relies on a time evolution scheme it is possible to calculate these properties for systems that would otherwise be intractible with a brute-force exact method. Our results can be extended to generic time evolution methods, allowing to describe the slowly decaying processes with a relatively short dynamical evolution.

As a general outlook, we note that the interplay between local and collective dissipation beyond the all-to-all connected model demands further investigation with the adoption of both analytical and numerical approximation techniques. Exploiting other symmetries, such as translational invariance, it should be possible to further reduce the numerical resources for Liouvillian representation. Moreover, it will be interesting to further investigate the system's time evolution toward the steady state, as transient processes may display even starker differences between mean-field or classical results and full quantum dynamics. Additionally, this method can also grant access to a study of the universal exponents near the phase transition in this system through a proper rescaling of the systems parameters and studying e.g. the order parameter. This would shed further light on the nature of the transitions for these highly dimensional models.

The study of the emerging time crystalline behavior requires a more in depth investigation that is part of ongoing research. Currently, we are extending the study of the low-lying spectrum by including more eigenvalues of the spectrum where signs of a very slowly emerging time crystal may be observed. Furthermore, the investigating is continued in a wider parameter regime where the mean-field results predict time crystalline behaviour. More specifically in a regime where we can calculate exact results for larger system sizes, and thus dimensionality. The present study also shows that a wider study, similar to the one performed for the dissipative XYZ Heisenberg model, can give a clearer view on the validity of the mean-field approximation throughout the phase diagram of this driven-dissipative Bose Hubbard model, at least for strong nonlinearity.

In low-dimensional systems our results have shown that quantum correlations that go beyond the size of the used clusters are needed to accurately describe the dissipative XYZ Heisenberg model. One way to include these long-range quantum correlations is through a correlation hierarchy containing the various moments

of the magnetization, on the level of the master equation as well as the level of quantum trajectories. The advantage of this method is that it is a straight forward extension of the Gutzwiller mean-field approach as well as the Gutzwiller quantum trajectory approach. Indeed, the aformentioned methods are obtained at first order in the hierarchy. Going to higher order then allows to go beyond the standard factorization of the system's state. Currently, we are pursuing this line of research and we expect this to be a promising method due to the notion that the dissipation present in the system destroys multipartite entanglement or higher order correlations between the spins. Therefore, a correlation hierarchy that is truncated at low order should already give good predictions of the system's properties. This immediately shows another interesting line of research for these models, and that is the study of such multipartite entanglement in driven-dissipative systems through various entanglement witnesses and under influence of various dissipation schemes. The method based on the correlation hierarchies can also be used to study the regime of large J_y where the paramagnetic phase re-enters the phase diagram as well as the region of the phase diagram where ferromagnetic order was found that is ascribed solely to quantum correlations.

Finally, the method presented to calculate the low-lying spectrum and eigenmatrices of the Liouvillian superoperator through standard time evolution methods shows much promise as it can also be generalized to other time evolution methods. An implementation using e.g. the Corner space renormalization method or tensor networks could push the size of systems that can be studied beyond what is possible with a standard master equation approach. Furthermore, preliminary results have shown that the method may also be extended to the quantum trajectory approach. Finally, we note that work on an open source implementation of the method is ongoing, as well as its implementation with more sophisticated methods than the standard Arnoldi iteration used in this work.

APPENDIX A

Open quantum systems

A.1 Photon counting trajectory simulation scheme

Where the equations (2.53) and (2.54) determine the stochastic time evolution of the wave function, it is more of a formal way to formulate it in an equation than it provides a way to explicitely calculate the time evolution. Nonetheless, its numerical simulation can be expressed in a few simple and straight forward steps. Assume an initial (normalized) state $|\psi(t)\rangle$ of which the unitary dynamics is given by a Hamiltonian $\hat{H}$ and the dissipation is governed by a set of N jump operators $\hat{L}_j$, where we assume a uniform dissipation rate γ for simplicity. Furthermore, we chose a small time step δt such that the Markov approximation is valid (i.e. big with respect to the time at which the correlations in the environment decay, but small with regard to the timescale at which the system changes) and also small enough so that the deterministic evolution can be smoothly simulated. The time evolution of the wave function $|\psi(t)\rangle$ until a final time T in its most simple formulation is then given by the following steps.

For each time step δt

1. Generate a random number ϵ uniformly distributed between 0 and 1, and calculate the probabilities $p_j = \gamma\delta t\langle\psi(t)|\hat{L}_j^\dagger\hat{L}_j|\psi(t)\rangle$ for $j \in [1, N]$. With these probabilites construct a set of boundary values b_ν such that $b_0 = 0$, $b_1 = p_1$, $b_2 = p_1 + p_2$, ... , $b_N = \sum_j p_j$ and $b_{N+1} = 1$.

2. **IF** $b_{j-1} \leq \epsilon < b_j$ a jump $\hat{L}_j$ takes place and the wave function becomes

$$|\psi(t + \delta t)\rangle = \hat{L}_j|\psi(t)\rangle. \tag{A.1}$$

ELSE IF $\epsilon \geq b_N$ no jump occurs and the wave function is time evolved with its non-Hermitian Hamiltonian (see the second and third term in (2.53))

$$|\psi(t+\delta t)\rangle = |\psi(t)\rangle - i\left(\hat{H} - i\frac{\gamma}{2}\sum_j \hat{L}_j^\dagger \hat{L}_j\right)\delta t|\psi(t)\rangle. \tag{A.2}$$

3. Normalize the wave function $|\psi(t+\delta t)\rangle$

$$|\psi(t+\delta t)\rangle = \frac{|\psi(t+\delta t)\rangle}{\sqrt{\langle\psi(t+\delta t)|\psi(t+\delta t)\rangle}} \tag{A.3}$$

4. Go back to step 1 if the final time T in the evolution is not reached.

The above scheme gives the time evolution up to first order in δt. There however exists a more efficient way to do the time evolution. It is based on determining the time t' (with $t' > t$) at which the next jump will occur, rather than checking if a jump will occur in a time step δt. It utilizes the so-called waiting time distribution for a jump to take place [5]. It holds a close connection to the value of the norm of the wave function $|\psi(t)\rangle$. The norm decreases due to the deterministic time evolution with the effective non-Hermitian Hamiltonian

$$\hat{H}_{\text{eff}} = \hat{H} - i\frac{\gamma}{2}\sum_j \hat{L}_j^\dagger \hat{L}_j. \tag{A.4}$$

In (2.53) the norm was conserved due to the presence of the first term in the deterministic term (i.e. the term multiplied with dt), which is exaclty the decrease in the norm of $|\psi(t)\rangle$ at each time step. This allows us to formulate the following time evolution for an initial (normalized) wave function $|\psi(t)\rangle$

1. Generate a random number ϵ_1 uniformly distributed between 0 and 1.

2. Time evolve the wave function $|\psi(t)\rangle$ with the effective Hamiltonian (A.4) until the time t' where $\langle\psi(t')|\psi(t')\rangle = \epsilon_1$ as long as $t' < T$.

3. Generate a new random number ϵ_2 uniformly distributed between 0 and 1 and calculate

$$p_j = \frac{\gamma\langle\psi(t')|\hat{L}_j^\dagger \hat{L}_j|\psi(t')\rangle}{\sum_k \gamma\langle\psi(t')|\hat{L}_k^\dagger \hat{L}_k|\psi(t')\rangle}, \tag{A.5}$$

for all $j \in [1, N]$. With these probabilites construct a set of boundary values b_ν such that $b_0 = 0$, $b_1 = p_1$, $b_2 = p_1 + p_2$, ... , $b_N = \sum_j p_j = 1$.

4. A jump $\hat{L}_j$ occurs for which $b_{j-1} \leq \epsilon_2 < b_j$, the wave function becomes

$$|\tilde{\psi}(t')\rangle = \hat{L}_j|\psi(t')\rangle. \tag{A.6}$$

5. Normalize the wave function

$$|\psi(t')\rangle = \frac{|\tilde{\psi}(t')\rangle}{\sqrt{\langle\tilde{\psi}(t')|\tilde{\psi}(t')\rangle}}. \tag{A.7}$$

6. Go back to step 1 if the final time T in the evolution is not reached.

The time evolution in step 2 is governed by the equation

$$\frac{\partial|\psi(t)\rangle}{\partial t} = -i\left(\hat{H} - i\frac{\gamma}{2}\sum_j \hat{L}_j^\dagger \hat{L}_j\right)|\psi(t)\rangle, \tag{A.8}$$

which can be solved through standard numerical solvers.

APPENDIX B

Permutational invariance

B.1 Scaling of the method

To calculate the scaling of the method for two-level systems, that is the number of coefficients one needs to keep track of, the following sum should be calculated

$$n_{coeff} = \sum_{n_{00}+n_{01}+n_{10}+n_{11}=N} 1. \tag{B.1}$$

One can rewrite this sum as

$$n_{coeff} = \sum_{n_{00}=0}^{N} \left(\sum_{n_{01}=0}^{N-n_{00}} \left(\sum_{n_{10}=0}^{N-n_{00}-n_{01}} 1 \right) \right), \tag{B.2}$$

and calculate this using the expressions

$$\sum_{k=1}^{n} k = \frac{n\,(n+1)}{2} \quad \text{and} \quad \sum_{k=1}^{n} k^2 = \frac{1}{6} n\,(n+1)\,(2n+1)\,, \tag{B.3}$$

this yields

$$\begin{aligned} \sum_{n_{00}=0}^{N} \left(\sum_{n_{01}=0}^{N-n_{00}} \left[N - n_{00} - n_{01} + 1 \right] \right) &= \sum_{n_{00}=0}^{N} \left(\frac{N^2}{2} + \frac{n_{00}^2}{2} + \frac{3}{2} N - \frac{3}{2} n_{00} - N n_{00} + 1 \right) \\ &= \frac{1}{6} N\,(N+1)\,(N+2) \\ &= \binom{N+3}{N}. \end{aligned} \tag{B.4}$$

For p-level systems an equivalent calculation can be performed by employing Faulhaber's formula for the sum of the p-th powers of the first n positive integers

$$\sum_{k=1}^{n} k^p = \frac{n^{p+1}}{p+1} + \frac{1}{2}n^p + \sum_{k=2}^{p} \frac{B_k}{k!} \frac{p!}{(p-k+1)!} n^{p-k+1}, \tag{B.5}$$

with B_k the Bernouilli numbers. Note that is the generalized expression for the sums in (B.3).

However, such a calculation would be, albeit straightforward, quite tedious. An alternative derivation is found from combinatorial considerations by noting that the problem requires all possible ways to divide N indistinguishable balls into p^2 distinguishable boxes. This problem is also known as the stars and bars problem. We will introduce a simple graphical notation and use it to derive the expression for a general number of p-level systems. As an example, assume that we have $N = 6$ *stars* that have to be distributed over $B = p^2 = 4$ boxes, then a possible configuration can be visualized as

$$\star\star|\star||\star\star\star\,. \tag{B.6}$$

where $B - 1 = p^2 - 1 = 3$ *bars* divide the four boxes. One can then note that the problem can be equivalently formulated as the number of ways there are to divide N stars and $p^2 - 1$ bars over $N + p^2 - 1$ positions. Or in other words, the number of ways to distribute N balls over $N + p^2 - 1$ boxes (with a maximum of 1 bar at each position). The expression for this is given by a simple binomial coefficient, since the distribution of the N balls determines the remaining spots of the bars. Thus, we obtain that the number of coefficients one needs to keep track of for N p-level systems is given by

$$n_{coeff} = \binom{N + p^2 - 1}{N}. \tag{B.7}$$

Note that, from a physical point of view, this type of graphical proof was also used by Paul Ehrenfest and Heike Kamerlingh Onnes as a simple proof for Max Planck's expression of complexions, i.e. the number of possible ways to distribute E energy elements over N resonators [221, 222].

B.2 A code example of the permutational invariant solver

Here we give an example of the usage of the solver we have implemented into Python, we will refer to it as `permutational_invariant_solver` in the following. It allows for the construction of the Liouvillian of all-to-all connected p-level systems. As an example we will calculate the Liouvillian for the model studied in chapter 6. The code is dependent on the NumPy module, the SciPy module, as well as the QuTiP module.

[1]:
```
import numpy as np
from qutip import *
from permutational_invariant_solver import *
```

Next, one has to define the system parameters. For our example we use parameters similar to those of Fig. 6.1, but for five all-to-all connected 3-level systems.

[2]:
```
# Define the system parameters...
gamma = 1       # dissipation rate
U = 20*gamma    # Kerr non-linearity
D = (1/3)*U     # detuning
F = 0.35*U      # pumping strength
J = -1.5*U      # hopping amplitude (not normalised with coordination number)
Ncav = 5        # number of cavities
Nlvl = 3        # levels of the system (i.e. p-level system)
```

Having defined the parameters we can now move onto defining the constructors for the dissipation operators (called *collapse operators* in the code), the local Hamiltonian terms and the nearest-neighbour Hamiltonian.

[3]:
```
# Define the annihilation operator...
a = destroy(Nlvl)

# Define the collapse operator...
c_ops = [np.sqrt(gamma)*a]

# Define the terms of the local Hamiltonian and their coefficients...
Hlocal = [[-D, a.dag()*a], [(U/2), a.dag()*a.dag()*a*a], [F,(a.dag() + a)]]

# Define the terms of the nearest-neighbour Hamiltonian and their coefficients...
Hnonlocal = [[J/(Ncav - 1), a.dag(), a]]
```

Note that each term of the local Hamiltonian is implicitely accompanied by

a sum over all sites, i.e. it consists of collective operators. Similarly, the terms of the nearest-neighbour, i.e. non-local Hamiltonian, is accompanied by a sum over all sites and a sum over their respective neighbours. Importantly, this is different from a sum over the links by a factor 2, which is also the reason that for the model under consideration the Hermitian conjugate part present in the model Hamiltonian need not be explicitely taken into account in the definition of `Hnonlocal`.

Having defined all objects that govern the time evolution, and thus the Liouvillian, we can use them to construct the permutational solver and calculate all operators needed in the permutationally reduced basis.

[4]:
```
# Setting up the permutational solver...
psolver = permsolver(Nlvl, Ncav)

psolver.set_dynamics(Hlocal, Hnonlocal, c_ops)
psolver.calculate_all_operators()
```

For the last step we calculate the Liouvillian.

[5]:
```
# Calculate the Liouvillian...
Liouvillian = psolver.Construct_L()
```

As an example we can use the calculated Liouvillian in combination with the QuTiP functionallity to calculate its eigenvalues and eigenvectors. For the considered system size this can still be done with the standard method.

[6]:
```
# Example: calculate the eigendecomposition using QuTiP:
eigenvalues, eigenvectors = Liouvillian.eigenstates()
```

It can also be combined with the method from chapter 9 since the calculated Liouvillian can be used to simulate the time evolution of the system.

APPENDIX C

Mean-field validity XYZ model

C.1 Mean-field stability analysis: local dissipation

We consider the model presented in section 5.1. To compare the mean-field analysis to the full quantum solution, we interpret the all-to-all coupled spin system as a d-dimensional system. Every time we add a spin the dimension of the system is also increased by one. This implies that a d-dimensional system consists of d spins and that infinite dimensions are reached when the system has an infinite amount of spins. The coordination number can be written as $Z = d - 1$. The mean-field equations for the magnetization read

$$\begin{aligned}
\frac{d\langle\hat{\sigma}_n^{(x)}\rangle}{dt} &= -\frac{\gamma}{2}\langle\hat{\sigma}_n^{(x)}\rangle + \frac{2}{Z}\sum_m \left(J_y\langle\hat{\sigma}_n^{(z)}\rangle\langle\hat{\sigma}_m^{(y)}\rangle - J_z\langle\hat{\sigma}_n^{(y)}\rangle\langle\hat{\sigma}_m^{(z)}\rangle\right), \\
\frac{d\langle\hat{\sigma}_n^{(y)}\rangle}{dt} &= -\frac{\gamma}{2}\langle\hat{\sigma}_n^{(y)}\rangle + \frac{2}{Z}\sum_m \left(J_z\langle\hat{\sigma}_n^{(x)}\rangle\langle\hat{\sigma}_m^{(z)}\rangle - J_x\langle\hat{\sigma}_n^{(z)}\rangle\langle\hat{\sigma}_m^{(x)}\rangle\right), \\
\frac{d\langle\hat{\sigma}_n^{(z)}\rangle}{dt} &= -\gamma\left(\langle\hat{\sigma}_n^{(z)}\rangle + 1\right) + \frac{2}{Z}\sum_m \left(J_x\langle\hat{\sigma}_n^{(y)}\rangle\langle\hat{\sigma}_m^{(x)}\rangle - J_y\langle\hat{\sigma}_n^{(x)}\rangle\langle\hat{\sigma}_m^{(y)}\rangle\right).
\end{aligned} \tag{C.1}$$

Note that the sum with index m is a sum over the neighbours, i.e. there are $Z = d - 1$ terms in the sum. The fixed point solution is given by $\langle\hat{\sigma}_n^{(x)}\rangle = 0$, $\langle\hat{\sigma}_n^{(y)}\rangle = 0$ and $\langle\hat{\sigma}_n^{(z)}\rangle = -1$. This is defined as the paramagnetic (PM) phase. We now study the influence of small perturbations α_n to this fixed point solution, i.e. through the substitution $\langle\hat{\sigma}_n^{(\alpha)}\rangle \to \langle\hat{\sigma}_n^{(\alpha)}\rangle + \alpha_n$ with $\alpha = x, y, z$. We can thus rewrite the equations as

$$\begin{aligned}
\frac{dx_n}{dt} &= -\frac{\gamma}{2}x_n + \frac{2}{Z}\sum_m \left(J_y(-1+z_n)y_m - J_z y_n(-1+z_m)\right), \\
\frac{dy_n}{dt} &= -\frac{\gamma}{2}y_n + \frac{2}{Z}\sum_m \left(J_z x_n(-1+z_m) - J_x(-1+z_n)x_m\right), \\
\frac{dz_n}{dt} &= -\gamma z_n + \frac{2}{Z}\sum_m \left(J_x y_n x_m - J_y x_n y_m\right).
\end{aligned} \tag{C.2}$$

From the last equation we find that $z_n = 0$ for all n in the steady-state solution as the terms $x_n y_m$ contribute to second order and can be neglected. We wish to study the stability of the paramagnetic phase to a ferromagnetic or antiferromagnetic perturbation of the system. To this end we perform a Fourier transform and consider d-dimensional perturbations with wave vector $\vec{k} = (k_1, k_2, ..., k_d)$. Remember that for a d-dimensional lattice there are $Z = d - 1$ possible summations over m. The remaining two equations can thus be written as

$$\frac{d}{dt}\sum_k x_k e^{i\vec{k}.\vec{n}} = -\frac{\gamma}{2}\sum_k x_k e^{i\vec{k}.\vec{n}} + \frac{2}{Z}\left(-J_y\sum_m\sum_k y_k e^{i\vec{k}.\vec{m}} + J_z\sum_m\sum_k y_k e^{i\vec{k}.\vec{n}}\right), \tag{C.3}$$

$$\frac{d}{dt}\sum_k y_k e^{i\vec{k}.\vec{n}} = -\frac{\gamma}{2}\sum_k y_k e^{i\vec{k}.\vec{n}} + \frac{2}{Z}\left(-J_z\sum_m\sum_k x_k e^{i\vec{k}.\vec{n}} + J_x\sum_m\sum_k x_k e^{i\vec{k}.\vec{m}}\right). \tag{C.4}$$

The summation over m can be written as

$$\begin{aligned}
\sum_m e^{i\vec{k}.\vec{m}} = e^{i\vec{k}.\vec{n}}\Big(&e^{ik_1} + e^{ik_2} + ... + e^{ik_d} + e^{i(k_1+k_2)} + e^{i(k_1+k_3)} + ... \\
&+ e^{i(k_1+k_2+k_3)} + ... + e^{i(k_1+k_2+...+k_d)}\Big).
\end{aligned} \tag{C.5}$$

As there is only one neighbour in each direction, i.e. $\vec{m} = \vec{n} + 1_l$ with 1_l a d-dimensional vector with a one on the entries where $\vec{n}$ does not coincide with $\vec{m}$, i.e. the translation needed to go from site m to n. The wave numbers k_i can take the values $k_i = 0, \pi$. Now, we note that the system of equations (3) and (4) can be written as a linear system, and the time evolution of the small perturbations x_n and y_n diverge when the eigenvalues of the 2×2 matrix of this linear system are positive. We denote the sum between the brackets of equation (C.5) as S, if we write down the above condition for the eigenvalues we find:

$$-\frac{\gamma^2}{16} > \left(\frac{S}{Z}J_x - J_z\right)\left(\frac{S}{Z}J_y - J_z\right). \tag{C.6}$$

To check whether an antiferromagnetic (AFM) phase can occur we look at the instability when $k_i = \pi$ for all i. We find that the term S in the brackets from (C.5) is equal to

$$-d + \binom{d}{2} - \binom{d}{3} + ... = \sum_i^d (-1)^i \binom{d}{i}. \tag{C.7}$$

Using $\sum_{i=1}^d \binom{d}{i} r^i = (1+r)^d - 1$ and $r = -1$ we find that this equals -1. Substituting this in (C.6) we find in the thermodynamic limit $d \to \infty$

$$-\frac{\gamma^2}{16} > J_z^2. \tag{C.8}$$

This equation cannot be satisfied for any value J_z, which has to be real.
The ferromagnetic (FM) phase results from the instability of the PM phase to $k_l = 0$ for all l. The sum from (C.5) then becomes equal to $S = Z$. We obtain

$$-\frac{\gamma^2}{16} > (J_x - J_z)\left(J_y - J_z\right), \tag{C.9}$$

which is identical to the nearest-neighbor mean-field result. The phase diagram thus only consists of a PM phase and FM phase.

C.2 Collective dissipation only: Symmetry and relation with superradiant light-matter models

In the main text in chapter 5, we mainly consider the presence of either local and collective dissipation, or only of the local one. Here, let us briefly consider the properties of the system in the presence of collective dissipation only, $\Gamma \neq 0$ and $\gamma = 0$ in Eq. (3.3) [98, 99, 101]. In this case, the total spin length

$$\hat{S}^2 \;=\; \left(\hat{S}^x\right)^2 + \left(\hat{S}^y\right)^2 + \left(\hat{S}^z\right)^2, \tag{C.10}$$

is a conserved quantity,

$$\left[\hat{S}^2, \hat{H}\right] \;=\; \left[\hat{S}^2, \hat{S}^-\right] = 0, \tag{C.11}$$

and therefore the presence of conserved quantities implies the existence of several steady states for the Lindbladian dynamics [67, 184]. In more physical terms, this indicates that there exist different multiplets, which are eigenstates of $\hat{S}^2$, that are

not connected by the dissipative dynamics. These multiplets are known as Dicke ladders [163].

This terminology is inherited from the study of the Dicke model. The similarities between the all-to-all connected XYZ and Dicke models are both due to mathematical similarities, which become even more apparent when exploiting the permutational symmetry, and because this is another benchmark model thoroughly used to investigate both quantum phase transitions and dissipative phase transitions, this time in the field of cavity QED and quantum optics [101], instead of spin models.

Describing the collective interaction between an ensemble of two-level systems with a unique photonic field, the Dicke model is known to display superradiant photon emission in the presence of collective dissipation [223–225]. Superradiance is also know to occur in crystals of molecular nanomagnets [226]. Here with superradiant emission we refer to the fact that the light emission intensity scales as N^2 and occurs on a timescale that shrinks with the size of the system, a macroscopic manifestation of cooperative behavior. Note that this phenomenon does not require any strong coupling between light and matter to occur (differently from the superradiant phase transitions), so that one can map the light-matter model to an effective spin model that fulfils Eq. (C.11), with $\hat{H} = \omega_z \hat{S}^z$, where ω_z is the resonance frequency. Superradiance has also recently been experimentally observed in novel optical materials, such as Erbium-doped Yttrium Orthosilicate [227] and Lead Halide Perovskite [228].

Note that, in the presence of collective coupling only, a Holstein-Primakoff transformation can be performed to map the system to a bosonic model [229], whose first-order approximation is valid in the low-excitation regime and is good in the thermodynamic limit. The main assumption of coupling only to a collective field is based on the assumption of identical two-level systems (spins) and their identical coupling to the photonic field. When these assumptions are relaxed, intermediate superradiant regimes can still be obtained [32, 36, 230–233], resulting from the population of different Dicke ladders [160, 234], experimentally verified in solid-state systems [176, 180, 182]. In that case, a bosonic approximation in terms of polaritonic populations can be performed, but only in the low-excitation regime [234, 235]. In the presence of local incoherent pumping and collective dissipation, the superradiant phase [236] and steady-state superradiant emission [237] have been proposed and observed in cavity QED setups with atomic clouds

[238, 239]. Similarly, trapped ions and atomic lattices provide the opportunity to engineer long-range interactions and dissipation [240, 241], relevant also for the implementation of the anisotropic Heisenberg models [242].

APPENDIX D

Time-dependent variational principle for the (cluster-)Gutzwiller ansatz

The time-dependent variational principle ensures that the time evolution of a variational wave function with the system's Hamiltonian is restricted to the manifold of the wave function under consideration [243]. Let us for a moment assume that our variational wave function is given by a single-site Gutzwiller ansatz

$$|\psi\rangle = \bigotimes_i |\psi_i\rangle, \tag{D.1}$$

and we wish to use it to calculate the time evolution of a system governed by an effective Hamiltonian

$$\hat{H}_{\text{eff}} = \hat{H} - i\frac{\gamma}{2}\sum_i \hat{L}_i^\dagger \hat{L}_i = \sum_k \hat{H}_k + \sum_{\langle k,k'\rangle} \hat{H}_{k,k'}, \tag{D.2}$$

where $\hat{H}$ consists of a sum over local terms $\hat{H}_k$ as well as a sum over nearest-neighbour interactions $\hat{H}_{k,k'}$. In the quantum trajectory approach this corresponds to a (unnormalized) time evolution between the jumps that is given by

$$|\psi(t)\rangle = \exp\left(-i\hat{H}_{\text{eff}}\right)|\psi_0\rangle, \tag{D.3}$$

with $|\psi_0\rangle$ an initially normalized wave function of the Gutzwiller form (D.1). Since the Hamiltonian $\hat{H}_{\text{eff}}$ consists of a sum of operators acting on the various sites in the system (as well as its neighbors), its action on $|\psi_0\rangle$ will result in a "new" wave function that is no longer of the form (D.1). In other words, the wave function has left the variational manifold of Gutzwiller wave functions. After each time step one thus has to project back onto this variational manifold. To remedy this, one can

employ the time-dependent variational principle. It is based on the minimization of the functional

$$\mathcal{F}\left[\psi,\psi^{\dagger}\right]=\left\langle\psi\middle|\partial_t+i\hat{H}_{\text{eff}}\middle|\psi\right\rangle, \tag{D.4}$$

which leads to an expression for a "new" Hamiltonian whose action keeps the wave function in the variational manifold at all times. Derivation of $\mathcal{F}\left[\psi,\psi^{\dagger}\right]$ with respect to $\langle\psi_i|$, which coincides with restricting the wave function $|\psi\rangle$ to the manifold of Gutzwiller states, and equating the result to zero yields

$$\left(\bigotimes_{j\neq i}\langle\psi_j|\right)\left[\left(\partial_t+i\hat{H}_{\text{eff}}\right)|\psi\rangle\right]=0. \tag{D.5}$$

This allows us to write for every $|\psi_i\rangle$, by using the last term of the equality in (D.2) and the fact that $\langle\psi_j|\psi_j\rangle=1$, the following expression

$$\frac{\partial}{\partial t}|\psi_i\rangle=-i\left(\hat{H}_i+\sum_{j\neq i}\langle\psi_j|\hat{H}_{i,j}|\psi_j\rangle\right)|\psi_i\rangle, \tag{D.6}$$

with the sum $\sum_{j\neq i}$ running over the nearest neighbours j of the site i. The terms $\langle\psi_j|\hat{H}_{i,j}|\psi_j\rangle$ are nothing more than the mean-field terms, i.e. those terms across the boundary of the applied cluster (in our example here a single-site cluster). By writing $\hat{H}_{i,j}$ as the product of the local operators acting on site i and j this becomes immediately clear

$$\langle\psi_j|\hat{H}_{i,j}|\psi_j\rangle=\sum_r J_{ij}^r\langle\psi_j|\hat{X}_i^r\otimes\hat{Y}_j^r|\psi_j\rangle=\sum_r J_{ij}^r\hat{X}_i^r\langle\psi_j|\hat{Y}_j^r|\psi_j\rangle, \tag{D.7}$$

with J_{ij}^r a coupling parameter for an interaction of type r and $\hat{X}_i^r$ and $\hat{Y}_j^r$ the corresponding operators acting on site i and j respectively. This derivation can be straight-forwardly extended to bigger cluster sizes, leading exactly to an equation of the form (7.12). Using the cluster notation introduced in section 7.2 and for local dissipation with a jump operator $\hat{L}_i$ we can write

$$\partial_t|\psi_C\rangle=-i\left[\hat{H}_C+\hat{H}_{\mathcal{B}(C)}-i\frac{\gamma}{2}\sum_{i\in C}\hat{L}_i^{\dagger}\hat{L}_i\right]|\psi_C\rangle, \tag{D.8}$$

which is the non-Hermitian time evolution where the variational ansatz never leaves the manifold of cluster-Gutzwiller wave functions, as desired.

APPENDIX E

(Pseudo-)algorithms for the Krilov time evolution

Algorithm 1 Arnoldi iteration

Input: $\hat{\sigma}$, a random initial density matrix; $\mathcal{L}$ the superoperator; the number m of required eigenvalues; tolerance τ.
Output: The m pairs $(\lambda_j^{\text{eff}}, \hat{\rho}_j^{\text{eff}})$ of approximated eigenvalues and eigenmatrices.

$\hat{\sigma}_1 \leftarrow \hat{\sigma}/\|\hat{\sigma}\|]$
$k \leftarrow 1$
while Convergence is not reached **do**
    $k \leftarrow k+1$
    $\hat{\nu} \leftarrow \mathcal{L}\hat{\sigma}_{k-1}$
    for $1 \leq j \leq k-1$ **do**
        $l_{j,k-1} \leftarrow \text{Tr}\left[\hat{\sigma}_j^\dagger \hat{\nu}\right] = \left\langle \hat{\sigma}_j | \hat{\nu} \right\rangle$ [recall that $l_{j,k-1}$ are the elements of $\mathcal{L}_n^{\text{eff}}$ in (9.7)]
        $\hat{\nu} \leftarrow \hat{\nu} - l_{j,k-1}\hat{\sigma}_j$
    end for
    $l_{k,k-1} \leftarrow \|\hat{\nu}\|$
    diagonalize $\mathcal{L}_n^{\text{eff}}$ and define the pairs $(\lambda_j^{\text{eff}}, \hat{\rho}_j^{\text{eff}})$
    if $l_{k,k-1} = 0$ (numerically) **or** $\|(\mathcal{L} - \lambda_l^{\text{eff}})\hat{\rho}_j^{\text{eff}}\| < \tau$ for all $l < m$ **then**
        Convergence is reached
    else
        $\hat{\sigma}_k \leftarrow \hat{\nu}/\|\hat{\nu}\|$
    end if
end while

Algorithm 2 Krilov time evolution

Input: $\hat{\sigma}$, a random initial density matrix; $\hat{H}$ the Hamiltonian; $\{\hat{J}_\mu\}$ the set of jump operators; time T for each step; the number m of required eigenvalues; tolerance τ.
Output: The m pairs $(\lambda_j^{\text{eff}}, \hat{\rho}_j^{\text{eff}})$ of approximated eigenvalues and eigenmatrices of the Liouvillian.

define two functions, one which returns $\mathcal{L}\rho(t)$, and one which returns $\hat{\rho}(t+T)$ given $\hat{\rho}(t)$ using the Hamiltonian $\hat{H}$, $\{\hat{J}_\mu\}$ and the jump operators. We will indicate them as $\mathcal{L}\rho$ and $\mathcal{E}\rho$ even if $\mathcal{L}$ or $\mathcal{E}$ are never explicitly used
$\hat{\sigma}_1 \leftarrow \hat{\sigma}/\|\hat{\sigma}\|]$
$k \leftarrow 1$
while Convergence is not reached **do**
    $k \leftarrow k+1$
    $\hat{v} \leftarrow$ time evolution of $\hat{\sigma}_{k-1}$ for a time T
    for $1 \le j \le k-1$ **do**
        $e_{j,k-1} \leftarrow \text{Tr}\left[\hat{\sigma}_j^\dagger \hat{v}\right] = \langle \hat{\sigma}_j | \hat{v} \rangle$ [recall that $e_{j,k-1}$ are the elements of $\mathcal{E}_n^{\text{eff}}$ in (9.13)]
        $\hat{v} \leftarrow \hat{v} - e_{j,k-1}\hat{\sigma}_j$
    end for
    $e_{k,k-1} \leftarrow \|\hat{v}\|$
    diagonalize $\mathcal{E}_n^{\text{eff}}$ and define the pairs $(\epsilon_j^{\text{eff}}, \hat{\rho}_j^{\text{eff}})$
    if $e_{k,k-1} = 0$ (numerically) **or** $\left\| \text{Tr}\left[\left(\hat{\rho}_j^{\text{eff}}\right)^\dagger \mathcal{L}\hat{\rho}_j^{\text{eff}}\right]\right\|^2 - \left\| \text{Tr}\left[\left(\hat{\rho}_j^{\text{eff}}\right)^\dagger \mathcal{L}^2\hat{\rho}_j^{\text{eff}}\right]\right\| < \tau$ for all $l < m$ **then**
        Convergence is reached
    else
        $\hat{\sigma}_k \leftarrow \hat{v}/\|\hat{v}\|$
    end if
end while

Bibliography

[1]D. Huybrechts and M. Wouters, "Cluster methods for the description of a driven-dissipative spin model", Phys. Rev. A **99**, 043841 (2019).

[2]D. Huybrechts, F. Minganti, F. Nori, M. Wouters, and N. Shammah, "Validity of mean-field theory in a dissipative critical system: liouvillian gap, $\mathbb{PT}$-symmetric antigap, and permutational symmetry in the *XYZ* model", Phys. Rev. B **101**, 214302 (2020).

[3]D. Huybrechts and M. Wouters, "Dynamical hysteresis properties of the driven-dissipative bose-hubbard model with a gutzwiller monte carlo approach", Phys. Rev. A **102**, 053706 (2020).

[4]M. A. Nielsen and I. L. Chuang, *Quantum computation and quantum information: 10th anniversary edition*, 10th (Cambridge University Press, USA, 2011).

[5]H. Breuer and F. Petruccione, *The theory of open quantum systems* (OUP Oxford, 2007).

[6]C. Gardiner and P. Zoller, *Quantum noise: a handbook of markovian and non-Markovian quantum stochastic methods with applications to quantum optics* (Springer, 2004).

[7]H. Wiseman and G. Milburn, *Quantum measurement and control* (Cambridge University Press, 2010).

[8]S. Haroche and J. M. Raimond, *Exploring the quantum: atoms, cavities, and photons* (Oxford University Press, 2006).

[9]D. F. Walls and G. J. Milburn, *Quantum optics* (Springer Science & Business Media), 424 pp.

[10]H. J. Carmichael, *Statistical methods in quantum optics 1: master equations and fokker-planck equations* (Springer-Verlag, 1999).

[11]A. G. Redfield, "On the theory of relaxation processes", IBM Journal of Research and Development **1**, 19–31 (1957).

[12]V. Gorini, A. Kossakowski, and E. C. G. Sudarshan, "Completely positive dynamical semigroups of n-level systems", Journal of Mathematical Physics **17**, 821–825 (1976).

[13]G. Lindblad, "On the generators of quantum dynamical semigroups", Communications in Mathematical Physics **48**, 119–130 (1976).

[14]I. Carusotto and C. Ciuti, "Quantum fluids of light", Reviews of Modern Physics **85**, 299–366 (2013).

[15]S. Barnett, *Quantum information* (OUP Oxford, 2009).

[16]Á. Rivas and S. F. Huelga, *Open quantum systems: an introduction* (Springer Berlin Heidelberg, 2011).

[17]A. D. Greentree, C. Tahan, J. H. Cole, and L. C. L. Hollenberg, "Quantum phase transitions of light", Nature Physics **2**, 856 (2006).

[18]M. J. Hartmann, F. G. S. L. Brandão, and M. B. Plenio, "Strongly interacting polaritons in coupled arrays of cavities", Nature Physics **2**, 849 (2006).

[19]D. G. Angelakis, M. F. Santos, and S. Bose, "Photon-blockade-induced Mott transitions and *XY* spin models in coupled cavity arrays", Phys. Rev. A **76**, 031805 (2007).

[20]M. J. Hartmann, F. G. S. L. Brandão, and M. B. Plenio, "Quantum many-body phenomena in coupled cavity arrays", Laser and Photonics Reviews **2**, 527–556 (2008).

[21]J. Lebreuilly, A. Biella, F. Storme, et al., "Stabilizing strongly correlated photon fluids with non-Markovian reservoirs", Phys. Rev. A **96**, 033828 (2017).

[22]M. Greiner, O. Mandel, T. Esslinger, T. W. Hänsch, and I. Bloch, "Quantum phase transition from a superfluid to a Mott insulator in a gas of ultracold atoms", Nature **415**, 39 (2002).

[23]I. Bloch, J. Dalibard, and W. Zwerger, "Many-body physics with ultracold gases", Rev. Mod. Phys. **80**, 885–964 (2008).

[24]H. J. Carmichael, "Photon antibunching and squeezing for a single atom in a resonant cavity", Phys. Rev. Lett. **55**, 2790–2793 (1985).

[25]A. Imamoglu, H. Schmidt, G. Woods, and M. Deutsch, "Strongly interacting photons in a nonlinear cavity", Phys. Rev. Lett. **79**, 1467–1470 (1997).

[26]A. Miranowicz, M. Paprzycka, Y.-x. Liu, J. c. v. Bajer, and F. Nori, "Two-photon and three-photon blockades in driven nonlinear systems", Phys. Rev. A **87**, 023809 (2013).

[27]A. Kowalewska-Kudłaszyk, S. I. Abo, G. Chimczak, J. Peřina, F. Nori, and A. Miranowicz, "Two-photon blockade and photon-induced tunneling generated by squeezing", Phys. Rev. A **100**, 053857 (2019).

[28]K. M. Birnbaum, A. Boca, R. Miller, A. D. Boozer, T. E. Northup, and H. J. Kimble, "Photon blockade in an optical cavity with one trapped atom", Nature **436**, 87 (2005).

[29]C. Lang, D. Bozyigit, C. Eichler, et al., "Observation of resonant photon blockade at microwave frequencies using correlation function measurements", Phys. Rev. Lett. **106**, 243601 (2011).

[30]L. D. Landau and E. M. Lifshitz, *Statistical physics*, Vol. 5, Course of Theoretical Physics (Elsevier Science, 2013).

[31]S. Sachdev, *Quantum phase transitions* (Cambridge University Press, 2001).

[32]E. M. Kessler, G. Giedke, A. Imamoglu, S. F. Yelin, M. D. Lukin, and J. I. Cirac, "Dissipative phase transition in a central spin system", Phys. Rev. A **86**, 012116 (2012).

[33]E. G. Dalla Torre, E. Demler, T. Giamarchi, and E. Altman, "Dynamics and universality in noise-driven dissipative systems", Phys. Rev. B **85**, 184302 (2012).

[34]J. Marino and S. Diehl, "Driven markovian quantum criticality", Phys. Rev. Lett. **116**, 070407 (2016).

[35]F. Minganti, A. Biella, N. Bartolo, and C. Ciuti, "Spectral theory of Liouvillians for dissipative phase transitions", Phys. Rev. A **98**, 042118 (2018).

[36]P. Kirton and J. Keeling, "Suppressing and restoring the Dicke superradiance transition by dephasing and decay", Phys. Rev. Lett. **118**, 123602 (2017).

[37]P. Kirton, M. M. Roses, J. Keeling, and E. G. Dalla Torre, "Introduction to the Dicke model: from equilibrium to nonequilibrium, and vice versa", Advanced Quantum Technologies **2**, 1800043 (2019).

[38]S. Diehl, A. Micheli, A. Kantian, B. Kraus, H. P. Büchler, and P. Zoller, "Quantum states and phases in driven open quantum systems with cold atoms", Nat. Phys. **4**, 878 (2008).

[39]F. Verstraete, M. M. Wolf, and J. I. Cirac, "Quantum computation and quantum-state engineering driven by dissipation", Nat. Phys. **5**, 633 (2009).

[40]N. Lambert, Y.-n. Chen, R. Johansson, and F. Nori, "Quantum chaos and critical behavior on a chip", Phys. Rev. B **80**, 165308 (2009).

[41]S. Diehl, A. Tomadin, A. Micheli, R. Fazio, and P. Zoller, "Dynamical phase transitions and instabilities in open atomic many-body systems", Phys. Rev. Lett. **105**, 015702 (2010).

[42]T. E. Lee, S. Gopalakrishnan, and M. D. Lukin, "Unconventional magnetism via optical pumping of interacting spin systems", Phys. Rev. Lett. **110**, 257204 (2013).

[43]J. Iles-Smith, N. Lambert, and A. Nazir, "Environmental dynamics, correlations, and the emergence of noncanonical equilibrium states in open quantum systems", Phys. Rev. A **90**, 032114 (2014).

[44]J. Jin, A. Biella, O. Viyuela, et al., "Cluster mean-field approach to the steady-state phase diagram of dissipative spin systems", Phys. Rev. X **6**, 031011 (2016).

[45]F. Minganti, "Out-of-Equilibrium Phase Transitions in Nonlinear Optical Systems", Theses (Université Sorbonne Paris Cité, Oct. 2018).

[46]F. Wilczek, "Quantum time crystals", Phys. Rev. Lett. **109**, 160401 (2012).

[47]T. Li, Z.-X. Gong, Z.-Q. Yin, et al., "Space-time crystals of trapped ions", Phys. Rev. Lett. **109**, 163001 (2012).

[48]P. Bruno, "Comment on "quantum time crystals"", Phys. Rev. Lett. **110**, 118901 (2013).

[49]P. Nozières, "Time crystals: can diamagnetic currents drive a charge density wave into rotation?", EPL (Europhysics Letters) **103**, 57008 (2013).

[50]G. E. Volovik, "On the broken time translation symmetry in macroscopic systems: precessing states and off-diagonal long-range order", EPL (Europhysics Letters) **98**, 491 (2013).

[51]H. Watanabe and M. Oshikawa, "Absence of quantum time crystals", Phys. Rev. Lett. **114**, 251603 (2015).

[52]V. Khemani, R. Moessner, and S. L. Sondhi, "A brief history of time crystals", arXiv:1910.10745 (2019).

[53]D. V. Else, B. Bauer, and C. Nayak, "Floquet time crystals", Phys. Rev. Lett. **117**, 090402 (2016).

[54]V. Khemani, A. Lazarides, R. Moessner, and S. L. Sondhi, "Phase structure of driven quantum systems", Phys. Rev. Lett. **116**, 250401 (2016).

[55]C.-h. Fan, D. Rossini, H.-X. Zhang, J.-H. Wu, M. Artoni, and G. C. La Rocca, "Discrete time crystal in a finite chain of rydberg atoms without disorder", Phys. Rev. A **101**, 013417 (2020).

[56]S. Choi, J. Choi, R. Landig, et al., "Observation of discrete time-crystalline order in a disordered dipolar many-body system", en, Nature **543**, 221–225 (2017).

[57]J. Zhang, P. W. Hess, A. Kyprianidis, et al., "Observation of a discrete time crystal", en, Nature **543**, 217–220 (2017).

[58]F. Iemini, A. Russomanno, J. Keeling, M. Schirò, M. Dalmonte, and R. Fazio, "Boundary time crystals", Phys. Rev. Lett. **121**, 035301 (2018).

[59]N. Shammah, S. Ahmed, N. Lambert, S. De Liberato, and F. Nori, "Open quantum systems with local and collective incoherent processes: efficient numerical simulations using permutational invariance", Phys. Rev. A **98**, 063815 (2018).

[60]K Tucker, B Zhu, R. J. Lewis-Swan, et al., "Shattered time: can a dissipative time crystal survive many-body correlations?", New J. Phys. **20**, 123003 (2018).

[61]C. Lledó, T. K. Mavrogordatos, and M. H. Szymańska, "Driven bose-hubbard dimer under nonlocal dissipation: a bistable time crystal", Phys. Rev. B **100**, 054303 (2019).

[62]B. Buča, J. Tindall, and D. Jaksch, "Non-stationary coherent quantum many-body dynamics through dissipation", Nat. Commun. **10**, 1730 (2019).

[63]K. Seibold, R. Rota, and V. Savona, "Dissipative time crystal in an asymmetric nonlinear photonic dimer", Phys. Rev. A **101**, 033839 (2020).

[64]F. Minganti, I. I. Arkhipov, A. Miranowicz, and F. Nori, "Correspondence between dissipative phase transitions of light and time crystals", arXiv:2008.08075 (2020).

[65]A. Riera-Campeny, M. Moreno-Cardoner, and A. Sanpera, "Time crystallinity in open quantum systems", Quantum **4**, 270 (2020).

[66]G. Piccitto, M. Wauters, F. Nori, and N. Shammah, "Symmetries and conserved quantities of boundary time crystals in generalized spin models", arXiv:2101.05710 (2021).

[67]V. V. Albert and L. Jiang, "Symmetries and conserved quantities in Lindblad master equations", Phys. Rev. A **89**, 022118 (2014).

[68]V. V. Albert, B. Bradlyn, M. Fraas, and L. Jiang, "Geometry and response of lindbladians", Phys. Rev. X **6**, 041031 (2016).

[69]B. Baumgartner and H. N., "Analysis of quantum semigroups with GKS-Lindblad generators: ii. general", Journal of Physics A: Mathematical and Theoretical **41**, 395303 (2008).

[70]R. J. Schoelkopf and S. M. Girvin, "Wiring up quantum systems", Nature **451**, 664 EP – (2008).

[71]J. Q. You and F. Nori, "Atomic physics and quantum optics using superconducting circuits", Nature **474**, 589–597 (2011).

[72]B. Deveaud, *The physics of semiconductor microcavities: from fundamentals to nanoscale devices* (Wiley, 2007).

[73]A. Kavokin, J. J. Baumberg, G. Malpuech, and F. P. Laussy, *Microcavities* (Oxford University Press, Oxford, 2007).

[74]D. Ballarini and S. De Liberato, "Polaritonics: from microcavities to sub-wavelength confinement", Nanophotonics **8**, 641–654 (2019).

[75]M. Aspelmeyer, T. J. Kippenberg, and F. Marquardt, "Cavity optomechanics", Rev. Mod. Phys. **86**, 1391–1452 (2014).

[76]J. J. Hopfield, "Theory of the contribution of excitons to the complex dielectric constant of crystals", Phys. Rev. **112**, 1555–1567 (1958).

[77]C. Ciuti, P. Schwendimann, and A. Quattropani, "Theory of polariton parametric interactions in semiconductor microcavities", Semiconductor Science and Technology **18**, S279 (2003).

[78]H. J. Carmichael, "Breakdown of photon blockade: a dissipative quantum phase transition in zero dimensions", Phys. Rev. X **5**, 031028 (2015).

[79]H. Weimer, "Variational principle for steady states of dissipative quantum many-body systems", Phys. Rev. Lett. **114**, 040402 (2015).

[80]M. Benito, C. Sánchez Muñoz, and C. Navarrete-Benlloch, "Degenerate parametric oscillation in quantum membrane optomechanics", Phys. Rev. A **93**, 023846 (2016).

[81]J. J. Mendoza-Arenas, S. R. Clark, S. Felicetti, et al., "Beyond mean-field bistability in driven-dissipative lattices: bunching-antibunching transition and quantum simulation", Phys. Rev. A **93**, 023821 (2016).

[82]W. Casteels, F. Storme, A. Le Boité, and C. Ciuti, "Power laws in the dynamic hysteresis of quantum nonlinear photonic resonators", Phys. Rev. A **93**, 033824 (2016).

[83]N. Bartolo, F. Minganti, W. Casteels, and C. Ciuti, "Exact steady state of a Kerr resonator with one- and two-photon driving and dissipation: controllable Wigner-function multimodality and dissipative phase transitions", Phys. Rev. A **94**, 033841 (2016).

[84]W. Casteels and C. Ciuti, "Quantum entanglement in the spatial-symmetry-breaking phase transition of a driven-dissipative Bose-Hubbard dimer", Phys. Rev. A **95**, 013812 (2017).

[85]W. Casteels, R. Fazio, and C. Ciuti, "Critical dynamical properties of a first-order dissipative phase transition", Phys. Rev. A **95**, 012128 (2017).

[86]M. Foss-Feig, P. Niroula, J. T. Young, et al., "Emergent equilibrium in many-body optical bistability", Phys. Rev. A **95**, 043826 (2017).

[87]M. Biondi, G. Blatter, H. E. Türeci, and S. Schmidt, "Nonequilibrium gas-liquid transition in the driven-dissipative photonic lattice", Phys. Rev. A **96**, 043809 (2017).

[88]A. Biella, F. Storme, J. Lebreuilly, et al., "Phase diagram of incoherently driven strongly correlated photonic lattices", Phys. Rev. A **96**, 023839 (2017).

[89]V. Savona, "Spontaneous symmetry breaking in a quadratically driven nonlinear photonic lattice", Phys. Rev. A **96**, 033826 (2017).

[90]C. Sánchez Muñoz, A. Lara, J. Puebla, and F. Nori, "Hybrid systems for the generation of nonclassical mechanical states via quadratic interactions", Phys. Rev. Lett. **121**, 123604 (2018).

[91]F. Vicentini, F. Minganti, R. Rota, G. Orso, and C. Ciuti, "Critical slowing down in driven-dissipative Bose-Hubbard lattices", Phys. Rev. A **97**, 013853 (2018).

[92]W. Verstraelen and M. Wouters, "Gaussian quantum trajectories for the variational simulation of open quantum-optical systems", Applied Sciences **8**, 10.3390/app8091427 (2018).

[93]W. Verstraelen and M. Wouters, "Classical critical dynamics in quadratically driven kerr resonators", Phys. Rev. A **101**, 043826 (2020).

[94]W. Verstraelen, R. Rota, V. Savona, and M. Wouters, "Gaussian trajectory approach to dissipative phase transitions: the case of quadratically driven photonic lattices", Phys. Rev. Research **2**, 022037 (2020).

[95]L. M. Sieberer, S. D. Huber, E. Altman, and S. Diehl, "Dynamical critical phenomena in driven-dissipative systems", Phys. Rev. Lett. **110**, 195301 (2013).

[96]L. M. Sieberer, S. D. Huber, E. Altman, and S. Diehl, "Nonequilibrium functional renormalization for driven-dissipative Bose-Einstein condensation", Phys. Rev. B **89**, 134310 (2014).

[97]E. Altman, L. M. Sieberer, L. Chen, S. Diehl, and J. Toner, "Two-dimensional superfluidity of exciton polaritons requires strong anisotropy", Phys. Rev. X **5**, 011017 (2015).

[98]S. Morrison and A. S. Parkins, "Collective spin systems in dispersive optical cavity QED: quantum phase transitions and entanglement", Phys. Rev. A **77**, 043810 (2008).

[99]S. Morrison and A. S. Parkins, "Dynamical quantum phase transitions in the dissipative Lipkin-Meshkov-Glick model with proposed realization in optical cavity qed", Phys. Rev. Lett. **100**, 040403 (2008).

[100]T. E. Lee, H. Häffner, and M. C. Cross, "Antiferromagnetic phase transition in a nonequilibrium lattice of Rydberg atoms", Phys. Rev. A **84**, 031402 (2011).

[101]T. E. Lee, C.-K. Chan, and S. F. Yelin, "Dissipative phase transitions: independent versus collective decay and spin squeezing", Phys. Rev. A **90**, 052109 (2014).

[102]C. Chan, T. E. Lee, and S. Gopalakrishnan, "Limit-cycle phase in driven-dissipative spin systems", Phys. Rev. A **91**, 051601 (2015).

[103]M. F. Maghrebi and A. V. Gorshkov, "Nonequilibrium many-body steady states via Keldysh formalism", Phys. Rev. B **93**, 014307 (2016).

[104]R. Rota, F. Storme, N. Bartolo, R. Fazio, and C. Ciuti, "Critical behavior of dissipative two-dimensional spin lattices", Phys. Rev. B **95**, 134431 (2017).

[105]V. R. Overbeck, M. F. Maghrebi, A. V. Gorshkov, and H. Weimer, "Multicritical behavior in dissipative Ising models", Phys. Rev. A **95**, 042133 (2017).

[106]D. Roscher, S. Diehl, and M. Buchhold, "Phenomenology of first-order dark-state phase transitions", Phys. Rev. A **98**, 062117 (2018).

[107]R. Rota, F. Minganti, A. Biella, and C. Ciuti, "Dynamical properties of dissipative XYZ Heisenberg lattices", New Journal of Physics **20**, 045003 (2018).

[108]H. Landa, M. Schiró, and G. Misguich, "Multistability of driven-dissipative quantum spins", Phys. Rev. Lett. **124**, 043601 (2020).

[109]J. M. Fink, A. Dombi, A. Vukics, A. Wallraff, and P. Domokos, "Observation of the photon-blockade breakdown phase transition", Phys. Rev. X **7**, 011012 (2017).

[110]A. A. Houck, H. E. Tureci, and J. Koch, "On-chip quantum simulation with superconducting circuits", Nat Phys **8**, 292 (2012).

[111]M. Fitzpatrick, N. M. Sundaresan, A. C. Y. Li, J. Koch, and A. A. Houck, "Observation of a dissipative phase transition in a one-dimensional circuit QED lattice", Phys. Rev. X **7**, 011016 (2017).

[112]M. Müller, S. Diehl, G. Pupillo, and P. Zoller, "Engineered open systems and quantum simulations with atoms and ions", Adv. At. Mol. Opt. Phys. **61**, 1 (2012).

[113]H. Bernien, S. Schwartz, A. Keesling, et al., "Probing many-body dynamics on a 51-atom quantum simulator", Nature **551**, 579 EP – (2017).

[114]E. Gil-Santos, M. Labousse, C. Baker, et al., "Light-mediated cascaded locking of multiple nano-optomechanical oscillators", Phys. Rev. Lett. **118**, 063605 (2017).

[115]J. Kasprzak, M. Richard, S. Kundermann, et al., "Bose-Einstein condensation of exciton polaritons", Nature **443**, 409–414 (2006).

[116]S. R. K. Rodriguez, W. Casteels, F. Storme, et al., "Probing a dissipative phase transition via dynamical optical hysteresis", Phys. Rev. Lett. **118**, 247402 (2017).

[117]T. Fink, A. Schade, S. Höfling, C. Schneider, and A. Imamoglu, "Signatures of a dissipative phase transition in photon correlation measurements", Nature Physics **14**, 365–369 (2018).

[118]M. J. Hartmann, F. G. S. L. Brandão, and M. B. Plenio, "Effective spin systems in coupled microcavities", Phys. Rev. Lett. **99**, 160501 (2007).

[119]A. Kay and D. G. Angelakis, "Reproducing spin lattice models in strongly coupled atom-cavity systems", EPL (Europhysics Letters) **84**, 20001 (2008).

[120]S. Puri, C. K. Andersen, A. L. Grimsmo, and A. Blais, "Quantum annealing with all-to-all connected nonlinear oscillators", Nature Communications **8**, 15785 (2017).

[121]J. Qian, G. Dong, L. Zhou, and W. Zhang, "Phase diagram of Rydberg atoms in a nonequilibrium optical lattice", Phys. Rev. A **85**, 065401 (2012).

[122]M. Viteau, P. Huillery, M. G. Bason, et al., "Cooperative excitation and many-body interactions in a cold Rydberg gas", Phys. Rev. Lett. **109**, 053002 (2012).

[123]A. W. Glaetzle, M. Dalmonte, R. Nath, C. Gross, I. Bloch, and P. Zoller, "Designing frustrated quantum magnets with laser-dressed Rydberg atoms", Phys. Rev. Lett. **114**, 173002 (2015).

[124]J. Qian, L. Zhang, J. Zhai, and W. Zhang, "Dynamical phases in a one-dimensional chain of heterospecies Rydberg atoms with next-nearest-neighbor interactions", Phys. Rev. A **92**, 063407 (2015).

[125]T. L. Nguyen, J. M. Raimond, C. Sayrin, et al., "Towards quantum simulation with circular Rydberg atoms", Phys. Rev. X **8**, 011032 (2018).

[126]A. Kshetrimayum, H. Weimer, and R. Orús, "A simple tensor network algorithm for two-dimensional steady states", Nature Communications **8**, 1291 (2017).

[127]A. Biella, J. Jin, O. Viyuela, C. Ciuti, R. Fazio, and D. Rossini, "Linked cluster expansions for open quantum systems on a lattice", Phys. Rev. B **97**, 035103 (2018).

[128]W. Casteels, R. M. Wilson, and M. Wouters, "Gutzwiller Monte Carlo approach for a critical dissipative spin model", Phys. Rev. A **97**, 062107 (2018).

[129]J. Jin, D. Rossini, M. Leib, M. J. Hartmann, and R. Fazio, "Steady-state phase diagram of a driven QED-cavity array with cross-Kerr nonlinearities", Phys. Rev. A **90**, 023827 (2014).

[130]E. T. Owen, J Jin, D Rossini, R Fazio, and M. J. Hartmann, "Quantum correlations and limit cycles in the driven-dissipative heisenberg lattice", New Journal of Physics **20**, 045004 (2018).

[131]X. Li and J. Jin, "Nonuniform phases in the geometrically frustrated dissipative xyz model", Phys. Rev. B **103**, 035127 (2021).

[132]S. Finazzi, A. Le Boité, F. Storme, A. Baksic, and C. Ciuti, "Corner-space renormalization method for driven-dissipative two-dimensional correlated systems", Phys. Rev. Lett. **115**, 080604 (2015).

[133]F. Verstraete, J. J. García-Ripoll, and J. I. Cirac, "Matrix product density operators: simulation of finite-temperature and dissipative systems", Phys. Rev. Lett. **93**, 207204 (2004).

[134]M. Zwolak and G. Vidal, "Mixed-state dynamics in one-dimensional quantum lattice systems: a time-dependent superoperator renormalization algorithm", Phys. Rev. Lett. **93**, 207205 (2004).

[135]D. Kilda, A. Biella, M. Schiró, R. Fazio, and J. Keeling, *On the stability of the infinite projected entangled pair operator ansatz for driven-dissipative 2d lattices*, 2020.

[136]C. M. Keever and M. H. Szymańska, *Dynamics of two-dimensional open quantum lattice models with tensor networks*, 2020.

[137]A. Nagy and V. Savona, "Variational quantum monte carlo method with a neural-network ansatz for open quantum systems", Phys. Rev. Lett. **122**, 250501 (2019).

[138]M. J. Hartmann and G. Carleo, "Neural-network approach to dissipative quantum many-body dynamics", Phys. Rev. Lett. **122**, 250502 (2019).

[139]F. Vicentini, A. Biella, N. Regnault, and C. Ciuti, "Variational neural-network ansatz for steady states in open quantum systems", Phys. Rev. Lett. **122**, 250503 (2019).

[140]N. Yoshioka and R. Hamazaki, "Constructing neural stationary states for open quantum many-body systems", Phys. Rev. B **99**, 214306 (2019).

[141]M. Reh, M. Schmitt, and M. Gärttner, "Time-dependent variational principle for open quantum systems with artificial neural networks", arXiv:2104.00013v2 (2021).

[142]D. Luo, Z. Chen, J. Carrasquilla, and B. K. Clark, "Autoregressive neural network for simulating open quantum systems via a probabilistic formulation", arXiv:2009.05580 (2021).

[143]H. Weimer, A. Kshetrimayum, and R. Orús, "Simulation methods for open quantum many-body systems", Rev. Mod. Phys. **93**, 015008 (2021).

[144]W Casteels, S Finazzi, A. L. Boité, F Storme, and C Ciuti, "Truncated correlation hierarchy schemes for driven-dissipative multimode quantum systems", New Journal of Physics **18**, 093007 (2016).

[145]A. Le Boité, G. Orso, and C. Ciuti, "Bose-Hubbard model: relation between driven-dissipative steady states and equilibrium quantum phases", Phys. Rev. A **90**, 063821 (2014).

[146]M. Biondi, S. Lienhard, G. Blatter, H. E. Türeci, and S. Schmidt, "Spatial correlations in driven-dissipative photonic lattices", New Journal of Physics **19**, 125016 (2017).

[147]F. Vicentini, F. Minganti, A. Biella, G. Orso, and C. Ciuti, "Optimal stochastic unraveling of disordered open quantum systems: application to driven-dissipative photonic lattices", Phys. Rev. A **99**, 032115 (2019).

[148]A. Le Boité, G. Orso, and C. Ciuti, "Steady-state phases and tunneling-induced instabilities in the driven dissipative bose-hubbard model", Phys. Rev. Lett. **110**, 233601 (2013).

[149]P. D. Drummond and D. F. Walls, "Quantum theory of optical bistability. i. nonlinear polarisability model", J.Phys. A **13**, 725–741 (1980).

[150]P. D. Drummond and M. Hillery, *The quantum theory of nonlinear optics* (Cambridge University Press, 2014), 385 pp.

[151]A. Le Boité, G. Orso, and C. Ciuti, "Steady-state phases and tunneling-induced instabilities in the driven dissipative Bose-Hubbard model", Phys. Rev. Lett. **110**, 233601 (2013).

[152]M. Biondi, E. P. L. van Nieuwenburg, G. Blatter, S. D. Huber, and S. Schmidt, "Incompressible polaritons in a flat band", Phys. Rev. Lett. **115**, 143601 (2015).

[153]K. Vogel and H. Risken, "Quasiprobability distributions in dispersive optical bistability", Physical Review A **39**, 4675–4683 (1989).

[154]I. Carusotto and C. Ciuti, "Spontaneous microcavity-polariton coherence across the parametric threshold: quantum monte carlo studies", Phys. Rev. B **72**, 125335 (2005).

[155]M. Van Regemortel, W. Casteels, I. Carusotto, and M. Wouters, "Spontaneous beliaev-landau scattering out of equilibrium", Phys. Rev. A **96**, 053854 (2017).

[156]E. Mascarenhas, "Diffusive-gutzwiller approach to the quadratically driven photonic lattice", arXiv:1712.00987 (2017).

[157]D. Jaschke, S. Montangero, and L. D. Carr, "One-dimensional many-body entangled open quantum systems with tensor network methods", Quantum Science and Technology **4**, 013001 (2018).

[158]L. Bonnes, D. Charrier, and A. M. Läuchli, "Dynamical and steady-state properties of a bose-hubbard chain with bond dissipation: a study based on matrix product operators", Phys. Rev. A **90**, 033612 (2014).

[159]M. J. Hartmann, "Polariton crystallization in driven arrays of lossy nonlinear resonators", Phys. Rev. Lett. **104**, 113601 (2010).

[160]M. Gegg and M. Richter, "Efficient and exact numerical approach for many multi-level systems in open system CQED", New J. Phys. **18**, 043037 (2016).

[161]N. Shammah, S. Ahmed, N. Lambert, S. De Liberato, and F. Nori, "Open quantum systems with local and collective incoherent processes: efficient numerical simulations using permutational invariance", Phys. Rev. A **98**, 063815 (2018).

[162]G. Berman and K. Fryer, *Introduction to combinatorics* (Academic Press, 1972).

[163]R. H. Dicke, "Coherence in spontaneous radiation processes", Phys. Rev. **93**, 99–110 (1954).

[164]P. Kirton, M. M. Roses, J. Keeling, and E. G. Dalla Torre, "Introduction to the dicke model: from equilibrium to nonequilibrium, and vice versa", Advanced Quantum Technologies **2**, 1800043 (2019).

[165]L. Mandel and E. Wolf, *Optical coherence and quantum optics* (Cambridge University Press, 1995).

[166]M. Gegg and M. Richter, "Psiquasp–a library for efficient computation of symmetric open quantum systems", Scientific Reports **7**, 16304 (2016).

[167]J. Johansson, P. Nation, and F. Nori, "QuTiP: an open-source python framework for the dynamics of open quantum systems", Computer Physics Communications **183**, 1760–1772 (2012).

[168]J. Johansson, P. Nation, and F. Nori, "QuTiP 2: a python framework for the dynamics of open quantum systems", Computer Physics Communications **184**, 1234–1240 (2013).

[169]R. Pathria and P. Beale, *Statistical mechanics* (Elsevier Science, 2011).

[170]R. M. Wilson, K. W. Mahmud, A. Hu, A. V. Gorshkov, M. Hafezi, and M. Foss-Feig, "Collective phases of strongly interacting cavity photons", Phys. Rev. A **94**, 033801 (2016).

[171]J. Preskill, "Quantum Computing in the NISQ era and beyond", Quantum **2**, 79 (2018).

[172]A. Russomanno, F. Iemini, M. Dalmonte, and R. Fazio, "Floquet time crystal in the Lipkin-Meshkov-Glick model", Phys. Rev. B **95**, 214307 (2017).

[173]J. Zhang, G. Pagano, P. W. Hess, et al., "Observation of a many-body dynamical phase transition with a 53-qubit quantum simulator", Nature **551**, 601–604 (2017).

[174]Z. Davoudi, M. Hafezi, C. Monroe, G. Pagano, A. Seif, and A. Shaw, "Towards analog quantum simulations of lattice gauge theories with trapped ions", Phys. Rev. Research **2**, 023015 (2020).

[175]A. Ramos and C. Cormick, "Feasibility of the ion-trap simulation of a class of non-equilibrium phase transitions", Eur. Phys. J. D **73**, 237 (2019).

[176]G. T. Noe II, J.-H. Kim, J. Lee, et al., "Giant superfluorescent bursts from a semiconductor magneto-plasma", Nature Phys. **8**, 219–224 (2012).

[177]D. I. Tsomokos, S. Ashhab, and F. Nori, "Fully connected network of superconducting qubits in a cavity", New Journal of Physics **10**, 113020 (2008).

[178]K. Kakuyanagi, Y. Matsuzaki, C. Déprez, et al., "Observation of collective coupling between an engineered ensemble of macroscopic artificial atoms and a superconducting resonator", Phys. Rev. Lett. **117**, 210503 (2016).

[179]D. Marković, S. Jezouin, Q. Ficheux, et al., "Demonstration of an effective ultrastrong coupling between two oscillators", Phys. Rev. Lett. **121**, 040505 (2018).

[180]A. Angerer, K. Streltsov, T. Astner, et al., "Superradiant emission from colour centres in diamond", Nature Phys., 10.1038/s41567-018-0269-7 (2018).

[181]M. Gärttner, J. G. Bohnet, A. Safavi-Naini, M. L. Wall, J. J. Bollinger, and A. M. Rey, "Measuring out-of-time-order correlations and multiple quantum spectra in a trapped-ion quantum magnet", Nature Physics **13**, 781–786 (2017).

[182]C. Bradac, M. T. Johnsson, M. v. Breugel, et al., "Room-temperature spontaneous superradiance from single diamond nanocrystals", Nature Comm. **8**, 1205 (2017).

[183]A. Angerer, S. Putz, D. O. Krimer, et al., "Ultralong relaxation times in bistable hybrid quantum systems", Science Advances **3**, 10.1126/sciadv.1701626 (2017).

[184]B. Buča and T. Prosen, "A note on symmetry reductions of the Lindblad equation: transport in constrained open spin chains", New Journal of Physics **14**, 073007 (2012).

[185]R. El-Ganainy, K. G. Makris, M. Khajavikhan, Z. H. Musslimani, S. Rotter, and D. N. Christodoulides, "Non-Hermitian physics and PT symmetry", Nature Physics **14**, Review Article, 11 EP – (2018).

[186]M.-A. Miri and A. Alù, "Exceptional points in optics and photonics", Science **363**, 10.1126/science.aar7709 (2019).

[187]Ş. K. Özdemir, S. Rotter, F. Nori, and L. Yang, "Parity–time symmetry and exceptional points in photonics", Nature Materials (2019).

[188]S. Scheel and A. Szameit, "Pt-symmetric photonic quantum systems with gain and loss do not exist", EPL **122**, 34001 (2018).

[189]T. Prosen, "$\mathbb{PT}$-symmetric quantum Liouvillean dynamics", Phys. Rev. Lett. **109**, 090404 (2012).

[190]T. Prosen, "Generic examples of $\mathbb{PT}$-symmetric qubit (spin-1/2) Liouvillian dynamics", Phys. Rev. A **86**, 044103 (2012).

[191]M. van Caspel and V. Gritsev, "Symmetry-protected coherent relaxation of open quantum systems", Phys. Rev. A **97**, 052106 (2018).

[192]P. D. Nation, J. R. Johansson, M. P. Blencowe, and A. J. Rimberg, "Iterative solutions to the steady-state density matrix for optomechanical systems", Phys. Rev. E **91**, 013307 (2015).

[193]C. Joshi, F. Nissen, and J. Keeling, "Quantum correlations in the one-dimensional driven dissipative XY model", Phys. Rev. A **88**, 063835 (2013).

[194]P. Kirton and J. Keeling, "Superradiant and lasing states in driven-dissipative Dicke models", New J. Phys. **20**, 015009 (2018).

[195]B. S. Chissom, "Interpretation of the kurtosis statistic", The American Statistician **24**, 19–22 (1970).

[196]K Binder, "Finite size scaling analysis of Ising model block distribution functions", Z. Physik B - Condensed Matter **43**, 119–140 (1981).

[197]K. Binder, "Critical properties from Monte Carlo coarse graining and renormalization", Phys. Rev. Lett. **47**, 693–696 (1981).

[198]F. Carollo and I. Lesanovsky, "Exactness of mean-field equations for open dicke models with an application to pattern retrieval dynamics", Phys. Rev. Lett. **126**, 230601 (2021).

[199]Q. Niu and F. Nori, "Theory of superconducting wire networks and Josephson-junction arrays in magnetic fields", Phys. Rev. B **39**, 2134–2150 (1989).

[200]S. Schmidt and G. Blatter, "Strong coupling theory for the Jaynes-Cummings-Hubbard model", Phys. Rev. Lett. **103**, 086403 (2009).

[201] B. Olmos, I. Lesanovsky, and J. P. Garrahan, "Out-of-equilibrium evolution of kinetically constrained many-body quantum systems under purely dissipative dynamics", Phys. Rev. E **90**, 042147 (2014).

[202] S. Schütz, S. B. Jäger, and G. Morigi, "Dissipation-assisted prethermalization in long-range interacting atomic ensembles", Phys. Rev. Lett. **117**, 083001 (2016).

[203] N. Defenu, T. Enss, M. Kastner, and G. Morigi, "Dynamical critical scaling of long-range interacting quantum magnets", Phys. Rev. Lett. **121**, 240403 (2018).

[204] S. Pappalardi, A. Russomanno, B. Žunkovič, F. Iemini, A. Silva, and R. Fazio, "Scrambling and entanglement spreading in long-range spin chains", Phys. Rev. B **98**, 134303 (2018).

[205] J. R. González Alonso, N. Yunger Halpern, and J. Dressel, "Out-of-time-ordered-correlator quasiprobabilities robustly witness scrambling", Phys. Rev. Lett. **122**, 040404 (2019).

[206] R. Khasseh, R. Fazio, S. Ruffo, and A. Russomanno, "Many-body synchronization in a classical Hamiltonian system", Phys. Rev. Lett. **123**, 184301 (2019).

[207] V. DeGiorgio and M. O. Scully, "Analogy between the laser threshold region and a second-order phase transition", Phys. Rev. A **2**, 1170 (1970).

[208] R. Bonifacio, M. Gronchi, and L. A. Lugiato, "Photon statistics of a bistable absorber", Phys. Rev. A **18**, 2266–2279 (1978).

[209] B. R. Mollow and R. J. Glauber, "Quantum theory of parametric amplification. i", Phys. Rev. **160**, 1076–1096 (1967).

[210] P. Drummond and H. Carmichael, "Volterra cycles and the cooperative fluorescence critical point", Opt. Commun. **27**, 160–164 (1978).

[211] H. Landa, M. Schiró, and G. Misguich, "Multistability of driven-dissipative quantum spins", Phys. Rev. Lett. **124**, 043601 (2020).

[212] L. Garbe, M. Bina, A. Keller, M. G. A. Paris, and S. Felicetti, "Critical quantum metrology with a finite-component quantum phase transition", Phys. Rev. Lett. **124**, 120504 (2020).

[213] F. Minganti, A. Miranowicz, R. W. Chhajlany, and F. Nori, "Quantum exceptional points of non-hermitian hamiltonians and liouvillians: the effects of quantum jumps", Phys. Rev. A **100**, 062131 (2019).

[214] R. Rota, F. Minganti, C. Ciuti, and V. Savona, "Quantum critical regime in a quadratically driven nonlinear photonic lattice", Phys. Rev. Lett. **122**, 110405 (2019).

[215] J. B. Curtis, I. Boettcher, J. T. Young, et al., "Critical theory for the breakdown of photon blockade", Phys. Rev. Research **3**, 023062 (2021).

[216] M.-J. Hwang, P. Rabl, and M. B. Plenio, "Dissipative phase transition in the open quantum rabi model", Phys. Rev. A **97**, 013825 (2018).

[217] F. Minganti, *Private communication*, 2021.

[218] D. O. Krimer and M. Pletyukhov, "Few-mode geometric description of a driven-dissipative phase transition in an open quantum system", Phys. Rev. Lett. **123**, 110604 (2019).

[219] P. D. Nation, "Steady-state solution methods for open quantum optical systems", arXiv:1504.06768 (2015).

[220]C. Lledó and M. H. Szymańska, "Dissipative time crystal with or without Z_2 symmetry breaking", New Journal of Physics (2020).

[221]M. Planck, "Ueber das gesetz der energieverteilung im normalspectrum", Annalen der Physik **309**, 553–563 (1901).

[222]P. Ehrenfest and H. K. Onnes, "Xxxiii. simplified deduction of the formula from the theory of combinations which planck uses as the basis of his radiation theory", The London, Edinburgh, and Dublin Philosophical Magazine and Journal of Science **29**, 297–301 (1915).

[223]R. Bonifacio and G. Preparata, "Coherent spontaneous emission", Phys. Rev. A **2**, 336–347 (1970).

[224]R. Bonifacio, P. Schwendimann, and F. Haake, "Quantum statistical theory of superradiance. I", Phys. Rev. A **4**, 302–313 (1971).

[225]R. Bonifacio and L. A. Lugiato, "Cooperative radiation processes in two-level systems: superfluorescence", Phys. Rev. A **11**, 1507–1521 (1975).

[226]E. M. Chudnovsky and D. A. Garanin, "Superradiance from crystals of molecular nanomagnets", Phys. Rev. Lett. **89**, 157201 (2002).

[227]C. Braggio, F. Chiossi, G. Carugno, A. Ortolan, and G. Ruoso, "Spontaneous formation of a macroscopically extended coherent state", Phys. Rev. Research **2**, 033059 (2020).

[228]G. Rainò, M. A. Becker, M. I. Bodnarchuk, R. F. Mahrt, M. V. Kovalenko, and T. Stöferle, "Superfluorescence from lead halide perovskite quantum dot superlattices", Nature **563**, 671675 (2018).

[229]N. Lambert, C. Emary, and T. Brandes, "Entanglement and the phase transition in single-mode superradiance", Phys. Rev. Lett. **92**, 073602 (2004).

[230]R. H. Lehmberg, "Radiation from an N-atom system. I. General formalism", Phys. Rev. A **2**, 883–888 (1970).

[231]M. Buchhold, P. Strack, S. Sachdev, and S. Diehl, "Dicke-model quantum spin and photon glass in optical cavities: nonequilibrium theory and experimental signatures", Phys. Rev. A **87**, 063622 (2013).

[232]N. Lambert, Y. Matsuzaki, K. Kakuyanagi, N. Ishida, S. Saito, and F. Nori, "Superradiance with an ensemble of superconducting flux qubits", Phys. Rev. B **94**, 224510 (2016).

[233]E. G. Dalla Torre, Y. Shchadilova, E. Y. Wilner, M. D. Lukin, and E. Demler, "Dicke phase transition without total spin conservation", Phys. Rev. A **94**, 061802 (2016).

[234]N. Shammah, N. Lambert, F. Nori, and S. De Liberato, "Superradiance with local phase-breaking effects", Phys. Rev. A **96**, 023863 (2017).

[235]M. Cirio, N. Shammah, N. Lambert, S. De Liberato, and F. Nori, "Multielectron ground state electroluminescence", Phys. Rev. Lett. **122**, 190403 (2019).

[236]F. Dimer, B. Estienne, A. S. Parkins, and H. J. Carmichael, "Proposed realization of the Dicke-model quantum phase transition in an optical cavity QED system", Phys. Rev. A **75**, 013804 (2007).

[237] D. Meiser and M. J. Holland, "Steady-state superradiance with alkaline-earth-metal atoms", Phys. Rev. A **81**, 033847 (2010).

[238] K. Baumann, C. Guerlin, F. Brennecke, and T. Esslinger, "Dicke quantum phase transition with a superfluid gas in an optical cavity", Nature **464**, 1301–1306 (2010).

[239] J. G. Bohnet, Z. Chen, J. M. Weiner, D. Meiser, M. J. Holland, and J. K. Thompson, "A steady-state superradiant laser with less than one intracavity photon", Nature **484**, 78–81 (2012).

[240] A. E. Niederle, G. Morigi, and H. Rieger, "Ultracold bosons with cavity-mediated long-range interactions: a local mean-field analysis of the phase diagram", Phys. Rev. A **94**, 033607 (2016).

[241] J. Gelhausen, M. Buchhold, and P. Strack, "Many-body quantum optics with decaying atomic spin states: (γ, κ) Dicke model", Phys. Rev. A **95**, 063824 (2017).

[242] A. Bermudez, L. Tagliacozzo, G. Sierra, and P. Richerme, "Long-range Heisenberg models in quasiperiodically driven crystals of trapped ions", Phys. Rev. B **95**, 024431 (2017).

[243] P. Kramer and M. Saraceno, *Geometry of the time-dependent variational principle in quantum mechanics* (Springer-Verlag Berlin Heidelberg, Berlin, Heidelberg, 1981).